

SOILS and ROCKS

An International Journal of Geotechnical and Geoenvironmental Engineering

Editor

Renato Pinto da Cunha
University of Brasília, Brazil

Co-editor

Ana Vieira
National Laboratory for Civil Engineering, Portugal

Associate Editors

Andrea Brito
National Laboratory for Civil Engr, Portugal

Anna Silvia Palcheco Peixoto
São Paulo State University, Brazil

António Alberto S. Correia
University of Coimbra, Portugal

António Pinho
University of Évora, Portugal

Cristiana Ferreira
University of Porto, Portugal

Fernando Feitosa Monteiro
Unichristus, Brazil

Gilson de F. N. Gitirana Jr.
Federal University of Goiás, Brazil

Gregorio Luis Silva Araujo
University of Brasília, Brazil

Gustavo Pereira
Soletanche Bachy & Univ. Paris-Saclay, France

Jefferson Lins da Silva
University of São Paulo at São Carlos, Brazil

José A. Schiavon
Aeronautics Institute of Technology, Brazil

José Alberto Marques Lapa
University of Aveiro, Portugal

Leandro Neves Duarte
Federal University of São João del-Rei, Brazil

Luis Araújo Santos
Polytechnic Institute of Coimbra, Portugal

Marcio Leão
Federal University of Viçosa / IBMEC-BH, Brazil

Mariana Ramos Chrusciak
Federal University of Roraima, Brazil

Nuno Cristelo
University of Trás-os-Montes and Alto Douro, Portugal

Paulo J. R. Albuquerque
Campinas State University, Brazil

Rui Carrilho Gomes
Technical University of Lisbon, Portugal

Sara Rios
University of Porto, Portugal

Silvrano Adonias Dantas Neto
Federal University of Ceará, Brazil

Tales Moreira de Oliveira
Federal University of São João del-Rei, Brazil

Advisory Panel

Alejo O. Sfriso
University of Buenos Aires, Argentina

Harry Poulos
University of Sidney, Australia

Luis A. Vallejo
Complutense University of Madrid, Spain

Emanuel Maranha das Neves
Technical University of Lisbon, Portugal

Michele Jamiolkowski
Studio Geotecnico Italiano, Italy

Roger Frank
École des Ponts ParisTech, France

Willy Lacerda
Federal University of Rio de Janeiro, Brazil

Editorial Board

Abdelmalek Bouazza
Monash University, Australia

Alessandro Mandolini
University of Naples Federico II, Italy

Alessio Ferrari
École Polytechnique Fédérale de Lausanne, Switzerland

António Roque
National Laboratory for Civil Engineering, Portugal

António Viana da Fonseca
University of Porto, Portugal

Armando Antão
NOVA University Lisbon, Portugal

Beatrice Baudet
University College of London, UK

Catherine O'Sullivan
Imperial College London, UK

Cristhian Mendoza
National University of Colombia, Colombia

Cristina Tsuha
University of São Paulo at São Carlos, Brazil

Daniel Dias
Antea Group / Grenoble-Alpes University, France

Debasis Roy
Indian Institute of Technology Kharagpur, India

Denis Kalumba
Cape Town University, South Africa

Fangwei Yu
Inst. Mt. Haz. Env. Chinese Acad. of Sci. China

Ian Schumann M. Martins
Federal University of Rio de Janeiro, Brazil

Jean Rodrigo Garcia
Federal University of Uberlândia, Brazil

José Muralha
National Laboratory for Civil Engineering, Portugal

Kátia Vanessa Bicalho
Federal University of Espírito Santo, Brazil

Krishna R. Reddy
University of Illinois at Chicago, USA

Limin Zhang
The Hong Kong Univ. of Science Technology, China

Márcio de Souza Soares de Almeida
Federal University of Rio de Janeiro, Brazil

Marcelo Javier Sanchez Castilla
Texas A&M University College Station, USA

Marco Barla
Politecnico di Torino, Italy

Marcos Arroyo
Polytechnic University of Catalonia, Spain

Marcos Massao Futai
University of São Paulo, Brazil

Maria de Lurdes Lopes
University of Porto, Portugal

Maurício Martins Sales
Federal University of Goiás, Brazil

Nilo Cesar Consoli
Federal University of Rio Grande do Sul, Brazil

Olavo Francisco dos Santos Júnior
Federal University of Rio Grande do Norte, Brazil

Orianne Jenck
Grenoble-Alpes University, France

Paulo Vanda Oliveira
University of Coimbra, Portugal

Pijush Samui
National Institute of Technology Patna, India

Rafaela Cardoso
Technical University of Lisbon, Portugal

Roberto Quental Coutinho
Federal University of Pernambuco, Brazil

Sai K. Vanapalli
University of Ottawa, Canada

Samir Maghous
Federal University of Rio Grande do Sul, Brazil

Satoshi Nishimura
Hokkaido University, Japan

Siang Huat Goh
National University of Singapore, Singapore

Tácio Mauro Campos
Pontifical Catholic University of Rio de Janeiro, Brazil

Tiago Miranda
University of Minho, Portugal

Zhen-Yu Yin
Hong Kong Polytechnic University, China

Zhongxuan Yang
Zhejiang University, China

Honorary Members

André Pacheco de Assis
Clovis Ribeiro de M. Leme (in memoriam)
Delfino L. G. Gambetti
Eduardo Soares de Macedo
Ennio Marques Palmeira
Eraldo Luporini Pastore
Francisco de Rezende Lopes
Francisco Nogueira de Jorge
Jaime de Oliveira Campos
João Augusto M. Pimenta

José Carlos A. Cintra
José Carlos Virgili
José Couto Marques
José Jorge Nader
José Maria de Camargo Barros
Manuel Matos Fernandes
Maurício Abramento
Maurício Erlich
Newton Moreira de Souza
Orencio Monje Villar

Osni José Pejón
Paulo Eduardo Lima de Santa Maria
Paulo Scarano Hemi
Ricardo Oliveira
Ronaldo Rocha
Rui Taiji Mori (in memoriam)
Sussumu Niyama
Vera Cristina Rocha da Silva
Waldemar Coelho Hachich (in memoriam)
Willy Lacerda

Soils and Rocks publishes papers in English in the broad fields of Geotechnical Engineering, Engineering Geology, and Geoenvironmental Engineering. The Journal is published quarterly in March, June, September and December. The first issue was released in 1978, under the name *Solos e Rochas*, being originally published by the Graduate School of Engineering of the Federal University of Rio de Janeiro. In 1980, the Brazilian Association for Soil Mechanics and Geotechnical Engineering took over the editorial and publishing responsibilities of *Solos e Rochas*, increasing its reach. In 2007, the journal was renamed Soils and Rocks and acquired the status of an international journal, being published jointly by the Brazilian Association for Soil Mechanics and Geotechnical Engineering, by the Portuguese Geotechnical Society, and until 2010 by the Brazilian Association for Engineering Geology and the Environment.

Soils and Rocks

1978,	1 (1, 2)
1979,	1 (3), 2 (1,2)
1980-1983,	3-6 (1, 2, 3)
1984,	7 (single number)
1985-1987,	8-10 (1, 2, 3)
1988-1990,	11-13 (single number)
1991-1992,	14-15 (1, 2)
1993,	16 (1, 2, 3, 4)
1994-2010,	17-33 (1, 2, 3)
2011,	34 (1, 2, 3, 4)
2012-2019,	35-42 (1, 2, 3)
2020,	43 (1, 2, 3, 4)
2021,	44 (1, 2, 3, 4)
2022,	45 (1, 2, 3, 4)
2023,	46 (1, 2,

ISSN 1980-9743
ISSN-e 2675-5475

CDU 624.131.1

Soils and Rocks

An International Journal of Geotechnical and Geoenvironmental Engineering

ISSN 1980-9743 ISSN-e 2675-5475

Publication of

ABMS - Brazilian Association for Soil Mechanics and Geotechnical Engineering

SPG - Portuguese Geotechnical Society

Volume 46, N. 2, April-June 2023

Special Issue

COBRAMSEG 2022 – Congresso Brasileiro de Mecânica dos Solos e Engenharia Geotécnica

Guest Editors:

Paulo J.R. Albuquerque

Universidade Estadual de Campinas, Brazil

Marcos M. Futai

Universidade de São Paulo, Brazil.

Table of Contents

EDITORIALS

Soils and Rocks reviewers in 2022

Renato P. Cunha, Ana Vieira

Introduction to the Special Issue of Soils and Rocks entitled “COBRAMSEG 2022 – Congresso Brasileiro de Mecânica dos Solos e Engenharia Geotécnica”

Paulo José Rocha de Albuquerque, Marcos Massao Futai

LECTURE

The 2022 Pacheco Silva lecture: The influence of residual loads on pile foundation behavior

Bernadete Ragoni Danziger

ARTICLES

Numerical analysis of the contribution of side resistance to caisson bearing capacity

Bárbara Estéfany Pereira, Jean Rodrigo Garcia

Maximum shear modulus and modulus degradation curves of an unsaturated tropical soil

Jeferson Brito Fernandes, Breno Padovezi Rocha, Heraldo Luiz Giacheti

Comparative study of deterministic and probabilistic critical slip surfaces applied to slope stability using limit equilibrium methods and the First-Order Reliability Method

Higor Biondo de Assis, Caio Gorla Nogueira

Determination of the dynamic parameters of Speswhite kaolin with resonant column and centrifuge tests

Filipe Cavalcanti Fernandes, Bárbara Luiza Riz de Moura, Marcio de Souza Soares de Almeida, Luciano de Oliveira Souza Junior, Samuel Felipe Mollepaza Tarazona, Maria Cascão Ferreira de Almeida, José Maria de Camargo Barros

Three-dimensional numerical analysis of the generalized group effect in monitored continuous flight auger pile groups

Lorena da Silva Leite, Paulo César de Almeida Maia, Aldo Durand Farfán

Fiber reinforcement effectiveness in two different sand specimens

Murilo Pereira da Silva Conceição, Camilla Maria Torres Pinto, Miriam de Fátima Carvalho, Sandro Lemos Machado

Influence of coconut fiber on the microstructural, mechanical and hydraulic behavior of unsaturated compacted soil

Fernanda Santos Gomes, Mariana Ferreira Benessiuti Motta, George de Paula Bernardes, Paulo Valladares Soares

Mechanical and numerical behavior of water jet-driven under-reamed concrete piles

Cesar Alberto Ruver, Giovani Jordi Bruschi

Semi-empirical method for the bearing capacity of continuous flight auger piles based on installation energy
Carlos Medeiros Silva, José Camapum de Carvalho

Geotechnical behavior of gravity dams built on sedimentary rocks: pore pressures and deformations analysis of Dona Francisca HPP foundation

Verlei Oliveira dos Santos, Luiz Antônio Bressani, Camila de Souza Dahm Smirdele

TECHNICAL NOTE

Predicting driving transferred energy without needing the hammer efficiency: three case studies

André Querelli, Tiago de Jesus Souza

CASE STUDY

Shear strength of municipal solid waste rejected from material recovery facilities in the city of São Paulo, Brazil

Mariana Barbosa Juarez, Giulliana Mondelli, Heraldo Luiz Giacheti

REVIEW ARTICLE

Use of longitudinal wave in non-destructive methods: approach to foundation and retaining elements

Isabela Grossi da Silva, Vitor Pereira Faro

Soils and Rocks reviewers in 2022

Renato P. Cunha¹ , Ana Vieira² 

EDITORIAL

Soils and Rocks is grateful for the diligent contributions of anonymous referees who provided their manuscript assessments in 2022.

Abdulrahman Aldaood
Adriano Frutuoso da Silva
Afran Sampaio Moura
Ahmad Rajabian
Aldo Durand Farfán
Alexsander Silva Mucheti
Ali Lashkari
Amanda Vielmo Sagrilo
Ana Ghislane Henriques Pereira Van Elk
Andre Cezar Zingano
Andre Luís Brasil Cavalcante
André Luiz Delmondes Filho
André Pacheco Assis
André Pacheco Assis
Andrea Cardona Pérez
Antônio Aanhas Mendonça
Antônio Alberto S. Correia
Antônio Italcly de Oliveira Júnior
Aparupa Pani
Armando Nunes Antão
Bahram Salehi
Belkacem Moussai
Bendadi Hanumantha Rao
Bianca Penteado de Almeida Tonus
Bingli Gao
Breno Padovezi Rocha
Bruno Cavalcante Mota
Bruno Guimarães Delgado
Bruno Rodrigues de Oliveira
Carina Silvani
Carla Vieira Pontes
Carlos Rodrigues
Charles Malachy Okechukwu Nwaiwu
Claudio Fernando Mahler
Cristian Yair Soriano
Cristiano Comin
Cristina de Holanda Cavalcanti Tsuha
Cristina de Hollanda Cavalcanti Tsuha
Daniel Barreto
Dimas Betioli Ribeiro
Dionatas Hoffmann Andreghetto
Elisangela Aparecida Mazzutti

Ewerton Clayton Alves Fonseca
Fernando Henrique Martins Portelinha
Fernando Saboya Jr.
Francisco Dalla Rosa
Francisco Rezende Lopes
Georg Robert Sadowski
Gheorghe Juncu
Giovanna Monique Alelvan
Gisleine Coelho de Campos
Gisleiva Cristina dos Santos Ferreira
Gregório Araújo
Grover Romer Llanque Ayala
Guanxi Yan
Hamid Reza Manaviparast
Heitor Cardoso Bernardes
Heraldo Luiz Giacheti
Hong-Lam Dang
Iman Aghamolaie
Ingrid Belcavello Rigatto
Isabelle Moreira Santiago
Javier Manzano
Jayanthi N V Prathyusha
Jean Lucas dos Passos Belo
Jean Rodrigo Garcia
Jefferson Lins da Silva
João Marcelino
João Vítor de Azambuja Carvalho
John Small
John McCartney
Jorge Arturo Pineda Jaimés
José Daniel Jales Silva
José Wilson dos Santos Ferreira
Juan Carlos Ruge
Juan Felix Rodríguez Rebolledo
Julian Buritica Garcia
Juliana Pessin
Julio Esteban Colmenares
Karl Igor Martins Guerra
Krishna R Reddy
Laurent Briançon
Leila Maria Carvalho
Letícia Menezes Santos Sá

Editors

¹Universidade de Brasília, Brasília, DF, Brasil

²National Laboratory for Civil Engineering, Lisbon, Portugal

Luan Carlos de Sena Monteiro Ozelim
Lucas Festugato
Luciana Barbosa Amancio
Luciene Oliveira Menezes
Ludger O. Suarez-Burgoa
Luís Filipe Pereira
Luiz Fernando Anchar Lopes
Mafalda Lopes Laranjo
Magnos Baroni
Manoel P. Cordão Neto
Marcelo Correa da Silva
Márcia Maria dos Anjos Mascarenha
Marco Barla
Marco Rosone
Marcus Peigas Pacheco
Maria Araujo
Maria Claudia Barbosa
Maria Eugenia Boscov
Marina Dias Ferreira
Marlísio Oliveira Cecilio Junior
Maurício Martines Sales
Mayssa Alves da Silva Sousa
Mehmet Murat Monkul
Messaouda Boutahir Born Bencheikh
Messast Salah
Michael Andrey Vargas Barrantes
Mohammed Yousif Fattah
Muthukumar Mayakrishnan
Newton Moreira de Souza
Nilo Cesar Consoli
Nuno Raposo
Orlando Martini Oliveira
Otávio Coaracy Brasil Gandolfo

Paula Milheiro
Paula Taiane Pascoal
Paulo Gustavo Cavalcante Lins
Paulo José Venda Oliveira
Pérsio Leister de Leister de Almeida Barros
Pradeep T
Rafael Lima de Carvalho
Rafaela Baldi Fernandes
Raghuv eer Negi
Rahayu Rahayu
Renato Pinto da Cunha
Renato Resende Angelim
Riheb Hadji
Roberto Aguiar dos Santos
Roberto Quental Coutinho
Rodrigo Zorzal Velten
Rui Carrilho Gomes
Sadegh Ghavami
Saif Khalil Al-Ezzi
Sanjay Jha
Santhosh Kumar Vaddepalli
Satoshi Nishimura
Satyam Tiwari
Sérgio Tibana
Thais Aquino dos Santos
Thiago Augusto Mendes
Vesna Zalar Serjun
Victor Guedes
Vitor Nascimento Aguiar
Wilson Conciani
Yuri Barbosa

Introduction to the Special Issue of Soils and Rocks entitled “COBRAMSEG 2022 – Congresso Brasileiro de Mecânica dos Solos e Engenharia Geotécnica”

Paulo José Rocha de Albuquerque^{1#} , Marcos Massao Futai^{2#} 

EDITORIAL

There are 15 papers published in this special issue of Soils and Rocks. The papers were selected among the best of 1165 papers presented in the Brazilian Conference of Soil Mechanics and Geotechnical Engineering (XX COBRAMSEG), Luso-Brazilian Congress of Geotechnics (XI CLBG), Brazilian Symposium of Rock Mechanics (IX SBMR) and Brazilian Symposium of Young Geotechnical Engineers (IX SBEGJ). The papers published in this issue of Soils and Rocks are extended versions of the papers presented during the conference.

The theme of the conference was “Innovation and Technology in Geotechnical Engineering”. The papers selected for this issue present important contributions on multiple areas, such as fiber reinforcement, pile foundations, solid waste, small strain, unsaturated soils, centrifuge tests, reliability analysis and dams.

The Pacheco Silva Conference, presented by Bernadete Ragoni Danziger, is also included in this special issue,

This issue of Soils and Rocks reflects the Brazilian contribution to improving the knowledge of academic and practical applications of geotechnical engineering. The Organizing Committees of the conferences thank the authors and reviewers for their contribution to this special issue.

Guest Editors

#Corresponding author. E-mail address: pjra@unicamp.br; futai@usp.br

¹Universidade Estadual de Campinas - Unicamp, Faculdade de Engenharia Civil, Arquitetura e Urbanismo, Campinas, SP, Brasil.

²Universidade de São Paulo - USP, Escola Politécnica, Departamento de Estruturas e Geotécnica, São Paulo, SP, Brasil.



This is an Open Access article distributed under the terms of the Creative Commons Attribution License, which permits unrestricted use, distribution, and reproduction in any medium, provided the original work is properly cited.

LECTURE

Soils and Rocks
v. 46, n. 2

The 2022 Pacheco Silva lecture: The influence of residual loads on pile foundation behavior

Bernadete Ragoni Danziger^{1#} 

Lecture

Keywords

Residual loads
Load transfer
Settlement prediction
Pile stiffness

Abstract

Residual loads can affect the load transfer and the settlement-induced in-service loadings, although they do not alter the bearing capacity. When residual loads are present and not measured or evaluated, the settlement estimate is greater than predicted if these loads are known. Residual loads can be measured when the pile instrumentation is nullified before pile installation, in the case of displacement piles, or before the first loading in non-displacement piles, such as bored cast-in-place piles, continuous flight auger piles, and micro-piles. In the case of underpinning foundation and piled raft, when the loading transfer is shared by the original and new foundation, or by the piles and the raft, it is essential to know the stiffness of each foundation element to estimate the load partition. If residual loads are present, pile stiffness is greater than when not considered in the design. The paper revisits this theme of practical relevance. A historical review of the most relevant research involving pile residual load measurements, pile loading tests including the interpretation of residual loads locked at a pile toe, and a new procedure for residual loads prediction are provided. A comparison is made of the experimental residual loads observed in some of the instrumented cases and the values estimated with the suggested procedure. The development of residual loads at the pile toe as a function of the toe resistance to total capacity ratio is very similar to the variation of the soil density as a function of soil moisture content in soil compaction.

1. Introduction

When a pile is unloaded after undergoing compression, its shaft tends to return to its original length. The surrounding soil mass restricts the complete shaft unloading and causes negative friction at the pile shaft close to ground level, which is equilibrated by the positive skin friction and the residual load at the pile toe. The pile is loaded even when no force is applied to its top, as shown in Figure 1a. The pile is pre-compressed. The neutral plane is at the elevation where the compressive residual load is maximum, and the shear stress is zero. Until the pile undergoes a greater top load than the maximum residual load, the shear resistance is reversed, and negative friction is completely nullified with a very insignificant load transferred to the shaft below the neutral plane and the pile toe. Only with an additional load applied to the pile top can the settlement at the pile toe be felt in a relevant mode, as illustrated in Figure 1b.

Residual loads are the loads locked at the pile shaft and pile toe after unloading, due to driving or static or dynamic tests, as indicated in Figure 1a.

When an instrumented pile is loaded to failure and the transfer load is observed during the test, two distinct curves can result, as shown in Figure 2. In this figure, the instruments may be zeroed at different times. In Figure 2a on the left,

the true load transfer is obtained when the instruments are zeroed before driving (or before the first loading of a non-displacement pile in a static loading test). In Figure 2b on the right, the false load transfer is obtained in a test when the instruments are zeroed after driving, or after a previous loading in a test.

The true load transfer in Figure 2a captures the residual load locked into the pile shaft and toe after driving, and the additional load mobilized by the soil at pile lateral contact and at the pile toe. From the transferred true load at failure, it is possible to separate the total mobilized resistance at failure by lateral soil resistance, $Q_{l,rupt}$, from that available by the total point resistance, $Q_{p,rupt}$. The false load transfer obtained in Figure 2b is the residual loads already present after driving (or after the previous loading) subtracted from the total true load. Only this difference is captured by the instruments zeroed after driving or after the previous loading. It is clearly noticeable in Figure 2b that the transfer curve is not the true one, as it only illustrates the load mobilized during the test. It is also clear that at the surface, $z = 0$, both curves show the same total pile bearing capacity, but at the pile toe, at $z = l$, where l is the pile length, the false load transfer curve shows a reduced point resistance value and an increased lateral resistance. The measured lateral resistance includes the true lateral resistance and the negative lateral resistance

[#]Corresponding author. E-mail address: brdanzig@uerj.br

¹Universidade do Estado do Rio de Janeiro, Rio de Janeiro, RJ, Brasil.

Submitted on March 14, 2023; Final Acceptance on March 22, 2023; Discussion open until August 31, 2023.

<https://doi.org/10.28927/SR.2023.002523>



This is an Open Access article distributed under the terms of the Creative Commons Attribution License, which permits unrestricted use, distribution, and reproduction in any medium, provided the original work is properly cited.

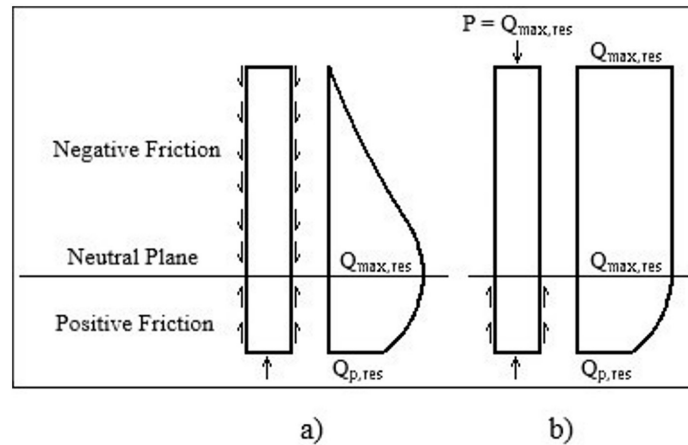


Figure 1. (a) Residual loads at pile shaft; (b) After loaded at the top with a load equal to the maximum residual load.

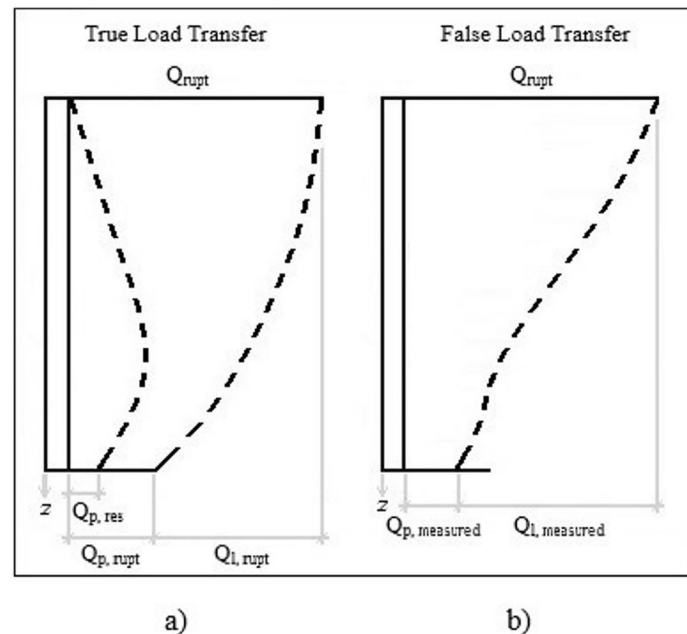


Figure 2. (a) True load transfer; (b) False load transfer.

locked into the pile shaft. The true lateral resistance is lower than the false while the true point resistance is higher than the false one, measured in a load test with instrumentation zeroed after driving or the previous loading.

According to Vesic (1977), the presence of residual loads results in an apparent concentration of skin resistance in the upper portion of the pile shaft which may cause a substantial reduction in the pile settlements. The cited author reported two projects he was involved in where the presence of residual loads had a relevant effect. In the first, the consideration of residual load resulted in a predicted settlement of one-sixth of what would be estimated by any conventional predictive method, with full confirmation by

load tests. The second case consisted of the foundation of an eight-legged oil platform in the North Sea. Each leg rested on a group of four 1.80 m outside diameter steel pipe-piles. The previous settlement analyses considering varied assumptions of over consolidation ratio of the clay occurring in the soil profile showed a value of 25 mm at working loads, without consideration of residual loads. In a revised analysis, Vesic (1977) considered the presence of residual load and estimated a settlement of 10 mm, or even smaller. Vesic (1977) also warned about the doubtful value of several theories of pile settlement behavior published in the literature in recent years which do not consider the residual load phenomenon.

2. General historical review

This session addresses a brief report of the most relevant contributions to the issue. Some contributions are also included in more detail in the following sessions, as their data are revisited in the present paper.

Hunter & Davisson (1969) proposed an interpretation of load tests considering the effect of residual stresses due to driving. The authors clarified that the residual stress does not affect the ultimate tension and compression load capacity, but solely the magnitude of toe and friction load and their distribution along the pile.

A series of loading tests on precast instrumented concrete piles driven in loose sand was described by Gregersen et al. (1973). The loading tests indicated considerable axial forces in the pile after driving, with residual loads acting in opposite ways, downwards along the top and upwards along the pile bottom.

Residual loads were also registered by Cooke & Price (1973) in a long-instrumented friction pile jacked into clay. The friction pile remained in compression after the installation force had been removed.

Holloway et al. (1978) stated that unidimensional pile interpretation for driving and static load tests lead to a satisfactory simulation when compared to measurements of residual loads.

Cooke (1979) emphasizes that residual and friction forces at the shaft arise because of the different rates of mobilization of bearing forces at the base and friction forces at the shaft in the case of driven and jacked piles. In the case of bored, cast-in-situ concrete piles, Cooke (1979) found much smaller residual forces.

Briaud & Tucker (1984) observed that the most important factors influencing the distribution and magnitude of residual loads are ultimate point and total resistance, pile length and relative pile-soil stiffness.

Goble & Hery (1984) proposed a successive-blow analysis repeated until a convergence criterion is satisfied, following a procedure suggested by Holloway et al. (1978). This proposed analysis allows the estimate of permanent displacements and residual loads.

Poulos (1987) presented an analysis for estimating the initial stresses in a driven or jacket pile in three idealized profiles: soft clay, stiff clay and medium-dense sand. He concluded that the residual toe stress is a substantial proportion of the ultimate resistance for all three types of soil, but the values of residual toe stresses are most significant for piles in sand and least significant for piles in clay.

Darrag & Lovell (1989), based on analyses made with the program from Goble et al. (1988), presented charts and equations for estimating residual stresses after pile driving.

Randolph (1991) suggested an approach for implementing residual force analysis in the interpretation of stress-wave measurements. The author's approach requires the application of the measured blow once or twice for each iteration of the

soil parameters and avoids the need for multiple repetitions of the hammer blow.

Back-analyses of closed-ended pipe piles embedded in calcareous sand for an offshore platform were performed by Danziger et al. (1992, 1999). They found high residual stresses at the pile toe, most significantly for deeper penetration.

Massad (1992) describes a mathematical model based on observed pile behavior in cases where residual stresses are locked at the pile toe from the previous loading.

Rausche et al. (1996) presented an analysis including a sequence of several blows. They included three examples of the application and described the benefits and limitations of such an analysis.

Liyanapathirana et al. (1998) presented a FEM investigation of impact driving with soil modelled as an elastic perfectly plastic material simulating one single blow. This model was then extended by Liyanapathirana et al. (2000) to simulate multiple blows. The authors could visualize the residual stresses and the soil flows around the simulated piles.

Costa et al. (2001) presented a new interpretation of a wave equation program. Instead of following most dynamic analysis, as Smith's (1960), with the set determined indirectly by subtracting the quake from the maximum displacement at pile toe, Costa et al. (2001) proposition is distinct from this one. In this new program, called DINEXP, Costa (1988), the set is determined directly, as a final longer time is previously chosen, and pile toe displacement is calculated up to this time. This final time of analysis can be adjusted until a stabilized displacement at the pile toe is achieved. When residual stresses are locked into the pile toe the stabilized displacement is higher. The difference in set (stabilized displacement) determination is called by Costa et al. (2001) residual displacement. The residual stress in a pile final driving can thus be obtained. The load locked at the pile toe is equal to the soil toe stiffness (kN/m) multiplied by the residual displacement (m).

Fellenius (2002) illustrates in Figure 3 the CPT and SPT diagrams of a test site indicating a soil of uniform density and the loads measured at the strain gauge levels at plunging failure for the static loading tests in two piles of distinct lengths. The measured load distribution curves show, for both piles, a slight S shape curve, a steep to less steep and then steep again. The slope of the load transfer curve gives an indication of the mobilized shaft resistance in the soil. Fellenius (2002) observes that the slight S-shape suggests that the shaft resistance along the middle third of the pile is larger than along the lower third. The soil field tests do not support this observed behavior. Hence, it is concluded that the S-shaped curve is typical for the results of a test on a pile affected by residual load. In this case, the measured distributions do not show the true distribution of resistance of the pile. This fact is the basis of the author's procedure to determine the true resistance.

Zhang & Wang (2007) presented a large field instrumentation program for measuring residual forces in

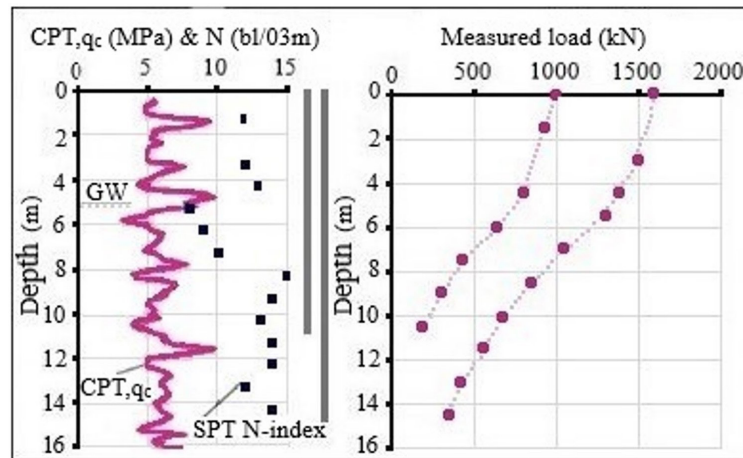


Figure 3. Field test results and measured load friction at the failure of two instrumented precast concrete piles, driven 11 m and 15 m into uniform loose sand, adapted from Fellenius (2002).

piles. The vibrating-wire strain gauges were installed before and after the installation was recorded. This study also verified that the residual forces increased when the test piles penetrated from weak layers into hard layers.

Kim et al. (2011) presented the results of a full-scale testing program involving two strain-gauge instrumented concrete piles, 600 mm outside diameter, at two nearby sites. The pile was driven to 56m, with its toe embedded into very dense sand. Three days after, the internal void was grouted. Kim et al. (2011) followed the build-up of residual load in the pile immediately after driving and up to 7 months later when static loading tests were carried out. The authors presented several results and emphasized that during the first 10 days, the strain changes were mostly due to temperature effects during hydration and swelling of the grout and concrete absorption of water from the ground.

Liu & Zhang (2012) presented the results of two 13 m long concrete pipe piles instrumented and then jacked. The field results showed that the post-jacking residual forces increased with the penetration depth. The maximum force that occurred at the neutral plane was found at 0.2 pile length above the pile toe.

Mascarucci et al. (2013) emphasized that even for cast in situ pile curing of the concrete can cause stress changes both in normal and shear stresses. In order to investigate the influence of residual loads on pile response to axial loading, they presented a parametrical study by numerical modelling.

Nie et al. (2014) compared the mechanism of residual stress in piles with negative friction after unloading. After instrumentation of a bored pile, they observed that residual stress distribution is similar to that occurring in presence of negative friction. In the case of residual stress, the adjacent soil mass prevents the pile from fully unloading.

Kou et al. (2016) instrumented five open-ended pipe piles with 13 or 18 m of embedded length. They found that the residual force increased when the pile penetrated the

hard alluvium layer from the marine deposits. They also found that the residual force distribution along the test piles is highest at a position above the toe. The neutral plane is closer to the pile toe when the piles are embedded in a hard layer. Their conclusion is the same as reported by Costa et al. (2001) who observed that the higher the toe resistance, the closer the neutral plane is to the pile toe. For the same toe resistance, when the available shaft resistance increases with depth the neutral plane is deeper than when the available shaft resistance is quite uniform.

3. Measurement of residual loads

In this and the following two sections, a more detailed analysis is presented. Some most relevant research that includes residual loads measurements, load test interpretation considering the presence of residual loads and design procedures for estimating these loads are shown. The analysis is very useful to sections 6 and 7, broadening new possibilities and discussions of future development of the issue.

Gregersen et al. (1973) instrumented four precast concrete piles embedded into very loose sand on an island called Holmen, in the city of Drammen, Norway. Pile elements denoted as A, B and D were cylindrical, 280 mm in diameter and 8 m long. The pile element C was conical with a uniform taper varying from 280 mm, at the top section, to 200 mm at the toe.

Piles A and C were first tested separately as 8 m long piles. After completion of the tests on the 8 m long piles, they were connected to elements D and B, respectively, resulting in two 16 m long piles. They were denoted as pile D/A, with a cylindrical section, and B/C, cylindrical at the top and conical at the bottom section. The instrumentation was zeroed before driving. Figure 4a shows the results of piles A and D/A and Figure 4b of piles C and B/C.

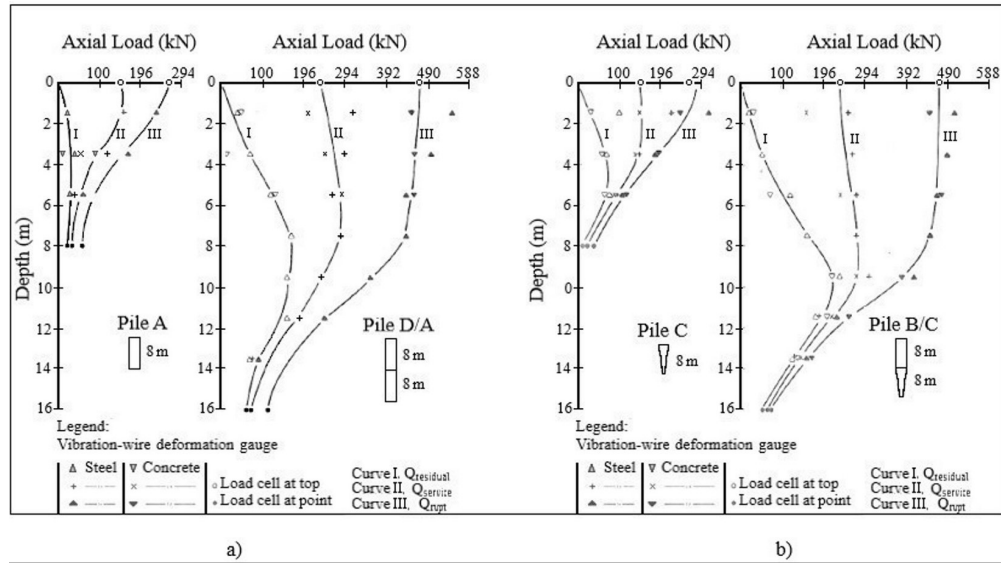


Figure 4. Compressive load on the pile with depth: (a) Piles A and D/A; (b) Piles C and B/C (adapted from Gregersen et al., 1973).

The authors verified considerable residual loads (type I curve) remaining in the piles after driving. The differences between the curves in the horizontal axis are related to the additional increment in external test loads applied to the pile top. The curves presented a similar pattern. The residual loads increase to a depth close to 2/3 the pile length, mobilizing negative skin friction, and then reduce from that level to the pile toe, mobilizing positive skin friction.

The hatched area in Figure 5 represents the false transfer curve for the service load of pile D/A. This is the curve that should be used for settlement estimation in design if the residual loads were known by measurement or prediction. This curve is obtained by the subtraction of the residual loads from the true transfer curve for service load measured when instrumentation is zeroed before driving.

Cooke (1979) instrumented a tubular steel pipe pile 0.17 m diameter and 5 m long, jacked into the London clay with undrained resistance of 35 kPa close to the surface and 78 kPa at 5 m depth. The limited travel of the hydraulic jack ram used in pile installation caused the need to unload the pile at each 0.10 m penetration. It was then possible to obtain the force-penetration diagram at 0.10 m intervals for the complete installation and the residual loads observed at each 0.1 m interval. Figure 6 presents the whole information, consisting of the continuous readings of the load cells in the pile shaft from the points where they passed beneath the ground level. At large penetrations, the residual loads at the pile base were approximately 75% of the maximum base load.

At several penetration levels, a pause was made for carrying out the incremental loading tests. The residual loads registered by the cells that had passed beneath the ground level were recorded and plotted in Figure 7. They were recorded in six different values of the penetration-diameter ratio. Cooke (1979) observed that at every ratio, the residual loads fall very

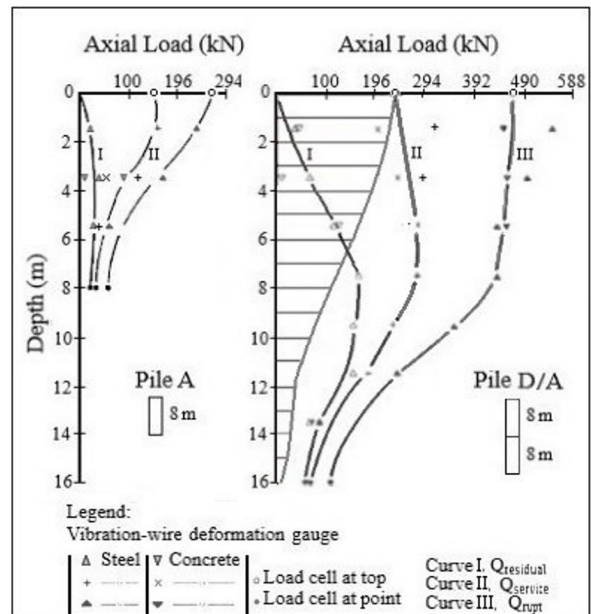


Figure 5. Hatched area illustrates the load transferred to the pile by the service load (adapted from Gregersen et al., 1973).

close to the curve through all the load cell records obtained for full penetration of the pile. The author observed that this curve represented the unique residual load relationship, a clear indication of the shaft loading expected to occur for any length of pile less than the maximum penetration.

Rieke & Crowser (1987) presented an instrumented pile load test program for a bridge foundation in W14 x 145 steel-driven piles. The soil profile consisted of 15m of loose sand superposed to compact sand with gravel. The piles were 3 m embedded into the compact sand layer. The most

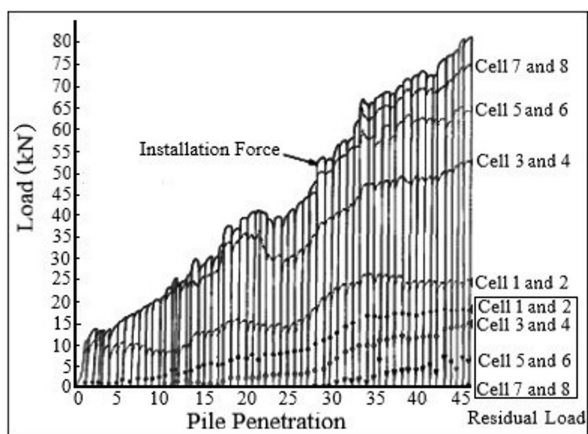


Figure 6. Installation force and pile loading at each cell position, illustrating the residual loads generated from each unloading of the pile (adapted from Cooke, 1979).

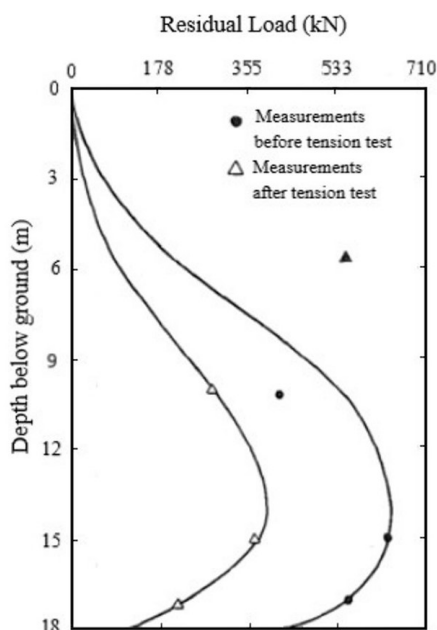


Figure 8. Residual forces in the pile before and after the tension test (adapted from Rieke & Crowser, 1987).

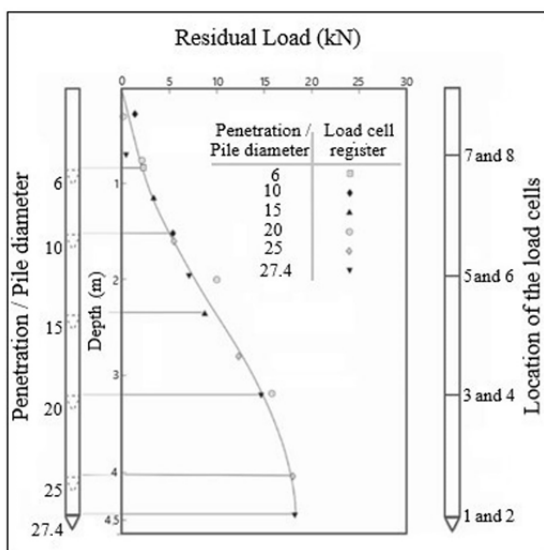


Figure 7. Residual load profile for all penetrations of the instrumented pile (adapted from Cooke, 1979).

relevant loading condition that controlled the project was the seismic loading that caused transient compressive and uplift loads. The authors observed relevant differences between the apparent (or false) and the true pile forces, a signal of the presence of residual loads. The soil was not susceptible to creep, but the authors observed that loading cycling can reduce, but not eliminate, the residual forces locked into the pile. Figure 8 illustrates the residual forces observed after driving, before the tension test, and obtained after the tension test. Rieke & Crowser (1987) concluded that both tension and compression load cycles can modify soil stresses from the original post-driving residual condition and that

the reduction in residual forces continues with additional cycles, but it is not eliminated. The authors identified two factors that can produce changes in residual loads in piles: the loading history in the case of cyclic loadings and the soil creep that can cause stress relaxation with time in plastic soils susceptible to secondary consolidation.

Briaud et al. (1989) presented an instrumented loading test of a pile group in a sandy profile and a single pile instrumented as a reference. The geometry of the closed-end-driven pile, the embedded length and the soil profile are shown in Figure 9. The instrumentation was part of a research project in San Francisco, California. The results consisted of the residual load distribution in the piles after driving, the load settlement curve of the single pile and the pile group, the load transfer curves and the maximum friction versus depth profile. Figure 10 shows the comparison between the load versus depth for different loading increments for the single pile and the central pile in the group.

The single pile presented a residual point load of 61 kN which is 11% of the ultimate point resistance. Piles in the group presented a residual load of 10 kN. Briaud et al. (1989) attributed this behavior to the fact that close to full penetration the pile driving loosens the prestressing existing under the toe of neighbouring piles.

The capacity of the group was 2499 kN, while the capacity of the single pile was 505 kN, an efficiency of 99%. At failure, the friction load of the single pile was 147 kN while the average friction load of the average pile in the group was 269 kN, a friction efficiency of 183%. The efficiency of the

point was 67%. Briaud et al. (1989) observed that a group of end-bearing piles may have efficiencies lower than 1, while a group of friction piles may have efficiencies higher than 1.

4. Load test interpretation for obtaining the residual loads

Decourt (1989) noted residual loads in piles caused by the previous loading. The significant change in the load transfer caused by the residual loads resulted in the author's suggestion of increasing the service load of excavated piles.

In a bidirectional static load test, an expansive cell is concreted together with the pile. The hydraulic activation of the cell causes its expansion, pushing the shaft upwards and the toe downward. The upward and downward displacements can be measured at cell levels (bottom and top) and the pile top. The reaction system is provided by the pile shaft and the test is carried out up to the exhaustion of the tip or friction capacity. At this moment:

$$Q_{p,mobilized} = Q_{l,rupt} \tag{1}$$

and:

$$Q_{t,mobilized} = Q_{p,mobilized} + Q_{l,rupt} = 2Q_{l,rupt} \tag{2}$$

Where $Q_{p,mobilized}$ is the toe resistance mobilized in the test that is in equilibrium with the available lateral resistance, considering the simplified premise that negative and positive skin frictions are equal. $Q_{l,rupt}$ is the ultimate lateral resistance, exhausted during the load test, and $Q_{t,mobilized}$ is the total capacity mobilized in the test.

Decourt (1989) suggests that the expansive cell should be grouted and attached to the pile. The service load could then be increased to a value up to the lateral friction mobilized in the second loading (false curve), which value would be at least double the lateral friction mobilized in the first loading. According to Figure 1, up to a load of $Q_{l,rupt}$ practically no loading would be added to the pile shaft below the neutral plane, and the lateral friction above the neutral plane would be zeroed.

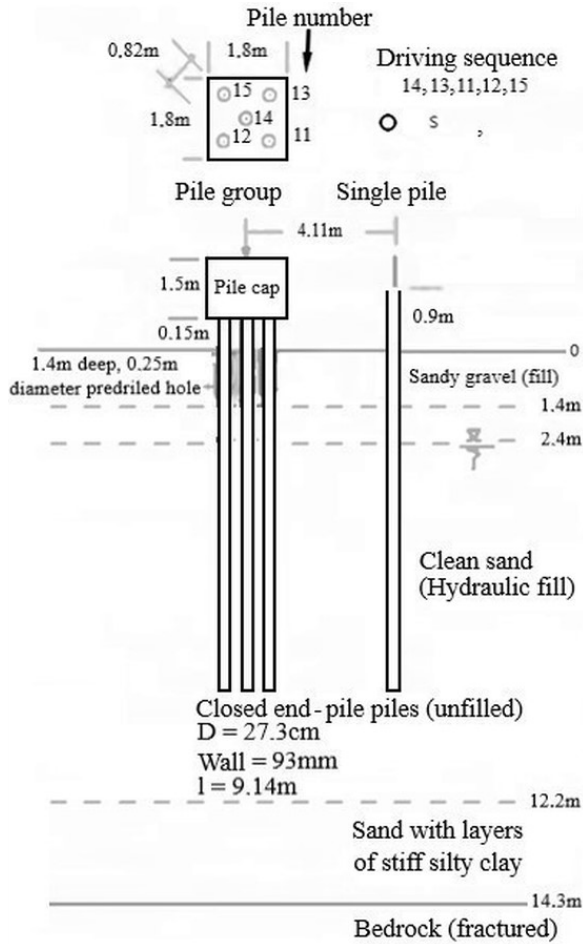


Figure 9. General test conditions (adapted from Briaud et al., 1989).

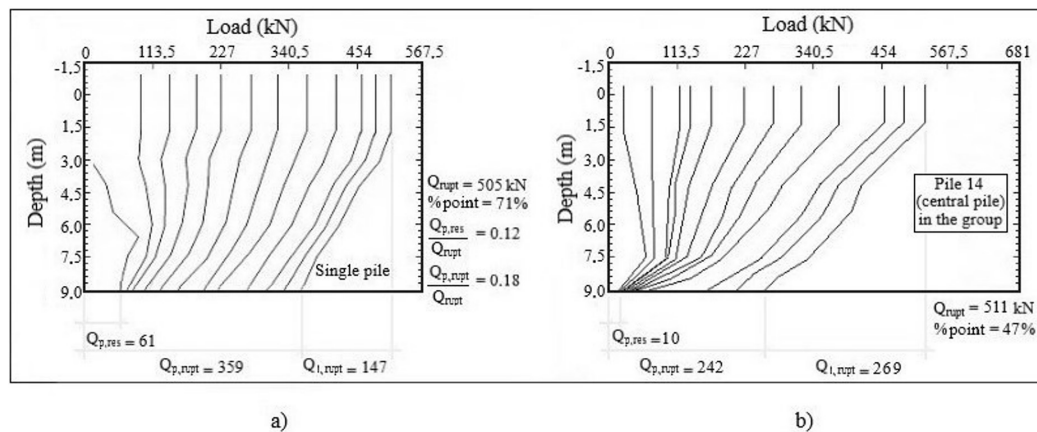


Figure 10. Load versus depth for (adapted from Briaud et al., 1989): (a) Single pile; (b) Pile 14, central pile in the group.

$2Q_{l,rupt}$, the added load would be mobilized by the positive friction above the neutral plane and the increase in the toe load would be negligible. In this condition, the settlement would be very small.

The author of the present article emphasizes two relevant issues not considered by Decourt (1989): i) although Decourt (1989) considers that friction resistance is the same in compression and in tension, which is on the safe side, the global safety factor of two is not assured if the service load is equal to $2Q_{l,rupt}$. The global safety factor of 2 is only assured if Q_{rupt} , the sum of $Q_{p,rupt}$ plus $Q_{l,rupt}$, is higher than twice the service load. ii) another simplification that is not emphasized by Decourt (1989) is the consideration of $Q_{p,residual}$ equal to $Q_{max,residual}$; it is true only if the neutral plane is at the pile toe, occurring only if the toe resistance is much greater than the lateral resistance. It is not the general case, as indicated by the piles instrumented by Gregersen et al. (1973) and Cooke (1979); iii) the cyclic loadings and the soil creep, which can cause stress relaxation over time in plastic soils susceptible to viscosity effects, must be considered in the design.

After the experience of interpreting nine (9) static load tests, most of them in instrumented piles, Decourt (1991) developed a simple method that can separate the toe and lateral resistance for piles not instrumented during the static loading test. The rebound method, as named by Decourt (1991), has the premise that the lateral resistance is the same, at compression and tension loading. As shown in Figure 2, after driving a displacement pile or after the first loading of a non-displacement pile, the true lateral load, $Q_{l,rupt}(T)$, can be obtained by Equation 3. In Equation 3 $Q_{l,measured}(F)$ is the apparent, or false, lateral load, measured during a second loading of the test, and $Q_{p,residual}$ is the unknown residual load locked into the pile toe after the previous loading. From Equation 3, Equation 4 can be easily written.

$$Q_{l,rupt}(T) = Q_{l,measured}(F) - Q_{p,residual} \quad (3)$$

$$Q_{p,residual} \leq Q_{l,rupt}(T) \quad (4)$$

The second loading in a loading test, according to Decourt (1991), has to be carried out up to at least twice the true lateral resistance, $Q_{l,rupt}$, according to Equation 5.

$$Q_{t,2} \geq 2Q_{l,rupt}(T) \quad (5)$$

In order to obtain $Q_{l,rupt}(T)$, Decourt (1991) suggests considering the loading corresponding to the displacement of 10 or 15 mm in the first loading curve, or half of the loading corresponding to the pile rebound ($Q_{rebound}$).

In order to determine $Q_{rebound}$, Decourt (1991) proposed the graphical solution illustrated by Figure 11.

The pile rebound, δ_{re} , in Figure 11 is the recoverable settlement of the second curve, known as the elastic settlement, which corresponds to the Q_{re} in Figure 11. This

rebound settlement, δ_{re} , is due to load transfer from the false $Q_{l,measured}$ in Equation 3. From Equations 3 and 4 it can be concluded that Q_{re} is at most equal to twice the $Q_{p,residual}$ and $Q_{l,rupt}$ or, inversely, $Q_{p,residual}$ or $Q_{l,rupt}$ is at least equal to half of Q_{re} . Table 1 indicates that half of Q_{re} is a satisfactory approximate prediction of the lateral resistance estimated as Q_{10} , Q_{15} or Q_{DQ} , the last being the estimated value by Decourt & Quaresma (1978). The half of Q_{re} is also a prediction of the residual load locked into the pile after a prior loading.

Continuing with the interpretation of load tests in the presence of residual loads, Massad (1992) presented a general mathematical model for both displacement and non-displacement piles that can separate the lateral and the toe resistance from the total capacity, including the residual load locked at the pile toe for homogeneous soil. Massad (1993) extended the model in the case of piles with an embedment into a much more resistant layer.

The presence of a residual load occurring at the pile toe explains the higher stiffness of the load x settlement curve in the second loading compared to the initial loading, as shown in Figure 12. Point A of the curve, in the first loading, is shifted

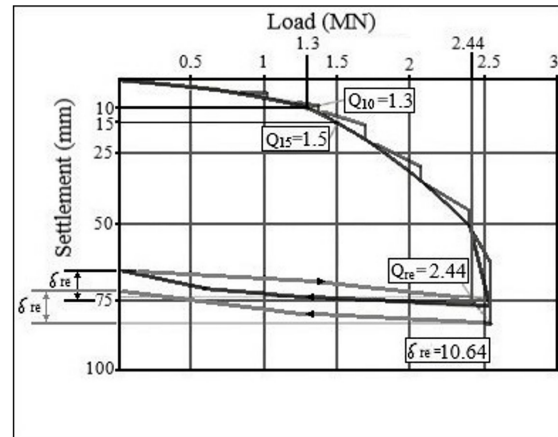


Figure 11. The Rebound Method, adapted from Decourt (1991).

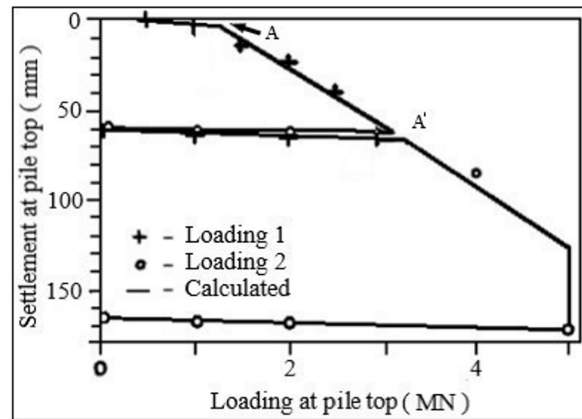


Figure 12. Load versus settlement curve at top of an excavated pile at USP Research Field (adapted from Massad, 1992).

Table 1. Different suggestions for $Q_{l,rupt}$ (adapted from Decourt, 1991).

Test	Q_{l0}	Q_{l5}	Q_{DQ}	$Q_{rd}/2$
1	1.30	1.50	1.08	1.22
2	0.95	1.18	1.16	1.20
3	1.62	1.85	–	>1.25
4	2.60	3.44	2.28	2.33
5	2.37	3.05	3.47	2.87
6	2.98	3.20	–	3.34
7	1.31	1.55	1.99	1.59
8	0.48	0.54	0.54	>0.29
9	2.15	2.40	–	>1.65

to the right, A' , in the second loading curve, characterizing the presence of residual load in the pile. The stiffness in the unloading phase is recoverable in the second loading and its large elastic extent is caused by the residual loads. The estimated curve obtained by Massad (1992) model in Figure 12 matched the experimental results very closely.

Massad (1992) defined the coefficient μ , in Equation 6, which considers the effect of the residual load in the model.

$$\mu = 1 + \frac{Q_{p,res}}{Q_{l,rupt}} \quad (6)$$

Massad (1992) modified the Camberfort Laws to consider the presence of residual loads and the reversion in lateral friction. He also showed that in a more general aspect, the load versus settlement curve in a static pile test consists of four (4) loading and three (3) unloading ranges. Massad (1992) used the proposed method to analyze each loading and unloading range and presented the formulations that allow the estimation of the model parameters in numerous cases, including rigid and flexible piles embedded into uniform soil layers or embedded partly in a residual soil or rock, Massad (1992, 1993, 1995, 2001), Massad & Lazo (1998), Fonseca et al. (2007), Marques & Massad (2004), Mussara & Massad (2015), among other contributions.

Fellenius (2002) proposed a simple graphical method to obtain the true load and residual load transfer from the measured (false) transfer curve in an instrumented load test, illustrated in Figure 13 in a case of homogenous soil. Fellenius (2023) also applies the method to the results from dynamic load tests. The method assumes that the shaft resistance measured along the upper length of the pile is the false resistance. The true resistance is considered equal to the negative resistance, and both are equal to half of the measured resistance. That is, the false distribution incorporates negative shaft friction and positive true friction. Fellenius (2002) begins the true curve by tracing half of the false curve. The other half corresponding to the negative friction is considered the residual load. Below the 8 m depth in Figure 13 the increasing rate of the transfer curve is reduced because of the proximity of the

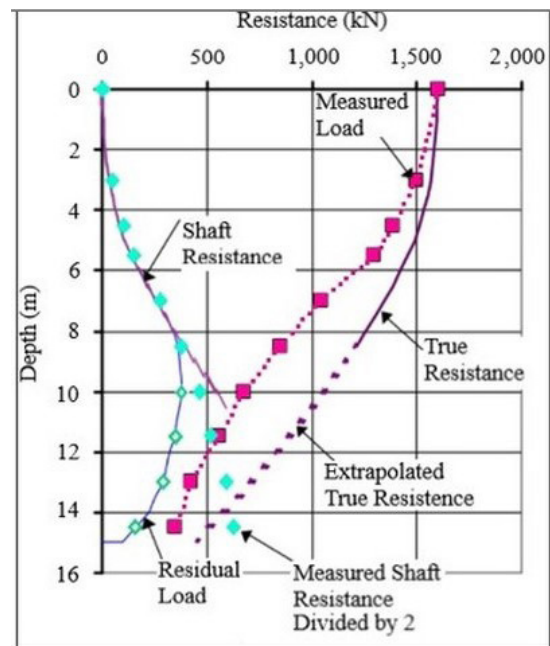


Figure 13. The graphical method (adapted from Fellenius, 2002).

neutral plane. The true curve is the sum of the residual and the measured curve. For a homogeneous soil profile, Fellenius (2002) proposes the extrapolation of the true curve by adjusting the beta value of the positive friction on the superior branch, Equation 7.

$$\tau_{rup} = \beta \sigma'_v \quad (7)$$

Finally, Fellenius (2002) completes the residual load distribution below the neutral plane by subtracting the measured curve from the true load.

Fellenius (2002) emphasizes that in inhomogeneous soil, with water pressure different from hydrostatical, adjacent piles or nearby excavations, it is necessary to use special software. Fellenius (2002) also point out that the method should also be applied with a good soil characterization.

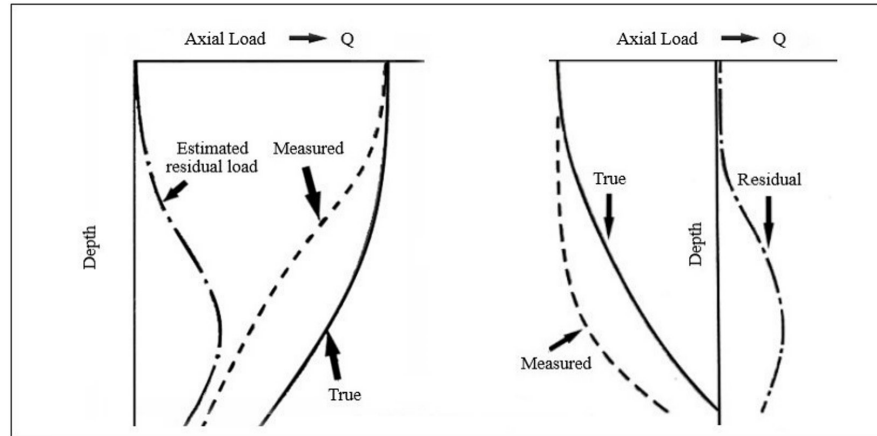


Figure 14. Comparison between the static and tension load tests (adapted from Holloway et al., 1978).

5. Methods for estimation of residual loads

Holloway et al. (1978) proposed a wave equation solution in finite differences, as proposed by Smith (1960), coupled with a static equilibrium solution after attenuation of the energy imposed on the pile from driving. This solution originated the RSA (Residual Stress Analyses) version of the GRLWEAP program (wave equation analysis). Holloway et al. (1978) showed a scheme of the load transfer of an instrumented static load pile in compression and another in tension, with the instruments zeroed before the load test, and not before the driving installation, Figure 14a and b. The residual stresses were estimated by the authors. Although in the static compression load test the true distribution is higher than the measured one, in the tension test the opposite occurs.

Briaud & Tucker (1984) proposed a prediction method to obtain the residual loads in piles embedded into sands. Even recognizing the proposition as a simple method having many simplifying hypotheses, the main advantage of the method is the ability to observe the factors influencing the residual loads.

Briaud & Tucker (1984) started with a failure condition, shown in Figure 15, and established the equilibrium equation to an elementary pile section, resulting in a differential equation. Applying the boundary conditions, they arrived at Equation 8, expressing the residual loads with depth.

$$Q_{z, res} = Q_{z,u} - Q_{rupt} \left[\frac{(E_p \omega + K'_p) e^{\omega(L-z)} - (E_p \omega - K'_p) e^{-\omega(L-z)}}{(E_p \omega + K'_p) e^{\omega L} - (E_p \omega - K'_p) e^{-\omega L}} \right] \quad (8)$$

$$\omega = \sqrt{K'_\tau P / E_p}$$

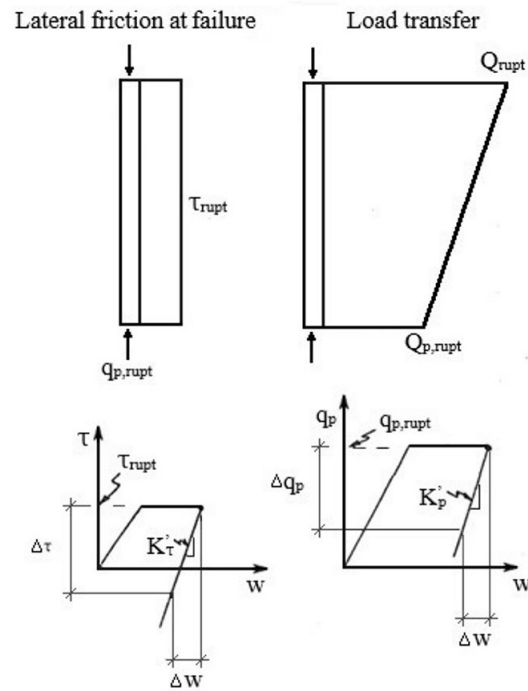


Figure 15. Unloading process starting from failure (adapted from Briaud & Tucker, 1984).

$Q_{z, residual}$ is the residual load at depth z

P is the pile perimeter

E_p is the pile Young modulus

K'_τ and K'_p are shown in Figure 12.

The residual load at a pile toe can be obtained by setting $z = L$, in Equation 8, resulting in Equation 9.

$$Q_{p, res} = Q_{p, rupt} - \left[\frac{2Q_{rupt}}{\left(1 + \frac{E_p \omega}{K'_p}\right) e^{\omega L} - \left(1 - \frac{E_p \omega}{K'_p}\right) e^{-\omega L}} \right] \quad (9)$$

The authors concluded that the distribution of residual loads depend on the failure load at pile point, the total failure load, the pile length and the pile and soil relative stiffness.

Although considering the dynamic analysis as the most adequate, Poulos (1987) presented a simple static method of residual loads estimates for driven and jacked piles. In this simplified estimate of residual loads, Poulos (1987) applied a static analysis for the final penetration in which the pile is loaded to failure and then unloaded. The analysis is the same as that of Poulos & Davis (1980), enabling the pile and soil relative displacement and incremental loading and unloading. The analysis was implemented in a software that includes the installation, static loading and unloading.

The same 50 m long pile with 1 m diameter was considered, with three different types of Young's modulus: stiff ($E_p = 250$ GPa); a moderate ($E_p = 25$ GPa) and extremely compressive pile ($E_p = 2.5$ GPa). Poulos (1987) pointed out that only the second case is of practical relevance, corresponding to a concrete pile. Table 2 summarizes the cases included in Poulos (1987)'s studies.

For the intermediate pile stiffness ($E_p = 25$ GPa), Figure 16 shows the estimated residual shear stresses along the pile shaft for the three soil types. The limiting shaft resistance values for both compression and tension loading are also shown. The residual shear stress is either negative or positive, above and below the neutral plane, respectively.

In the sandy profile, and because of the high point resistance, the residual shear stress may be negative throughout the pile.

Figure 17 shows the estimated distributions of the pile shaft residual load for the three pile stiffness values. It shows that the stiffer the pile, the smaller the pile shaft residual loads. In sandy soils, the neutral plane approaches the pile toe.

Darrag & Lovell (1989) reported that the wave equation analysis is the only analytical procedure that includes all important factors contributing to residual stresses. Darrag & Lovell (1989) utilized the earlier CUWEAP wave equation program, developed by Hery (1983) to develop a simplified procedure for predicting residual stress range and distributions. The authors ran the CUWEAP program more than 250 times to produce a set of charts to predict the residual stress percent (a_r) for a sand profile normally consolidated in its original condition. The charts include concrete and steel piles, and a typical chart is illustrated in Figure 18.

In Figure 18, a_r provides the ratio of residual load at pile toe to pile point capacity, in percentages. The authors produced the charts for $m = 40\%$, m being the ratio of shaft resistance to total pile resistance, in percentages. For m values other than 40%, Equations 10, 11, 12 can be used to obtain a corrected value for a_r .

$$(a_r)_{m\%} = (a_r)_{m=40\%} \times \beta \tag{10}$$

$$m < 55\% \beta = 0.025 \times m \tag{11}$$

Table 2. Cases analyzed by Poulos (1987).

Case	Soil profile	Soil Modulus		$f_{s,rupt}$	
		E_0 (MPa)	N_v (MPa/m)	$f_{s,z=0,rupt}$ (kPa)	β (kPa/m)
A	Stiff clay	50	0	75	0
B	Soft clay	0	1.0	0	1.5
C	Sand	0	1.5	0	2.0

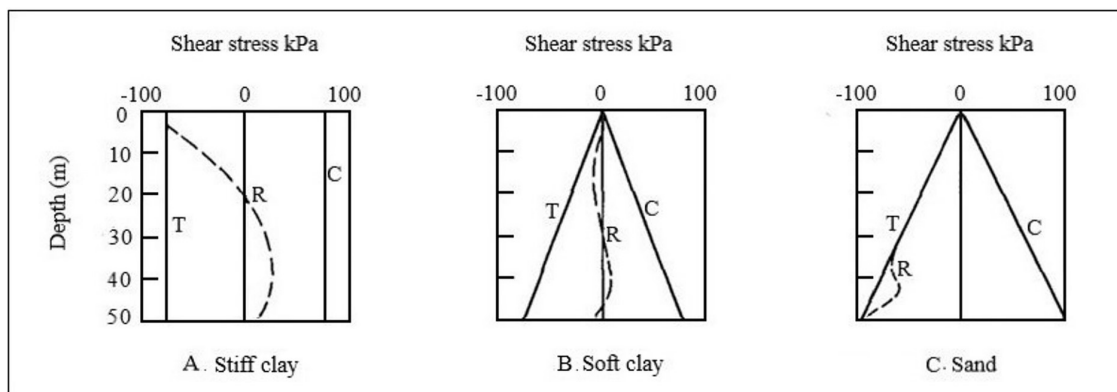


Figure 16. Residual stresses estimated for the three soil types, $E_p = 25$ GPa. R , residual stresses; T , failure stresses in tension; C , failure stresses in compression (adapted from Poulos, 1987).

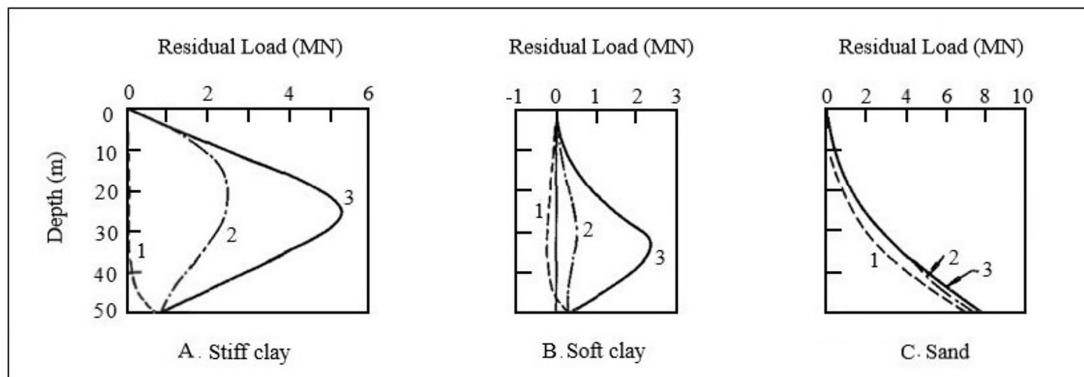


Figure 17. Distribution of residual load: Curve 1, $E_p = 250$ GPa; Curve 2, $E_p = 25$ GPa; Curve 3, $E_p = 2.5$ GPa (adapted from Poulos, 1987).

$$m > 55 \% \beta = 1.375 + 0.01 (m - 55) \quad (12)$$

Costa et al. (2001) presented a new finite element solution developed by Costa (1988) to analyze the pile during driving. One important feature of the DINEXP program is the possibility to estimate the residual stress. Instead of estimating the set as most pile drivability programs do, the maximum displacement minus the quake, DINEXP calculates it directly as the stabilized displacement occurring when toe particle velocity approaches zero. It is noticeable that the stabilized displacement is higher than the set calculated in most solutions. The difference is attributed to the residual load locked in the pile during unloading and causing an incomplete rebound. Figure 19 illustrates the difference.

If the elastic residual displacement, a in Figure 19, is multiplied by the soil stiffness at the pile toe (toe capacity divided by toe quake) the pile toe residual load is obtained. Figure 20 presents a typical comparison of the sets calculated by most drivability programs and that determined directly.

Costa et al. (2001) proposed the application of this new procedure to estimate the permanent pile displacement and the residual loads locked in the pile at the end of driving. The authors confirmed an existing conclusion established by the main research in the literature and disclosed some new aspects. The residual toe load ratio to total bearing capacity first increases and then decreases with the increase of the toe to total resistance percentage. With the increase in toe resistance percentage the neutral plane deepens, approaching the pile toe. Considering the shaft friction distribution, the higher the toe resistance percentage the lower its influence on residual loads.

6. Comparison of different residual load estimation proposals to main instrumented solutions

An initial comparison will be shown for a typical hypothetical steel pile double I section (12 x 4 5/8 inches), $154.6 \times 10^{-4} \text{ m}^2$ cross section, 20 m long, $E_p = 210$ GPa driven

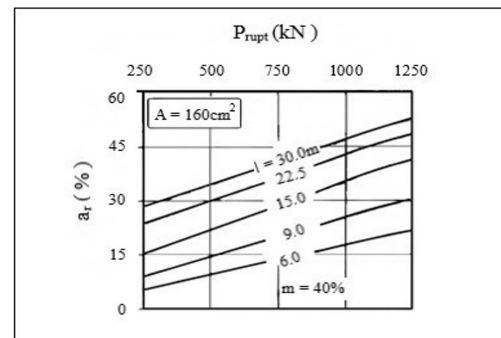


Figure 18. Typical Darrag and Lovell chart for steel pile with cross section A and length varying from 6 to 30m (adapted from Darrag & Lovell, 1989).

into a sand deposit of varying density. For a total capacity of 2400 kN and toe percentage varying from 20%, 50% and 80%, the solutions from Briaud & Tucker (1984), Darrag & Lovell (1989), GRLWEAP (Goble et al., 1988), Costa et al. (2001) are compared in Figure 21. Because Briaud & Tucker (1984) considered a constant unitary friction along the pile shaft, the same premise was considered in Figure 21 for the other methods, except for the Darrag & Lovell (1989) charts which were based on unitary friction increasing linearly with depth.

Most solutions first show an increase and then a decrease of the residual toe load ratio to total capacity versus the point to total capacity. Only the GRLWEAP in its 2001 version showed a residual load ratio to total capacity always increasing with the toe resistance percentage, a feature differing from the other solutions, even for a previous version of the same program, CUWEAP. The Darrag & Lovell (1989) charts indicated the maximum residual toe load to total capacity at the same toe percentage as the Costa et al. (2001) solution. Although the Briaud & Tucker (1984) equations were based on many simplified assumptions, their results are close to more complete solutions, except the toe percentage related to the maximum residual load.

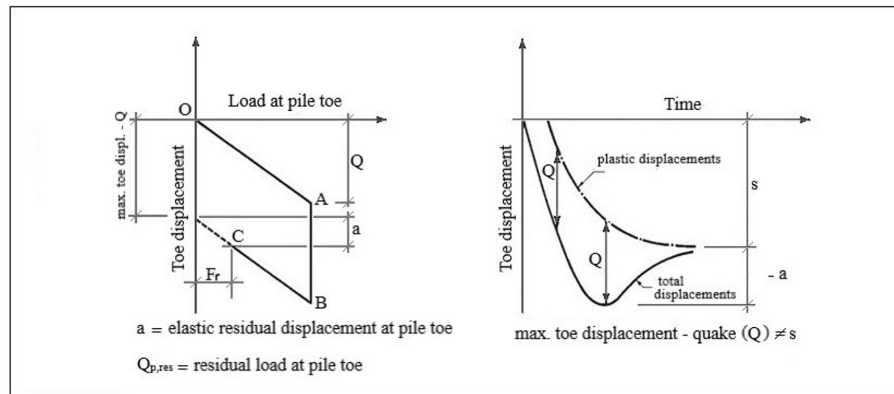


Figure 19. Load versus displacement and displacement versus time when residual loads occur at pile toe (adapted from Costa et al., 2001).

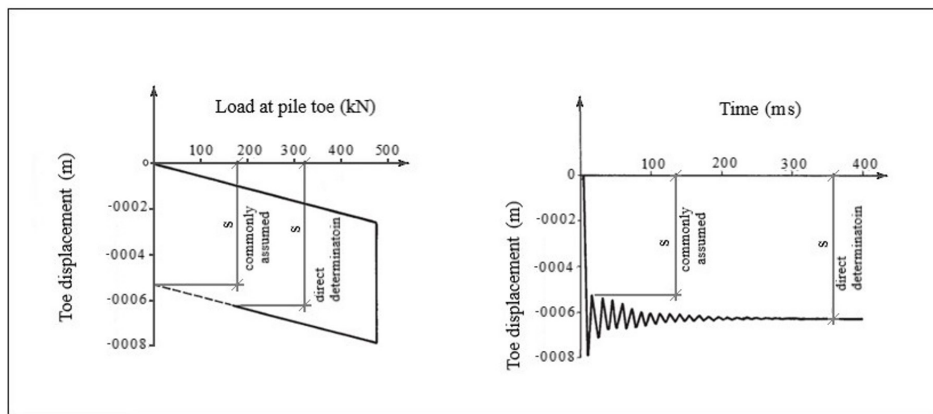


Figure 20. Different features of set determination (adapted from Costa et al., 2001).

For the Costa et al. (2001) solution, a comparison was made for two distinct unitary friction variation: a uniform, the same shown in Figure 21, and a linear variation. For the linear variation, the GRLWEAP solution is also shown in Figure 22.

Figure 22 shows two types of curves. The upper curves express the residual toe load ratio to point resistance, here named toe mobilization ratio, and the lower curves express the residual toe load ratio to total capacity. For the low point resistance percentage, both curves differ widely, but for a higher point resistance percentage they come closer to each other as the point resistance percentage approaches 100%. In fact, for low point resistance percentage, the shaft friction is high, thereby the friction distribution plays a different role, mainly in the toe mobilization ratio. For high point resistance percentage, the curves tend to intercept. The yellow region diminishes its area as point resistance percentage approaches 100%.

7. Comparison of residual load estimation proposal to main instrumented solutions

Zhang & Wang (2007) described an extensive instrumented field-monitoring program for studying the residual loads in

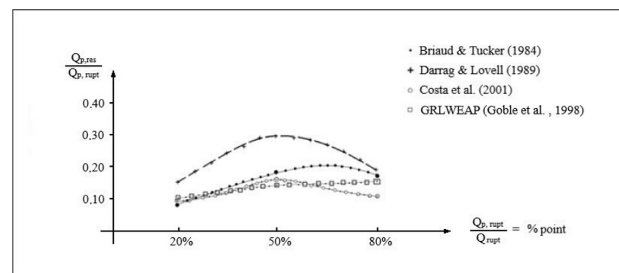


Figure 21. Residual toe load ratio to total capacity versus percentage of point to total resistance for different solution.

long steel driven piles. Eleven H piles were instrumented, monitored and load tested. They have a $285 \times 10^{-4} \text{m}^2$ section and length varying from 34.2 m to 59.8 m. The soil profile consisted of a fill layer, marine deposits, an alluvium layer and fully or moderately decomposed granite. The piles were driven and embedded into the decomposed granite. Danziger & Lopes (2008) interpreted the whole database and selected the same dimensional values, the measured point resistance percentage at failure obtained in the static instrumented test in the horizontal axis and the residual toe load ratio to total capacity in the vertical. Figure 23 shows that the instrumentation

follows the same pattern of the prediction curve in Figure 22. Only one of six instrumented piles with complete data, named IB3-3, fell outside a line passing through the instrumented piles.

Ganju et al. (2020) presented the results of a static and two (2) dynamic load tests performed on a closed-ended steel pile of 0.6 m outside diameter and 18m long. Locked-in residual loads

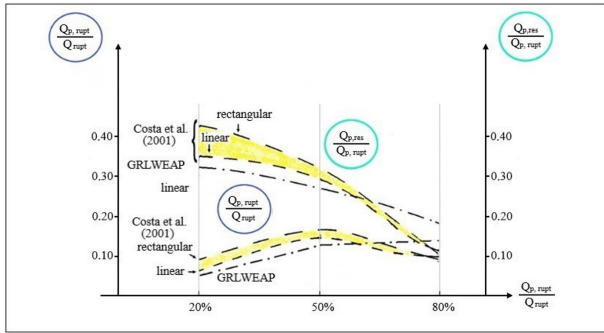


Figure 22. Influence of variation in unitary friction: uniform (rectangular) and linear.

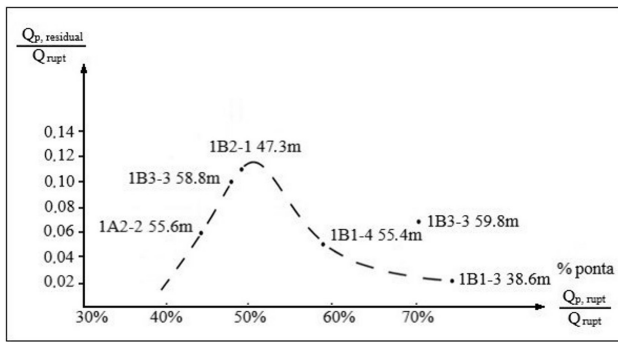


Figure 23. Zhang & Wang (2007) (data interpreted by Danziger & Lopes, 2008).

were measured at the end of driving and used to correct the pile capacity components measured at the static load test. The soil profile consisted of several layers of sand and gravel mixtures.

Figure 24 shows, on the left, the blow counts per unit length of pile versus depth and on the right the SPT blow counts, soil profile, and CPT q_c results. Driving resistance peaked at 7.5 m penetration, on the same horizon where the soil profile indicated a gravelly sand and the N_{60} and q_c profile registered a sharp increase.

Figure 25 illustrated the measured residual loads at the end of driving and the unitary friction. Figure 25 follows the same pattern observed in Figure 4 by Gregersen et al. (1973) in concrete piles in a sandy profile.

Figure 25 illustrates, at 7 m depth on the right, the corrected true unit shaft resistance of 58 kPa as the sum of the false shaft resistance, 98 kPa, and the -40 kPa negative unit shaft friction. The maximum negative unit shaft resistance is 70% of the true shaft resistance at 7 m depth.

Figure 26 is obtained if the whole instrumented database in sandy soils is now superposed in the same dimensionless axis as the curves representing Costa et al. (2001) analysis.

The calculated pile stiffness is included in the table within Figure 26. The first four (4) piles in the table are the precast piles from Gregersen et al. (1973). The 8m pile with uniform section has the same stiffness as the steel piles of Costa et al. (2001). Its position coincides with that of the curve for linear unitary shaft friction distribution of Costa et al. (2001), not only for the mobilization ratio curve but also for the toe residual load ratio to total capacity. The conical pile with a uniform taper is less rigid than the uniform section pile. Because of its small section at pile toe, it has a smaller percentage of point resistance and is positioned on the left in the horizontal axis in Figure 26, in a region not covered by Costa et al. (2001) analyses. However, its position is within the possible extrapolation of the mobilization curve and the curve expressing the toe residual

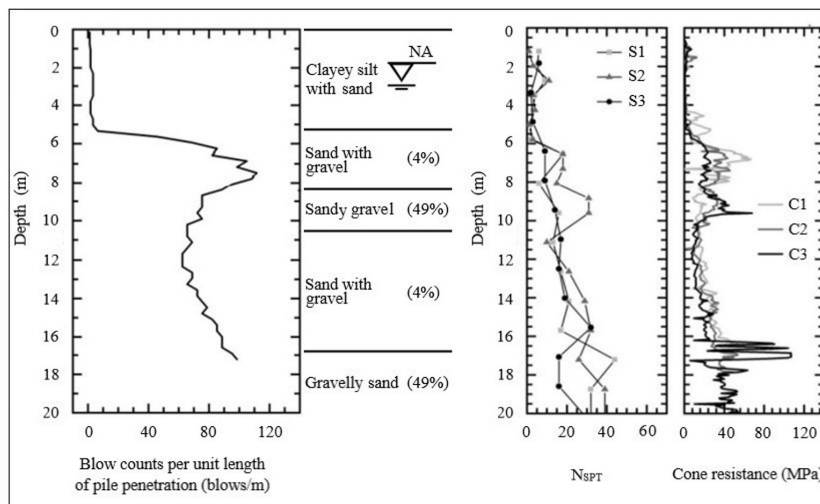


Figure 24. Blow counts during pile penetration compared do field tests (adapted from Ganju et al., 2020).

load ratio to total capacity. The corresponding 16m long piles from Gregersen et al. (1973) are more flexible piles, and both are positioned in Figure 26 above the 8m piles. It agrees with the Poulos (1987) findings that the stiffer the pile, the smaller the residual loads. Another aspect that is clear in the position of the data from Gregersen et al. (1973) is its parallelism to the Costa et al. (2001) curves. While the 8 m piles are positioned very close to the Costa et al. (2001) curves, the more flexible 16 m piles indicate higher residual loads but with the same variation with the point percentage.

The following instrumented pile in Figure 26 is the single pile from Briaud et al. (1989). Its stiffness is very close to the pile studied by Costa et al. (2001). While Gregersen et al.

(1973) precast concrete piles were embedded into a very loose sand, the single steel pile instrumented by Briaud et al. (1989) is embedded into a much denser sand with a high point resistance percentage, positioned to the right of the horizontal axis. This Briaud et al. (1989) pile is also positioned very close to Costa et al. (2001) curves, as illustrated in Figure 26.

The next pile on the list is that instrumented by Ganju et al. (2020). Although its stiffness is one and a half times higher than the reference pile from Costa et al. (2001), its position is also very close to the curves from Costa et al. (2001). The last pile driven in sand analyzed herein is from Rieke & Crowser (1987), the stiffness of which is more than twice the reference pile used by Costa et al. (2001) to construct their curves. In fact, it is

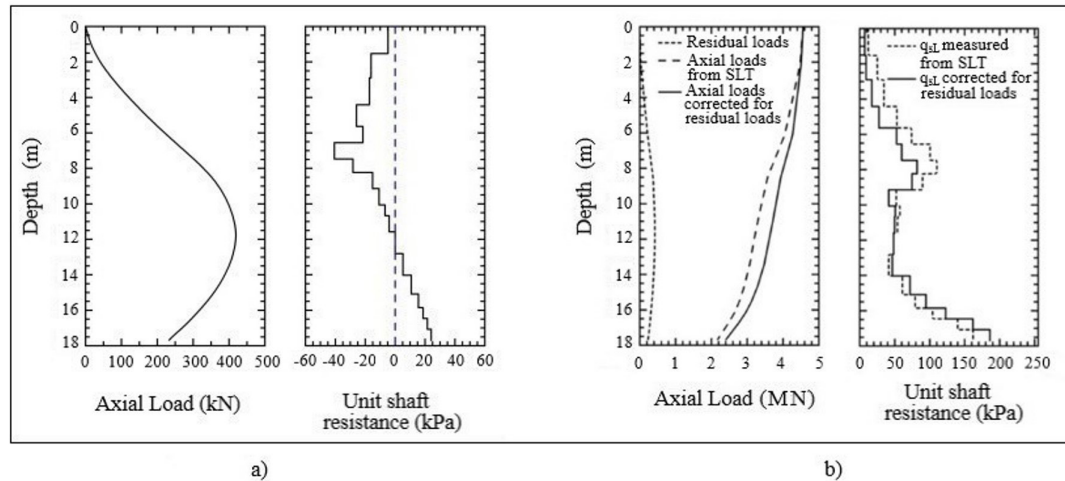


Figure 25. (a) Residual axial loads and unit shaft friction; (b) measured and corrected load transfer curves and unit shaft resistance at failure (adapted from Ganju et al., 2020).

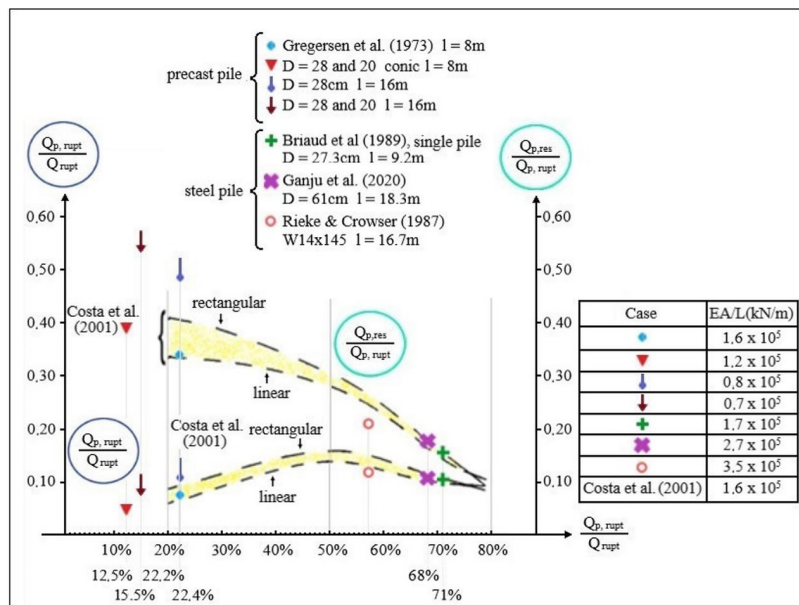


Figure 26. Documented cases including measured residual load in concrete and steel piles in sandy soil.

positioned below the Costa et al. (2001) curves, in agreement with Poulos (1987), Briaud & Tucker (1984) and others.

Revisiting the results from Cooke (1979), who measured the total, the point and, by difference, the lateral friction of a single pile continuously, in addition to the residual load, it was possible to interpret the same data positioning them in the same dimensionless axis of the previous documented cases in sand. A series of piles of varying length were now considered for the same penetration interval used in Cooke (1979) experiments. The longer the piles, the lower their point resistance in a uniform soil layer. Cooke (1979)'s tubular steel pipe pile, 0.17 m diameter, jacked into London clay was then interpreted as a series of piles with varying L/D ratios. The series of data was expressed in the same two curves obtained by Costa et al. (2001). All data were gathered in Figure 27.

Although presenting few outliers, the main data in Figure 27 have very clear behavior. The lower curve shows the same pattern first observed by Danziger & Lopes (2008) who pointed out that: if the measured point resistance percentage at failure is fixed in the horizontal axis and the toe residual load ratio to total capacity is positioned in the vertical axis, the resulting curve shows that, as the point resistance increases the curve first exhibits a positive derivative. There exists a point resistance percentage in which the pile toe residual load ratio to total capacity reaches a maximum value, after which this ratio drops to rising values of point resistance percentage. This maximum occurs, in this case, at 2.7 m penetration, $L/D = 16$ and toe resistance of 33% of total capacity. For the full penetration, L/D equals 27.4 at a depth of 4.7 m, with a toe resistance percentage of 30% and with a toe residual load reaching 75% of the toe resistance, the maximum mobilization.

Massad reasoned in a personal communication with the author that a similar behavior can also be obtained theoretically by applying his mathematical model conceived for interpreting pile behavior in a load test, Massad (1992, 1993).

8. Conclusions

The residual loads occurring after driving or after the first loading in a static or dynamic pile load test have an important effect on piling behavior (Serviceability Limit State - SLS). Its relevance must be assured especially in piled raft foundations and underpinning designs, where different foundations share the same structural loads. The loads are partitioned according to the different response from each foundation element. In this case an approximate prediction of residual load is essential to obtain a behavior close to the desired serviceability.

When the residual loads are obtained by means of two or more loading cycles in a static load test, it is recommended that the cycles have the same loading rate. This recommendation is especially relevant to clay soils which could exhibit a viscous shear strength with the loading rate (Lopes et al., 2021).

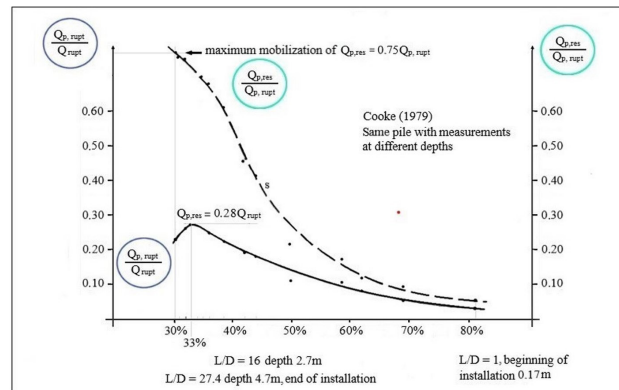


Figure 27. Typical case of piles driven in London clay (data from Cooke, 1979).

The residual shear stresses in soil due to unloading are generated rapidly and might retain a viscous component in plastic soils more susceptible to relaxation effects over time.

The reduction in residual loads after tension load cycling also occurs after compression cycles but resulting in increased residual loads. The final effect concerning the extension of decrease or increase is an issue for future research.

The residual loads affect the settlement prediction of isolated piles. In case of pile groups with pile spacing of three-pile diameters, the effect of residual loads in reducing group settlement is much lower. For a piled raft with greater pile spacing, the reduction of the residual load at pile toe due to the driving neighboring piles is possibly much lower and the effect of residual loads much higher.

The prediction of the residual loads by the wave equation analysis after final stabilized toe displacement is a simple, direct, and accurate procedure with the advantage of including all important factors contributing to residual stresses.

The curves illustrating a first increase and then a decrease of the toe residual load ratio to total capacity versus the point to total capacity percentage were found in stratified, over-consolidated clay and different documented piles in sandy profiles.

In sandy soils the maximum toe residual load to total capacity ratio was found for high point resistance percentage whereas for clayey soils the peak occurred at a much lower percentage.

The ratio of the toe residual load to point resistance, called toe mobilization ratio, revealed a steady downward rate. This curve limits the region of possible curves expressing the ratio of the toe residual load to total capacity ratio and forces the latter's decreasing offset.

Gregersen et al. (1973) results illustrated a high ratio of toe residual load to point resistance for lower stiff pile, and Rieke & Crowser (1987) showed a lower ratio of the toe residual load to point resistance for stiffer piles.

The two curves shown in Figures 22, 26 and 27, expressing the ratio of toe residual load to point resistance

and the ratio of toe residual load to total capacity versus point resistance percentage are similar, respectively, to specific dry soil weight and saturation curve versus water content in soil compaction. The influence of a compaction energy increase in the compaction curve is the same as the pile stiffness reduction in residual toe generated after pile driving or previous pile loading. Furthermore, as the water content increases, the influence of compaction energy in specific dry soil weight tends to decrease. The last comment can also be observed in Figure 26. Although the piles instrumented by Briaud et al. (1989) and Ganju et al. (2020) were stiffer than the piles numerically analyzed by Costa et al. (2001), they were positioned very close to the Costa et al. (2001) curves, unlike the Gregersen et al. (1973) piles. The reduced impact of the stiffness of piles in Briaud et al. (1989) and Ganju et al. (2020) in the proximity to the Costa et al. (2001) curve can be attributed to the high point resistance percentage in the embedded penetration of those piles. This conclusion is the same as the decrease of the influence of compaction energy in specific dry soil weight as the water content increase in a soil sample undergoing compaction.

Acknowledgements

The author is very grateful to the Brazilian Association for Soil Mechanics (ABMS) and honoured for their invitation to present the Pacheco Silva lecture at the 20th Brazilian Conference on Soil Mechanics and Geotechnical Engineering in Campinas (SP) in August 2022. The author also expresses her gratitude to Kesslyn Nogueira Ramos for her valuable support in preparing the figures in the article.

Declaration of interest

The author has no conflicts of interest to declare.

Data availability

No dataset was generated or evaluated in the course of the current study; therefore, data sharing is not applicable.

List of symbols

a_r	Residual load ratio at pile toe to pile point capacity in percentage
d	Pile diameter
m	Ratio of shaft resistance to total pile resistance in percentage
E_p	Young's pile modulus
E_s	Soil Young modulus
$f_{s,rupt}$	The pile soil friction on pile shaft available at failure
K_p	Pile and soil relative stiffness at the pile toe

K'_τ	Pile and soil relative stiffness at the pile lateral surface
L	Pile embedded length
N_y	The variation of Young's modulus of soil with depth
P	Load applied at pile top
$Q_{l, measured}$	Load difference between measurement at pile top and toe
$Q_{l, measured} (F)$	Load difference between measurement at pile top and toe at failure when instruments are zeroed before the test, false value.
$Q_{l, rupt}$	Pile lateral bearing capacity
$Q_{l, rupt} (T)$	True pile lateral bearing capacity (the same as $Q_{l, rupt}$)
$Q_{max, res}$	Maximum residual load at the neutral plane
$Q_{p, measured}$	Load measured at pile toe
$Q_{p, mobilized}$	Resistance mobilized at pile toe
$Q_{p, res}$	Residual load at pile toe
$Q_{p, rupt}$	Pile point bearing capacity
$Q_{rebound}$	Load corresponding to the recoverable settlement
Q_{rupt}	Pile total bearing capacity
$Q_{t, mobilized}$	Total mobilized resistance in a load test
$Q_{t,2}$	Maximum total load in the second loading of a pile load test
$Q_{z, res}$	Residual load at depth z
β	Rate of increase of shaft friction with depth
$\delta_{rebound}$	Recoverable settlement of the second loading of the load test

References

- Briaud, J., & Tucker, L. (1984). Piles in sand: a method including residual stresses. *Journal of Geotechnical Engineering*, 110(11), 1666-1680. [http://dx.doi.org/10.1061/\(ASCE\)0733-9410\(1984\)110:11\(1666\)](http://dx.doi.org/10.1061/(ASCE)0733-9410(1984)110:11(1666)).
- Briaud, J., Tucker, L., & Ng, E. (1989). Axially loaded 5 pile group and single pile in sand. In *Proceedings of the 12th International Conference on Soil Mechanics and Foundation Engineering* (Vol. 2, pp. 1121-1124). Rotterdam: Balkema.
- Cooke, R.W. (1979). Influence of residual installation forces on the stress transfer and settlement under working loads of jacked and bored piles in cohesive soils. In *Symposium on Behavior of Deep Foundation* (Publication STP 670, pp. 231-249). West Conshohocken: ASTM.
- Cooke, R.W., & Price, G. (1973). Strains and displacements around friction piles. In *Proceedings of the 8th Conference on Soil Mechanics and Foundation Engineering* (Vol. 2, pp. 53-60). Moscow: SIMSG ISSMGE.
- Costa, A. M. (1988). *DINEXP Manual*. PETROBRÁS Internal Report. (in Portuguese).
- Costa, L.M., Danziger, B.R., & Lopes, F.R. (2001). Prediction of residual driving stresses in piles. *Canadian Geotechnical Journal*, 38(2), 410-421. <http://dx.doi.org/10.1139/t00-095>.
- Danziger, B.R., & Lopes, F.R. (2008). Discussion of development of residual forces in long driven piles in weathered soils. *Journal of Geotechnical and Geoenvironmental*

- Engineering*, 134(10), 1420-1421. [http://dx.doi.org/10.1061/\(ASCE\)1090-0241\(2008\)134:9\(1420\)](http://dx.doi.org/10.1061/(ASCE)1090-0241(2008)134:9(1420)).
- Danziger, B.R., Costa, A.M., Lopes, F.R., & Pacheco, M.P. (1992). Back-analyses of closed-end pipe piles for an offshore platform. In *Proceedings of the 4th International Conference on the Application of Stress Wave Theory to Piles* (Vol. 1, pp. 557-562). Rotterdam: Balkema.
- Danziger, B.R., Costa, A.M., Lopes, F.R., & Pacheco, M.P. (1999). Back-analyses of offshore pile driving with an improved soil model. *Geotechnique*, 49(6), 777-799. <http://dx.doi.org/10.1680/geot.1999.49.6.777>.
- Darrag, A.A., & Lovell, C.W. (1989). A simplified procedure for predicting residual stresses for piles In *12th International Conference on Soil Mechanics & Foundation Engineering* (pp. 1127-1130). Rotterdam: Balkema.
- Decourt, L. (1989). Instrumented bored piles in residual soils. In *12th International Conference on Soil Mechanics and Foundation Engineering*. Rotterdam: Balkema.
- Decourt, L. (1991). Thoughts concerning the interpretation of successive load tests on the same pile. In *9th Panamerican Conference on Soil Mechanics and Foundation Engineering* (Vol. 2, pp.585-597). Santiago: Sociedad Chilena de Geotecnia.
- Decourt, L., & Quaresma, A.R. (1978). Capacidade de carga de estacas a partir de valores de SPT. In *6th Congresso Brasileiro de Mecânica dos Solos e Engenharia de Fundações* (Vol. 1, pp. 45-53). São Paulo: ABMS.
- Fellenius, B.H. (2002). Determining the residual distribution in piles. Part 2: method for determining the residual load. *Geotechnical News Magazine*, 20(3), 25-29.
- Fellenius, B.H. (2023). *Basics of foundation design*. Lulu.
- Fonseca, A.V., Santos, J.A., Esteves, E.C., & Massad, F. (2007). Analysis of piles in residual soil from granite considering residual loads. *Soils & Rocks*, 30(2), 63-80. <http://dx.doi.org/10.28927/SR301063>.
- Ganju, E., Han, F., Prezzi, M., & Salgado, R. (2020). Static capacity of closed-ended pipe pile driven in gravelly sand. *Journal of Soil Mechanics and Environmental Engineering*, 146(4), [http://dx.doi.org/10.1061/\(ASCE\)GT.1943-5606.0002215](http://dx.doi.org/10.1061/(ASCE)GT.1943-5606.0002215).
- Goble, G.G., & Hery, P. (1984). Influence of residual forces on pile driveability. In *Proceedings of the 2nd International Conference on the Application of Stress Wave Theory to Piles* (pp. 154-161). Stockholm: Swedish Pile Commission.
- Goble, G.G., Rausche, F., & Likins, G.E. (1988). *GRLWEAP program: wave equation analysis of pile driving: procedures and models – program manual*. Pile Dynamics Inc.
- Gregersen, O.G., Aas, G., & DiBiagio, E. (1973). Load tests on friction piles in loose sand. In *8th International Conference on Soil Mechanics and Foundation Engineering* (pp. 109-117). Moscow: SIMSG ISSMGE.
- Hery, P. (1983). *Residual stress analyses in WEAP* [Doctoral thesis]. University of Colorado.
- Holloway, D.M., Clough, G.W., & Vesic, A.S. (1978). The effects of residual driving stress on piles performance under axial loads. In *Proceedings of Offshore Technology Conference* (pp. 2225-2236). New York: American Society of Mechanical Engineers.
- Hunter, A.H., & Davisson, M.T. (1969). Measurement of pile load transfer. In R. Lundgren & E. D'Appolonia (Eds.), *Performance of deep foundation* (Special Technical Publication, pp. 106-117). ASTM.
- Kim, S.R., Chung, S.G., & Fellenius, B.H. (2011). Distribution of residual load and true shaft resistance for a driven instrumented test pile. *Canadian Geotechnical Journal*, 48(4), 583-598. <http://dx.doi.org/10.1139/t10-084>.
- Kou, H.L., Chu, J., Guo, W., & Zhang, M.Y. (2016). Field study of residual forces developed in pre-stressed high-strength concrete (PHC) pipe piles. *Canadian Geotechnical Journal*, 53(4), 696-707. <http://dx.doi.org/10.1139/cgj-2015-0177>.
- Liu, M., & Zhang, M. (2012). Measurement of residual force locked in open-ended pipe pile using FBG-based sensors. *The Electronic Journal of Geotechnical Engineering*, 17, 2145-2154.
- Liyanapathirana, D.S., Deeks, A.J., & Randolph, M.F. (1998). Numerical analysis of soil plug behavior inside open-ended piles during driving. *International Journal for Numerical and Analytical Methods in Geomechanics*, 22(4), 303-322. [http://dx.doi.org/10.1002/\(SICI\)1096-9853\(199804\)22:4<303:AID-NAG919>3.0.CO;2-P](http://dx.doi.org/10.1002/(SICI)1096-9853(199804)22:4<303:AID-NAG919>3.0.CO;2-P).
- Liyanapathirana, D.S., Deeks, A.J., & Randolph, M.F. (2000). Numerical modelling of large deformations associated with driving of open-ended piles. *International Journal for Numerical and Analytical Methods in Geomechanics*, 24(14), 1079-1101. [http://dx.doi.org/10.1002/1096-9853\(20001210\)24:14<1079:AID-NAG113>3.0.CO;2-E](http://dx.doi.org/10.1002/1096-9853(20001210)24:14<1079:AID-NAG113>3.0.CO;2-E).
- Lopes, F.R., Santa Maria, P.E.L., Danziger, F.A.B., Martins, I.S.M., Danziger, B.R., & Tassi, M.C. (2021). A proposal for static load test in piles: the equilibrium method. *Soils & Rocks*, 44(1), 1-10. <http://dx.doi.org/10.28927/SR.2021.057920>.
- Marques, J.A.F., & Massad, F. (2004). Provas de carga instrumentadas em estacas escavadas com bulbos, executadas na Região Praieira de Maceió, Alagoas. *Solos e Rochas*, 2(3), 243-260.
- Mascarucci, Y., Mandolini, A., & Miliziano, S. (2013). Effects of residual stresses on shaft friction of bored cast in situ piles in sand. *Journal of Geo-engineering Sciences*, 1, 37-51. <http://dx.doi.org/10.3233/JGS-13009>.
- Massad, F. (1992). Sobre a interpretação de provas de cargas em estacas considerando as cargas residuais na ponta e a reversão do atrito lateral. Parte I: solos relativamente homogêneos. *Solos e Rochas*, 15(2), 103-115.
- Massad, F. (1993). Sobre a interpretação de provas de cargas em estacas considerando as cargas residuais na ponta e a reversão do atrito lateral. Parte II: estaca embutida em solo mais resistente. *Solos e Rochas*, 16(2), 93-112.
- Massad, F. (1995). The analysis of piles considering soil stiffness and residual stresses. In *10th Panamerican*

- Conference on Soil Mechanics and Foundation Engineering* (Vol. 2, pp. 1199-1210). Mexico: Sociedad Mexicana de Mecánica de Suelos.
- Massad, F. (2001). On the use of elastic rebound to predict pile capacity. In *15th International Conference on Soil Mechanics on Soil Mechanics and Geotechnical Engineering* (Vol. 2, pp. 1199-1210). Istanbul: Maya.
- Massad, F., & Lazo, G. (1998). Graphical method for the interpretation of the load-settlement curve from vertical load tests on rigid and short piles. In *11 Congresso Brasileiro de Mecânica dos Solos e Engenharia Geotécnica* (Vol. 3, pp. 1407-1414). Brasília, DF: ABMS.
- Mussara, M., & Massad, F. (2015). Static load tests in an instrumented rock socket barrete pile. *Soils & Rocks*, 38(2), 163-177. <http://dx.doi.org/10.28927/SR382163>.
- Nie, R., Leng, W., Wu, A., Li, F., & Chen, Y.F. (2014). Field measurement and analysis of residual stress in bored piles. *Journal of Highway and Transportation Research and Development*, 8(4), 57-62. <http://dx.doi.org/10.1061/JHTRCQ.0000411>.
- Poulos, H. (1987). Analysis of residual stress effects in piles. *Journal of Geotechnical Engineering*, 113(3), 216-229. [http://dx.doi.org/10.1061/\(ASCE\)0733-9410\(1987\)113:3\(216\)](http://dx.doi.org/10.1061/(ASCE)0733-9410(1987)113:3(216)).
- Poulos, H., & Davis, E.H. (1980). *Pile foundation analysis and design*. John Wiley & Sons.
- Randolph, M.F. (1991). The effect of residual stress in interpreting stress wave data. *Computer Methods and Advances in Geomechanic*, 1, 777-782.
- Rausche, F., Richardson, B., & Likins, G. (1996). Multiple blow CAPWAP analysis of pile dynamic records. In *Proceedings of the 5th International Conference on the Application of Stress Wave Theory to Pile* (Vol. 1, pp. 435-446). Rotterdam: Balkema.
- Rieke, R.D., & Crowser, J.C. (1987). Interpretation of pile load test considering residual stresses. *Journal of Geotechnical Engineering*, 113(4), 320-334. [http://dx.doi.org/10.1061/\(ASCE\)0733-9410\(1987\)113:4\(320\)](http://dx.doi.org/10.1061/(ASCE)0733-9410(1987)113:4(320)).
- Smith, E.A.L. (1960). Pile driving analysis by the wave equation. *Journal of the Soil Mechanics and Foundations Division*, 86(4), 35-61. <http://dx.doi.org/10.1061/JSFEAQ.0000281>.
- Vesic, A.S. (1977). On the significance of residual loads for response of piles. In *9th International Conference on Soil Mechanics and Foundation Engineering* (Vol. 3, pp. 374-379). Tokyo: ICSMFE.
- Zhang, L.M., & Wang, H. (2007). Development of residual forces in long driven piles in weathered soils. *Journal of Geotechnical and Geoenvironmental Engineering*, 133(10), 1216-1228. [http://dx.doi.org/10.1061/\(ASCE\)1090-0241\(2007\)133:10\(1216\)](http://dx.doi.org/10.1061/(ASCE)1090-0241(2007)133:10(1216)).

ARTICLES

Soils and Rocks
v. 46, n. 2

Numerical analysis of the contribution of side resistance to caisson bearing capacity

Bárbara Estéfany Pereira¹ , Jean Rodrigo Garcia^{1#} 

Article

Keywords

Numerical analysis
Load-settlement curve
Skin friction on shaft
Large tip (bell)
Caisson

Abstract

The use of deep foundations is a common practice in geotechnical civil engineering designs, in which the bearing capacity of these foundations occurs by side resistance, tip, or through the combination of both. In the case of caisson, the bearing capacity is often obtained by considering only the resistance of the lower end due to its bell-shaped geometry, neglecting the skin friction resistance of the shaft, which may represent an oversizing in some cases. In this context, this paper analyzed the behavior of nine caisson prototypes laid at 10 m, 15 m and 20 m deep. At each depth, three types of caissons were analyzed, with and without an expanded base, and a third type with deformable material at the top of the base. The axisymmetric numerical analyses were conducted by using the finite element method considering an isotropic medium. Thus, it was found that with increasing depth, the skin frictional resistance of the surrounding soil of shaft contributes significantly to the bearing capacity of the caisson suggesting that little load would reach the base of the caisson in situations that would negligible the side resistance of the shaft in the design phase. This may be an important consideration in foundation design using caisson, as it would reduce risks to human life, as well as reduce material consumption and the generation of carbon released into the atmosphere.

1. Introduction

According to Carneiro (1999) estimating the bearing capacity of a foundation element is essential so that it can proper behave to the needs of the design for which it was intended. In this case, there is the need to know this behavior through theoretical procedures and through accumulated knowledge from the experience of designers, the use of field and laboratory correlations, which represent the essence of the empirical and semi-empirical methods established in Brazil.

The bearing capacity of caisson foundations may consider in its composition, the resistance coming from side resistance, provided a length equal to a diameter of the base, immediately above it, is disregarded for load transfer calculation purposes. This consideration of the friction resistance coming from the caisson shaft may be interesting in certain cases for optimization, economy and safety of the geotechnical design, because depending on the depth of laying of the caisson base, the resistance of the shaft may represent a significant portion of the load capacity of the foundation element (ABNT, 2019).

2. Expressions for calculation caisson foundation

Theoretical, semi-empirical, and prototype load tests can be used to calculate the bearing capacity of tubular foundations, but due to the large dimensions of this type of

foundation, the bearing capacity is high, requiring highly resistant equipment that provides for the application of loads of great magnitude on the foundation, which increases the cost of load tests. Therefore, it is opted to use established methods for such determination. Theoretical methods applied to sandy soils are used. Meyerhof (1951) proposed an expression for calculation of the bearing capacity of deep foundations, analogous to the equation proposed by Terzaghi in 1943 (Albuquerque & Garcia, 2020), as shown in the Equation 1.

According to several authors, the theoretical expression proposed by Meyerhof can lead to optimistic results regarding the bearing capacity, but not too divergent from reality for the cases observed in sandy soils. Another way to find the bearing capacity is through semi-empirical methods based on correlations between soil strength properties (SPT and CPT) and settlement, which mostly do not consider the side resistance by skin friction, as seen in Alonso (1983) and Aoki & Velloso (1975). Besides these, other renowned methods in the Brazilian scenario for bearing capacity of deep foundations are those proposed by Décourt & Quaresma (1978), Velloso (1981), Décourt (1989) and Albiero & Cintra (2016), which according to Albuquerque & Garcia (2020), based on the estimation for shallow presented a proposal that can be extended to the case of deep foundations by including the effect of depth in effective terms, geostatic stress, at the support quota of the caisson base, as shown in the Equations 2, 3 and 4.

#Corresponding author. E-mail address: jean.garcia@ufu.br

¹Universidade Federal de Uberlândia, Faculdade de Engenharia Civil, Uberlândia, MG, Brasil.

Submitted on January 3, 2023; Final Acceptance on February 9, 2023; Discussion open until August 31, 2023.

<https://doi.org/10.28927/SR.2023.000123>



This is an Open Access article distributed under the terms of the Creative Commons Attribution License, which permits unrestricted use, distribution, and reproduction in any medium, provided the original work is properly cited.

$$\text{Terzaghi (1943)} \quad \sigma_{rup} = c \cdot N_c + q \cdot N_q + 0.5 \cdot \gamma \cdot B \cdot N_\gamma \quad (1)$$

$$\text{Décourt (1989)} \quad \sigma_{adm} = 25 \cdot \bar{N}_{SPT} + \sigma'_{vb} \quad (\text{in kPa}) \quad (2)$$

$$\text{Albiero \& Cintra (2016)} \quad \sigma_{adm} = 20 \cdot \bar{N}_{SPT} + \sigma'_{vb} \quad (\text{in kPa}) \quad (3)$$

$$\text{Alonso (1983)} \quad \sigma_{adm} = 33.33 \cdot \bar{N}_{SPT} \quad (\text{in kPa}) \quad (4)$$

In theoretical and semi-empirical applications, it has been usual practice to assume that the lateral stress along the shaft is null, and thus the load of the structure is transferred to the subsoil by the support of the base. However, several load tests performed on deep caissons indicate that, for small displacements, the friction resistance of deep wells is significant and develops fully for displacements of the order of 5 to 10 mm, regardless of the diameter of the shaft. However, the full mobilization of the base resistance is only effective for large displacements, on the order of 10% to 20% of the base diameter. Therefore, for the allowable load, the caisson may present a behavior different from that foreseen in the design if the friction resistance is not considered (Hachich & Falconi, 1998).

According to Teixeira (1997) the influence of skin friction on the bearing capacity of a caisson is very important, even in shorter caissons with lengths of approximately 4 meters, because the instrumentation performed in the tests indicated an average of 48% of skin friction and 52% for the base.

Carneiro (1999) performed load tests on open caisson under humidity in situ and flooded conditions. This author states that the portion coming from skin friction is of utmost importance when considering the bearing capacity calculation of these foundations, since there is an effective collaboration, especially when it comes to collapsible soils, where his conclusion is in line with that reported by Mello (1975) who, through load tests performed on prototypes in London clays and sands in the United States, shows that such friction should not be disregarded.

The magnitude of settlements due to the allowable load is low and the displacement records come basically from the elastic deformations of the concrete (shaft). According to Falconi et al. (2016), when it comes to estimating settlements for tubulars, we find great difficulties to perform such a calculation, because numerous factors such as the scarcity of information in geotechnical literature with respect to calibration of the various methods available, the high cost to perform load tests due to the order of magnitude of the element and the several variations characteristic of soils, These factors can lead to erroneous results regarding the actual behavior of the soil underlying the base, since skin friction at the caisson shaft may reduce the load on the base, whether or not this was considered in the calculations.

3. Foundations and characteristics analyzed

Three types of caisson foundations were analyzed, and each type was also analyzed at three different depths of 10 m, 15 m and 20 m (Figure 1). Thus, the increase of the skin frictional resistance could be evaluated in relation to the base resistance. Therefore, the values for shaft diameter (d), base diameter (B), shaft height (L), laying depth (H), and widened base height (h_b) were established based on values commonly employed in caisson foundation designs (Table 1).

For the analyses, the length “ L ” of the shafts was varied in 10, 15 and 20 meters, keeping the other geometries unchanged. The region with failure material, i.e., with low strength employed above the base of the defective caisson. Thus, a cylindrical segment of 0.5 m height (y) and diameter (d) equal to the caisson shaft was adopted. The use of this element aims to obtain the full mobilization of skin frictional resistance before the beginning of the mobilization of the widened base. In this situation, the caisson base would only be mobilized for more significant deformations, on the order of 10% to 20% of the base diameter, as recommended by (Hachich & Falconi, 1998).

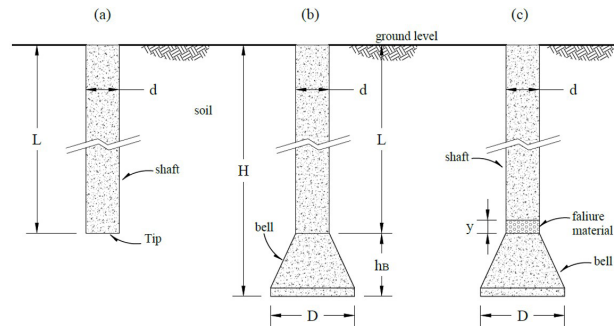


Figure 1. Schematic of the analyzed foundation types: a) pile (no bell); b) unimpaired caisson (with bell); c) defective caisson (with bell).

Table 1. Geometric characteristics of the analyzed foundations.

Types of foundations	d (m)	D (m)	L (m)	H (m)	h_b (m)
Pile-10	0.80	-	10	10	-
Caisson-10	0.80	2.70	10	11.80	1.80
Defective Caisson-10	0.80	2.70	10	11.80	1.80
Pile-15	0.80	-	15	-	-
Caisson-15	0.80	2.70	15	16.80	1.80
Defective Caisson-15	0.80	2.70	15	16.80	1.80
Pile-20	0.80	-	20	-	-
Caisson-20	0.80	2.70	20	21.80	1.80
Defective Caisson-20	0.80	2.70	20	21.80	1.80

With the adopted geometry it was ensured that the inclination of the widened base is greater than 60° so that tensile stresses at the bottom of the base can be neglected without the need for reinforcement for this purpose.

Therefore, a total of nine analyses were performed, being three analyses for each depth and foundation type, with variation of the shaft length (L) in 10, 15 and 20 meters, according to Table 1.

4. Axisymmetric FEM 2D model

An axisymmetric geometry was used to numerically simulate the caisson foundation prototypes, since the shaft and base have the same axis of symmetry (Figure 2). This technique allows representing the three-dimensional behavior of foundations by means of a plane model. Based on this, 2D finite element mesh elements of the triangular type were used, composed of 6 nodes, 3 nodes at each vertex and 3 nodes at the midpoint of each edge. The convergence of the model with the number of degrees of freedom was evaluated. Both the mesh density and the discretization of the model contour impact the number of degrees of freedom. Therefore, all models were subjected to convergence tests to achieve the necessary accuracy to them be used in the analyses. The numerical simulation phases are composed of a) RS Modeler (preprocessing); b) RS Compute (processing) and c) RS Interpret (postprocessing). The resolution of the numerical models follows the Absolute Force and Energy criterion, in which the simultaneous convergence of the values of the internal and external forces acting on the nodes of the elements is evaluated. The use of this criterion increases the accuracy of the simulation results.

The half-space considered in the analysis has adequate dimensions that validate the established boundary conditions. On the side boundaries of the half-space, the displacements are released in the vertical direction and restricted in the horizontal direction. At the base of the half-space, the displacement constraints were assigned in both directions (Figure 2). The same concept was employed for the numerical models of the pile (Figure 2a), pipe (Figure 2b) and defective

caisson (Figure 2c). Thus, the dimensions of 30 m x 30 m were adopted for the domain of the three foundation models, preventing the extension of the domain from affecting the comparison between the simulation results.

The load was applied axially to compression at the top of the shaft of the foundation elements, being subdivided into 11 load stages, with the increment equal to 10% of the maximum estimated load, until reaching a displacement that would characterize the failure of the foundation element. In this case, as recommended by the international literature, a value of 10% of the shaft diameter (i.e., a settlement of 80 mm) was fixed as the displacement that corresponds to the failure. The displacements were measured in the same plane of load application, from an average of five measurements.

To reproduce the material failure, the Mohr-Coulomb criterion was used, which has been employed in numerical analyses to relate shear and normal stress acting in a plane:

$$\tau = c + \sigma \cdot \tan \phi \quad (5)$$

Where σ is the normal stress; c is the cohesion intercept and ϕ is the friction angle.

5. Material properties

For the simulation of the cases analyzed, the geotechnical parameters were defined as constant in depth for a homogeneous and isotropic soil, allowing the analysis of the stresses caused by the contact between the foundation element and the soil, without the influence of the characteristics of the soil type variation. The soil input parameters were based on the characterization performed by Oliveira (2022) for a silty-clayey sand (Table 2).

The concrete with a compressive strength of 20 MPa was adopted for the caisson material, which is the most used in the concreting of this type of foundation. The elastic modulus of concrete was obtained by following the procedures of NBR 6118 (ABNT, 2014). The input properties in the Mohr-Coulomb model for concrete and low strength material with high deformability were obtained based on the work of Ardiaca (2009).

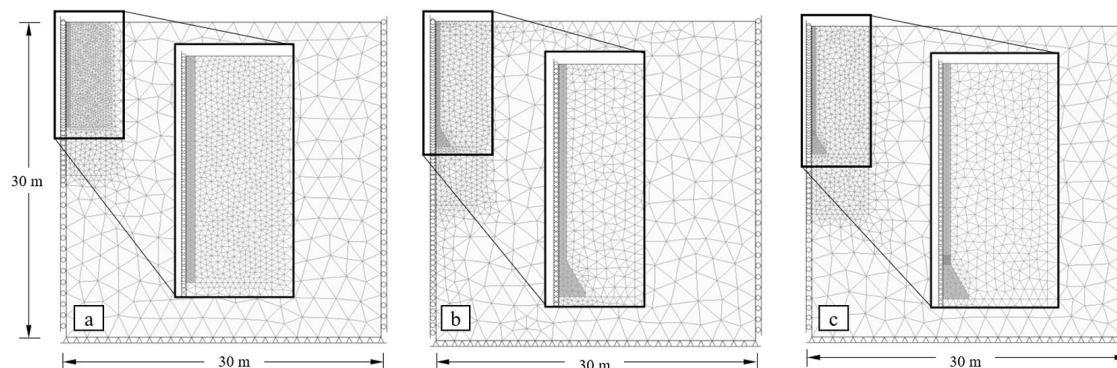


Figure 2. Numerically simulated axisymmetric models of: a) pile; b) pipe; c) defective caisson.

Table 2. Parameters for the Mohr-Coulomb criteria.

Material	E (MPa)	ν	K_0	γ (kN/m ³)	Model	ϕ (°)	c (kPa)
Soil	22	0.3	0.6	17	Elastoplastic	23	10
failure material	2.2	0.40	-	-	Elastoplastic	10	3
Concrete	30.000	0.20	-	25	Elastic	35	442

Note: E is the elastic modulus; ν is the Poisson's ratio; K_0 is the coefficient of earth pressure at rest; γ is the unit weight; ϕ is the soil friction angle; c is the cohesion.

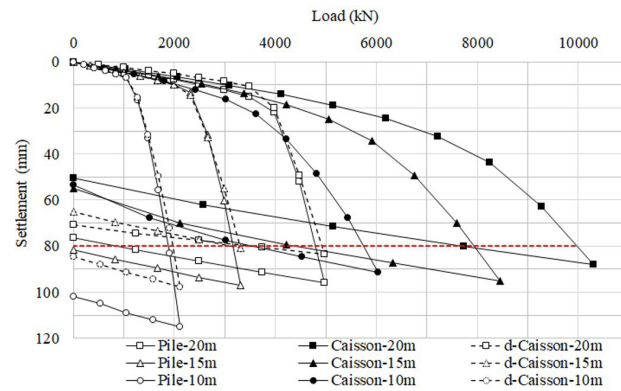
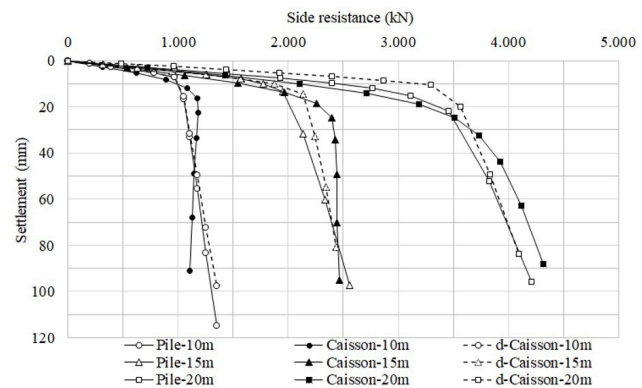
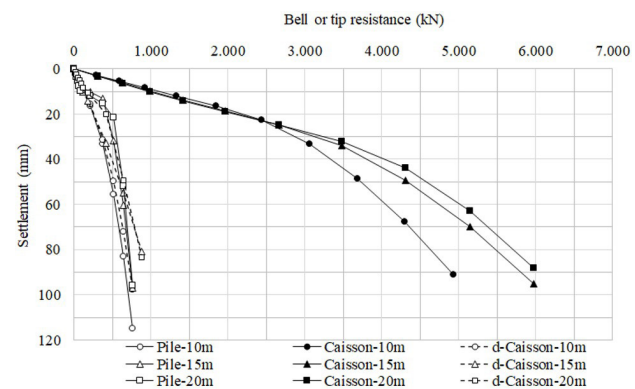
6. Analysis and discussion of the results

The load versus settlement curves obtained with the aid of (see Figure 3) was used to obtain the ultimate load for the displacement of 80 mm (10% of the diameter of the shaft of the analyzed foundations). With the readings of the top and tip of the shaft, the friction and tip resistance plots were determined, as well as the respective load vs. settlement curves (Figures 4 and 5). In these, this resistance increases linearly with the increase in shaft length. The same does not occur with the tip resistance for the cases of isolated pile and defective caisson, which remained constant with increasing shaft length in depth. On the other hand, for the intact caisson case, tip resistance increases with depth, presenting a significant increase when comparing the 10 m shaft with the 15 and 20 m lengths.

Comparing the piles and caisson with defective induced at the top of the widened base, they presented similar behavior to each other, i.e., they were close to the behavior of a single pile. And, considering the specific conditions of this paper, these foundations have a predominance of skin friction resistance in their bearing capacity, as previously mentioned by Das (2010). Such hypothesis is proven when we observe the results from the numerical analysis of the caisson with the low strength material placed at the top of the widened base, since this material prevents the load transfer to the base due to its higher deformability and lower strength. The values for ultimate load, allowable load and respective settlement were extracted from the load vs. settlement curves and are presented in Table 3.

The presence of the widened base directly influences the load transfer of the caisson foundation because the presence of the defect above the top of the caisson base caused the load transfer by skin frictional resistance to present similar behavior to the pile (Figure 6).

In the case of the foundation in an intact caisson consisting of shaft and widened base, it is verified that the tip resistance predominates in the bearing capacity (Table 3), as observed by Murthy (2002). However, this predominance of the tip resistance is more significant for loading stages greater than 60% of the ultimate bearing capacity of the caisson (20% d) and tends to reduce with increasing depth of settlement of the caisson, i.e., with increasing length " L " of the shaft (Figure 6b, 6e and 6h). On the other hand, skin frictional resistance shows predominance in the early stages of loading, between 10% and 60% of the caisson bearing


Figure 3. Load-settlement curves of the analyzed cases.

Figure 4. Skin friction resistance vs. settlement curves of the analyzed cases.

Figure 5. Tip resistance vs. settlement curves of the analyzed cases.

capacity, as well as an increasing tendency with increasing caisson settlement depth (Figure 6).

Table 3. Summary of ultimate and allowable loads.

Analyse cases	Ultimate Load - for 80 mm			Allowable Load			
	Q_{ult}	Q_{su}	Q_{tip}	Q_{all}	s_{all}	Q_{su}	Q_{tip}
	[kN]	[kN]	[kN]	[kN]	[mm]	[kN]	[kN]
Pile-10m	1.875	1.242	633	938	6.07	621	317
Caisson-10m	5.743	1.112	4.631	2.871	15.29	556	2.316
d-Caisson-10m	1.965	1.282	683	982	6.45	641	341
Pile-15m	3.163	2.338	708	1.582	7.52	1.169	354
Caisson-15m	7.936	2.452	5.484	3.968	17.14	1.226	2.742
d-Caisson-15m	3.306	2.431	875	1.653	7.89	1.215	438
Pile-20m	4.797	4.077	720	2.398	9.38	2.038	360
Caisson-20m	9.973	4.257	5.716	4.987	18.11	2.129	2.858
d-Caisson-20m	4.924	4.066	858	2.462	6.62	2.033	429

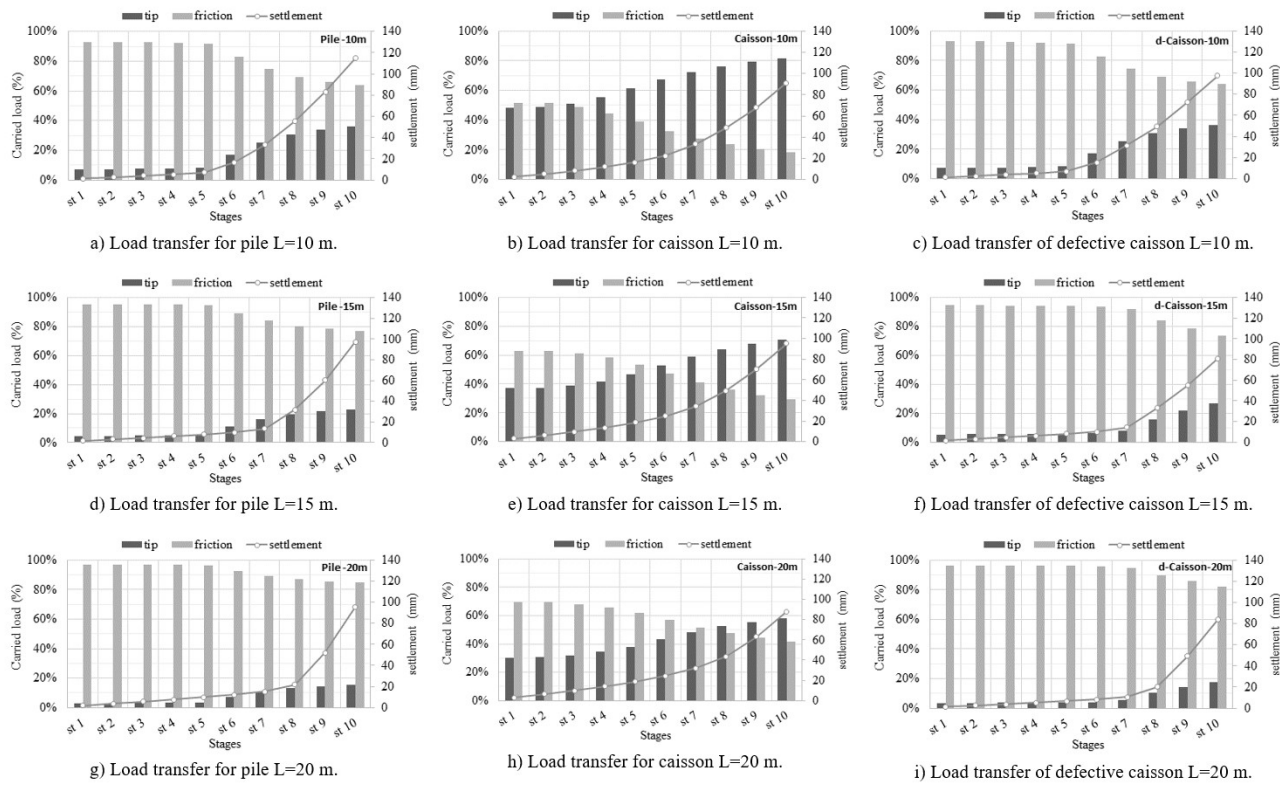


Figure 6. Load Transfer for piles, caisson and defective caisson for different shaft lengths.

From the cases analyzed, even for caisson foundations, side resistance becomes significant at greater depths. The opposite is observed for the resistance of the base, which is more significant when the caisson rests on shallower depths, and therefore, the potential for skin friction to develop is smaller, i.e., with less potential for skin friction development (Figure 6).

The presence of low strength material, as a way to represent a “constructive defective”, occurred in the top of the widened base modified the load distribution in the foundation, resulting in a situation similar to an single pile, except for the fact that in the pile, there is some tip resistance, while in the caisson with defective, there is a predominance of skin frictional resistance in the bearing capacity of the foundation (Figure 6).

In all cases analyzed, the tip or widened base resistance tends to decrease concomitantly with the increase of the shaft length. For the depths of 10, 15 and 20 m, this reduction is 19%, 24% and 18%, respectively for pile, intact caisson and defective caisson (Figure 7). On the other hand, it was observed that skin frictional resistance for the same depths increases in the same proportions.

The percentage of load transfer through the widened base decreases linearly with increasing shaft-base area ratio, since the area of the shaft increases with the depth of placement of the caisson. While the load transfer through the shaft increases with the same ratio (Figure 8).

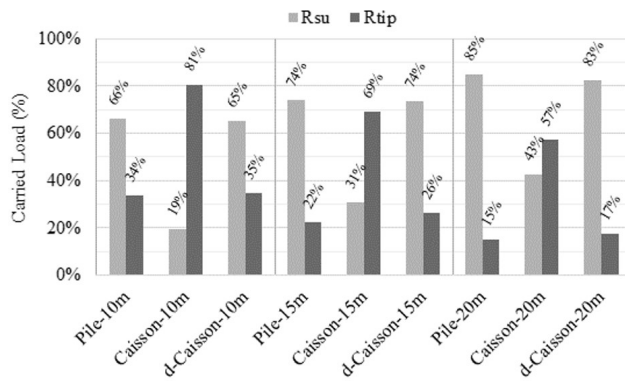


Figure 7. Skin friction and tip resistance of foundation types at different depths.

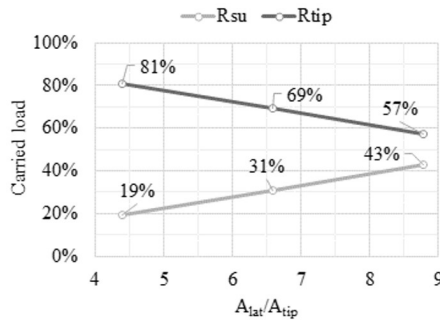


Figure 8. Load transfer to bell and shaft for different area ratios.

At greater depths, the lateral resistance increases and equals 43% of the caisson bearing capacity, against 57% for the base resistance. The obtained results agree with those observed by Teixeira (1997) e Carneiro (1999).

7. Conclusion

This paper analyzed the behavior of caisson with and without a widened base, laid at 10, 15 and 20 m of depth, three of which had deformable material at the top of the widened base. Thus, it was found that with increasing depth, the frictional resistance of the surrounding soil contributes significantly to the bearing capacity of the caissons at hand.

For situations in which the caissons rest in deep layers, the base widening can be removed, since the foundation behaves similarly to a pile, as occurred in the case of the caisson with a defective low strength material at the top of the widened base that modified the load distribution in the foundation.

The widened base caisson may represent only an economic expense of material, labor and time, since in all cases analyzed, the strength of the tip or widened base tends to decrease concomitantly with the increase in length of the shaft. On the other hand, for situations in which the foundation rest at shallow depths, one can choose to enlarged the base or not, leaving to the designer's discretion the decision of sizing it as a pile or caisson with a belled geometry, since in

this case the base resistance is preponderant in the bearing capacity of the caisson.

The non-widening of the base may be an important consideration in foundation designs that use caisson, as it would reduce risks to human lives, besides providing a lower consumption of materials and reducing the generation of carbon released into the atmosphere.

Acknowledgements

We thank the Federal University of Uberlândia for obtaining the software license used in the analyses of this article.

Declaration of interest

The authors have no conflicts of interest to declare. All co-authors have observed and affirmed the contents of the paper and there is no financial interest to report.

Authors' contributions

Bárbara Estéfany Pereira: conceptualization, methodology, validation, writing – original draft. Jean Rodrigo Garcia: data analysis, supervision, validation, writing – review & editing, funding acquisition.

Data availability

The datasets generated analyzed in the course of the current study are available from the corresponding author upon request.

List of symbols

c	intercept cohesion
d	shaft diameter
h_B	base height
q	surcharge
B	footing width
D	base diameter
E	Young's modulus
H	base installation depth
K_0	coefficient of at-rest earth pressure
N_c, N_q, N_γ	bearing capacity factors
\bar{N}_{SPT}	blow count average
γ	unit weight
ν	Poisson's ratio
σ	normal stress
σ_{adm}	allowable stress
σ_{vb}	vertical effective stress in the toe
σ_{rup}	bearing pressure
τ	shear stress
ϕ	soil friction angle

References

- ABNT NBR 6118. (2014). *Projeto de estruturas de concreto, procedimento*. ABNT - Associação Brasileira de Normas Técnicas, Rio de Janeiro, RJ (in Portuguese).
- ABNT NBR 6122. (2019). *Projeto e execução de fundações*. ABNT - Associação Brasileira de Normas Técnicas, Rio de Janeiro, RJ (in Portuguese).
- Albiero, J.H., & Cintra, J.C.A. (2016). Análise e projeto de fundações profundas: tubulões caixões. In F.F. Falconi, C.N. Corrêa, C. Orlando, C. Schimdt, W.R. Antunes, P.J.R. Albuquerque, W. Hachich & S. Niyama (Orgs.), *Fundações: teoria e prática* (pp. 297-322). Pini (in Portuguese).
- Albuquerque, P.J.R., & Garcia, J.R. (2020). *Engenharia de fundações*. LTC (in Portuguese).
- Alonso, U.R. (1983). *Exercícios de fundações* (2nd ed.). Blucher (in Portuguese).
- Aoki, N., & Velloso, D.A. (November 17-22, 1975). An approximate method to estimate the bearing capacity of piles. In S.J. Trevisán (Org.), *Fifth Panamerican Conference on Soil Mechanics and Foundation Engineering* (pp. 367-376). Montreal, Canada: International Society for Soil Mechanics and Foundation Engineering.
- Ardiaca, D.H. (2009). Mohr-Coulomb parameters for modelling of concrete structures. *Plaxis Bulletin*, 25, 12-15.
- Carneiro, B.J.I. (1999). *Comportamento de tubulões à céu aberto, instrumentados, em solo não-saturado, colapsível* [Doctoral thesis]. Universidade de São Paulo (in Portuguese).
- Das, M.B. (2010). *Principle of geotechnical engineering* (7th ed.). Cengage Learning.
- Décourt, L. (August 13-18, 1989). Part 2 the standard penetration test, state of-the-art report. In Pubns Committee of the XII Icsmf Staff (Ed.), *Proceedings of the 12th International Conference on Soil Mechanics and Foundation Engineering* (p. 2405). Oxfordshire, England: Taylor & Francis.
- Décourt, L., & Quaresma, A.R. (1978). Capacidade de carga de estacas a partir de valores SPT. In Associação Brasileira de Mecânica dos Solos e Engenharia Geotécnica (Org.), *Congresso Brasileiro de Mecânica dos Solos e Engenharia de Fundações* (pp. 45-54). São Paulo, Brazil: ABMS (in Portuguese).
- Falconi, F.F., Corrêa, C.N., Orlando, C., Schimdt, C., Antunes, W.R., Albuquerque, P.J.R., Hachich, W., & Niyama, S. (2016). *Fundações: teoria e prática* (3rd ed). Pini (in Portuguese).
- Hachich, W., & Falconi, F.F. (1998). *Fundações - teoria e prática* (2nd ed). Pini (in Portuguese).
- Mello, V.F.B. (1975). Deformações como base fundamental de escolha da fundação. *Geotecnia Journal*, 12, 55-75 (in Portuguese).
- Meyerhof, G.G. (1951). The ultimate bearing capacity of foundations. *Geotechnique*, 2(4), 301-332. <http://dx.doi.org/10.1680/geot.1951.2.4.301>.
- Murthy, V.N.S. (2002). *Geotechnical engineering: principles and practices of soil mechanics and foundation engineering*. Marcel Dekker.
- Oliveira, E. (2022). *Análise experimental e numérica do comportamento de sapata estaqueada em solo tropical* [Master's dissertation]. Universidade Federal de Uberlândia (in Portuguese). <https://doi.org/10.14393/ufu.di.2022.5055>.
- Teixeira, C. (1997). *Capacidade de carga de sapatas, estacas de pequeno diâmetro e tubulões curtos em função do SPT: um estudo em solos residuais de gnaisses para a região Sul de Minas* [Doctoral thesis]. Universidade de São Paulo (in Portuguese).
- Velloso, P.P. (1981). *Estacas em solo: dados para a estimativa do comprimento*. Clube de Engenharia (in Portuguese).

Maximum shear modulus and modulus degradation curves of an unsaturated tropical soil

Jeferson Brito Fernandes¹ , Breno Padovezi Rocha² , Heraldo Luiz Giacheti^{1#} 

Article

Keywords

Maximum shear modulus
Modulus degradation
Triaxial test
Bender elements
SDMT
Soil suction

Abstract

The maximum shear modulus (G_0) and the modulus degradation curve (G/G_0 versus γ) are important information in the evaluation of the soil mechanical behavior, both for dynamic and static loads. Dynamic tests (resonant column and cyclic triaxial tests) are not routinely performed in geotechnical practice in Brazil, and the geotechnical literature on the dynamic behavior of unsaturated tropical soils is limited. This paper presents and discusses seismic dilatometer (SDMT), resonant column, and triaxial test with bender elements and internal instrumentation to determine G_0 and the modulus degradation curve in an unsaturated tropical sandy soil profile. It was observed that G_0 tends to increase non-linearly with soil suction and net stress ($\sigma - u_a$). It was also observed that the in situ G_0 values determined with the SDMT were higher than those from laboratory tests (bender elements and resonant column). The modulus degradation curves determined with resonant column were used to define the reference curve via SDMT for the studied site. Soil suction influence in shear modulus degradation curves determined with unsaturated triaxial compression tests with local instrumentation is also presented and discussed.

1. Introduction

The maximum shear modulus (G_0) and the modulus degradation curve (G/G_0 versus γ) are important information to analyze the mechanical behavior of soils. It is necessary to determine these parameters and this curve due to the increase demand for nuclear facilities, offshore structures, and machine foundation design. The ground motion of the site is significantly affected by the local site condition during an earthquake, and the average shear wave velocity (V_s) up to 30 m is the key variable for site characterization in geotechnical earthquake engineering (Bang & Kim, 2007; ICC, 1997). Moreover, the G_0 values can be used for a static deformation analysis such as slope stability, settlement estimative, an evaluation for ground improvements, as well as assessment of collapsible soils (Burland et al., 1977; Kim & Park, 1999; Rocha et al., 2022). Tests to determine soil dynamic parameters are not currently performed in Brazil and the geotechnical literature on the dynamic behavior of tropical soils is limited.

The crosshole test is the most effective technique for determining V_s , and to calculate the maximum shear modulus (G_0) via Elasticity theory. Recently, the seismic dilatometer (SDMT) has being widely used since it allows the site characterization together with the determination of V_s profiles, consequently G_0 (Marchetti et al., 2008). Resonant

column tests and the bender elements incorporated to triaxial tests can be used to determine V_s under controlled conditions in laboratory, such as confining stress, strain amplitude and soil suction influence.

The soil behavior is highly non-linear and has an important influence on the selection of design parameters for simple routine geotechnical projects (Atkinson, 2000). So, the direct application of G_0 to evaluated deformations problems is not applicable, and the shear modulus decay curve is necessary. The non-linear soil stress-strain behavior can be estimated with in situ and laboratory tests. In situ tests, like the crosshole and downhole can be used to determine shear modulus at small strains; dilatometer, pressuremeter, and plate load tests for medium strains; cone penetration and standard penetration tests for largely deformed soils (Amoroso, 2011; Atkinson, 2000; Ishihara, 2001). Laboratory tests, such as the bender elements or the resonant column, the cyclic triaxial or torsional shear tests, or even monotonic triaxial tests, or double specimen direct simple shear can be used to estimate the non-linear soil behavior (Amoroso, 2011).

A large portion of Brazil is covered by unsaturated tropical soils and the geotechnical literature about dynamic parameters of these soils is limited since dynamic tests are not currently carried out. The term tropical soil includes both lateritic and saprolitic soils. Saprolitic soils are residual and retain the macro fabric of the parent rock. Lateritic soils can

[#]Corresponding author. E-mail address: h.giacheti@unesp.br

¹Universidade Estadual Paulista "Júlio de Mesquita Filho", Faculdade de Engenharia, Departamento de Engenharia Civil e Ambiental, Bauru, SP, Brasil.

²Instituto Federal de Educação, Ciência e Tecnologia de São Paulo, Campus Avançado Ilha Solteira, Ilha Solteira, SP, Brasil.

Submitted on December 2, 2022; Final Acceptance on February 20, 2023; Discussion open until August 31, 2023.

<https://doi.org/10.28927/SR.2023.013122>



This is an Open Access article distributed under the terms of the Creative Commons Attribution License, which permits unrestricted use, distribution, and reproduction in any medium, provided the original work is properly cited.

be either residual or transported and are distinguished by the occurrence of the laterization process, which is an enriching of a soil with iron and aluminum and their associated oxides (cementation), caused by weathering in regions which are hot, acidic, and at least seasonally humid (Nogami & Villibor, 1981). Cementation and soil suction affects the soil behavior of unsaturated tropical soils, both in situ and in laboratory (Fernandes et al., 2022; Giacheti et al., 2019; Rocha et al., 2021). The contribution of microstructure (cementation) and soil suction to the soil stiffness depends on the strain level the soil will experience (Atkinson, 2000). These characteristics increase the overconsolidation stress and cohesion intercept (Vaughan et al., 1988) and the most existing empirical correlation should be employed with caution (Robertson, 2016).

In this paper, SDMT, triaxial tests with bender elements and internal instrumentation, as well as resonant column carried out in an unsaturated tropical soil are presented and discussed. G_0 values determined by these different techniques were compared. The modulus degradation curves (G/G_0 versus γ) determined via resonant column tests were used to define the reference curve for the SDMT based on the approach proposed by Amoroso et al. (2014). In addition, the effect of the unsaturated soil condition on the modulus degradation curves obtained from triaxial tests with suction control and internal instrumentation are presented and discussed.

2. Study site

SDMT, resonant column and triaxial tests with bender elements were conducted at the Experimental Research Site

at the São Paulo State University (Unesp), located in the city of Bauru, State of São Paulo, Brazil. The study site includes a colluvial Neo-Cenozoic deposit up to about 13 m depth, followed by a residual soil formed during the Quaternary (De Mio, 2005). The soil profile consists in an unsaturated clayey fine sand with lateritic behavior up to about 13 m depth. The MCT Classification System (Mini, Compacted, and Tropical) proposed by (Nogami & Villibor, 1981) for tropical soils was used to define and classify the soils with regards to the lateritic behavior. These soils have undergone pedogenic and morphogenetic processes (Giacheti et al., 2019). Consequently, this soil has high porosity, high saturated hydraulic conductivity (10^{-5} to 10^{-6} m/s), and a cohesive-frictional behavior. A major geotechnical problem for this soil is collapsibility caused by soil wetting.

Several site characterization programs including Standard Penetration Tests (SPT), Standard Penetration Tests with Torque (SPT-T), Seismic Cone Penetration (SCPT), Flat Dilatometer (DMT), Pressuremeter (PMT), and Seismic tests (crosshole - CH and downhole - DH) were carried at the site. Sample pits were also excavated to retrieve undisturbed and disturbed soil blocks. Soil samples from these blocks were tested in laboratory for soil characterization and determination of mechanical properties and parameters. Figure 1 summarizes laboratory and in-situ tests carried out at the study site: grain size distribution (with and without dispersant), some index properties, SCPT, SPT, PMT and Seismic tests data along the soil profile.

3. In situ and laboratory tests

Four SDMTs were carried out at the study site up to 15 m depth. The SDMT testing procedures were conducted

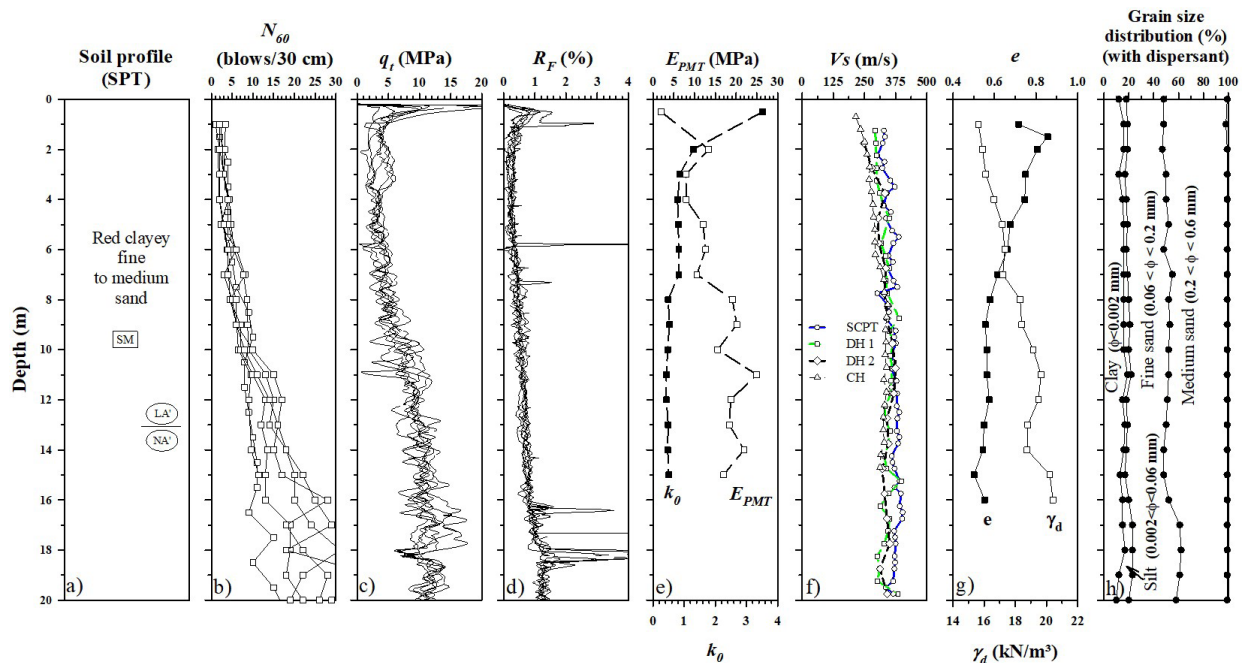


Figure 1. Summary of in situ and laboratory tests carried out at the study site [adapted from Rocha & Giacheti (2018)].

in accordance with Marchetti et al. (2006). A multi-function penetrometer with a 150 kN thrust capacity (Model Pagani TG 63 – 150 DP), which was anchored to the ground by helical augers, was used to carry this in situ test. The SDMT blade was pushed into the ground at a constant rate of 20 mm/s. The readings A-pressure and B-pressure were taken at intervals of 200 mm, and then these pressures were corrected for membrane stiffness and converted into p_0 and p_1 . The three intermediate DMT parameters (I_D : material index; K_D : horizontal stress index; E_D : dilatometer modulus) were calculated from the p_0 and p_1 values. Field measurements of the shear wave velocity (V_s) were taken at 0.5 or 1 m depth interval.

The resonant column tests were presented by Giacheti (1991). The triaxial tests were performed with internal instrumentation and bender elements by Fernandes (2022). The modulus degradation curves were determined from the resonant column, triaxial and SDMT test data.

Cylindrical specimens of about 36 mm in diameter and 80 mm in height were used in the resonant column tests. They were rigidly fixed to the base of the triaxial chamber by means of a blade embedded in the porous stone (Giacheti, 1991). Table 1 shows some geotechnical indexes, the confining stresses, and the moisture content conditions for each of them. The multi-stage technique was employed in the resonant column tests, as described by Anderson & Stokoe (1978). A very low amplitude torsional excitation was applied to the top of the specimen and the shear wave velocities were determined over the logarithmic time interval up to 1,000 minutes or up to 10,000 minutes in some cases for each confining stress stage. Subsequently, the excitation force was gradually increased and the variation of the ratio of shear modulus to strain amplitude was determined.

The saturated and unsaturated triaxial tests with internal instrumentation and bender elements were performed using 50 mm diameter specimens with the height ranging from 100 to 120 mm. The determination of V_s (and hence G_0) via bender elements was performed for the samples collected at 1.5, 5, 7, 11, and 13 m depth. The phase angle between the waves and the frequency domain method (Ferreira, 2002) were used to determine the wave propagation time. Suction values of 0 (saturated), 50, 200 and 400 kPa were imposed for samples collected at 1.5 and 5 m depth and suction values of 0 (saturated), 50, 100 and 200 kPa for samples collected at 7, 11 and 13 m depth. The applied confining stresses were 25, 50, 100, and 200 kPa for all samples tested. The axial (ϵ_a) and radial (ϵ_r) strains were measured by internal instrumentation

(LVDTs with axial and radial displacement measurement) for the sample collected at 2 m depth, with a confining stress of 50 kPa and suction values equal to 0, 50, 200, and 400 kPa. The shear strain for individual soils elements (ϵ_s) can be calculated from Equation 1 based on ϵ_a and ϵ_r , and it was transformed in shear strain (γ) with Equation 2. The modulus of elasticity (E) was obtained from the triaxial test data and a Poisson ratio (μ) equal to 0.2 was assumed to determine the modulus degradation curve (Equation 3).

$$G = \frac{E}{2 \cdot (1 + \mu)} \quad (1)$$

$$\epsilon_s = (2/3 \cdot (\epsilon_a - \epsilon_r)) \quad (2)$$

$$\gamma = 3/2 \cdot \epsilon_s \quad (3)$$

3.1 Modulus degradation curve via SDMT

The modulus degradation curve can be estimated from a reference degradation curve determined in the laboratory by cyclic testing (Marchetti et al., 2008). This curve can be defined from two points obtained by means of SDMT: (1) maximum soil shear modulus (G_0), and (2) shear modulus at the working condition (G_{DMT}). Amoroso et al. (2014) presents a procedure to estimate the modulus degradation curve via SDMT based on the findings of Marchetti et al. (2008). This procedure is schematically represented by Figure 2, and it consists of the following steps:

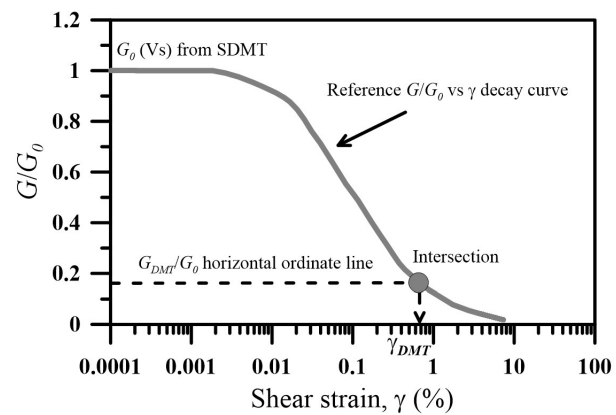


Figure 2. Amoroso et al. (2014) approach to derive modulus degradation curves from SDMT [adapted from Amoroso et al. (2014)].

Table 1. Some information of the previously performed resonant column tests [adapted from Giacheti (1991)].

Depth (m)	Confinant stresses (kPa)	Liquid limit W_L (%)	Plastic index P_I (%)	Unit weight γ_n (kN/m ³)	Water content condition
0.95	25, 50 and 100	19	4	16.45	Natural
4.8	50, 100 and 200	22	5	17.1	Natural
8.85	50, 100 and 200	23	7	17.9	Natural

- Determine G_0 based on V_s from SDMT, at the same depth of the available reference modulus degradation curve;
- Calculate G_{DMT} based on the constrained modulus obtained from SDMT data (M_{DMT}) (Equation 4) and normalized by its maximum shear modulus (G_0).

$$G_{DMT} = \frac{1-2\mu}{2 \cdot (1-\mu)} \cdot M_{DMT} \quad (4)$$

Where μ is the Poisson ratio.

- Assume the shear strain associated with working strain DMT moduli (γ_{DMT}) based on the available information [e.g., Amoroso (2011)];
- Then, use Equation 5, proposed by Amoroso (2011), to assess the shear modulus reduction curve by SDMT.

$$\frac{G}{G_0} = \frac{1}{1 + \left(\frac{G_0}{G_{DMT}} - 1 \right) \left(\frac{\gamma}{\gamma_{DMT}} \right)} \quad (5)$$

Therefore, the ratio G_{DMT}/G_0 obtained from SDMT and the estimated shear strain γ_{DMT} were used to plot the corresponding hyperbolic curve at each investigated test site.

According to Amoroso et al. (2014), the “typical range” of shear strain (γ_{DMT}) associated to the working strain moduli G_{DMT} can be approximately assumed as 0.01 to 0.45% for sand, 0.1 to 1.9% for silt and clay, and higher than 2% for soft clay. The authors considers that this approach can provide a first estimate of the modulus degradation curve (G/G_0 versus γ) of the soil.

3.2 SDMT

Figure 3 shows the intermediate DMT parameters (I_D , K_D , and E_D) and the shear wave velocity, and consequently

maximum shear modulus profiles for the study site. I_D , K_D , and E_D were calculated by Marchetti’s equations (Marchetti, 1980). Shear wave velocity determined with SDMT, and total mass density (ρ) determined using undisturbed soil samples collected in a sample pit excavated at the study site were used to calculate G_0 values based on Elastic Theory (Equation 6).

$$G_0 = \rho \cdot V_s^2 \quad (6)$$

Where V_s is shear wave velocity, and ρ is the total mass density.

Figure 3 shows a good agreement between the V_s and G_0 profiles determined by all the performed tests. The values of V_s and G_0 increase with depth up to 10 m and this trend becomes almost constant after that depth.

3.3 Triaxial tests with bender elements (BE) and internal instrumentation

The shear wave velocity (V_s) and consequently G_0 were determined using bender elements. G_0 shows a tendency to increase non-linearly with the suction and with the net stress ($\sigma - u_a$) for sandy soils, and tends asymptotically to a limit (Nyunt et al., 2011). A hyperbolic function was used to evaluate the influence of the suction and the net stress variables on the maximum shear modulus (Equation 7).

$$G_0 = G_{0,sat} + a(\sigma - u_a) + \frac{s}{b + c(s)} \quad (7)$$

Where $G_{0,sat}$ is the maximum saturated shear modulus, s is the soil suction, and a , b , and c are empirical parameters of the fit. G_0 and $G_{0,sat}$ are expressed in MPa and the net stress ($\sigma - u_a$) and suction in kPa.

Figure 4 shows the variation of G_0 with suction and with net stress, as well as the fitting for the samples collected at

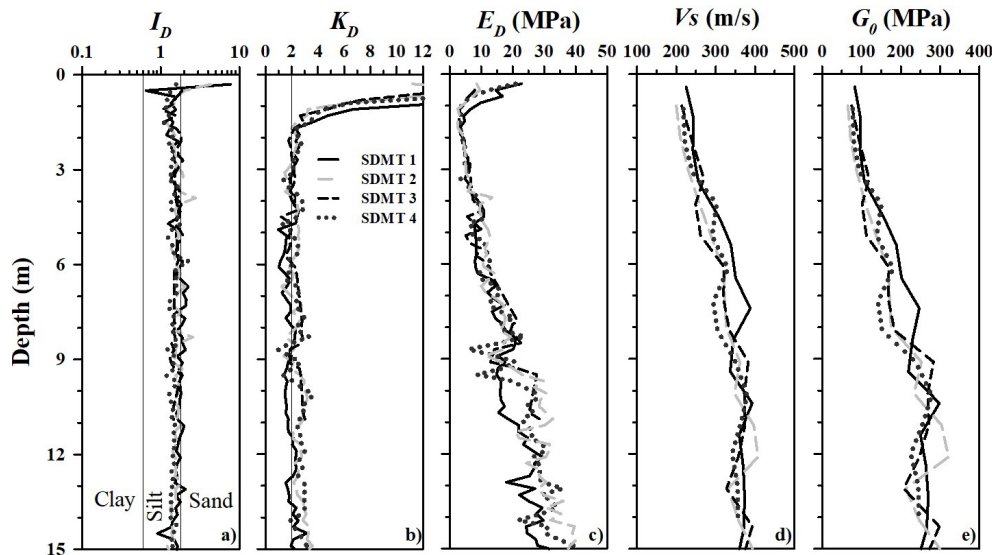


Figure 3. SDMT data at the study site.

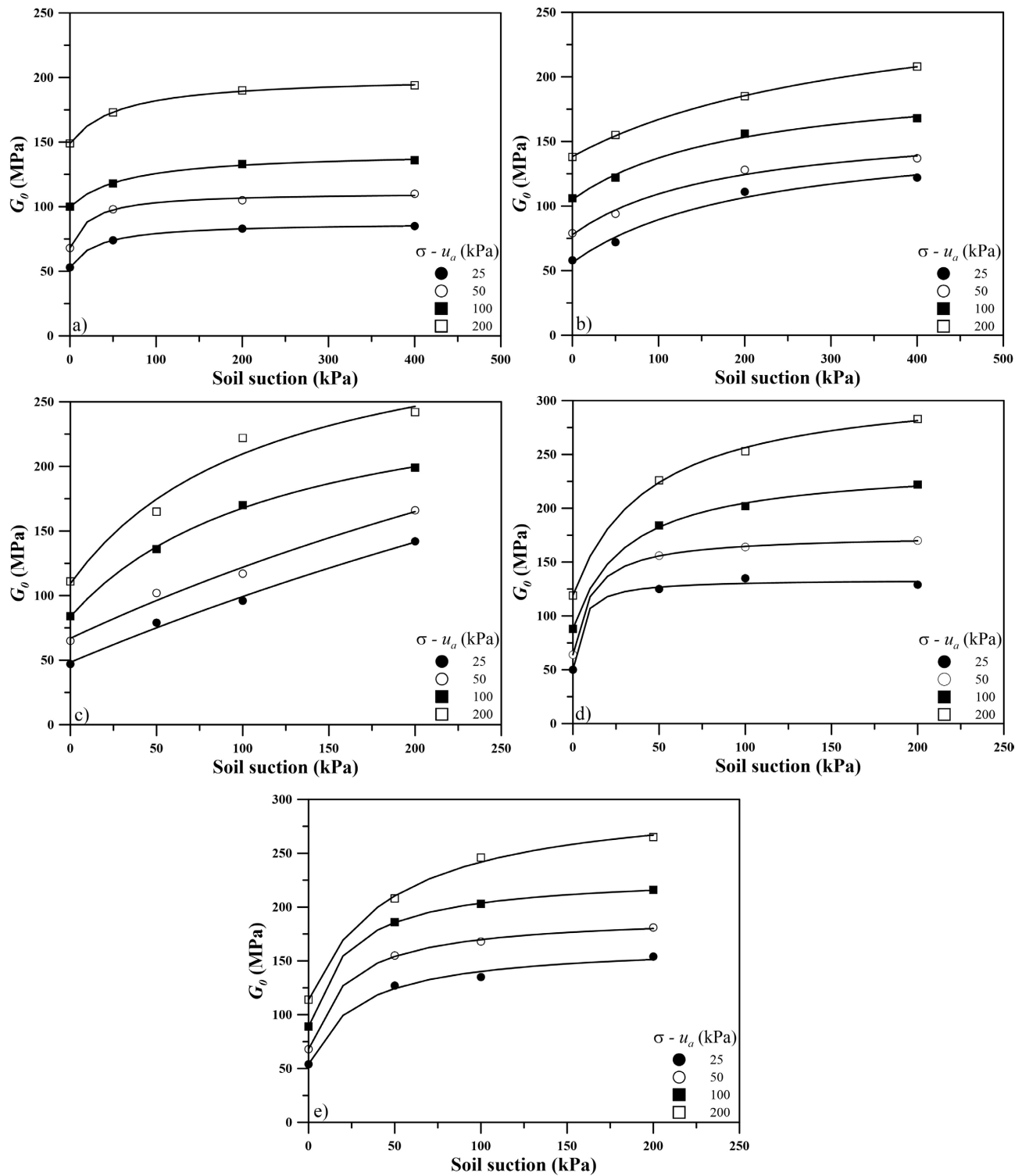


Figure 4. Variation of G_0 with net stress ($\sigma - u_a$) and with suction for the undeformed soil samples collected at (a) 1.5 m, (b) 5 m, (c) 7 m, (d) 11 m, and (e) 13 m depth.

1.5, 5, 7, 11, and 13 m depth. As the soil suction increases from 0 to 400 kPa, the shear moduli at small strain (assumed equal to 0.001%) also increase. Table 2 shows the fitting parameters for the Equation 7 at the 100 kPa net stress

for all the investigated depths. It can be seen from this figure that the experimental data are well represented by a non-linear relationship (Equation 7) between G_0 and the variables suction and net stress, except for the net stresses

of 25 and 50 kPa for the depth of 7 m, which showed a quasi-linear behavior.

Figure 5 shows the absolute values of the shear modulus at a small shear strain of 0.001% and at a finite strain of 1% for the sample collected at 2 m depth. It also can be seen from this figure that the soil shows a relatively high and fast variation of the shear modulus as the shear strain increases from 0.001 to 1%.

3.4 Resonant column (RC) tests

Giacheti (1991) presented the maximum shear modulus (G_0) as a function of time of confinement by performing resonant column tests and observed that the samples tested (Table 1) showed an almost linear increase of G_0 with logarithmic time, practically from the beginning of drainage, which is a typical behavior for sands. Figure 6 shows the value of G_0 at 1,000 minutes of confinement at different confinement stresses for the samples collected at 0.95, 4.8, and 8.85 m depth (Giacheti, 1991). Figure 7 shows the modulus degradation curves (G/G_0 versus γ) determined for different confinement stresses for the samples collected at 0.95, 4.8, and 8.85 m depth (Giacheti, 1991).

Figure 7 shows the modulus degradation curves for the samples collected at 0.95, 4.8, and 8.85 m depth at different confinement stress (σ_3). It can be seen from Figure 7 that

the modulus G presents a small reduction for shear strains higher than $10^{-4}\%$, which is accentuated from γ greater than $10^{-3}\%$. Furthermore, a lower influence of confining stresses and depth on G values is observed for the range of strains investigated, with a tendency for a lower degradation of the modulus with increasing confining stress (σ_3).

4. Discussion

4.1 G_0 from in situ and laboratory tests

In order to compare G_0 values determined by SDMT, resonant column (RC) and bender elements (BE), in situ confining stresses were defined based on at-rest earth pressure coefficient (K_0) estimated from the Jaky (1948) equation.

All values were considered for the bender element tests with suction equal to 50, 100, and 200 kPa for the investigated depths (1.5, 5, 7, 11, and 13 m depth) since the SDMT and resonant column tests were performed in the natural soil condition. These suction values were defined from the suction monitoring by tensiometers, and watermark sensors presented by Giacheti et al. (2019). In addition, an average G_0 profile from four SDMTs was adopted.

Figure 8 shows the differences between the G_0 values determined by the average SDMT, average SDMT plus and

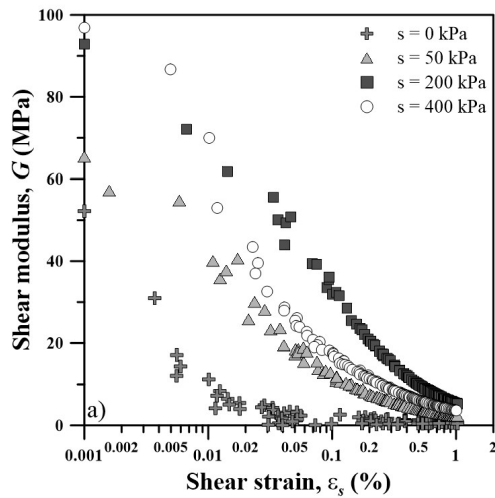


Figure 5. Modulus degradation curves for the tested samples from 2 m depth with suction values equal to 0, 50, 200, and 400 kPa.

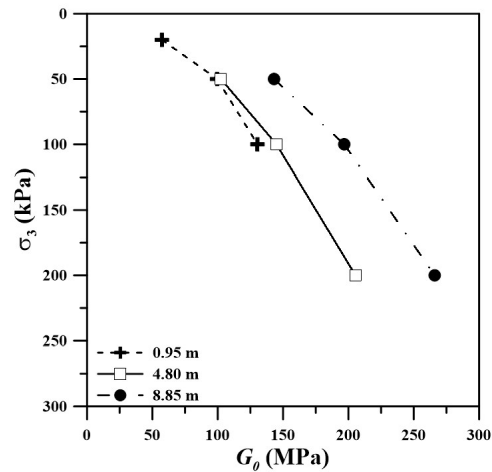


Figure 6. G_0 at 1,000 minutes of confinement for the samples collected at 0.95, 4.8, and 8.85 m depth at different confinement stresses [adapted from Giacheti (1991)].

Table 2. Fitting parameter for the Equation 7 at 100 kPa net stress.

Fitting parameters	Depth (m)				
	1.5	5	7	11	13
$G_{0,sat}$ (MPa)	52.1	53.3	40.9	47.9	53.1
a	0.478	0.517	0.427	0.401	0.334
b	1.534	2.059	0.656	0.202	0.703
c	0.023	0.010	0.005	0.006	0.006

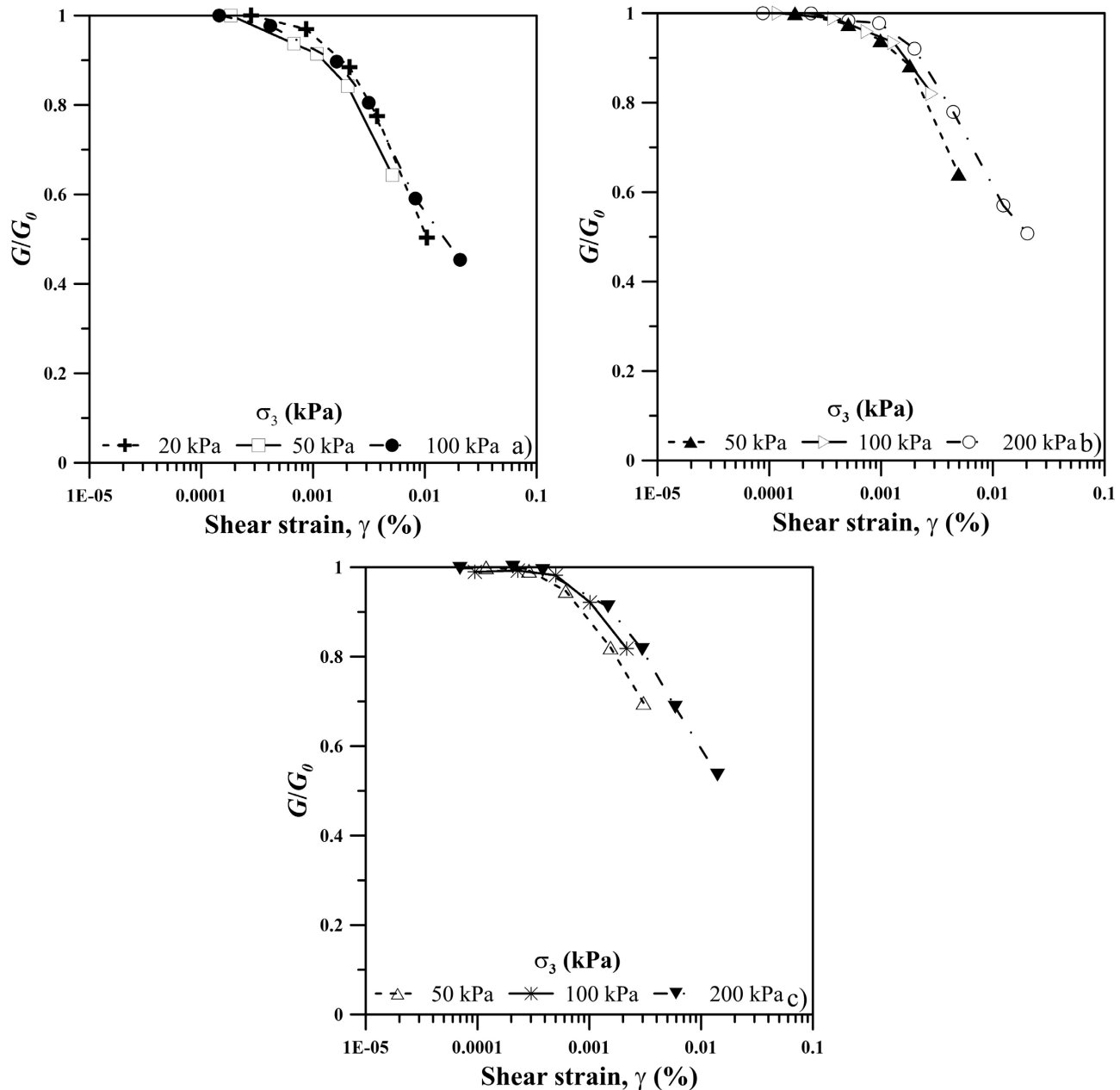


Figure 7. Modulus degradation curves (G/G_0 versus γ) for samples collected at 0.95 (a), 4.8 (b) and 8.85 (c) m depth [adapted from Giacheti (1991)].

minus one standard deviation (SD), RC and BE tests. The average SDMT values were higher than those determined by RC and BE. These values were 8% and 35% higher than those determined via BE, and 6% and 28% higher than those determined via RC. It is important to mention that the G_0 values determined by RC and BE are positioned at the lower limit or slightly outside the range. These differences may be related to possible disturbances during the sampling process and specimens preparation, errors in the estimation of the in situ confining stresses (Ferreira et al., 2011) as well as the influence of soil suction in G_0 (Nyunt et al., 2011).

4.2 Modulus degradation curve

4.2.1 SDMT and resonant column

Amoroso et al. (2014) suggest a method to estimate the modulus degradation curve (G/G_0 versus γ) by using SDMT, based on the parameters G_0 , G_{DMT} and γ_{DMT} , as previously discussed in item 3.1. This approach allows a preliminary definition of the modulus degradation curve, which needs to be interpreted in conjunction with reference G/G_0 versus γ determined in the laboratory via cyclic triaxial or resonant

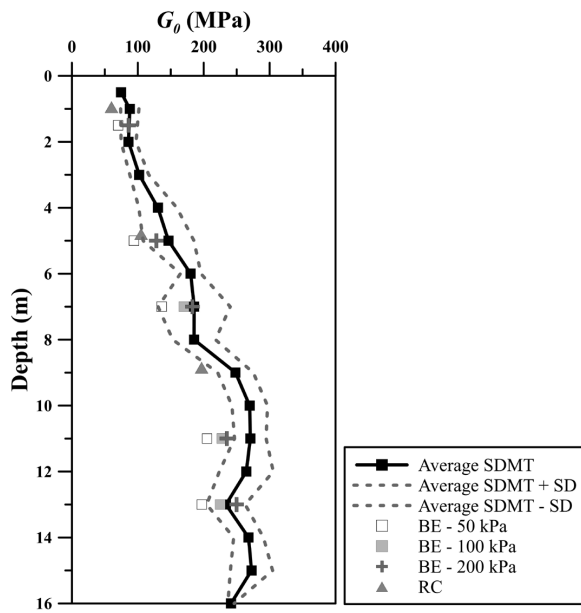


Figure 8. G_0 values determined by SDMT, bender elements, and resonant column for the study site.

column tests. So, the degradation curves presented in Figure 7 were considered representative and an average degradation curve was assumed. Table 3 presents the average values of G_0 , M_{DMT} , G_{DMT}/G_0 determined by means of the four SDMTs performed, as well as the shear strain imposed with the expansion of the DMT blade (γ_{DMT}) determined from the average degradation curve assumed by the resonant column tests.

Figure 9 shows the value of the G_{DMT}/G_0 ratio determined via SDMT, the shear strain fitted from the resonant column data (γ_{DMT} - gray symbol), and the average stiffness degradation curve obtained by Equation 3 (in gray dashed line). The G_{DMT}/G_0 value is equal to 0.051 for the studied site, which is slightly lower than the typical values reported in the literature (shaded areas), which can be associated to the natural cementation of the particles and the unsaturated condition, typical of tropical soil sites. At the working condition (G_{DMT}), the stiffness due to cementation and soil suction is lost. On the other hand, the value of the shear strain imposed by SDMT blade pushing into the soil (γ_{DMT}) for the studied soil is in the range of values commonly reported in the literature for sands and silty sands to sandy silts (0.1 to 0.5%) (Amoroso et al., 2014). It is important to mention that the multistage technique (Anderson & Stokoe, 1978) used to perform the resonant column tests can generate accumulated deformations and disturbances in the structure of the specimen, resulting in cementation bond breakage, realignment of grains, and changes in void ratios (Barros, 1997); therefore, the modulus degradation for the soil of the study site can be lower than those presented in Figures 7 and 9.

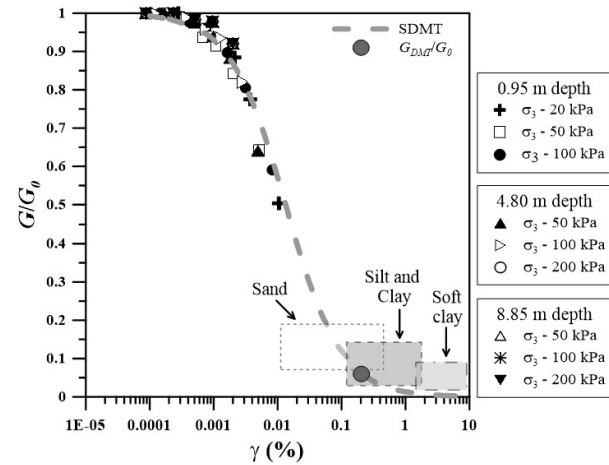


Figure 9. Modulus degradation curve via SDMT from Amoroso et al. (2014) method and the resonant column test data for the study site.

Table 3. Best-fit parameters for Amoroso et al. (2014) method for the study site.

G_0 (MPa)	M_{DMT} (MPa)	G_{DMT}/G_0	γ_{DMT} (%)
140.5	12.5	0.051	0.391

4.3 G/G_0 versus γ determined via unsaturated triaxial tests with internal instrumentation

The modulus degradation curves were also determined via unsaturated triaxial tests with internal instrumentation (LVDTs) for the sample collected at 2 m depth for soil suctions equal to 0, 50, 200, and 400 kPa (Figure 10). The objective is to evaluate the soil suction influence in the pattern and shape of the shear modulus degradation curve. Figure 10a shows that the shear modulus reduction curves are not monotonically related to the change in soil suction and reaches a maximum for a suction value equal to 200 kPa. The modulus degradation curve for the suction equal to 400 kPa is equivalent or slightly lower than those of suction equal to 50 kPa. It shows that the G/G_0 versus γ curves firstly rises and then falls in a certain range with the increase in soil suction. This trend is different from that found by Ng et al. (2021) for compacted unsaturated lateritic sandy clays and for eight different soil types as reported by Dong et al. (2018). However, Ng & Xu (2012) observed that the G/G_0 curves shift towards higher shear strain values with increasing soil suction for yellowish-brown completely decomposed tuff (CDT).

In order to describe the non-linear soil behavior, several researchers have proposed a mathematical model to capture the features of modulus reduction curve (Darendeli, 2001; Iwasaki et al., 1978; Kokusho, 1980;

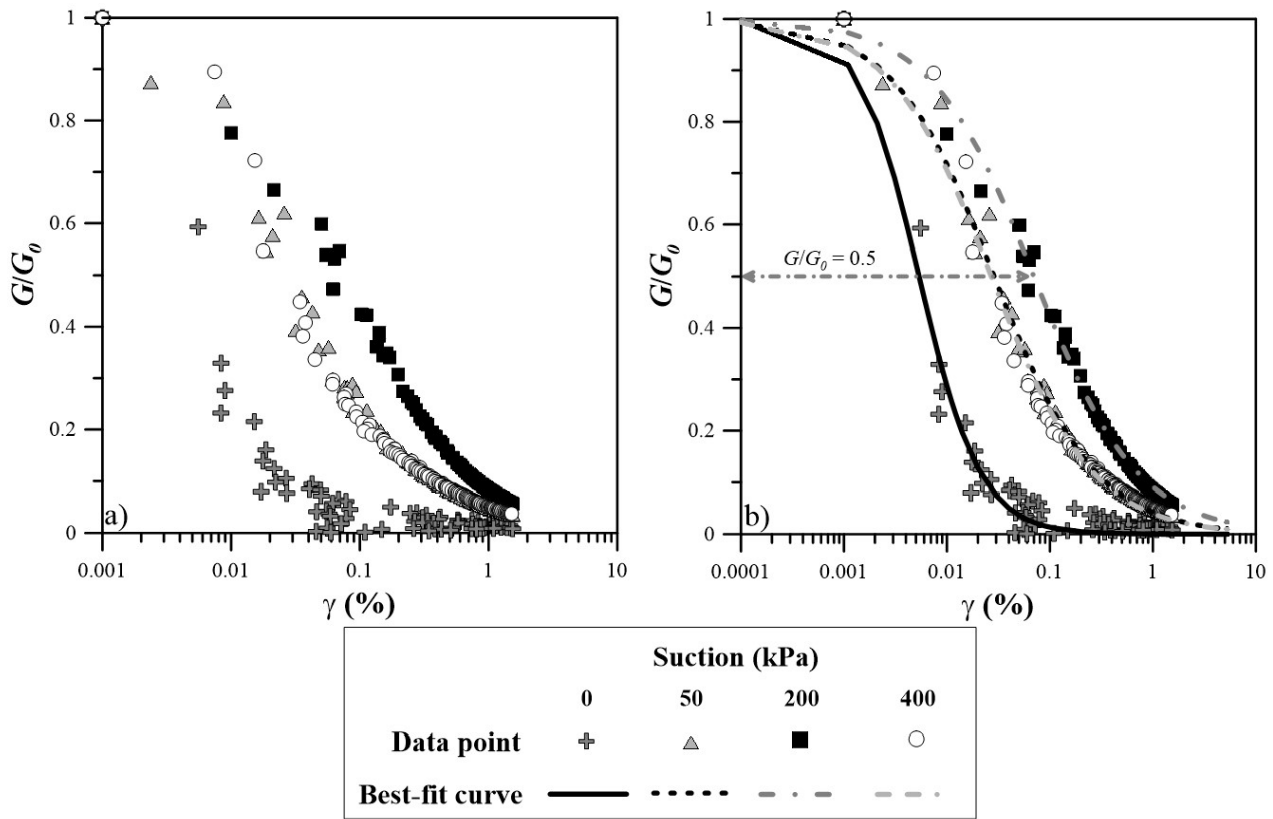


Figure 10. Modulus degradation curves: (a) determined from unsaturated triaxial tests with internal instrumentation; (b) fitted with Darendeli (2001) model.

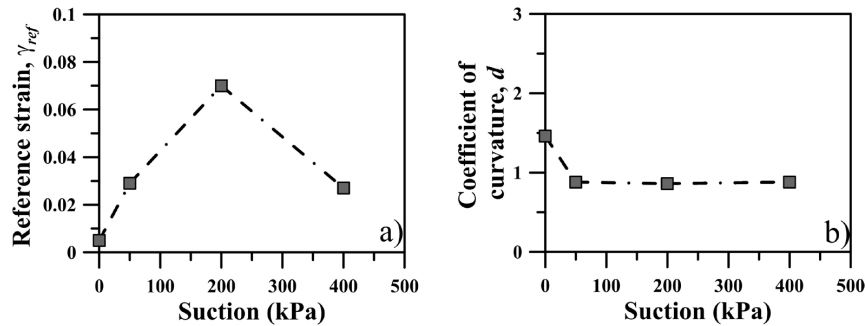


Figure 11. Soil suction influence on: (a) reference strain (γ_{ref}); (b) curvature coefficient a for the soil from the study site.

Seed et al., 1986; Vucetic & Dobry, 1991). According to Amoroso et al. (2014), the G/G_0 versus γ curves proposed by Darendeli (2001) include all other reference curves. Darendeli (2001) equation was used to represent the modulus reduction curves, as follows:

$$\frac{G}{G_0} = \frac{1}{1 + \left(\frac{\gamma}{\gamma_{ref}}\right)^d} \quad (8)$$

Where d is the constant that represents the curvature of the modulus reduction curve, and the γ_{ref} is the reference

strain controls the location where G decreases to half of its maximum value as the shear strain increases.

Figure 10b shows the modulus reduction curves for the tested samples. The dashed line at $G/G_0 = 0.5$ reflects the positions of the reference shear strain for each modulus reduction curve. Figure 10b also allows to examine the dependencies of the reference strain (γ_{ref}), and coefficient of curvature (d) on soil suction. The relationships between reference strain and suction are shown in Figure 11a, whereas the relationships between coefficient de curvature and suction are shown in Figure 11b for the soil from the study site. The reference strain increases with soil suction up to 200 kPa and decreases

for soil suction equal to 400 kPa. The coefficient of curvature presents a slight reduction between saturated and soil suction equal to 50 kPa and remains approximately constant as the soil suction increases from 50 kPa to 400 kPa, indicating no suction dependence on this parameter.

5. Conclusion

The main conclusions drawn from the study are as follows:

- The maximum shear modulus of the studied soil increases nonlinearly with suction and net confining stress based on the bender elements test data;
- The maximum shear modulus values from the SDMT were higher than those determined in the laboratory via resonant column and bender elements tests. This behavior can be related to possible soil disturbances during the sampling and preparation of the specimens, errors in estimating the in situ confining stresses, as well as the influence of soil suction on G_0 ;
- The average modulus degradation curve defined from resonant column was used to obtain the modulus degradation curve from SDMT. The approach proposed by Amoroso et al. (2014) for SDMT is interesting and can be used as a first tentative to represent the modulus degradation curve for the soil from the study site;
- The modulus degradation curves from the suction-controlled, internally instrumented triaxial tests are not monotonically related to the change in soil suction and it was maximum for a suction value equal to 200 kPa, and this behavior is different from which was observed by other researchers. Additional tests on samples collected at other depths as well as for other suction values should be done to explore and confirm the relation between soil suction and modulus degradation curves for the studied soil.

Acknowledgements

The authors thank the São Paulo Research Foundation - FAPESP (Grants 2015/17260-0 and 2017/23174-5), the National Council for Scientific and Technological Development - CNPq (Grant 436478/2018-8), and the Coordination for the Improvement of Higher Education Personnel – CAPES, for supporting their research. The last author also thanks the Institute for Technological Research of São Paulo State, particularly Dr. José Maria de Camargo Barros, where the resonant column tests were performed.

Declaration of interest

The authors have no conflicts of interest to declare. All co-authors have observed and affirmed the contents of the paper and there is no financial interest to report.

Authors' contributions

Jeferson Brito Fernandes: conceptualization, data curation, visualization. Breno Padovezi Rocha: conceptualization, data curation, formal analysis, investigation, methodology, writing – original draft, writing – review & editing. Heraldo Luiz Giacheti: conceptualization, methodology, supervision, funding acquisition, project administration, writing – review & editing.

Data availability

The datasets generated during and/or analyzed during the current study are available from the corresponding author on reasonable request.

List of symbols

a	fitting parameter
b	fitting parameter
c	fitting parameter
d	constant that represents the curvature of the modulus reduction curve
e	void ratio
p_0	corrected first reading
p_1	corrected second reading
q_c	cone resistance
s	soil suction value
w_L	liquid limit
BE	bender elements
CH	crosshole tests
CPT	cone penetration test
$CPTu$	piezocone penetration test
DH	downhole test
DMT	flat dilatometer
E	elasticity modulus
E_D	dilatometer modulus
E_{PMT}	Menard PMT modulus
G	shear modulus
G_{DMT}	working strain modulus
G_0	maximum shear modulus
$G_{0,sat}$	maximum shear modulus at the saturated condition
I_D	material index
I_P	plastic index
K_D	horizontal stress index
K_0	in situ coefficient of lateral earth pressure
M_{DMT}	constrained modulus obtained by DMT
N_{60}	SPT N values for an efficiency of 60%
PMT	Menard pressuremeter test
RC	resonant column
R_f	friction ratio
$SCPT$	seismic cone
SD	standard deviation

<i>SDMT</i>	seismic dilatometer
<i>SPT</i>	standard penetration test
<i>SPT-T</i>	standard penetration test with torque measurement
V_s	shear wave velocity
ϵ_a	axial strain
ϵ_r	radial strain
γ_d	dry unit weight
γ	shear strain
γ_{ref}	reference strain
γ_{DMT}	shear strain associated to the working strain modulus (G_{DMT})
ρ	soil bulk density
σ_3	confining stress
$\sigma - u_a$	net confining stress
μ	Poisson' ratio

References

- Amoroso, S. (2011). *G- γ decay curves by seismic dilatometer (SDMT)* [Doctoral thesis]. University of L'Aquila.
- Amoroso, S., Monaco, P., Marchetti, D., & Lehane, B.M. (2014). Examination of the potential of the seismic dilatometer (SDMT) to estimate in situ stiffness decay curves in various soil types. *Soils and Rocks*, 37(3), 177-194. <http://dx.doi.org/10.28927/SR.373177>.
- Anderson, D., & Stokoe, K. (1978). Shear modulus: a time-dependent soil property. In ASTM International (Ed.), *Dynamic geotechnical testing* (pp. 66-90). ASTM International. <https://doi.org/10.1520/STP35672S>.
- Atkinson, J.H. (2000). Non-linear soil stiffness in routine design. *Geotechnique*, 50(5), 487-508. <http://dx.doi.org/10.1680/geot.2000.50.5.487>.
- Bang, E.S., & Kim, D.S. (2007). Evaluation of shear wave velocity profile using SPT based uphole method. *Soil Dynamics and Earthquake Engineering*, 27(8), 741-758. <http://dx.doi.org/10.1016/j.soildyn.2006.12.004>.
- Barros, J.M.C. (1997). *Maximum shear modulus of tropical soils* [Doctoral thesis]. Universidade de São Paulo (in Portuguese).
- Burland, J.B., Longworth, T.I., & Moore, J.F.A. (1977). A study of ground movement and progressive failure caused by a deep excavation in Oxford Clay. *Geotechnique*, 27(4), 557-591. <http://dx.doi.org/10.1680/geot.1977.27.4.557>.
- Darendeli, M.B. (2001). *Development of a new family of normalized modulus reduction and material damping curves* [Doctoral thesis, University of Texas at Austin]. University of Texas at Austin's repository. Retrieved in February 20, 2023, from <http://hdl.handle.net/2152/10396>
- De Mio, G. (2005). *Geological conditioning aspects for piezocone test interpretation for stratigraphical identification in geotechnical and geo-environmental site investigation* [Doctoral thesis, University of São Paulo]. University of São Paulo's repository (in Portuguese). <https://doi.org/10.11606/T.18.2005.tde-27042006-170324>.
- Dong, Y., Lu, N., & McCartney, J.S. (2018). Scaling shear modulus from small to finite strain for unsaturated soils. *Journal of Geotechnical and Geoenvironmental Engineering*, 144(2), [http://dx.doi.org/10.1061/\(ASCE\)GT.1943-5606.0001819](http://dx.doi.org/10.1061/(ASCE)GT.1943-5606.0001819).
- Fernandes, J., Saab, A., Rocha, B., Rodrigues, R., Lodi, P., & Giacheti, H. (2022). Geomechanical parameters in the active zone of an unsaturated tropical soil site via laboratory tests. *Soils and Rocks*, 45(4), 1-15. <http://dx.doi.org/10.28927/SR.2022.000422>.
- Fernandes, J.B. (2022). *Strength and deformability study of an unsaturated tropical soil profile* [Master's dissertation, São Paulo State University]. São Paulo State University's repository (in Portuguese). Retrieved in February 20, 2023, from <http://hdl.handle.net/11449/217501>
- Ferreira, C., Fonseca, A.V., & Nash, D.F.T. (2011). Shear wave velocities for sample quality assessment on a residual soil. *Soil and Foundation*, 51(4), 683-692. <http://dx.doi.org/10.3208/sandf.51.683>.
- Ferreira, C.M.F. (2002). *Implementação e aplicação de transdutores piezoelétricos na determinação de velocidades de ondas sísmicas em provetes: avaliação da qualidade de amostragem em solos residuais* [Master's dissertation, University of Porto]. University of Porto's repository. Retrieved in February 20, 2023, from <https://hdl.handle.net/10216/13001>
- Giacheti, H.L. (1991). *Experimental study of dynamic parameters of some tropical soils in the state of São Paulo* [Doctoral thesis, University of São Paulo]. University of São Paulo's repository. <https://doi.org/10.11606/T.18.1991.tde-22092022-105014>.
- Giacheti, H.L., Bezerra, R.C., Rocha, B.P., & Rodrigues, R.A. (2019). Seasonal influence on cone penetration test: an unsaturated soil site example. *Journal of Rock Mechanics and Geotechnical Engineering*, 11(2), 361-368. <http://dx.doi.org/10.1016/j.jrmge.2018.10.005>.
- International Code Council – ICC. (1997). *Uniform building code (international building code)*. ICC.
- Ishihara, K. (May 21-24, 2001). Estimate of relative density from in-situ penetration tests. In P.P. Rahardjo & T. Lunne (Eds.), *Proceedings of the International Conference on In Situ Measurement of Soil Properties and Case Histories* (pp. 17-26). Bandung, Indonesia: Parahyangan Catholic University.
- Iwasaki, T., Tatsuoka, F., & Takagi, Y. (1978). Shear moduli of sands under cyclic torsional shear loading. *Soil and Foundation*, 18(1), 39-56. <http://dx.doi.org/10.3208/sandf1972.18.39>.
- Jaky, J. (June 21-30, 1948). Earth pressure in soils. In International Conference on Soil Mechanics and Foundation Engineering (Org.), *Proceedings of the Second International Conference on Soil Mechanics and Foundation Engineering* (pp. 103-107). Rotterdam, Netherlands: ICSMFE.
- Kim, D.S., & Park, H.C. (1999). Evaluation of ground densification using spectral analysis of surface waves

- (SASW) and resonant column (RC) tests. *Canadian Geotechnical Journal*, 36(2), 291-299. <http://dx.doi.org/10.1139/t98-103>.
- Kokusho, T. (1980). Cyclic triaxial test of dynamic soil properties for wide strain range. *Soil and Foundation*, 20(2), 45-60. http://dx.doi.org/10.3208/sandf1972.20.2_45.
- Marchetti, S. (1980). In situ tests by flat dilatometer. *Journal of the Geotechnical Engineering Division*, 106(GT3), 299-321.
- Marchetti, S., Monaco, P., Totani, G., & Calabrese, M. (April 2-5, 2006). The flat dilatometer test (DMT) in soil investigations - a report by the ISSMGE Committee TC16. In R.A. Failmezger & J.B. Anderson (Eds.), *Proceedings from the Second International Conference on the Flat Dilatometer* (pp. 7-48). Lancaster, USA: In-Situ Soil Testing.
- Marchetti, S., Monaco, P., Totani, G., & Marchetti, D. (March 9-23, 2008). In situ tests by seismic dilatometer (SDMT). In American Society of Civil Engineers (Org.), *Symposium Honoring Dr. John H. Schmertmann for His Contributions to Civil Engineering at Research to Practice in Geotechnical Engineering Congress 2008* (pp. 292-311). Reston, USA: ASTM. [https://doi.org/10.1061/40962\(325\)7](https://doi.org/10.1061/40962(325)7).
- Ng, C.W.W., & Xu, J. (2012). Effects of current suction ratio and recent suction history on small-strain behaviour of an unsaturated soil. *Canadian Geotechnical Journal*, 49(2), 226-243. <http://dx.doi.org/10.1139/t11-097>.
- Ng, C.W.W., Bentil, O.T., & Zhou, C. (2021). Small strain shear modulus and damping ratio of two unsaturated lateritic sandy clays. *Canadian Geotechnical Journal*, 58(9), 1426-1435. <http://dx.doi.org/10.1139/cgj-2019-0460>.
- Nogami, J.S., & Villibor, D.F. (September 21-23, 1981). A new soil classification for highway purposes. In Universidade Federal do Rio de Janeiro, Conselho Nacional de Pesquisas & Associação Brasileira de Mecânica dos Solos (Orgs.), *Simpósio Brasileiro de Solos Tropicais em Engenharia* (pp. 30-41). Rio de Janeiro: COPPE/UFRJ (in Portuguese).
- Nyunt, T.T., Leong, E.C., & Rahardjo, H. (2011). Strength and small-strain stiffness characteristics of unsaturated sand. *Geotechnical Testing Journal*, 34(5), 103589. <http://dx.doi.org/10.1520/GTJ103589>.
- Robertson, P.K. (2016). Cone penetration test (CPT)-based soil behaviour type (SBT) classification system: an update. *Canadian Geotechnical Journal*, 53(12), 1910-1927. <http://dx.doi.org/10.1139/cgj-2016-0044>.
- Rocha, B.P., & Giacheti, H.L. (2018). Site characterization of a tropical soil by in situ tests. *Dyna*, 85(206), 211-219. <http://dx.doi.org/10.15446/dyna.v85n206.67891>.
- Rocha, B.P., Rodrigues, A.L.C., Rodrigues, R.A., & Giacheti, H.L. (2022). Using a seismic dilatometer to identify collapsible soils. *International Journal of Civil Engineering*, 20(7), 857-867. <http://dx.doi.org/10.1007/s40999-021-00687-9>.
- Rocha, B.P., Rodrigues, R.A., & Giacheti, H.L. (2021). The flat dilatometer test in an unsaturated tropical soil site. *Geotechnical and Geological Engineering*, 39(8), 5957-5969. <http://dx.doi.org/10.1007/s10706-021-01849-1>.
- Seed, H.B., Wong, R.T., Idriss, I.M., & Tokimatsu, K. (1986). Moduli and damping factors for dynamic analyses of cohesionless soils. *Journal of Geotechnical Engineering*, 112(11), 1016-1032. [http://dx.doi.org/10.1061/\(ASCE\)0733-9410\(1986\)112:11\(1016\)](http://dx.doi.org/10.1061/(ASCE)0733-9410(1986)112:11(1016)).
- Vaughan, P.R., Maccarini, M., & Mokhtar, S.M. (1988). Indexing the engineering properties of residual soil. *Quarterly Journal of Engineering Geology*, 21(1), 69-84. <http://dx.doi.org/10.1144/GSL.QJEG.1988.021.01.05>.
- Vucetic, M., & Dobry, R. (1991). Effect of soil plasticity on cyclic response. *Journal of Geotechnical Engineering*, 117(1), 89-107. [http://dx.doi.org/10.1061/\(ASCE\)0733-9410\(1991\)117:1\(89\)](http://dx.doi.org/10.1061/(ASCE)0733-9410(1991)117:1(89)).

Comparative study of deterministic and probabilistic critical slip surfaces applied to slope stability using limit equilibrium methods and the First-Order Reliability Method

Higor Biondo de Assis^{1#} , Caio Gorla Nogueira¹ 

Article

Keywords

Slope stability
Limit equilibrium methods
Factor of safety
Direct coupling
Reliability
Quantitative risk assessment

Abstract

This work presents the validation of the Morgenstern-Price method implemented in the Risk Assessment applied to Slope Stability (RASS) computational program to carry out deterministic and probabilistic analyses of slope stability. Deterministic analyses, based on the factor of safety approach, are performed using limit equilibrium methods. The probabilistic ones, on the other hand, are carried out through the direct coupling of these methods to the First Order Reliability Method (FORM). Initially, two benchmark cases are presented for validation of the computational routine related to the Morgenstern-Price method. Next, two illustrative examples are presented, with the investigation of the critical surfaces defined by deterministic and probabilistic criteria, which correspond to the minimum factor of safety, the maximum probability of failure, and the maximum quantitative risk. In the set of stability analyses, it was verified that both the numerical responses and the geometry of the critical surfaces can vary depending on the choice of the limit equilibrium method and the criterion for identifying the critical surface. The different possibilities presented by the methodology used in this study define not only a critical surface, but a set of critical surfaces that can help in the engineering decision-making process and slope risk management, complementing the widely used purely deterministic analyses in geotechnics.

1. Introduction

The problem of slope stability is quite recurrent in everyday life, whether on natural or built slopes. Every year several cases of failure are reported in the most diverse places around the world, especially in inhabited places, on highways, railways or even in the mining industry. The causes can be diverse, either by anthropic actions, extreme natural phenomena or a combination of both. For this reason, geotechnical engineering is also dedicated to the study of this type of engineering problem, in which the consequences usually cause economic and environmental damage and loss of human lives, for instance.

In traditional deterministic analyses of slope stability, the uncertainties related to the problem are commonly neglected. The better understanding of these uncertainties, intrinsic or epistemic, has become an object of great interest in geotechnical research in the last two decades (Jiang et al., 2022).

The intrinsic uncertainties are mainly related to the spatial variability of the materials that constitute the analyzed

engineering systems. In slope stability problems, the natural variability of soil strength and other properties is a source of intrinsic uncertainty. On the other hand, the epistemic uncertainties, those that theoretically can be reduced by the adoption of good practices, are originated by diverse sources, such as simplified mathematical mechanical models, ground investigation methods, as well as the difficulty to reproduce in laboratory what happens in nature (Melchers & Beck, 2018). All these practices allow simplifications in order to make it possible for Geotechnical Engineering to perform consistent analyses, although they are not exact (Husein Malkawi et al., 2000).

An important source of epistemic uncertainty in slope stability analysis is the variability of the answers provided by the limit equilibrium methods widely used in most of the software dedicated to this discipline. In this context, the aim of this paper is to show how deterministic and probabilistic responses behave as a function of the choice of different limit equilibrium methods. The deterministic analyses are performed from the factor of safety (*FS*) concept, and the probabilistic analyses, from the direct coupling of these limit equilibrium

[#]Corresponding author. E-mail address: higor.assis@unesp.br

¹Universidade Estadual Paulista, Departamento de Engenharia Civil e Ambiental, Bauru, SP, Brasil.

Submitted on December 3, 2022; Final Acceptance on April 1, 2023; Discussion open until August 31, 2023.

<https://doi.org/10.28927/SR.2023.013522>



This is an Open Access article distributed under the terms of the Creative Commons Attribution License, which permits unrestricted use, distribution, and reproduction in any medium, provided the original work is properly cited.

methods to the First-Order Reliability Method (Ang & Tang, 1984). The variability of FS considering several limit equilibrium methods is discussed when the analyses are performed by deterministic and especially probabilistic approaches.

2. Methodology

Probabilistic analyses of slope stability can be performed using different methodologies such as direct coupling of limit equilibrium methods to reliability methods and simulation techniques (Leonel et al., 2011; Siacara et al., 2020). In this approach, the transformation methods are used to provide the probabilistic response for each of the listed failure modes. Each failure mode is represented by a limit state function, which is a response given by a representative mechanical model (Phoon, 2008). In the slope stability problem, the FS is the response provided by the limit equilibrium methods, which feeds the probabilistic model and represents the failure mode, which is the rupture of the slope by shear. To carry out the analyses presented in this paper, it was used the program Risk Assessment applied to Slope Stability (RASS), developed by the authors for deterministic and probabilistic analyses of slope stability. The Morgenstern-Price method implemented in RASS follows the formulation presented in detail by Zhu et al. (2005). RASS also has the Ordinary, Simplified Bishop (Bishop) (Bishop, 1955), Simplified Janbu (Janbu) and Corrected Simplified Janbu (Janbu (f_0)) methods (Janbu, 1954a, b, 1973). The Spencer method (Spencer, 1967, 1973) is a particular case of the Morgenstern-Price method (Morgenstern & Price, 1965), contemplated by the formulation presented in this paper. The detailed formulation of the mentioned limit equilibrium methods are presented by Fredlund & Krahn (1977), Abramson et al. (2001).

2.1 Morgenstern-Price method

Several limit equilibrium methods, based on the slice method, have been developed throughout the 20th century for slope stability analyses. These methods are based on statics equations and require some assumptions to make the problem statically determined. In general, these assumptions are related to the interslice normal forces and interslice tangential forces. The Morgenstern-Price method is considered a rigorous method because it completely satisfies the equilibrium of forces in two directions and moments (Morgenstern & Price, 1965). To make this possible, the method adopts an interslice force function, which relates the tangential forces to the normal forces acting on the sides of the slices positioned on the abscissa x , establishing a relationship that can be constant or variable along the horizontal extension of the slope slip surface, according to Equation 1:

$$S = \lambda \cdot f(x) \cdot E \quad (1)$$

where S is the tangential interslice force, E is the normal interslice force, λ is an unknown scaling factor e $f(x)$ is the

interslice force function. As presented by Zhu et al. (2005), $f(x)$ can be written as given by Equation 2:

$$f(x) = sen^{\mu} \left[\pi \left(\frac{x - x_L}{x_R - x_L} \right)^{\nu} \right] \quad (2)$$

where x_L and x_R are abscissa of the left and right ends of the failure surface, respectively, so that $x \in [x_L, x_R]$. Therefore, the FS can be written as presented by Equation 3:

$$FS = \frac{\sum_{i=1}^{n-1} \left(R_i \prod_{j=i}^{n-1} \psi_j \right) + R_n}{\sum_{i=1}^{n-1} \left(T_i \prod_{j=i}^{n-1} \psi_j \right) + T_n} \quad (3)$$

in which, R_i is the sum of the shear resistances contributed by all forces acting on the i th slice except the normal shear forces, and T_i is the sum of the components of these forces tending to cause instability, as given by Equations 4 and 5:

$$R_i = \left[W_i \cos \alpha_i + Q_i \cos(\omega_i - \alpha_i) - U_i \right] \cdot \tan \varphi_i' + c_i' b_i \sec \alpha_i \quad (4)$$

$$T_i = W_i sen \alpha_i - Q_i sen(\omega_i - \alpha_i) \quad (5)$$

where W_i is the self-weight of i th slice, α_i is the slope of the base of the slice relative to the horizontal, Q_i is the external force acting on the i th slice, ω_i is the angle between the vertical and the direction of the external force Q_i , U_i is the resultant water force acting on the base of the i th slice, φ_i' is the soil friction angle along the base of the i th slice, c_i' is the soil cohesion along the base of the i th slice. From imposing the force equilibrium of i th slice and resolving in the perpendicular direction and in the direction parallel to the slip surface, and substituting the former into the latter, Equation 6 is given in the form:

$$E_i \left[(\sin \alpha_i - \lambda f_i \cos \alpha_i) \tan \varphi_i' + (\cos \alpha_i + \lambda f_i \sin \alpha_i) FS \right] = E_{i-1} \left[(\sin \alpha_i - \lambda f_{i-1} \cos \alpha_i) \tan \varphi_i' + (\cos \alpha_i + \lambda f_{i-1} \sin \alpha_i) FS \right] + FST_i - R_i \quad (6)$$

where E_i and E_{i-1} corresponds to the normal interslice forces acting on the left and right side of i th slice, respectively, and f_i and f_{i-1} are the values of $f(x)$ assumed on the left and right side of the i th slice, respectively.

Equations 7, 8 and 9 refer to a rearrangement of the equations using the variables ψ_{i-1} , ϕ_{i-1} , ϕ_i for changing variables:

$$\psi_{i-1} = \left[\frac{(\sin \alpha_i - \lambda f_{i-1} \cos \alpha_i) \tan \varphi_i' + (\cos \alpha_i + \lambda f_{i-1} \sin \alpha_i) FS}{(\cos \alpha_i + \lambda f_{i-1} \sin \alpha_i) FS} \right] / \phi_{i-1} \quad (7)$$

$$\phi_{i-1} = (\text{sen}\alpha_{i-1} - \lambda f_{i-1} \cos\alpha_{i-1}) \tan \varphi_{i-1} + (\cos\alpha_{i-1} + \lambda f_{i-1} \text{sen}\alpha_{i-1}) FS \quad (8)$$

$$\phi_i = (\text{sen}\alpha_i - \lambda f_i \cos\alpha_i) \tan \varphi_i + (\cos\alpha_i + \lambda f_i \text{sen}\alpha_i) FS \quad (9)$$

According to the Morgenstern-Price method, the value of FS is defined at the intersection between the curves of the factor of safety of forces (FS_f) and the factor of safety of moments (FS_m) as a function of λ . The calculation of λ is given according to the Equation 10:

$$\lambda = \frac{\sum_{i=1}^n [b_i (E_i + E_{i-1}) \tan \alpha_i + 2Q_i \text{sen}\omega_i h_i]}{\sum_{i=1}^n [b_i (f_i E_i + f_{i-1} E_{i-1})]} \quad (10)$$

2.2 First-Order Reliability Method

The First-Order Reliability Method (FORM) has been widely used in structural reliability (Ang & Tang, 1984). Recently, FORM has been also considered as an important alternative to Monte Carlo Simulation method (MCS) (Cho, 2007, 2010) in probabilistic slope stability analysis, since it provides significantly lower computational cost (Ji et al., 2018; Siacara et al., 2022). The method involves defining a representative failure mode function, which is linearised from the Taylor series expansion by a tangent hyperplane around the most probable failure point, named the design point (\mathbf{y}^*). This function is called the limit state function ($g(\mathbf{X})$), in which \mathbf{X} is a vector of random variables associated with the problem ($\mathbf{X} = [X_1, X_2, \dots, X_n]^T$). In summary, it consists in solving an optimization problem, which seeks to find \mathbf{y}^* , in order to minimize the reliability index (β), subject to $g(\mathbf{X}) = 0$. The solution of the problem is performed using the Hasofer-Lind-Rackwitz-Fiessler (HLRF) algorithm (Hasofer & Lind, 1974; Rackwitz & Fiessler, 1978), and requires the transformation of the random variables from the physical space (\mathbb{X}) to the standard uncorrelated normal space (\mathbb{Y}) (Lebrun & Dutfoy, 2009), where β is defined, according to Equation 11:

$$\beta = \sqrt{(\mathbf{y}^*)^T (\mathbf{y}^*)} \quad (11)$$

Thus, the probability of failure, given by $Pf = P[g(\mathbf{X}) \leq 0]$ can be estimated as Equation 12:

$$Pf \approx \Phi(-\beta) \quad (12)$$

in which $\Phi(\cdot)$ is the standard normal cumulative distribution function (Ang & Tang, 1984).

2.3 Slope stability limit state function

Slope stability analyses consist of assessing the shear strength of the soil mass on a given slip surface. According

to the limit equilibrium theory, the slope instability is verified when $FS \leq 1$. In agreement with this condition, the limit state function is given by Equation 13:

$$g(\mathbf{X}) = FS(\mathbf{X}) - 1.00 \quad (13)$$

Thus, the solution of the slope stability problem, according to the reliability approach, provides a probabilistic response that represents the probability of the FS of the slope assuming a value less than or equal to 1.00 (Fenton & Griffiths, 2008).

2.4 Quantitative risk assessment

One of the widely accepted definitions of risk is that it can be quantified from the product of the probability of failure and the consequence associated with that failure (Melchers & Beck, 2018). In the probabilistic stability analyses of two-dimensional slopes, the values of Pf are obtained for the evaluated multiple surfaces of rupture. Each of these surfaces has a mobilized soil area corresponding to the sum of the areas of the lamellae. This area is also called the active zone and is delimited by the slope surface and the slip surface. Considering a slope strip of unit width, the consequence of shear failure can be represented in a simplified way by the constant C (Jiang et al., 2022; Zhang & Huang, 2016), which represents the mobilized volume of soil ($[C] = L^3 L^{-1}$). Thus, for the slope stability problem, the quantitative risk (Rv) can be written according to Equation 14:

$$Rv = P_f \cdot C \quad (14)$$

2.5 Criteria for identifying critical slip surfaces

According to the deterministic approach to slope stability, the critical slip surface is defined by investigation and identified from the lowest calculated FS value, among a predefined set of trial slip surfaces. In this way, the minimum FS value (FS_{min}) is the criterion that defines the critical deterministic slip surface. Conversely, the critical probabilistic slip surfaces can be defined by different criteria, such as maximum Pf value (Pf_{max}) and maximum Rv (Rv_{max}) value, according to the methodology presented for carrying out the probabilistic analyses via direct coupling of the limit equilibrium methods to the FORM.

2.6 Benchmarks

Two cases are presented to validate the RASS code implemented to evaluate the FS using the Morgenstern-Price method. In both cases the slopes consist of homogeneous soil and the same slip surface is evaluated. The difference is that in case 2 there is the inclusion of the piezometric line, while in case 1 there is not, as presented in Figure 1:

The Morgenstern-Price formulation implemented in RASS followed the algorithm presented by Zhu et al. (2005)

and for this reason these cases were chosen for validation of the computational code written by the authors. The geotechnical parameters used in the analyses are the same as in the original example. For deterministic analyses, only the mean values (μ_x) of the random variables are used. Table 1 brings a description of the variability of these parameters, with their respective coefficients of variation (COV_x) and probability density function (PDF_x) that best describes the random variable X :

The values of COV_x and PDF_x will be used only in the probabilistic analyses, at the appropriate moment of this work. It is important to note that Spencer's method is a particular

case of the Morgenstern-Price method, where $f(x)$ takes constant value over the entire domain of x . According to this particularity, Table 2 presents the FS and λ values calculated with the RASS program using the Spencer's method, in which interslice force function is constant ($\mu = \nu = 0 \Rightarrow f(x) = 1$):

Table 3 presents the FS and λ results for the Morgenstern-Price method with variable $f(x)$, called half-sine function, in which $\mu = \nu = 1$:

As shown, RASS provided results very similar to those reported by the reference papers, with maximum relative errors of 0.109% and 0.309% for FS and λ , respectively. These results then allow the validation of the Morgenstern-Price method calculation routine included in RASS, to be used in direct coupling.

Table 1. Variability of geotechnical parameters according to Phoon & Kulhawiy (1999).

X	c' (kPa)	ϕ' (°)
μ_x	28.74	20.00
COV_x	30%	10%
PDF_x	Lognormal	Lognormal

The soil unit weight (γ) was considered as a deterministic variable: $\gamma = 18.85$ kN/m³.

2.7 Critical slip surfaces

As an extension of the benchmarks presented, in this section a set of deterministic and probabilistic analyses is presented, with investigation of the critical surfaces of the slopes relative to cases 1 and 2. About 10,000 experimental

Table 2. Comparison of FS and λ values computed by RASS using Spencer's method.

Case	FS			λ			Error* (%)	
	Fredlund & Krahn (1977)	Zhu et al. (2005)	RASS	Fredlund & Krahn (1977)	Zhu et al. (2005)	RASS	FS	λ
1	2.076	2.075	2.074	0.254	0.258	0.258	0.048	0.000
2	1.833	1.831	1.833	0.234	0.240	0.240	0.109	0.000

* Relative error between values reported by Zhu et al. (2005) and RASS.

Table 3. Comparison of FS and λ values computed by RASS using Morgenstern-Price method.

Case	FS			λ			Error* (%)	
	Fredlund & Krahn (1977)	Zhu et al. (2005)	RASS	Fredlund & Krahn (1977)	Zhu et al. (2005)	RASS	FS	λ
1	2.076	2.074	2.073	0.318	0.324	0.323	0.096	0.309
2	1.832	1.831	1.832	0.290	0.299	0.299	0.055	0.000

* Relative error between values reported by Zhu et al. (2005) and RASS.

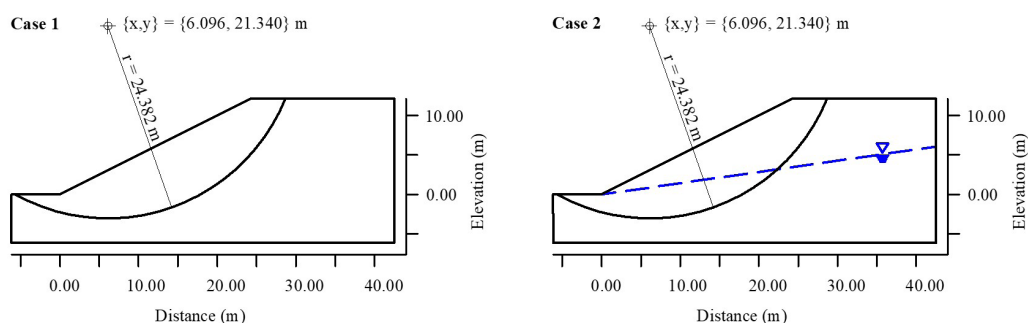


Figure 1. Benchmark cases (Zhu et al., 2005).

sliding surfaces were analysed, using different limit equilibrium methods. The surfaces analysed are circular and defined by the coordinates of centre (x_c, y_c) and radius (r). The critical surfaces were identified according to the deterministic and probabilistic criteria of FS_{min} , Pf_{max} and Rv_{max} . The results are presented in Table 4:

Figure 2 illustrates the deterministic and probabilistic critical surfaces, defined by the different identification criteria and limit equilibrium methods used in the analyses:

The knowledge of the geometry of the critical surface of a slope is important because it is the boundary between the passive and active zones, which corresponds to the volume of soil to be mobilized in an eventual slope rupture. Knowing

the boundary that delimits these zones is essential for project development or even the verification of existing reinforced slopes, for example. In a nail-reinforced slope, the length of the anchors that enter the passive zone is determinant in the safety condition of the system. Therefore, if there are uncertainties in the methods employed in the analyses, due to the simplifying hypotheses that they adopt, it is expected that different critical surfaces are identified, as well as different safety levels are observed through the values of FS_{min} , Pf_{max} and Rv_{max} . Another behaviour observed is the position of the Rv_{max} surfaces, which in most cases were positioned between the deeper FS_{min} and shallower Pf_{max} surfaces. This was the main reason for the adoption of the

Table 4. Results of the deterministic and probabilistic critical slip surfaces for cases 1 and 2.

Case	Limit equilibrium method	Criterion	x_c (m)	y_c (m)	R (m)	FS	β	Pf	Rv (m ³ /m)
1	Bishop	FS_{min}	7.0000	25.0000	25.9608	1.9959	5.2161	9.15E-08	1.39E-05
		Pf_{max}	5.0000	25.7500	26.2336	2.0377	4.9977	2.91E-07	3.35E-05
		Rv_{max}	5.0000	25.7500	26.2336	2.0377	4.9977	2.91E-07	3.35E-05
	Janbu	FS_{min}	8.2500	19.5000	21.6113	1.8333	4.5201	3.09E-06	5.48E-04
		Pf_{max}	6.2500	21.5000	22.7350	1.8725	4.3614	6.47E-06	8.67E-04
		Rv_{max}	6.7500	21.0000	22.4334	1.8544	4.3714	6.18E-06	8.90E-04
	Janbu (f_0)	FS_{min}	8.0000	21.0000	22.7779	1.9860	5.2119	9.36E-08	1.60E-05
		Pf_{max}	5.5000	24.5000	25.2043	2.0374	4.9897	3.03E-07	3.72E-05
		Rv_{max}	5.7500	24.0000	24.8103	2.0284	4.9956	2.94E-07	3.72E-05
	Spencer	FS_{min}	7.0000	25.0000	25.9608	1.9926	5.1999	9.99E-08	1.52E-05
		Pf_{max}	4.7500	26.0000	26.4172	2.0460	4.9748	3.27E-07	3.64E-05
		Rv_{max}	5.0000	25.7500	26.2336	2.0341	4.9804	3.18E-07	3.66E-05
	Morgenstern-Price	FS_{min}	7.0000	25.0000	25.9608	1.9925	5.1988	1.00E-07	1.53E-05
		Pf_{max}	4.7500	26.0000	26.4172	2.0455	4.9738	3.29E-07	3.66E-05
		Rv_{max}	5.0000	25.7500	26.2336	2.0336	4.9768	3.24E-07	3.73E-05
2	Bishop	FS_{min}	7.7500	21.7500	24.8095	1.8132	4.3463	6.93E-06	1.54E-03
		Pf_{max}	6.5000	21.0000	23.6666	1.8349	4.2591	1.03E-05	1.92E-03
		Rv_{max}	6.7500	20.7500	23.5563	1.8273	4.2635	1.01E-05	1.95E-03
	Janbu	FS_{min}	7.2500	20.7500	23.7641	1.6624	3.4405	2.90E-04	6.04E-02
		Pf_{max}	7.0000	20.7500	23.6595	1.6680	3.4367	2.95E-04	5.91E-02
		Rv_{max}	7.2500	20.7500	23.7641	1.6624	3.4405	2.90E-04	6.04E-02
	Janbu (f_0)	FS_{min}	7.5000	21.2500	24.2867	1.8049	4.1725	1.51E-05	3.25E-03
		Pf_{max}	6.7500	20.7500	23.5563	1.8191	4.1244	1.86E-05	3.60E-03
		Rv_{max}	7.0000	20.7500	23.6595	1.8119	4.1279	1.83E-05	3.68E-03
	Spencer	FS_{min}	7.7500	21.7500	24.8095	1.8116	4.3461	6.93E-06	1.54E-03
		Pf_{max}	6.2500	21.2500	23.7809	1.8415	4.2554	1.04E-05	1.88E-03
		Rv_{max}	6.7500	20.7500	23.5563	1.8253	4.2610	1.02E-05	1.97E-03
	Morgenstern-Price	FS_{min}	7.7500	21.7500	24.8095	1.8109	4.3447	6.98E-06	1.55E-03
		Pf_{max}	6.2500	21.2500	23.7809	1.8408	4.2542	1.05E-05	1.89E-03
		Rv_{max}	6.7500	20.7500	23.5563	1.8245	4.2597	1.02E-05	1.98E-03

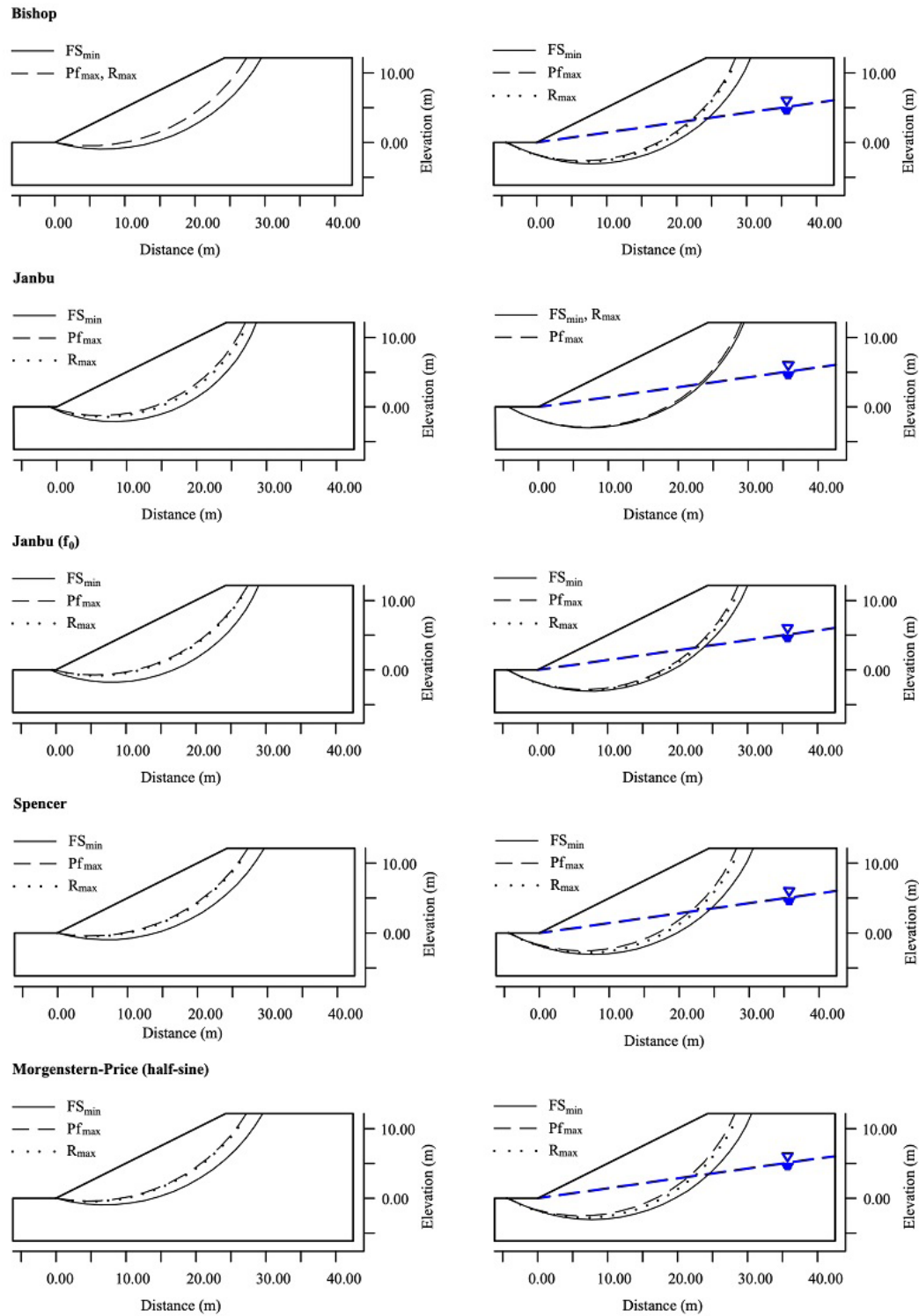


Figure 2. Deterministic and probabilistic critical slip surfaces.

$R_{v_{max}}$ identification criterion, because a Pf_{max} surface can be shallow enough to mobilize a volume corresponding to a relatively low failure consequence. On the other hand, there

may be another surface with Pf slightly smaller than Pf_{max} , but which mobilizes a volume of soil capable of causing more severe consequences if it ruptures.

2.8 Cumulative distribution function

In an attempt to explain the variability of the probabilistic analysis responses regarding the found critical surfaces, the constant a was used to modify the limit state function. This modification enables the construction of a cumulative density

function $F_X(X)$ of $FS(X)$, such that $F_X(X) = P[FS(X) \leq a]$ with $a \in [0.5, 3.5]$, as shown in Figure 3:

Differences are observed in the probability curves due to the choice of the limit equilibrium methods, the different critical surfaces identified and the existence of acting or non-acting pore water pressure. In the presented analyses, the probability

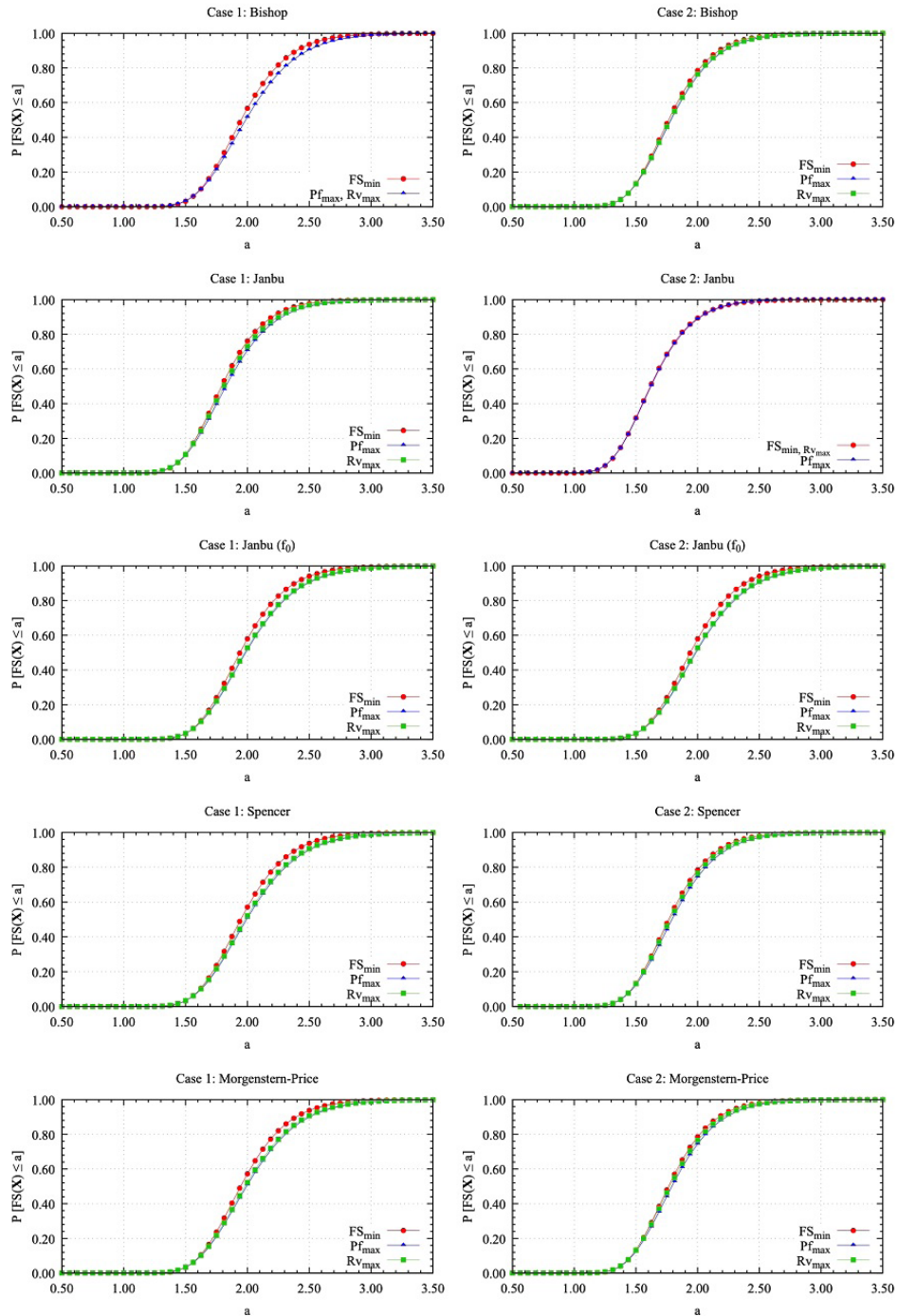


Figure 3. Cumulative density functions of critical slip surfaces.

curves of the FS_{min} surfaces were more distant from the curves of Pf_{max} and Rv_{min} . However, the curves of Pf_{max} and Rv_{max} were much closer to each other, when compared to those of FS_{min} .

2.9 Probability density function

The curve representing the probability density function $f_X(X)$ of $FS(X)$ can be constructed from the numerical derivation

of $F_X(X)$, so that $F_X'(X) = f_X(X)$. Figure 4 presents the curve $f_X(X)$ for the cases analysed:

The probability curves $f_X(X)$ facilitate the visualization of the variability of $FS(X)$, because the differences become more apparent regarding to those of $F_X(X)$ curves. No change in behaviour occurs in relation to the curves $F_X(X)$, because they are just different ways to show the same results.

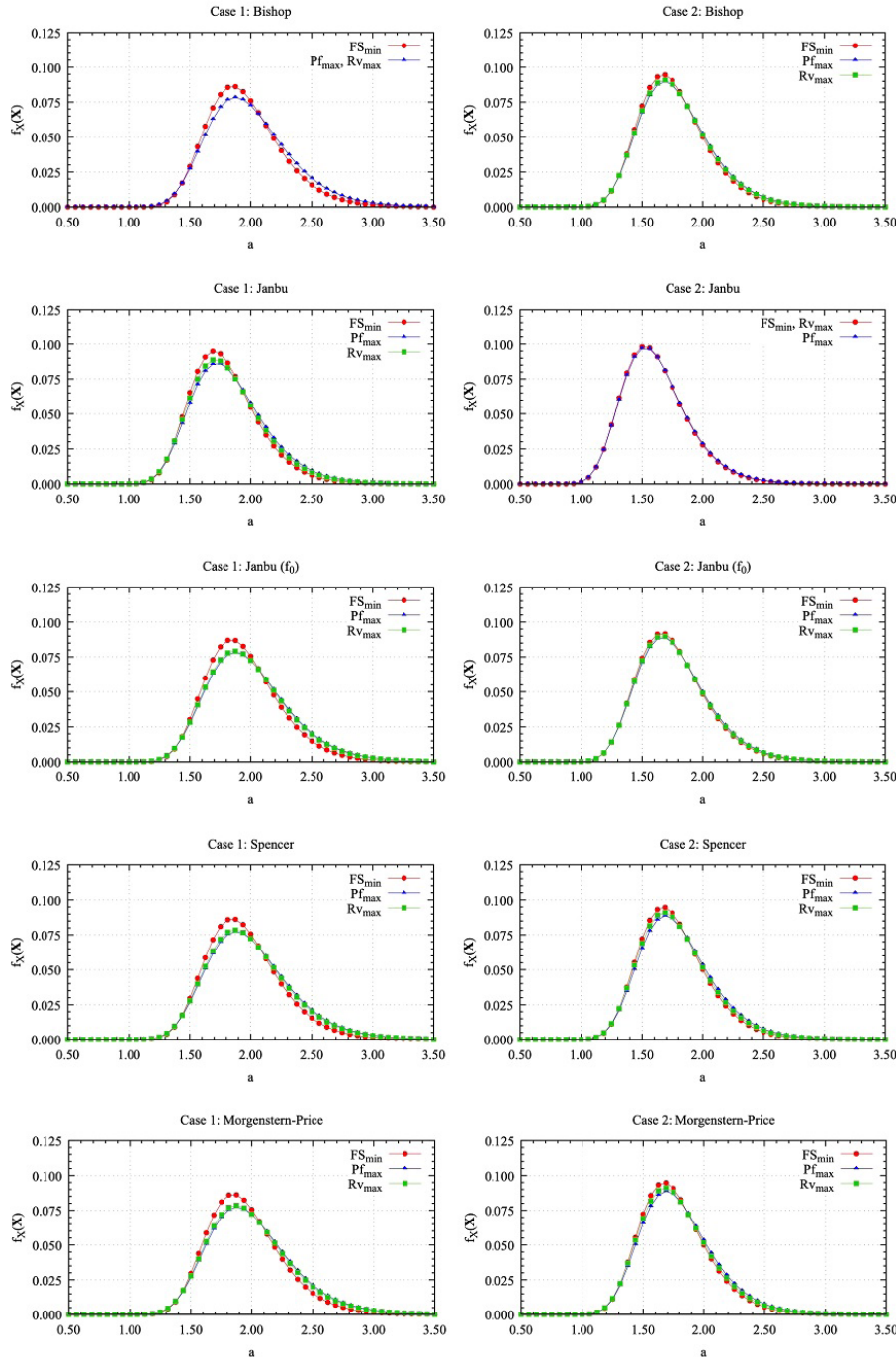


Figure 4. Probability density functions of critical slip surfaces.

2.10 Fixed slip surface

To complement the analyses already presented, the same procedure of construction of $F_X(\mathbf{X})$ and $f_X(\mathbf{X})$ was employed to a slip surface fixed in the region delimited by the set of all critical surfaces, according to Figure 5:

These analyses are intended to show the differences in the probability distributions of $FS(\mathbf{X})$ of the same slip surface, resulting from the choice of different limit equilibrium methods in direct coupling. Figure 6 presents the probability distribution curves of $FS(\mathbf{X})$ of all critical surfaces, including the surface fixed in the critical region:

It is observed that the various possibilities of direct coupling produce different probabilistic responses in at least two aspects. For the same sliding surface, the curves

of probability distributions of $FS(\mathbf{X})$ do not coincide with each other. Furthermore, when the analyses involve the investigation of critical surfaces, the results show that these surfaces may be non-coincident. The non-coincidence of the identified critical surfaces results in a set of deterministic and probabilistic surfaces that define a critical region in the analysed cross section instead of a single slip surface. These results explain the existence of variability in the responses provided by the most widespread methods of limit equilibrium in geotechnical practice. Larger differences are observed in the responses given by the uncorrected Janbu method. These differences evidence the fact that the correction proposed by the author of the method, through correction factor f_θ , ensures a better approximation of its response regarding to the other methods. It is interesting to note that this procedure

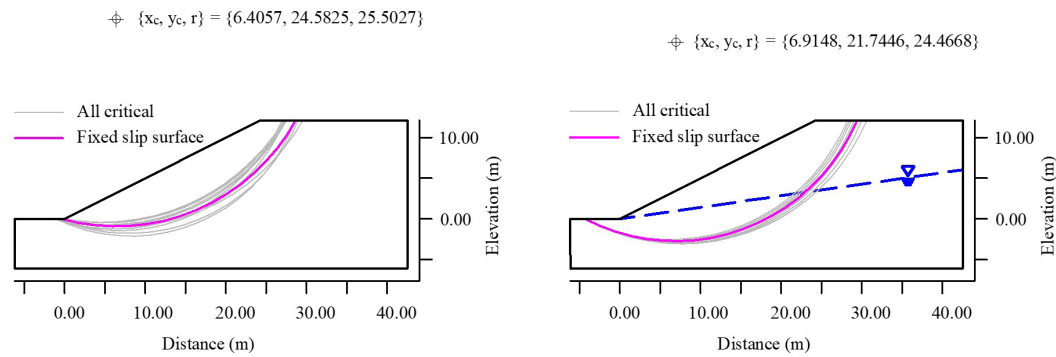


Figure 5. An overlap of all critical surfaces identified by deterministic and probabilistic criteria and different limit equilibrium methods employed in direct coupling.

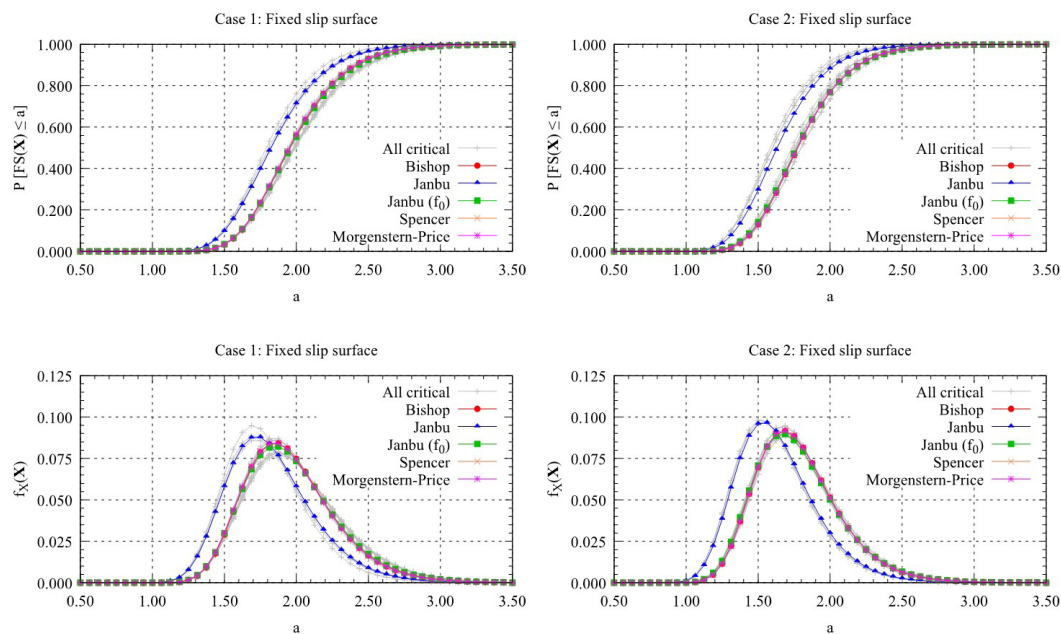


Figure 6. $FS(\mathbf{X})$ probability distribution curves of the fixed slip surface and all critical surfaces.

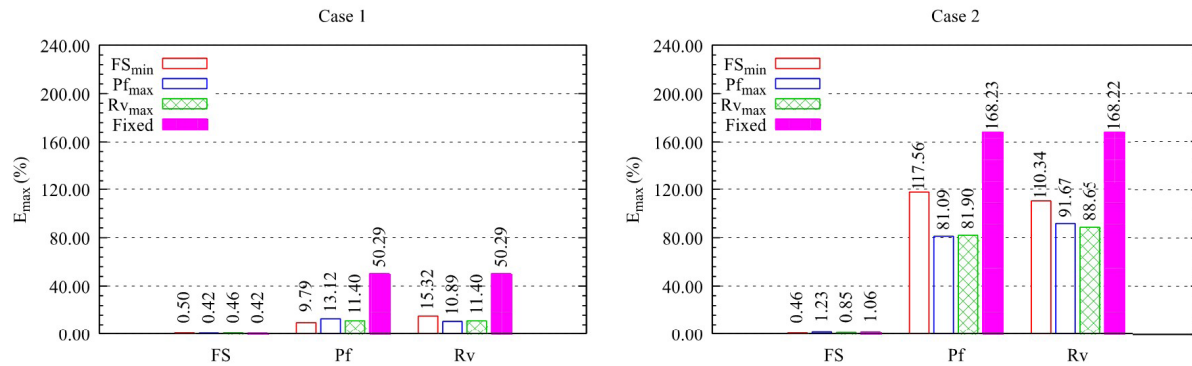


Figure 7. E_{max} of the answers provided by the limit equilibrium methods, relative to the fixed and critical surfaces.

provides, in addition to Pf , the probability that $FS(X)$ assumes a value less than or equal to a , for any value of a . Thus, it is possible to calculate, for example, the probability of $FS(X)$ violating values recommended by technical standards or any a value of interest.

Another way of showing the variability of the responses of the limit equilibrium methods is presented. From then on, responses from the uncorrected Janbu method were discarded, due to its high discrepancy when compared to the other methods. The FS , Pf and Rv values calculated by the different limit equilibrium methods were compared, restricting this comparison to the critical surfaces identified by the same criterion. All identified critical surfaces have a FS , Pf and Rv value, as shown in Table 4. Thus, the maximum relative error (E_{max}) refers to the results of surfaces belonging to the same set of critical surfaces, identified by the criteria FS_{min} , Pf_{max} or Rv_{max} . The fixed slip surface results are also presented. Figure 7 shows the E_{max} values for the analyzed cases:

In both cases analysed, E_{max} values of FS were relatively low, between 0.42% and 1.23%. E_{max} values are quite pronounced in the probabilistic responses, especially for case 2, in which the pore water pressure acts on the slope. The highest E_{max} values of Pf and Rv refer to the fixed slip surface, reaching 50.29% for case 1 and 168.22% for case 2. However, it was observed that E_{max} decreased when the responses of different surfaces, defined by the same identification criteria, were compared, between 9.79% and 15.32% in case 1, and between 81.09% and 117.56% in case 2. These results suggest that the consideration of a set of critical surfaces, according to the identification criteria presented, tends to minimize the variability of the probabilistic responses provided by different limit equilibrium methods directly coupled to FORM. On the other hand, if only one slip surface is considered, even if positioned in the critical region of the slope, the variability of the probabilistic responses increases significantly as a function of the choice of method, while the deterministic responses are practically identical.

3. Concluding remarks

In this paper, analyses of slope stability were presented referring to two cases of a slope collected in the literature. Both cases served as benchmarks for validating the Morgenstern-Price method implemented in RASS. The deterministic responses of FS and λ were presented, providing relative errors of less than 0.3%. Next, the scheme of methods used in the direct coupling of limit equilibrium methods to the FORM was presented, which made it possible to calculate the probabilities of shear failure of the slope, considering c' and ϕ' as random variables of the problem. Five limit equilibrium methods and three critical surface identification criteria were employed, based on FS_{min} , Pf_{max} e Rv_{max} , which allowed the identification of a critical fault region in the slope cross section instead of a single surface. In addition, the results showed the importance of identifying critical surfaces using probabilistic and not just deterministic criteria, in order to prevent probability calculations from being performed only for surfaces determined by FS_{min} .

The deterministic and probabilistic results showed that the uncorrected Janbu method provides very conservative responses regarding to the other tested methods, reinforcing the importance of adopting the f_0 correction factor proposed by the author of the method. Another important conclusion is that for the analyzed cases, the critical surfaces defined by FS_{min} showed very low variability in the FS responses due to the choice of limit equilibrium method. The greatest variability observed refers to the probabilistic responses of the same surface, fixed in the critical region of the slope. On the other hand, less variability was observed in the surfaces identified by the probabilistic criteria, being lower in case 1 than in case 2.

The use of the analysis framework presented in this work, in which the slope stability analyses are carried out jointly by different limit equilibrium methods and according to deterministic and probabilistic approaches, enriches the range of information available to the analyst, assisting in the

engineering decision making process and in the geotechnical risk management. As there is no method that provides a real answer to the problem, because all methods adopt simplifying assumptions to make the problem statically determined, one cannot claim categorically which limit equilibrium method is better than the others. Thus, the authors suggest the use of more than one limit equilibrium method and also the adoption of deterministic probabilistic criteria to identify critical surfaces, because in general these surfaces are not coincident.

Acknowledgements

The authors gratefully acknowledge the financial support of the Coordenação de Aperfeiçoamento de Pessoal de Nível Superior - Brasil (CAPES) - Finance Code 001.

Declaration of interest

The authors have no conflicts of interest to declare. All co-authors have observed and affirmed the contents of the paper and there is no financial interest to report.

Authors' contributions

Higor Biondo de Assis: Conceptualization, Data curation, Methodology, Software, Writing – original draft. Caio Gorla Nogueira: Conceptualization, Methodology, Supervision, Validation, Writing – review & editing.

Data availability

The datasets generated analyzed in the course of the current study are available from the corresponding author upon request.

List of symbols

a	Constant used in the modification of the limit state function for the construction of the curves $F_X(\mathbf{X})$ and $f_X(\mathbf{X})$
b_i	Width of i th slice
c'	Effective soil cohesion
c'_i	Effective soil cohesion along the base of the i th slice
C	Constant representing the consequence associated to the slope failure
$f(x)$	Interslice force function
f_i	Interslice force function value on the left side of i th slice
f_{i-1}	Interslice force function value on the right side of i th slice
h_i	Height of i th slice
i	Integer counter for the number of slices
j	Integer counter that depends on i

n	Total amount of slices
r	Radius of the circle describing the critical slip surface
x_c	Abscissa of the centre of the circle describing the critical slip surface
x_L	Abscissa of the left end of the slip surface
x_R	Abscissa of the right end of the slip surface
y_c	Ordinate of the centre of the circle describing the critical slip surface
\mathbf{y}^*	Design point
COV_X	Coefficient of variation of the random variable X
E	Normal interslice force
E_i	Normal interslice force acting on the left side of the i th slice
E_{i-1}	Normal interslice force acting on the right side of the i th slice
E_{max}	Maximum relative error
FS	Factor of safety
FS_{min}	Minimum factor of safety
$FS(\mathbf{X})$	Factor of safety as a function of the random variable vector
$F_X(\mathbf{X})$	Cumulative density function of $FS(\mathbf{X})$
$f_X(\mathbf{X})$	Probability density function of $FS(\mathbf{X})$
$g(\mathbf{X})$	Limit state function
$P[\cdot]$	Probability of occurrence of the condition of interest $[\cdot]$
P_f	Probability of failure
$P_{f,max}$	Maximum probability of failure
PDF_X	Probability density function of the random variable X
Q_i	External force acting on the i th slice
R_i	Sum of the shear resistances contributed by all the forces acting on the i th slice except the normal shear interslice forces
R_n	Sum of the shear resistances contributed by all the forces acting on the n th slice except the normal shear interslice forces
R_V	Risk value given by the constant representing the volume of soil mobilised at the slope failure
$R_{V,max}$	Maximum risk value
S	Tangential interslice force
T_i	Sum of the components of the R_i forces relating to the i th slice that tend to cause instability
T_n	Sum of the components of the R_n forces relating to the n th slice that tend to cause instability
U_i	Resultant water force acting on the base of the i th slice
W_i	Self-weight of i th slice
\mathbf{X}	Random variable vector X Abscissa of slope cross section
α_i	Angle formed between the horizontal and base of the i th slice
β	Reliability index
γ	Soil unit weight
λ	Scaling factor
μ	Non-negative exponent specified in function $f(x)$
μ_X	Mean value of the random variable X
ν	Non-negative exponent specified in function $f(x)$
$\Phi(\cdot)$	Standard normal cumulative distribution function

ϕ'	Effective friction angle of the soil
Φ_i	Variable used to rearrange the equations of the Morgenstern-Price method
ϕ_i'	Effective soil friction angle along the base of the i th slice
Φ_{i-1}	Variable used to rearrange the equations of the Morgenstern-Price method
Ψ_{i-1}	Variable used to rearrange the equations of the Morgenstern-Price method
Ψ_j	Variable used to rearrange the equations of the Morgenstern-Price method
ω_i	Angle between the vertical and the direction of the external force Q_i acting on the i th slice
\mathbb{X}	Physical space of random variables
\mathbb{Y}	Standard Gaussian space

References

- Abramson, L.W., Lee, T.S., Sharma, S., & Boyce, G.M. (2001). *Slope stability and stabilization methods*. John Wiley & Sons.
- Ang, A.H., & Tang, W.H. (1984). *Probability concepts in engineering planning and design: decision, risk, and reliability* (Vol. 2). John Wiley & Sons.
- Bishop, A.W. (1955). The use of the slip circle in the stability analysis of slopes. *Geotechnique*, 5(1), 7-17.
- Cho, S.E. (2007). Effects of spatial variability of soil properties on slope stability. *Engineering Geology*, 92(3-4), 97-109. <http://dx.doi.org/10.1016/j.enggeo.2007.03.006>.
- Cho, S.E. (2010). Probabilistic assessment of slope stability that considers the spatial variability of soil properties. *Journal of Geotechnical and Geoenvironmental Engineering*, 136(7), 975-984. [http://dx.doi.org/10.1061/\(ASCE\)GT.1943-5606.0000309](http://dx.doi.org/10.1061/(ASCE)GT.1943-5606.0000309).
- Fenton, G.A., & Griffiths, V.D. (2008). *Risk assessment in geotechnical engineering*. John Wiley & Sons New Jersey.
- Fredlund, D.G., & Krahn, J. (1977). Comparison of slope stability methods of analysis. *Canadian Geotechnical Journal*, 14(3), 429-439.
- Hasofer, A.M., & Lind, N.C. (1974). Exact and invariant second-moment code format. *Journal of the Engineering Mechanics Division*, 100(1), 111-121.
- Husein Malkawi, A.I., Hassan, W.F., & Abdulla, F.A. (2000). Uncertainty and reliability analysis applied to slope stability. *Structural Safety*, 22(2), 161-187. [http://dx.doi.org/10.1016/S0167-4730\(00\)00006-0](http://dx.doi.org/10.1016/S0167-4730(00)00006-0).
- Janbu, N. (1954a). Application of composite slip surface for stability analysis. In *Proceedings of European Conference on Stability of Earth Slopes* (pp. 43-49), Sweden, 1954.
- Janbu, N. (1954b). *Stability analysis for slopes with dimensionless parameters* [Doctoral thesis]. Harvard University Soil Mechanics Series.
- Janbu, N. (1973). Slope stability computations. In R.C. Hirschfeld and S.J. Poulos (Eds.), *Embankment-dam engineering*. John Wiley & Sons.
- Ji, J., Zhang, C., Gao, Y., & Kodikara, J. (2018). Effect of 2D spatial variability on slope reliability: a simplified FORM analysis. *Geoscience Frontiers*, 9(6), 1631-1638. <http://dx.doi.org/10.1016/j.gsf.2017.08.004>.
- Jiang, S., Huang, J., Griffiths, D.V., & Deng, Z. (2022). Advances in reliability and risk analyses of slopes in spatially variable soils: a state-of-the-art review. *Computers and Geotechnics*, 141, 104498. <http://dx.doi.org/10.1016/j.compgeo.2021.104498>.
- Lebrun, R., & Dufloy, A. (2009). Do Rosenblatt and Nataf isoprobabilistic transformations really differ? *Probabilistic Engineering Mechanics*, 24(4), 577-584. <http://dx.doi.org/10.1016/j.probenmech.2009.04.006>.
- Leonel, E.D., Beck, A.T., & Venturini, W.S. (2011). On the performance of response surface and direct coupling approaches in solution of random crack propagation problems. *Structural Safety*, 33(4), 261-274. <http://dx.doi.org/10.1016/j.strusafe.2011.04.001>.
- Melchers, R.E., & Beck, A.T. (2018). *Structural reliability analysis and prediction*. John Wiley & Sons.
- Morgenstern, N.R., & Price, V.E. (1965). The analysis of the stability of general slip surfaces. *Geotechnique*, 15(1), 79-93.
- Phoon, K. (2008). *Reliability-based design in geotechnical engineering: computations and applications*. CRC Press.
- Phoon, K., & Kulhawy, F.H. (1999). Characterization of geotechnical variability. *Canadian Geotechnical Journal*, 36(4), 612-624.
- Rackwitz, R., & Fiessler, B. (1978). Structural reliability under combined random load sequences. *Computers & Structures*, 9(5), 489-494. [http://dx.doi.org/10.1016/0045-7949\(78\)90046-9](http://dx.doi.org/10.1016/0045-7949(78)90046-9).
- Siacara, A.T., Beck, A.T., & Futai, M.M. (2020). Reliability analysis of rapid drawdown of an earth dam using direct coupling. *Computers and Geotechnics*, 118, 103336. <http://dx.doi.org/10.1016/j.compgeo.2019.103336>.
- Siacara, A.T., Napa-García, G.F., Beck, A.T., & Futai, M.M. (2022). Reliability analysis of an earth dam in operating conditions using direct coupling. *SN Applied Sciences*, 4(4), 99. <http://dx.doi.org/10.1007/s42452-022-04980-7>.
- Spencer, E. (1967). A method of analysis of the stability of embankments assuming parallel inter-slice forces. *Geotechnique*, 17(1), 11-26.
- Spencer, E. (1973). Thrust line criterion in embankment stability analysis. *Geotechnique*, 23(1), 85-100.
- Zhang, J., & Huang, H.W. (2016). Risk assessment of slope failure considering multiple slip surfaces. *Computers and Geotechnics*, 74, 188-195. <http://dx.doi.org/10.1016/j.compgeo.2016.01.011>.
- Zhu, D., Lee, C., Qian, Q., & Chen, G. (2005). A concise algorithm for computing the factor of safety using the Morgenstern Price method. *Canadian Geotechnical Journal*, 42(1), 272-278.

Determination of the dynamic parameters of Speswhite kaolin with resonant column and centrifuge tests

Filipe Cavalcanti Fernandes^{1#} , Bárbara Luiza Riz de Moura² ,

Marcio de Souza Soares de Almeida² , Luciano de Oliveira Souza Junior³ ,

Samuel Felipe Mollepaza Tarazona⁴ , Maria Cascão Ferreira de Almeida⁵ ,

José Maria de Camargo Barros⁶ 

Article

Keywords

Resonant column
Centrifuge models
Dynamic parameters
Soft soil
Speswhite kaolin

Abstract

Understanding the dynamic behavior of soils is essential to the study of the influence of seismic loads on the instability of submarine slopes, an important issue in Brazil and other countries. The shear modulus and the damping ratio are two fundamental parameters for the study of this behavior. Determining these parameters for Speswhite kaolin clay is the object of the present study using resonant column tests and dynamic centrifuge tests with accelerometers and pairs of bender elements. The curves obtained in the laboratory are compared with empirical curves and comparable data in the literature. Good agreement was observed between experimental data and the empirical prediction for the degradation curve of the normalized shear modulus. The damping curve for very low strains, obtained with resonant column tests, was consistent with the empirical curve. However, consistent with a trend observed in the literature, the centrifuge test results presented considerable scatter (dispersion), attributable to the difficulty in modelling damping dissipation mechanisms in the centrifuge.

1. Introduction

The typical geological profiles of submarine slopes on the Brazilian continental margin consist of normally to slightly overconsolidated clays with depths ranging from a few meters to hundreds of meters (Kowsmann et al., 2015). These slopes are often subjected to different types of loading conditions, including dynamic loading, such as earthquakes.

Borges et al. (2020a) observed an important concentration of epicenters in Campos, Santos, and Pelotas basins in southeastern Brazil, along the continental slope. Additionally, topographic surveys have indicated a great concentration of steep seabed slopes in the same area. Due to these unfavorable local conditions, regional earthquakes pose significant risk when they trigger submarine landslides, what could cause major impacts to offshore structures (Mérindol et al., 2022).

Therefore, the evaluation of risk imposed by earthquakes on submarine slopes should include an understanding of local soil behavior under dynamic conditions. Local soil and topographic settings can strongly influence the nature of

vibrations from seismic events, resulting in signal amplification at certain frequencies. The determination of dynamic soil properties, such as shear modulus and damping ratio, is necessary for predicting non-linear stress-strain behavior and for analyzing the stability of geotechnical structures under cyclic loading. Some types of tests can be used to determine the shear wave velocity (V_s) and the maximum shear modulus (G_{max}) of the soil, such as the in situ seismic cone penetration test – *SCPTu* (Borges et al., 2020b) – and the laboratory tests with bender elements and resonant column techniques (Kondner, 1963; Hardin & Drnevich, 1972; Liu et al., 2021; Jafari et al., 2022).

Shear modulus (G) and damping ratio (D) can be obtained employing resonant column (*RC*) tests for a wide range of strains (Atkinson, 2007) with satisfactory control of the test conditions at low strain levels in a range of 10^{-4} to $10^{-1}\%$ (Madhusudhan & Kumar, 2013; Lang et al., 2020).

Instead of *RC* tests, the G_{max} determination corresponding to strains lower than $3 \times 10^{-2}\%$ (Jia, 2018) can be done using bender element (*BE*) testing. The *BE* test enables

#Corresponding author. E-mail address: fcfernandes@me.com

¹EFEEX Engenharia, Natal, RN, Brasil.

²Universidade Federal do Rio de Janeiro, Instituto Alberto Luiz Coimbra, Rio de Janeiro, RJ, Brasil.

³Klohn Crippen Berger, Belo Horizonte, MG, Brasil.

⁴Vale S.A., Nova Lima, MG, Brasil.

⁵Universidade Federal do Rio de Janeiro, Escola Politécnica, Rio de Janeiro, RJ, Brasil.

⁶Instituto de Pesquisas Tecnológicas, Unidade de Ensino Tecnológico, São Paulo, SP, Brasil.

Submitted on December 3, 2022 ; Final Acceptance on April 1, 2023; Discussion open until August 31, 2023.

<https://doi.org/10.28927/SR.2023.013422>



This is an Open Access article distributed under the terms of the Creative Commons Attribution License, which permits unrestricted use, distribution, and reproduction in any medium, provided the original work is properly cited.

measurement of this parameter for strains below $10^{-3}\%$, a range in which G is almost constant (Mair, 1993; Youn et al., 2008; Wang et al., 2021).

The goal of this study is to present the dynamic geotechnical characterization of Speswhite kaolin which has been used in seismic response studies for submarine slopes (Tarazona et al., 2020; Soriano et al., 2021; Soriano et al., 2022) especially for its high permeability - favorable to centrifuge tests - and for being commercially available. This research uses traditional resonant column tests and centrifuge tests of submerged canyon models instrumented with accelerometers and bender elements to obtain the dynamic parameters of Speswhite kaolin: the moduli, G and G_{max} , and the damping ratio D .

2. Studied soil

Speswhite kaolin (*SK*), a clay of industrial origin, has long been used in geotechnical centrifuges for physical modeling by laboratories around the world (Almeida et al., 1985). The static properties of the *SK* used in this test program was characterized by means of monotonic loading tests (triaxial tests of the *CIU* and *CAU* type, and isotropic consolidation tests) and by index tests such as plastic limit and liquid limit tests. Table 1 presents a summary of the main static properties of the studied material – obtained from Fernandes (2018) – which are in agreement with the literature reports (Al-Tabbaa, 1987; Phillips, 1988; Kutter & James, 1989), where w_L is the liquid limit, I_p the plasticity index, G_s the specific gravity, c_v the coefficient of consolidation, M the critical state friction ratio, λ the slope of the isotropic compression line and κ the slope of the isotropic unload-reload line.

3. Resonant column tests

The preparation of the material for *RC* tests started with the consolidation (to 80 kPa) of a slurry mixture at 1.5 times the liquidity limit to obtain a block of clay from which small samples were extracted. Prior to the *RC* tests, an isotropic consolidation was carried out in a triaxial chamber under a confining stress of 150 kPa, using $5\text{ cm} \times 15\text{ cm}$ cylindrical samples, to reduce any disturbance due to the transfer of the samples and to guarantee a better consistency of the material for the final molding of the samples (Barros et al., 2007). The final geometry of the samples for the *RC* tests was 3.5 cm in diameter by 8 cm in height.

The *RC* test program was conducted in two phases: (1) the loading phase, or normally consolidated phase, where

each confining stress is the maximum applied stress, and (2) the unloading or overconsolidated phase (overconsolidated ratio, *OCR*, of 2, 4, 7.85 and 15.7).

The *RC* test essentially consists of the application of sinusoidal torsion vibrations, which result in very small shear strains (on the order of 10^{-4} to $10^{-2}\%$) in a cylindrical specimen, previously subjected to a confining stress in a triaxial chamber. The test apparatus presented in Figure 1 is composed of various electronic components (Fernandes, 2018).

A Hall type oscillator (Hall & Richart, 1963) was used in the test in “fixed-free” model, using a rigid mass on top of the specimen for better distribution of strains along the specimen (Richart et al., 1970). The scope of the present study only covers at hydrostatic state of stress.

The oscillator allows a certain stiffness added to one of the ends to add a polar moment of inertia (I_0) at the top

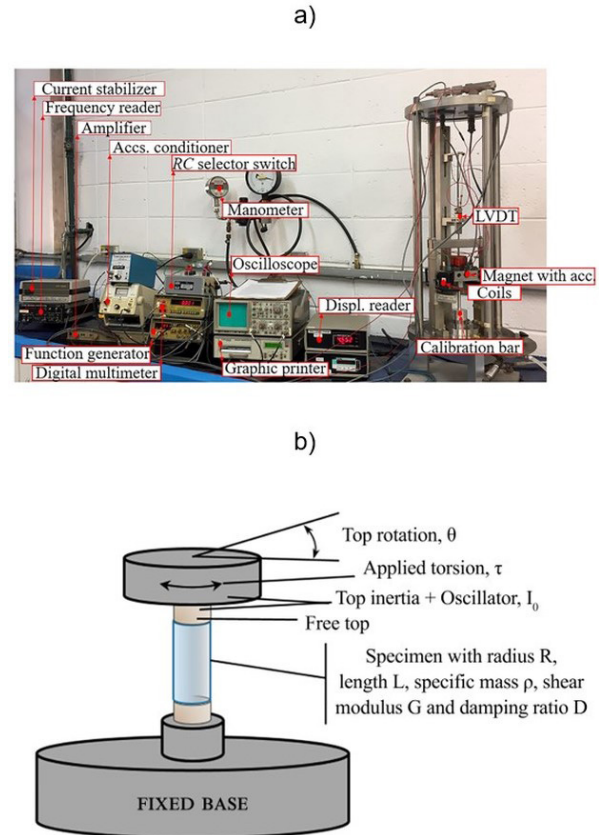


Figure 1. Resonant column test apparatus: a) overview (Adapted from Fernandes, 2018); b) test specimen torsion scheme and variables (adapted from Richart et al., 1970).

Table 1. Main properties of the studied soil (Fernandes, 2018).

Parameter	Parameters of Speswhite kaolin						
	w_L (%)	I_p (%)	G_s	c_v (10^{-8} m ² /s)	M	λ	κ
Fernandes (2018)	62	39	2.615	3.4–34.7	0.93	0.145–0.190	0.039–0.050

of the specimen (Figure 1b). This procedure of applying a torsion (τ) to the “free” end provides an approximately linear variation of angular rotation (θ) along the specimen of radius (R), length (L) and specific weight (ρ), and parameters G and D , thus obtaining a more uniform distribution of the shear strain along the length of the sample (Richart et al., 1970).

The main feature of the Hall-type oscillator is that it does not have a damper system (longitudinal and torsional springs as used in other types of oscillators (Richart et al., 1970)). As proposed by Hall & Richart (1963), the “fixed-free” system coupled to the Hall-type oscillator also enables the determination of the damping ratio (D) by the free-vibration decay method.

3.1 Measurements

The maximum shear modulus (G_{max}) of the soil is measured after 1000 minutes of consolidation. Anderson & Stokoe (1978) disregarded the creep or secondary consolidation effects of consolidation in the sample. Due to a variation in the start time of the tests, sometimes the measurement was not carried out exactly at the instant of 1000 minutes after the beginning of the consolidation stage. Therefore, an interpolation was made based on previous measurements to infer the G_{max} .

In order to determine the G modulus in the resonant condition (ASTM, 2007), measurements of the tangential acceleration of the specimen are performed during the application of vibration (measured by the voltmeter) and vibration frequency (measured directly by the frequency meter). The resonance condition of the system occurs when the signals of the vibration emission frequency and the ground response frequency are in phase. The phase between the torque application signals and the ground response is given by formation of the Lissajous ellipse (ASTM, 2007) on the oscilloscope screen, indicating a lag of 0.5π radians, and the occurrence of resonance in the ground-oscillator system.

In RC tests, the damping ratio can be calculated in more than one way. One of them, standardized by ASTM D4015-07 (ASTM, 2007), involves measuring free vibration decay. Free decay, as presented by Richart et al. (1970), occurs when the function generator is turned off while the amplitude of the accelerometer response is monitored as a function of time (Fernandes, 2018).

4. Centrifuge tests

A series of centrifuge tests were carried out to evaluate the seismic response of submarine slopes and/or canyons, determining the evolution of dynamic soil properties for different earthquake events (Tarazona, 2019; Tarazona et al., 2020, Souza, 2021; Soriano et al., 2021, 2022). The results of these centrifuge tests are useful for the dynamic characterization of the material, complementing the results of RC tests.

The centrifuge tests discussed here were carried out in a submerged clayey model, tested initially in the flat configuration and then as a canyon with a 30° angle. The model made with Speswhite kaolin was consolidated up to a stress of 250 kPa in an ESB (Equivalent Shear Beam) type test box in four successive layers. This level of consolidation stress was chosen to reproduce the undrained shear strength (S_u) profiles observed in the seabed of southeastern Brazil (Soriano et al., 2021). Sensors (such as accelerometers and bender elements) were arranged along its entire depth and were positioned during the consolidation process.

The ESB box was placed on the shaking table and embarked on the centrifuge. The model was then accelerated to 40 times the Earth’s gravity (g) and subjected to two different types of seismic loads, one sinusoidal and the other based on an earthquake that occurred in Italy in 2012 (Emilia Earthquake), applied alternately and with increasing peak ground accelerations (PGA) (Table 2). Additional information on the centrifuge experiments used here can be obtained in Tarazona (2019), Tarazona et al. (2020) and Souza (2021).

Figure 2 shows the final configuration of the centrifuge model with accelerometer sensors A and pairs of bender elements BE and Figure 3 shows one of the inputs applied, the Emilia earthquake, with an amplitude of $0.05g$.

The accelerometers enabled the determination of the shear modulus and damping parameters as a function of the strains using the sinusoidal input motion data. The bender elements, in turn, were used to calculate the maximum shear modulus at each excitation stage.

For each configuration of the model, flat F and canyon C , a penetration test was performed using a T-bar (Randolph & Houlsby, 1984) at the beginning of the $40g$ tests to obtain the profiles of undrained strength S_u and shear wave velocity V_s (Figure 4).

The theoretical S_u profiles were obtained from Equation 1 (Wroth, 1984), also shown in Figure 4a, where K is the normalized strength parameter, σ'_{vo} the effective vertical stress, and m the exponent. The K and m values adopted are shown in Table 3.

$$S_u = K \cdot \sigma'_{vo} \cdot OCR^m \quad (1)$$

Table 2. Input motions applied to the model.

Sequence	Type	PGA
1	Emilia	
2	Sinusoidal	0.05g
3	Emilia	
4	Sinusoidal	0.075g
5	Emilia	
6	Sinusoidal	0.10g
7	Emilia	
8	Sinusoidal	0.15g

Figure 4a shows a clear decrease in strength between the canyon and the flat model up to 4 m depth, showing the effect of the degradation that occurred during the excitation

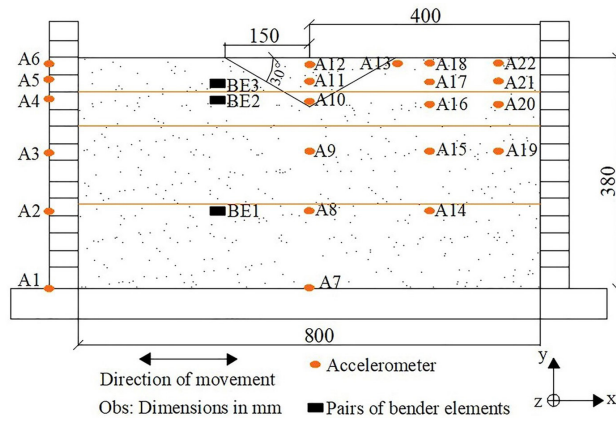
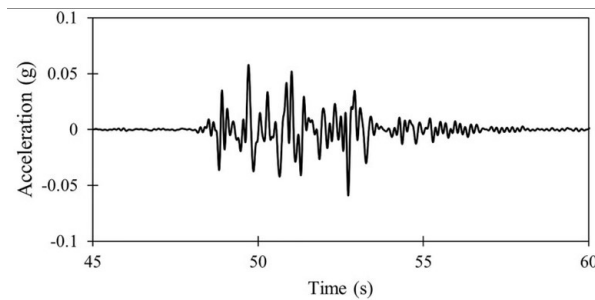
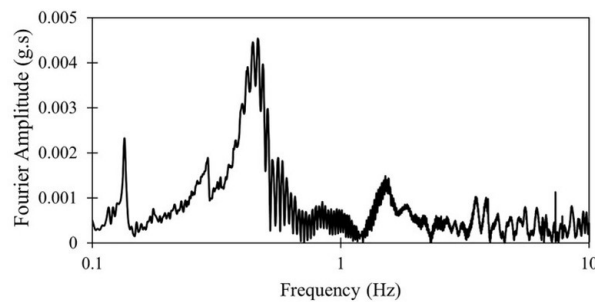


Figure 2. Model configuration and instrumentation.



a)



b)

Figure 3. Emilia input of 0.05g amplitude: a) accelerogram; b) Fourier amplitude.

Table 3. Parameters to calculate theoretical S_u .

Parameter	K	m
Fernandes (2018)	0.234	0.528
Garnier (2001)	0.19	0.59

of the flat model. For greater depths, this effect is not clearly observed.

The OCR profile obtained with Equation 1 from the S_u profile measured by the T-bar was used for the calculation of G_{max} as a function of depth according to Equation 2 (Viggiani & Atkinson, 1995), where p_r is the reference stress (equal to 1 kPa), p' is the mean effective stress and A , n and k are parameters used according to Viggiani & Atkinson (1995).

$$\frac{G_{max}}{p_r} = A \cdot \left(\frac{p'}{p_r} \right)^n \cdot OCR^k \quad (2)$$

The V_s profile (Figure 4b) is obtained from Equation 3 using the correlation with the density (ρ) of the model, $\rho = 1.74 \text{ g/cm}^3$ being the average model value used here.

$$V_s = \sqrt{\frac{G_{max}}{\rho}} \quad (3)$$

There was good agreement between the S_u data and the theoretical prediction, especially for the parameters reported by Fernandes (2018). Some humps are present due to the disturbance of the T-bar drive actuator system (Garala & Madabhushi, 2019; Tarazona, 2019 and Zhang et al., 2016). However, discontinuity between layers is not observed. The top of the clay model, up to approximately 1 m, prototype scale, exhibited S_u values higher than expected, possibly due to drying of the surface during model preparation, although care was taken to mitigate this problem such as covering the soil with wet geotextile and plastic.

4.1 Shear modulus and damping through accelerometers

The accelerometers installed in the centrifuge models by Tarazona et al. (2020) were used to obtain the shear modulus and the damping ratio based on the solution proposed by Brennan et al. (2005). In order to determine a value of G and D under a given shear strain (γ), three accelerometers were jointly analyzed at time and the accelerometers at the ends were used to measure the boundary conditions. For this purpose, a filter band of 0.75 Hz to 8.5 Hz was applied to the recorded accelerograms inside in a prototype scale.

Thus, for shear stress and strain histories calculated with the Brennan et al. (2005) formulation, the first 10 stress-strain cycles were individualized – including the first cycle of irregular behavior in blue –, and 10 values of G and D were obtained (Figure 5). Figure 5a shows the 10 hysteresis loops measured with the accelerometer A10 in the 0.15g sine signal and Figure 5b contains only one of the loops with an illustrative scheme for obtaining G (inclination of the highlighted secant line) and D (relative to the demarcated areas) with this method.

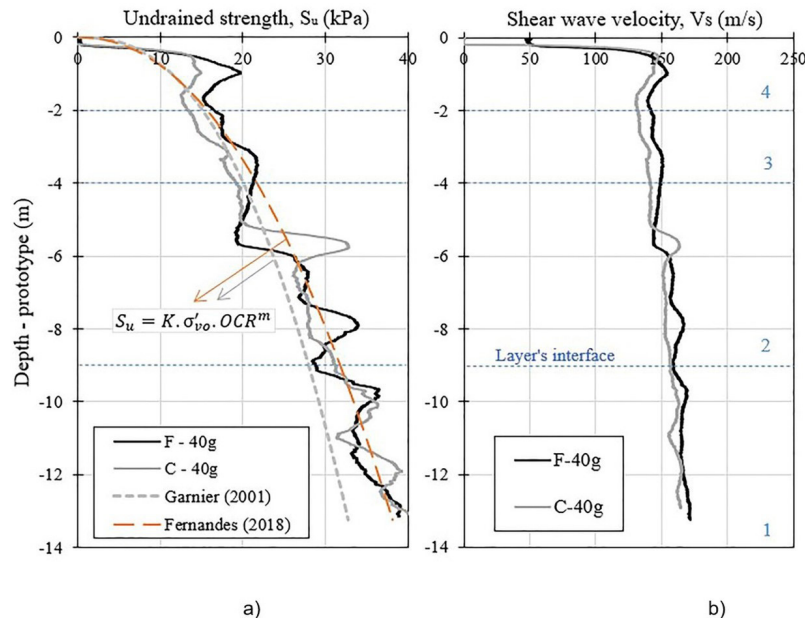


Figure 4. Profiles of a) S_u compared with theoretical predictions and of b) V_s for flat and canyon models.

The G results were obtained from the accelerometers with sine input motions in the flat and 30° canyon models. Results from Tarazona et al. (2020) data are also plotted for comparison.

4.2 Maximum shear modulus from bender element tests

The determination of the maximum shear modulus (G_{max}) was carried out using three pairs of bender elements ($BE1$, $BE2$ and $BE3$ shown in Figure 2). In each pair, one is the transmitter of the wave and the other, the receiver, depending on the arrangement of the cables and the applied polarization (Ingale et al., 2017).

The distance between transmitter and receiver benders (d) and the time interval (t) elapsed between the outgoing and incoming signals are needed for calculating the shear wave velocity V_s . The distance (d) was easily obtained by direct measurement when the sensors were installed in the model, namely: pair $BE1$ is positioned 100 mm apart, $BE2$ is 102 mm and $BE3$ is 108 mm. Ingale et al. (2017) and Lee & Santamarina (2005) present three methodologies for determining time t : in the time domain, in the frequency domain, and by cross-correlation.

In the present study, two methodologies were used to determine the travel time (t) of the shear wave, both in the time domain (TD). The time (t) is the average between two-time intervals used: the first and second peak between the input and output waves, resulting in time intervals t_1 and t_2 , respectively. In the output signal, the points of interest are first observed, and then the first low-amplitude inflection wave is disregarded (Lee & Santamarina, 2005). Figure 6 schematically

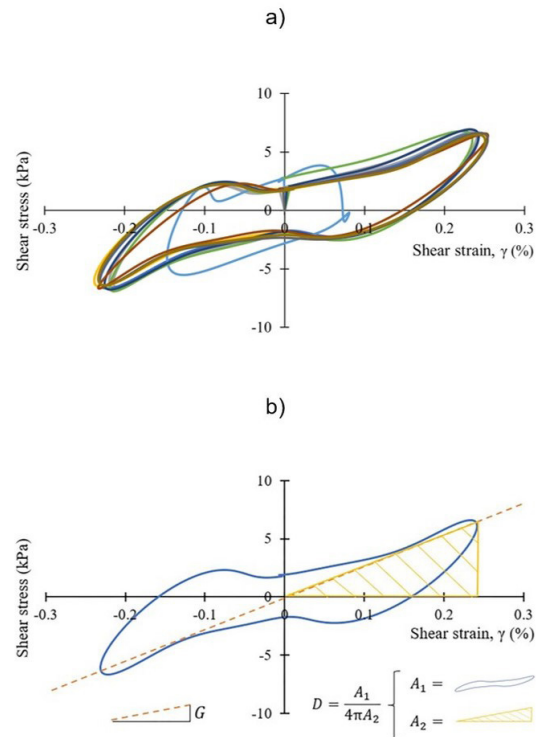


Figure 5. Linear equivalent solution of G and D : a) ten hysteresis loops for the 0.15g sine input motion (at A10); b) scheme for obtaining G and D .

summarizes the methodology used to obtain the intervals t_1 and t_2 for a sample of waves observed in pair $BE3$ after the 0.15g sinusoidal input motion (flat model).

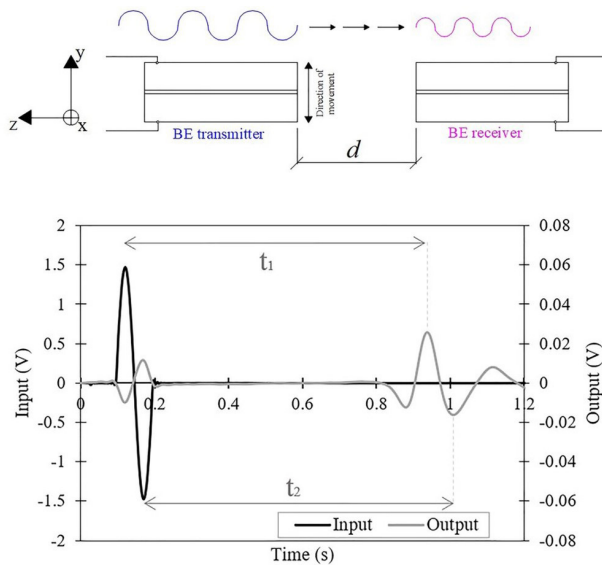


Figure 6. Schematic illustration for determining intervals t_1 e t_2 for the $BE3$ pair.

After determining the V_s using the relationship of $V_s = dl/t$, finally, the maximum shear modulus can be calculated using Equation 3.

G_{max} measurements were performed immediately before each input motion was applied to the base of the box, in order to track the results and map the variation of G_{max} to each input, allowing for a more accurate prediction of model degradation.

5. Shear modulus and damping ratio results

5.1 Shear modulus obtained from resonant column tests

Figure 7 shows the variation of shear modulus over time for the application of each confining stress in the RC tests for the normally consolidated test series. The results of the overconsolidated tests are not shown in this paper as they did not vary much over time, but this issue can be verified in Fernandes (2018).

G_{max} values were obtained by interpolating the last shear modulus measurements to find the modulus relative to 1000 minutes. The G_{max} values for each submitted confining stress are summarized in Table 4, where NC refers to the normally consolidated samples and OC to the overconsolidated ones.

5.2 Shear modulus obtained from centrifuge tests

Figure 8 presents the G modulus for the centrifuge tests, obtained from the accelerometers for model configurations F and C with the respective sinusoidal input amplitudes.

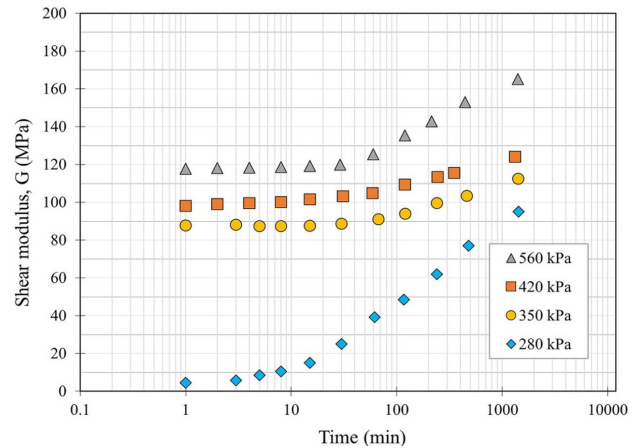


Figure 7. Shear modulus with advancing confined hydrostatic consolidation for the normally consolidated test series (adapted from Fernandes et al., 2020).

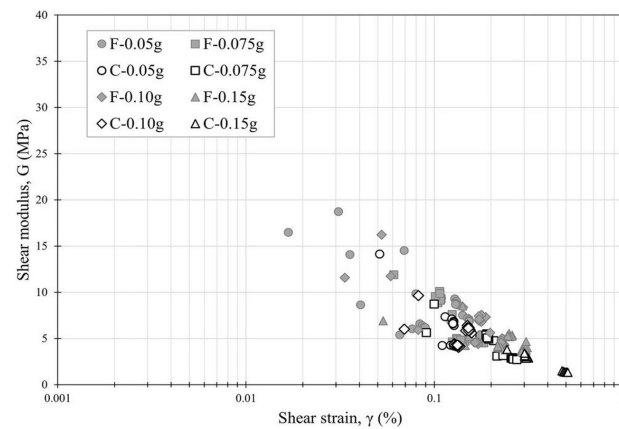


Figure 8. Shear modulus obtained from centrifuge tests.

Table 4. Summary of G_{max} results obtained from RC tests.

Consolidation condition	Confining stress (kPa)	OCR	G_{max} (MPa)
NC	280	1	87
	350	1	108
	420	1	121
	560	1	160
OC	280	2	168
	140	4	120
	70	8	97
	35	16	87

The data points obtained are limited to a strain γ equal to 0.5% but with strains mostly between 0.016% and 0.32%.

Larger values of strains γ are related to larger amplitudes of earthquakes, which are further accentuated in the canyon

model. Furthermore, when F and C models are compared for the same γ , the canyon model produced lower G values, even under lower amplitude loading than the flat model. This is consistent with the fact that the C model suffers from the cumulative effects of excitations as compared to the F model and, therefore, it degrades more. The data points in Figure 8 show the reduction in stiffness and consequent degradation of the shear modulus as seismic loads are applied during the tests.

It is important to note that the depth of the sensor played an important role in the response to shear strain. The deeper accelerometers presented greater shear modulus values for the same strain level, showing the impact of the effective confining stress on the stiffness results.

Table 5 presents the summary of the results of the G_{max} modulus. There is a clear influence of the confinement stress on the velocity results, as the deeper the sensor is, the higher results of V_s and, consequently, of G_{max} . Additionally, for the shallowest sensors (2.6 m and 6.1 m) there is a reduction in the G_{max} values caused by the strength degradation, a degradation that is even greater when comparing the flat and canyon models. As for the deepest sensor (9 m), there was a tendency for G_{max} to increase, caused by the process of consolidation of the model still in progress at this depth.

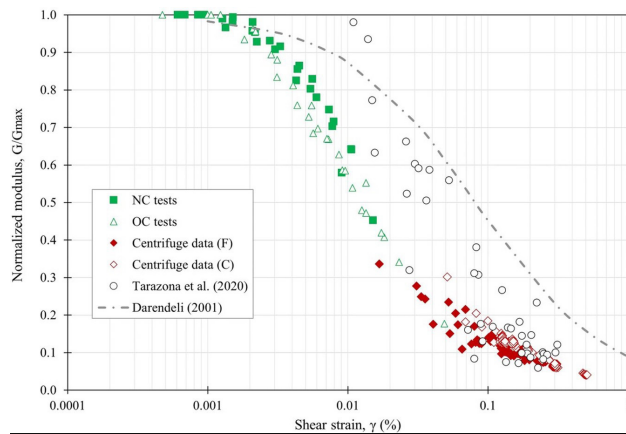


Figure 9. Normalized shear modulus from RC tests, present centrifuge tests, data from Tarazona et al. (2020) and empirical curve of Darendeli (2001).

5.3 Degradation curve by resonant column and centrifuge tests

Several studies have proposed curve models to represent the dynamic behavior of materials (Vucetic & Dobry, 1991; Ishibashi & Zhang, 1993; Darendeli, 2001), but each of these models can reproduce a limited number of behaviors and, therefore, may only be considered as estimates of actual field soil performance (Amir-Faryar et al., 2016).

Darendeli (2001) developed a database of soil samples for the elaboration of empirical curves of normalized shear modulus and damping of materials, which allow the characterization of their dynamic behavior. The data comes from a combination of resonant column and cyclic torsional shear ($RCTS$) tests on undisturbed samples. Statistical analysis was carried out to be able to calibrate the requested parameters, with a structure composed of equations that incorporate the parameters that control the non-linear behavior of the soil, such as overconsolidation ratio, soil plasticity index, mean effective confining stress, type of soil and loading conditions (such as number of cycles and frequency). This model seems to best capture all effects over a wider stress range (Guerreiro et al., 2012).

Figure 9 presents the normalized curve of the modulus G for both phases of confinement of the specimen in the RC tests (NC and OC tests). In addition, it shows the centrifuge results for the F and C models, the data from Tarazona et al. (2020) as well as the empirical curve (EC) from Darendeli (2001) for a material with a plasticity index equal to 39% and considering the average OCR of the model.

As shown in Figure 9, there is low dispersion in the resonant column data associated with strains below 0.01%. It is also observed that the greater the strain, the greater the difference between the G/G_{max} data obtained in the laboratory and the empirical curve. The combined curve formed by RC and centrifuge tests shows a similar trend to the EC , although they deviate significantly from the EC in the strain range between 0.01%–0.1%.

Considering both centrifuge results, those from Tarazona et al. (2020) better adhered to the empirical curve of Darendeli (2001) and are very similar to those of the present study in the range of strains between 0.08% and 0.3%, in which both approach the empirical prediction.

The low adhesion between the laboratory tests and the EC by Darendeli (2001) in some strain ranges can be

Table 5. Summary of G_{max} results obtained through centrifuge tests (in MPa).

Pair of BE	Model	Depth (m)	0.05g	0.75g	0.10g	0.15g
$BE3$	Flat	2.6	23.62	23.07	22.89	22.41
$BE2$		6.1	45.47	44.21	43.72	43
$BE1$		9	65.17	65.33	66.24	66.55
$BE3$	Canyon	2.6	14.7	14.48	14.54	13.35
$BE2$		6.1	31.58	31.29	31.34	28.89
$BE1$		9	-	60.89	-	63.27

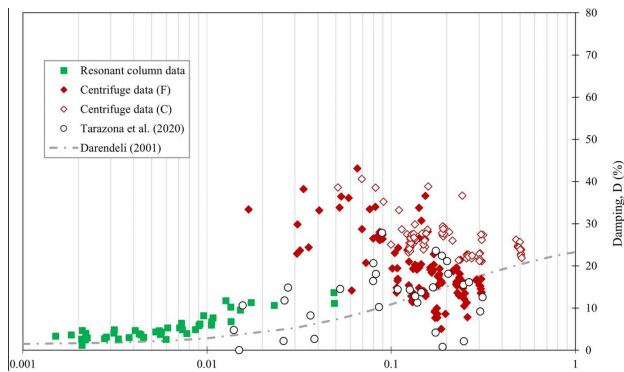


Figure 10. Damping ratio curve with results from resonant column tests, centrifuge tests, Tarazona et al. (2020) data and the Darendeli curve (2001).

explained by the limitation of the model for materials of high plasticity, as is the case of Speswhite kaolin. According to Guerreiro et al. (2012), the model proposed by Darendeli (2001) is quite suitable for materials of medium plasticity, which is not the case of the tested material.

The evolution of the damping ratio results relative to increasing shear strain for all previously analyzed experimental results are shown in Figure 10, along with the Darendeli (2001) curve. The *RC* data shows good agreement with the *EC* from Darendeli (2001). As the strain increases, the average damping data points tend to increase regardless of the method.

For the centrifuge data, the scatter is considerable. This behavior has also been reported by other authors, such as Afacan et al. (2013), Brennan et al. (2005) and Tarazona et al. (2020). Data dispersion is associated with the difficulty in modeling the damping dissipation mechanisms in the context of the centrifuge testing, diverging significantly from the actual damping conditions of the material. Despite this, the data from the *C* model consistently shows greater damping than the data from the *F* model, when subjected to the same strain. This reveals the cumulative effect of the application of dynamic load in reducing the stiffness in the *C* model.

The centrifuge data from the present study and those of Tarazona et al. (2020) present good agreement. Although they are close to Darendeli's (2001) curve, they present data dispersion caused by the centrifuge environment.

6. Conclusions

The present study employed two different methodologies to determine the dynamic parameters of Speswhite kaolin, a material widely used in geotechnical tests. Resonant column and centrifuge tests with *BE* and accelerometers were carried out in parallel to determine the degradation of the shear modulus *G* and the damping curve. These results are presented together with Darendeli's widely used empirical model for the analysis of the non-linear behavior of the soil.

The resonant column and centrifuge tests showed relatively good agreement with those of the empirical curves, both for the degradation of the shear modulus and for the damping ratio at low strains.

Centrifuge tests were effective in evaluating the lower part of the shear modulus degradation curve. For strains above 0.03%, a dispersion of the damping data and its distance from the empirical prediction is noted. This behavior has been reported in the literature and corroborates the difficulty of obtaining this parameter in centrifuge tests. In addition, the poor adherence of the data to the empirical curves in some strain ranges is possibly due to the high plasticity of Speswhite kaolin, an obstacle to the use of the Darendeli curve.

The resonant column tests yielded low dispersion for the shear modulus results and acceptable dispersion for the damping ratio results. The methodology used to carry out the resonant column tests showed yielded low dispersion between the results in the determination of the shear modulus and an acceptable dispersion regarding the damping ratio.

For future studies on this matter, the authors suggest to complement the curves with more data from new *RC* tests with increased consolidation time and new centrifuge tests with strength variation between layers reaching a wider range of strain. Regarding the *BE* results, it is suggested calculation of wave travel time in the frequency domain and the development of numerical studies to validate the presented data.

Acknowledgements

The work described in this article is part of two Cooperation Research Agreements, between PETROBRAS and Federal University of Rio de Janeiro, titled 'Seismic Centrifuge Modelling of Submarine Slopes' and 'Evaluation of Weak Layer on Submarine Landslides' (Contractual Instruments 0050.0094059.14.9 and 5850.0106073.17.9, respectively). The authors thank the staff of the Université Gustave Eiffel and the Institute for Technological Research (IPT) for carrying out the testing program presented in this work, as well as Dr. Sandra Escoffier and Dr. Zheng Li for their insightful recommendations.

Declaration of interest

The authors have no conflicts of interest to declare. All co-authors have observed and affirmed the contents of the paper and there is no financial interest to report.

Authors' contributions

Filipe Cavalcanti Fernandes: Conceptualization, Data curation, Visualization, Writing – original draft. Bárbara Luiza Riz de Moura: Conceptualization, Data curation, Visualization, Writing – original draft & editing. Marcio de

Souza Soares de Almeida: Methodology, Formal analysis, Funding acquisition, Visualization, Writing – review. Luciano de Oliveira Souza Junior: Conceptualization, Data curation, Visualization, Writing – original draft. Samuel Felipe Mollepaza Tarazona: Methodology, Supervision, Visualization. Maria Cascão Ferreira de Almeida: Methodology, Formal analysis, Funding acquisition, Visualization, Writing – review. José Maria de Camargo Barros: Methodology, Supervision, Formal analysis, Writing – review.

Data availability

The datasets generated and analyzed in the course of the current study are available from the corresponding author upon request.

List of symbols

c_v	Coefficient of consolidation
d	Distance between BE of the same pair
m	Exponent to calculate S_u according to Wroth (1984)
n	Parameter to calculate G_{max}/p_r according to Viggiani & Atkinson (1995)
p'	Mean effective stress
p_r	Reference stress (1 kPa)
t_1	Time interval between first peaks of the transmitter and receiver BE
t_2	Time interval between second peaks of the transmitter and receiver BE
t	Average between t_1 and t_2
w_L	Liquid limit
A	Parameter to calculate G_{max}/p_r according to Viggiani & Atkinson (1995)
Ax	Accelerometers with $x = 1, 2, \dots, 22$
BE	Bender elements
C	Canyon (referring to the model configuration)
CR	Resonant column
CAU	Consolidated Anisotropic Undrained
CIU	Consolidated Isotropic Undrained
D	Damping ratio
EC	Empirical curve
ESB	Equivalent shear beam (type of container test)
F	Flat (referring to the model configuration)
G	Shear modulus
G_{max}	Maximum shear modulus
G_s	Specific gravity
I_o	Top inertia + oscillator
I_p	Plasticity index
k	Parameter to calculate G_{max}/p_r according to Viggiani & Atkinson (1995)
K	Normalized strength parameter to calculate S_u according to Wroth (1984)
L	Sample length
NC	Normally consolidated samples

OC	Overconsolidated samples
OCR	Overconsolidation ratio
PGA	Peak ground acceleration
R	Specimen radius
$RCTS$	Cyclic torsional shear
$SCPTu$	Seismic cone penetration test
SK	Speswhite kaolin
S_u	Undrained strength
TD	Time domain
V_s	Shear wave velocity
γ	Shear strain
θ	Angular rotation
κ	Slope of the isotropic unload-reload line
λ	Slope of the isotropic compression line
M	Critical state friction ratio
ρ	Specific weight
σ'_{vo}	Effective vertical stress
τ	Torsion

References

- Afacan, K.B., Brandenburg, S.J., & Stewart, J.P. (2013). Centrifuge modeling studies of site response in soft clay over wide strain range. *Journal of Geotechnical and Geoenvironmental Engineering*, 140(2), 04013003. [https://10.1061/\(asce\)gt.1943-5606.0001014](https://10.1061/(asce)gt.1943-5606.0001014).
- Almeida, M.S.S., Davies, M.C.R., & Parry, R.H.G. (1985). Centrifuged embankments on strengthened and unstrengthened clay foundations. *Geotechnique*, 35(4), 425-441. <http://dx.doi.org/10.1680/geot.1985.35.4.425>.
- Al-Tabbaa, A. (1987). *Permeability and stress-strain response of Speswhite kaolin* [Doctoral thesis]. Cambridge University.
- Amir-Faryar, B., Aggour, M.S., & McCuen, R.H. (2016). Universal model forms for predicting the shear modulus and material damping of soils. *Geomechanics and Geoengineering*, 12(1), 60-71. <http://dx.doi.org/10.1080/017486025.2016.1162332>.
- Anderson, D.G., & Stokoe, K.H. (1978). Shear modulus: a time-dependent soil property. In R. J. Ebelhar, V. P. Drnevich & B. L. Kutter (Eds.), *Dynamic geotechnical testing* (pp. 66-90). ASTM. <https://doi:10.1520/STP35672S>.
- ASTM D4015-07. (2007). *Standard test methods for modulus and damping of soils by resonant-column method*. ASTM International, West Conshohocken, PA. <https://doi.org/10.1520/D4015-07>.
- Atkinson, J.H. (2007). *The mechanics of soils and foundations* (2nd ed.). Taylor & Francis.
- Barros, J.M.C., Silveira, R.M.S., & Amaral, C.S. (2007). Correlation between the maximum shear modulus and the undrained strength of a remolded marine clay. In *Proc. XIII Panamerican Conference on Soil Mechanics and Geotechnical Engineering* (pp. 514-519). Isla de Margarita, Venezuela. Sociedad Venezolana de Geotecnia.
- Borges, R.G., Assumpção, M.S., Almeida, M.C.F., & Almeida, M.S.S. (2020a). Seismicity and seismic hazard in the

- continental margin of southeastern Brazil. *Journal of Seismology*, 24(6), 1205-1224. <http://dx.doi.org/10.1007/s10950-020-09941-4>.
- Borges, R.G., Souza Junior, L.O., Almeida, M.C.F., & Almeida, M.S.S. (2020b). Relationship between shear wave velocity and piezocone penetration tests on the Brazilian continental margin. *Soils and Rocks*, 43, 219-230. <http://dx.doi.org/10.28927/SR.432219>.
- Brennan, A.J., Thusyanthan, N.I., & Madabhushi, S.P.G. (2005). Evaluation of shear modulus and damping in dynamic centrifuge tests. *Journal of Geotechnical and Geoenvironmental Engineering*, 131(12), 1488-1497. [http://dx.doi.org/10.1061/\(ASCE\)1090-0241\(2005\)131:12\(1488\)](http://dx.doi.org/10.1061/(ASCE)1090-0241(2005)131:12(1488)).
- Darendeli, M.B. (2001). *Development of a new family of normalized modulus* [Doctoral dissertation, University of Texas at Austin]. University of Texas at Austin's repository. Retrieved in December 3, 2022, from <http://hdl.handle.net/2152/10396>
- Fernandes, F.C. (2018). *Resonant column and bender element tests with Speswhite kaolin for shear modulus measurement* [Master's dissertation, Federal University of Rio de Janeiro]. Federal University of Rio de Janeiro's repository (in Portuguese). Retrieved in December 3, 2022, from <http://hdl.handle.net/11422/11402>.
- Fernandes, F.C., Tarazona, S.F.M., Almeida, M.C.F., Almeida, M.S.S., & Barros, J.M.C. (2020). Ensaaios de coluna ressonante em caulim Speswhite. In *Proc. XX Congresso Brasileiro de Mecânica dos Solos e Engenharia Geotécnica* (pp. 1-8). Campinas. Retrieved in December 3, 2022, from <https://proceedings.science/cobramseg-2022/trabalhos/ensaaios-de-coluna-ressonante-em-caulim-speswhite?lang=pt-br>. (in Portuguese).
- Garala, T.K., & Madabhushi, G.S. (2019). Seismic behaviour of soft clay and its influence on the response of friction pile foundations. *Bulletin of Earthquake Engineering*, 17(4), 1919-1939. <http://dx.doi.org/10.1007/s10518-018-0508-4>.
- Garnier, J. (2001). Modèles physiques en géotechnique. *Revue Française de Géotechnique*, 97, 3-29. <http://dx.doi.org/10.1051/geotech/2001097003>.
- Guerreiro, P., Kontoe, S., & Taborada, D. (2012). Comparative study of stiffness reduction and damping curves. In *Proc. 15th World Conference on Earthquake Engineering* (pp. 2-11). Lisbon. SPES.
- Hall, J., & Richart, F.E. (1963). Dissipation of elastic wave energy in granular soils. *Journal of the Soil Mechanics and Foundations Division*, 89(6), 27-56. <http://dx.doi.org/10.1061/JSFEAQ.0000568>.
- Hardin, B.O., & Drnevich, V.P. (1972). Shear modulus and damping in soils: design equations and curves. *Journal of the Soil Mechanics and Foundations Division*, 98(7), 667-692. <http://dx.doi.org/10.1061/JSFEAQ.0001760>.
- Ingale, R., Patel, A., & Mandal, A. (2017). Performance analysis of piezoceramic elements in soil: a review. *Sensors and Actuators. A, Physical*, 262, 46-63. <http://dx.doi.org/10.1016/j.sna.2017.05.025>.
- Ishibashi, I., & Zhang, X. (1993). Unified dynamic shear moduli and damping ratios of sand and clay. *Soils and Foundations*, 33(1), 182-191. <https://10.3208/sandf1972.33.182>.
- Jafari, S.H., Lajevardi, S.H., & Sharifipour, M. (2022). Correlation between small-strain dynamic properties and unconfined compressive strength of lime-stabilized soft clay. *Soil Mechanics and Foundation Engineering*, 59(4), 331-337. <http://dx.doi.org/10.1007/s11204-022-09819-2>.
- Jia, J. (2018). *Soil dynamics and foundation modeling*. Springer. <https://doi:10.1007/978-3-319-40358-8>.
- Kondner, R.L. (1963). Hyperbolic stress-strain response: cohesive soils. *Journal of the Soil Mechanics and Foundations Division*, 89(1), 115-143. <http://dx.doi.org/10.1061/JSFEAQ.0000479>.
- Kowmann, R.O., Falcão, A.P.C., & Curbelo-Fernandez, M.P. (2015). *Geologia e geomorfologia*. Elsevier (in Portuguese).
- Kutter, B., & James, R. (1989). Dynamic centrifuge model tests on clay embankments. *Geotechnique*, 39(1), 91-106. <http://dx.doi.org/10.1680/geot.1989.39.1.91>.
- Lang, L., Li, F., & Chen, B. (2020). Small-strain dynamic properties of silty clay stabilized by cement and fly ash. *Construction & Building Materials*, 237, 117646. <http://dx.doi.org/10.1016/j.conbuildmat.2019.117646>.
- Lee, J.-S., & Santamarina, C. (2005). Bender elements: performance and signal interpretation. *Journal of Geotechnical and Geoenvironmental Engineering*, 131(9), 1063-1070. [http://dx.doi.org/10.1061/\(asce\)1090-0241\(2005\)131:9\(1063\)](http://dx.doi.org/10.1061/(asce)1090-0241(2005)131:9(1063)).
- Liu, Z., Kim, J., Hu, G., Hu, W., & Ning, F. (2021). Geomechanical property evolution of hydrate-bearing sediments under dynamics loads: nonlinear behaviors of modulus and damping ratio. *Engineering Geology*, 295, 106427. <http://dx.doi.org/10.1016/j.enggeo.2021.106427>.
- Madhusudhan, B.N., & Kumar, J. (2013). Damping of sands for varying saturation. *Journal of Geotechnical and Geoenvironmental Engineering*, 139(9), 1625-1630. [http://dx.doi.org/10.1061/\(ASCE\)GT.1943-5606.0000895](http://dx.doi.org/10.1061/(ASCE)GT.1943-5606.0000895).
- Mair, R.J. (1993). Developments in geotechnical engineering research: application to tunnels and deep excavation. *Proceedings of the Institution of Civil Engineers. Civil Engineering*, 93, 27-41.
- Mérindol, M., St-Onge, G., Sultan, N., Lajeunesse, P., & Garziglia, S. (2022). Earthquake-triggered submarine landslides in the St. Lawrence Estuary (Québec, Canada) during the last two millennia and the record of the major 1663 CE $M \geq 7$ event. *Quaternary Science Reviews*, 291(1), 107640. <http://dx.doi.org/10.1016/j.quascirev.2022.107640>.
- Phillips, N. (1988). *Centrifuge lateral pile tests in clay: tasks 2 and 3: a report by Exxon Production Research Corp.* Lynxvale Ltd.

- Randolph, M.F., & Houlsby, G.T. (1984). The limiting pressure on a circular pile loaded laterally in cohesive soil. *Geotechnique*, 34(4), 613-623. <http://dx.doi.org/10.1680/geot.1984.34.4.613>.
- Richart, F.E., Hall, J.R., & Woods, R.D. (1970). *Vibrations of soils and foundations*. Prentice-Hall.
- Soriano, C., Almeida, M.C.F., Almeida, M.S.S., Madabhushi, G.S., & Stanier, S. (2022). Centrifuge modeling of the seismic behavior of soft clay slopes. *Journal of Geotechnical and Geoenvironmental Engineering*, 148(11), 04022089. [http://dx.doi.org/10.1061/\(ASCE\)GT.1943-5606.0002884](http://dx.doi.org/10.1061/(ASCE)GT.1943-5606.0002884).
- Soriano, C., Almeida, M.C.F., Madabhushi, S.P.G., Stanier, S.A., Almeida, M.S.S., Liu, H., & Borges, R.G. (2021). Seismic centrifuge modeling of a gentle slope of layered clay, including a weak layer. *Geotechnical Testing Journal*, 45(1), 125-144. <http://dx.doi.org/10.1520/GTJ20200236>.
- Souza, L.O. (2021). *Centrifuge modeling of submarine slopes subjected to seismic movements* [Master's dissertation, Federal University of Rio de Janeiro]. Federal University of Rio de Janeiro's repository.
- Tarazona, S.F.M. (2019). *Evaluation of seismic site response of submarine clay canyons* [Doctoral thesis, Federal University of Rio de Janeiro]. Federal University of Rio de Janeiro's repository.
- Tarazona, S.F.M., Almeida, M.C.F., Bretschneider, A., Almeida, M.S.S., Escoffier, S., & Borges, R.G. (2020). Evaluation of seismic site response of submarine clay canyons using centrifuge modelling. *International Journal of Physical Modelling in Geotechnics*, 20(4), 224-238. <https://doi.10.1680/jphmg.18.00084>.
- Viggiani, G., & Atkinson, J. (1995). Stiffness of fine-grained soil at very small strains. *Geotechnique*, 45(2), 249-265. <http://dx.doi.org/10.1680/geot.1995.45.2.249>.
- Vucetic, M., & Dobry, R. (1991). Effect of soil plasticity on cyclic response. *Journal of Geotechnical Engineering*, 117(1), 89-107. [http://dx.doi.org/10.1061/\(ASCE\)0733-9410\(1991\)117:1\(89\)](http://dx.doi.org/10.1061/(ASCE)0733-9410(1991)117:1(89)).
- Wang, F., Li, D., Du, W., Zarei, C., & Liu, Y. (2021). Bender element measurement for small-strain shear modulus of compacted loess. *International Journal of Geomechanics*, 21(5), 04021063. [http://dx.doi.org/10.1061/\(asce\)gm.1943-5622.0002004](http://dx.doi.org/10.1061/(asce)gm.1943-5622.0002004).
- Wroth, C.P. (1984). The interpretation of in situ soil tests. *Geotechnique*, 34(4), 449-489. <http://dx.doi.org/10.1680/geot.1984.34.4.449>.
- Youn, J.U., Choo, Y.W., & Kim, D.S. (2008). Measurement of small-strain shear modulus G_{max} of dry and saturated sands by bender element, resonant column, and torsional shear tests. *Canadian Geotechnical Journal*, 45(10), 1426-1438. <http://dx.doi.org/10.1139/T08-069>.
- Zhang, L., Goh, S.H., & Yi, J. (2016). A centrifuge study of the seismic response of pile-raft systems embedded in soft clay. *Geotechnique*, 67(6), 479-490. <http://dx.doi.org/10.1680/jgeot.15.p.099>.

Three-dimensional numerical analysis of the generalized group effect in monitored continuous flight auger pile groups

Lorena da Silva Leite^{1#} , Paulo César de Almeida Maia¹ , Aldo Durand Farfán¹ 

Article

Keywords

Group effect
Continuous flight auger pile
Finite element method
Deep foundation
Soil-pile interaction

Abstract

The interaction mechanisms related to the group effect between piles and between pile groups significantly influence the soil-structure interaction process. This interaction causes the superposition of stresses and, in general, makes the pile group settlement different from the settlement of an isolated pile. The objective of the present paper is to evaluate the soil-structure interaction mechanisms of buildings with foundations of monitored continuous flight auger piles (CFA) in a stratified soil mass, with the presence of an intermediate soft soil layer. Hence, it is particularly analyzed the group effect between piles of a group and the group effect between all pile groups from a foundation of a study case instrumented by means of numerical modeling, considering the effect of the soft soil layer. The results show the significant group effect on displacements, showing the increase in settlement due to the overlapping of the tension bulbs of the piles and neighboring pile groups.

1. Introduction

The soil-structure interaction (SSI) is responsible for the redistribution of efforts through structural rebalancing, which occurs with the construction evolution. The study of the processes of soil-structure interaction is important for predicting the behavior of the structure during the construction sequence. The interaction mechanisms related to the group effect between piles and pile groups significantly influence the soil-structure interaction process, more specifically, the pile-soil interaction process. This interaction causes overlap of the tension bulbs and, in general, makes the settlement of the group of piles different from the settlement of an isolated pile.

The group effect, defined by NBR 6122 (ABNT, 2019) as the process of interaction of the various elements that constitute a foundation by transmitting the loads applied to them to the soil, causes the overlap of the tension bulbs and causes the settlement of the group be, in general, different from the settlement of the isolated element. Velloso & Lopes (2010) define the group effect as the perceived difference in load capacity and settlement measured in a group of piles, connected by a pile block, and in an isolated pile, due to the interaction that occurs through the soil.

In the last decades, several studies, with different methodologies, have been dedicated to the analysis of the group effect between piles connected by the same block

(Poulos & Mattes, 1971; Randolph & Wroth, 1979; Poulos & Davis, 1980; Poulos & Randolph, 1983; Randolph, 1994; Guo & Randolph, 1999; Poulos, 2006; Sheil & McCabe, 2012; Guo, 2013; Randolph & Reul, 2019; among others). However, the analysis of the generalized group effect, that is, the group effect between all pile groups in the building, is generally disregarded. This is due, in general, to the computational effort required for the analysis of the entire foundation. Therefore, numerical analyzes of the group effect on piles are usually restricted to relatively small groups of piles (Randolph, 1994). However, with the development of technology, the use of the finite element method becomes more efficient and makes it possible to solve more complex problems, such as, for instance, the analysis of problems involving stratified subsoil, with a greater number of piles and pile blocks, enabling a more representative analysis of the performance of the entire building and the generalized group effect.

Therefore, the objective of this work is to evaluate, by means of three-dimensional numerical modeling, the soil-structure interaction mechanisms of a building with a monitored continuous flight auger pile foundation in a stratified subsoil, with the presence of an intermediate soft soil layer. Specifically, the group effect between piles connected by the same block and the group effect between all pile groups in the building of an instrumented case study are analysed. The effect of the soft soil layer is also evaluated.

[#]Corresponding author. E-mail address: lorenaleite@pq.uenf.br

¹Universidade Estadual do Norte Fluminense Darcy Ribeiro, Campos dos Goytacazes, RJ, Brasil.

Submitted on December 3, 2022; Final Acceptance on April 4, 2023; Discussion open until August 31, 2023.

<https://doi.org/10.28927/SR.2023.013722>



This is an Open Access article distributed under the terms of the Creative Commons Attribution License, which permits unrestricted use, distribution, and reproduction in any medium, provided the original work is properly cited.

2. Case study

The case study consists of a residential building with 19 floors with reinforced concrete structure and sealing masonry in ceramic material, located in the city of Campos dos Goytacazes-RJ, Brazil. The location of the case study is shown in Figure 1. The building consists of 3 garage floors that occupy the entire area of the terrain and the body of the building with 14 type floors and a penthouse, in addition to the water tank, occupying the central area.

The region where the case study is located is marked by the presence of plains of fluvial-marine origin and Cenozoic sedimentary basins, characterized by sub-horizontal surfaces consisting of well-selected sandy or clayey to clayey deposits, with extremely smooth and convergent gradients towards watercourses (Lazaretti et al., 2017).

The elevated part of the municipality presents soils resulting from the weathering of Pre-Cambrian rocks (gneisses and granites) and Tertiary sediments of the Barreiras Formation (Costa et al., 2008).

The investigation and characterization of the soil profile was performed through 8 standard penetration test (SPT) holes.

The foundation used were monitored continuous flight auger-type deep piles, with diameters of 500 mm, under the main body of the building, and of 400 mm, under the extension of the garage area. The monitored pillars and piles are positioned in the body of the building. All piles are 18m long, armed in the first four meters. Therefore, they are settled in a layer of silty clay with sand, which showed a high N_{SPT} value, with an average N_{60} value of approximately 58 blows.

The piles considered in the numerical model are located under the main body of the building and are divided, according to the loading level, into peripheral, intermediate and central piles.

Figure 2 shows the stakeout project, the location of instrumented piles, the division of piles into peripheral, intermediate and central piles and the location of SPT holes.

The following soil layers were identified in the SPT: yellow silty clay from 3.7 to 6.4 meters deep, clayey sand from 11.3 to 13.7 m, dark gray peaty clay from 11.3 to 13.7 m and impenetrable hard light gray silty clay from 19.5 to 20.5 m, as shown in Figure 3.

The monitoring of the work, since the first stages of construction, was carried out by Waked (2017) and Prellwitz (2016). Waked (2017) monitored the displacement relative to the pillars of 4 piles, using telltales and strain gauges, and Prellwitz (2016) monitored the settlement of all the pillars of the building, using a monitoring system based on the principle of communicating vessels and the data acquisition was done using photogrammetry.



Figure 1. Case study location.

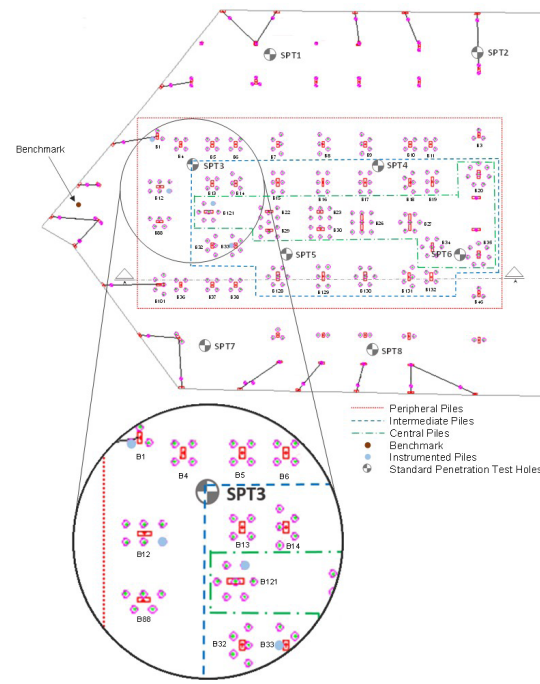


Figure 2. Stakeout project and location of instrumented piles and SPT holes.

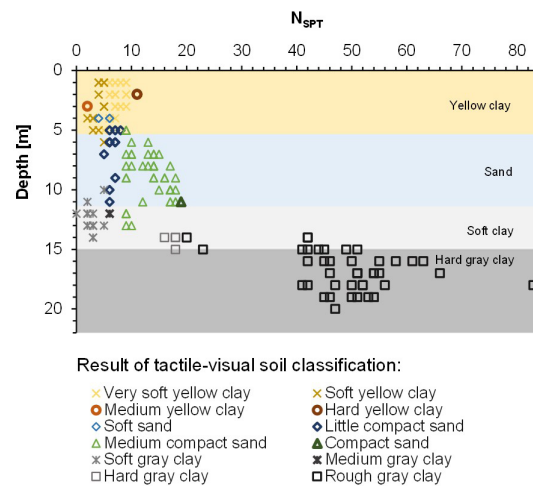


Figure 3. Simplified soil profile and SPT variation.

Table 1. Geometry of the blocks.

Block	Hight (z) [m]	Length (x) [m]	Width (y) [m]
B1	1.2	2.05	1.88
B3	1.2	2.05	1.88
B4	1.2	2.05	2.05
B5	1.2	2.05	2.05
B6	1.2	2.05	2.05
B7	1.2	1.88	3.30
B8	1.2	1.88	3.30
B9	1.2	1.88	3.30
B10	1.2	2.05	2.05
B11	1.2	2.05	2.05
B12	1.2	3.30	2.05
B13	1.2	2.05	2.05
B14	1.2	1.88	3.30
B15	1.2	2.05	3.30
B16	1.2	2.05	3.30
B17	1.2	2.05	3.30
B18	1.2	1.88	3.30
B19	1.2	2.05	3.30
B20	1.2	3.05	3.54
B22/29	1.2	3.30	4.55
B23/30	1.2	2.97	4.55
B26	1.2	3.30	3.30
B27	1.2	3.30	2.97
B32	1.2	1.88	3.30
B33	1.2	1.88	3.30
B34	1.2	3.30	2.97
B35	1.2	3.05	3.54
B36	1.2	2.05	2.05
B37	1.2	2.05	2.05
B38	1.2	2.05	2.05
B46	1.2	2.05	1.88
B88	1.2	3.30	1.88
B101	1.2	1.88	3.30
B121	1.2	3.30	2.97
B128	1.2	3.30	2.97
B129	1.2	2.05	3.30
B130	1.2	3.30	2.97
B131	1.2	1.88	3.30
B132	1.2	2.05	2.05

3. Numerical modeling

The analysis of the soil-structure interaction of the case study was carried out from three-dimensional numerical modeling using a software based on the finite element method (FEM), Plaxis 3D.

The piles used in the model are 0.5 m in diameter and 18 m long. The dimensions of the blocks are shown in Table 1.

The soil parameters were validated from parametric retroanalysis in a three-dimensional model based on correlations with the N_{SPT} obtained at the site and based on parameter values suggested by authors such as Décourt (1995), Marangon (2018), Ortigão (2007), Godoy (1972) & Bowles (1997). The validation of soil layer parameters is presented in Leite (2021). The parameters used in numerical modeling are presented in Table 2.

The numerical model developed is presented in Figure 4. The finite element mesh is formed by tetrahedral elements of 10 nodes and has a medium degree of refinement. The number of soil elements is 80,610, and the number of nodes is 119,303.

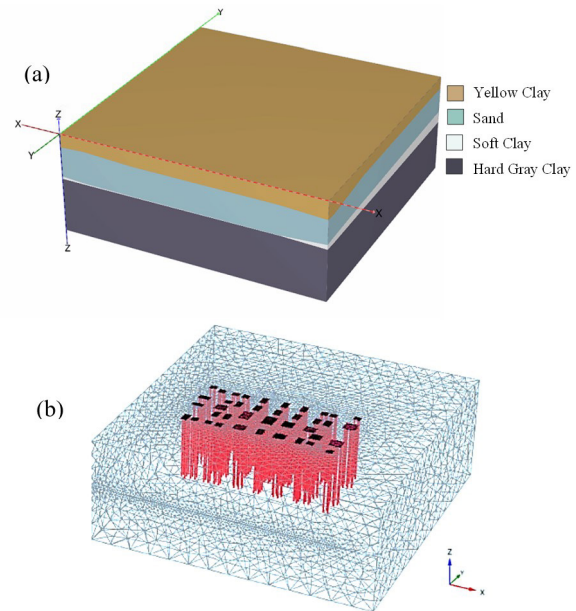


Figure 4. Numerical model (a) of the subsoil and (b) of piles and blocks.

Table 2. Parameters of piles, blocks and soil layers.

	Constitutive model	$\gamma^{(a)}$ [kN/m ³]	$E^{(b)}$ [GPa]	$\nu^{(c)}$	$R_t \max^{(d)}$ [kN]	$R_{lat} \max^{(e)}$ [kN]	$c^{(f)}$ [kPa]	$w^{(g)}$ [m/dia]
Pile	LE	20.7	14.8	0.11	800	1.400	-	-
Block	LE	20.7	148	0.11	-	-	-	-
Yellow clay	LE	17.0	0.023	0.30	-	-	-	0.01
Sand	LE	20.0	0.048	0.40	-	-	-	1.00
Soft gray clay	MC	13.0	0.010	0.40	-	-	25	0.01
Hard gray clay	LE	20.0	0.138	0.40	-	-	-	0.01

^(a)Specific weight obtained for pile and block from Maia et al. (2019) and for soil layer from Godoy (1972). ^(b)Modulus of elasticity obtained for pile and block from Maia et al. (2019) and for soil layers from Décourt correlations (Décourt, 1995). ^(c)Poisson coefficient values obtained for pile and block from Maia et al. (2019) and for soil layers as suggested by Marangon (2018). ^(d)Maximum tip resistance achieved by Waked (2017). ^(e)Maximum lateral resistance achieved by Waked (2017). ^(f)Cohesion value, as suggested by Marangon (2018). ^(g)Permeability values suggested by Ortigão (2007).

Sensitivity analyses showed that there was no significant change in the settlement values obtained in the models with the change in the degree of mesh refinement.

The water level was considered with the average depth identified in the soundings, 3.5 m. Therefore, the soil above this depth was configured as dry.

The adopted boundary conditions consider the deformations of the massif normally fixed horizontally (X_{min} , X_{max} , Y_{min} and Y_{max}), fully fixed at Z_{min} and free at Z_{max} and the groundwater flow closed at Z_{min} and open in the other directions.

The constitutive model used to represent the elements of piles and blocks was the Linear Elastic (LE), for the soft clay layer the linear elastic perfectly plastic model, called Mohr Coulomb model (MC), was used, the LE model was used for the other soil layers.

The modeling was carried out in several stages, in order to evaluate the effect of the interaction between pile groups. Initially, a model with an isolated pile was simulated, followed by a model with an isolated pile group, connected by the same pile block, the next stages included pile groups located at a radius n times the largest dimension (B) of the block considered initially. This evaluation process, increasing the simulated radius in the numerical model, was performed 9 times, 3 starting with peripheral blocks (B1, B6, B12), 3 with intermediate blocks (B15, B33, B129) and 3 with central blocks (B20, B23/30, B27). The location of these blocks is illustrated in Figure 5a. The division of blocks according to the distance to the center of block B129 is shown in Figure 5b.

Figure 6 shows the configuration sequence of the calculated models for the case in which the analysis started with block B129.

All numerical models were configured with and without the soft soil layer, for the analysis of the influence of this layer on the group effect. The soft clay layer was replaced by the layer of greater resistance, hard gray clay, in the models without soft soil.

Only four constructive steps were considered, in order to reduce computational effort and calculation time. The steps adopted are equivalent to approximately 25%, 50%, 75% and 100% of the load calculated for the columns. It is noteworthy that 100% of the loading of each column corresponds to the last constructive stage simulated by Prellwitz (2016), that is, the end of the execution of the sealing masonry.

4. Results and analysis

The results of the numerical simulation, showing the vertical displacements of the soil, with settlement isocurves, of the models with the isolated pile B129c, with the isolated pile group B129 and with the pile groups located at a distance of $2B$, $3B$, $4B$, $5B$, $6B$, $7B$, $8B$ and $9B$ of the initially analyzed block is shown in Figure 6. The AA cut, shown in Figure 7, passes through the center of the isolated pile E129c. The location of the AA cut in the plan is identified in Figure 2.

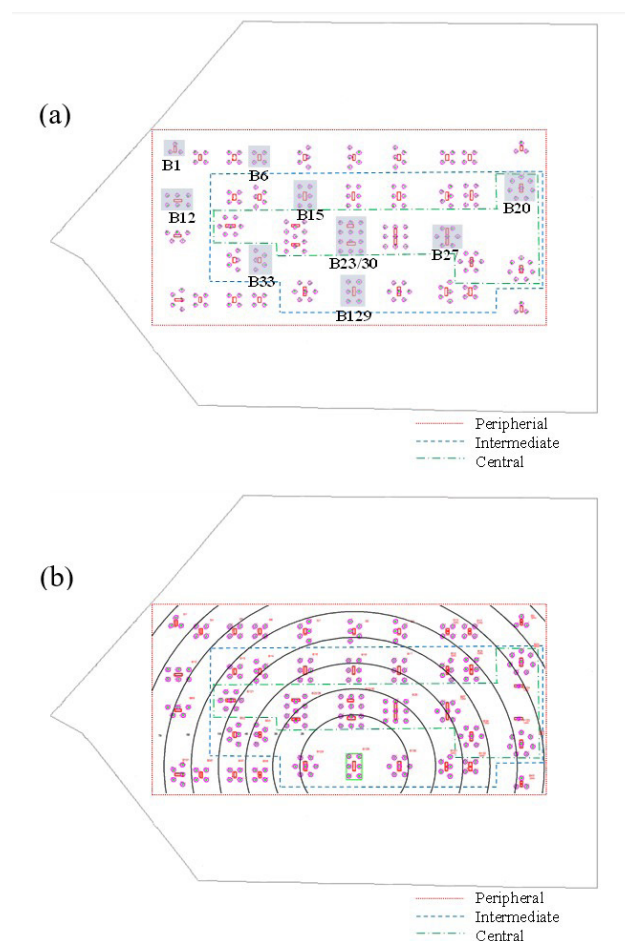


Figure 5. Foundation plan with (a) location of the analyzed blocks and (b) division of the blocks according to the distance to the center of B129.

These results were obtained from models of subsoil with soft soil layer. Figure 8 shows the results of the same test sequence, however, without the soft soil layer.

The comparison between the models with and without soft soil shows the difference in the behavior of the subsoil caused by the soft gray clay layer. In the models with soft soil, there is a change in the vertical displacement pattern of the soil in the depth of the soft gray clay layer, where there is an increase in the volume of displaced soil, presenting a sudden reduction of the displaced soil in the depth of the hard clay layer, located just below the soft clay layer. Furthermore, the level of settlement in numerical models with soft soil was higher than in models without soft soil.

The results show the significant group effect on the displacements, evidencing the increase in the settlement due to the overlapping of the tension bulbs of sided-placed piles and pile groups. It was observed that this effect occurs for blocks located up to an average radius of five times the largest dimension of the block, becoming relatively unimportant for greater distances. This effect can be observed in Figure 9,

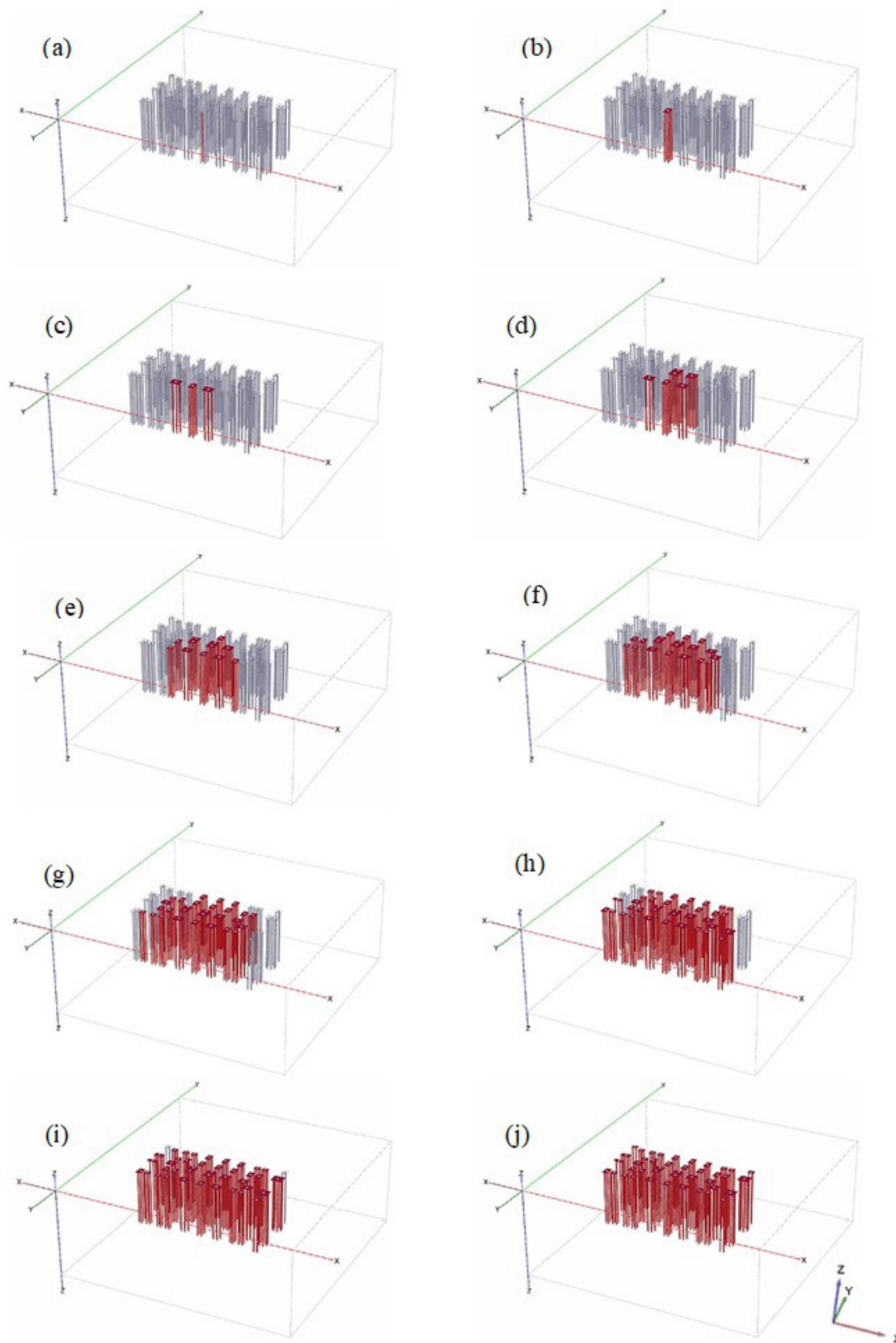


Figure 6. Sequence of numerical models starting with (a) pile E129c, (b) block B129, and blocks located at a distance of (c) 2B, (d) 3B, (e) 4B, (f) 5B, (g) 6B, (h) 7B, (i) 8B and (j) 9B.

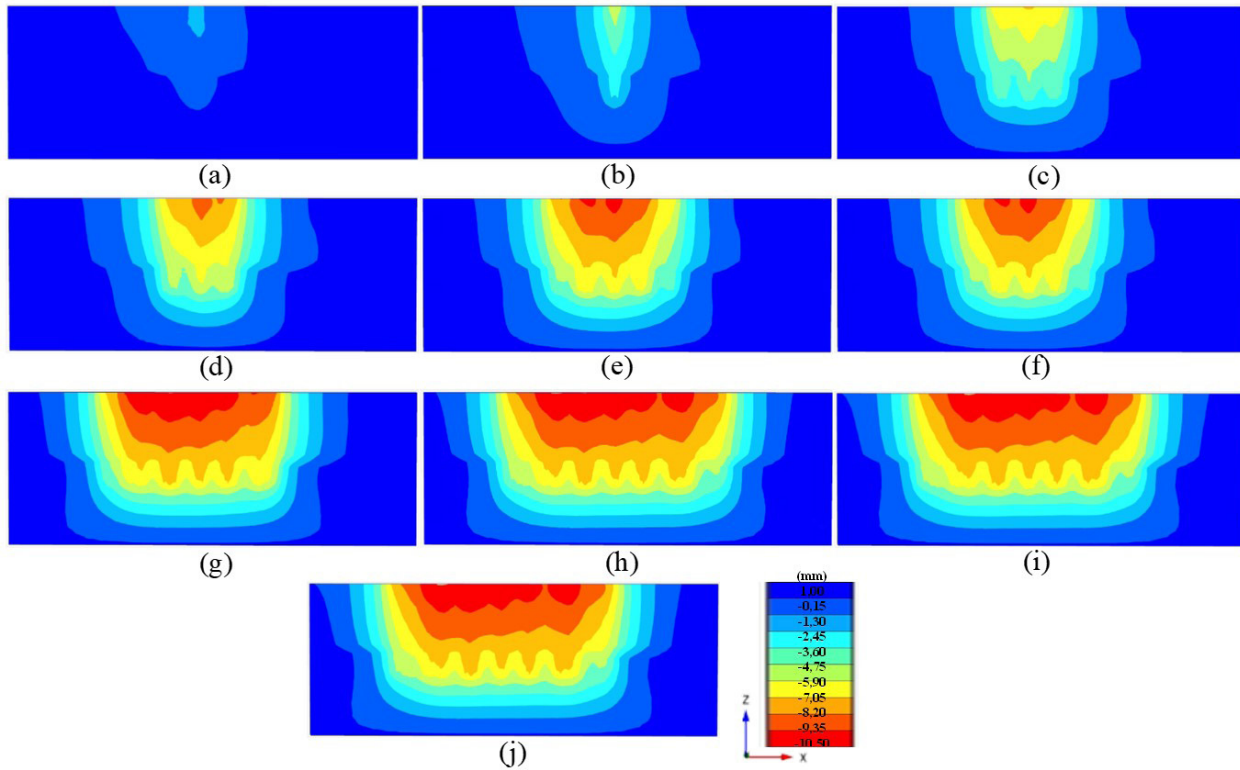


Figure 7. AA cut through the XZ plane showing vertical displacements of the soil in models with soft soil with (a) E129c, (b) B129, and pile groups located at a distance of (c) 2B, (d) 3B, (e) 4B, (f) 5B, (g) 6B, (h) 7B, (i) 8B, and (j) 9B.

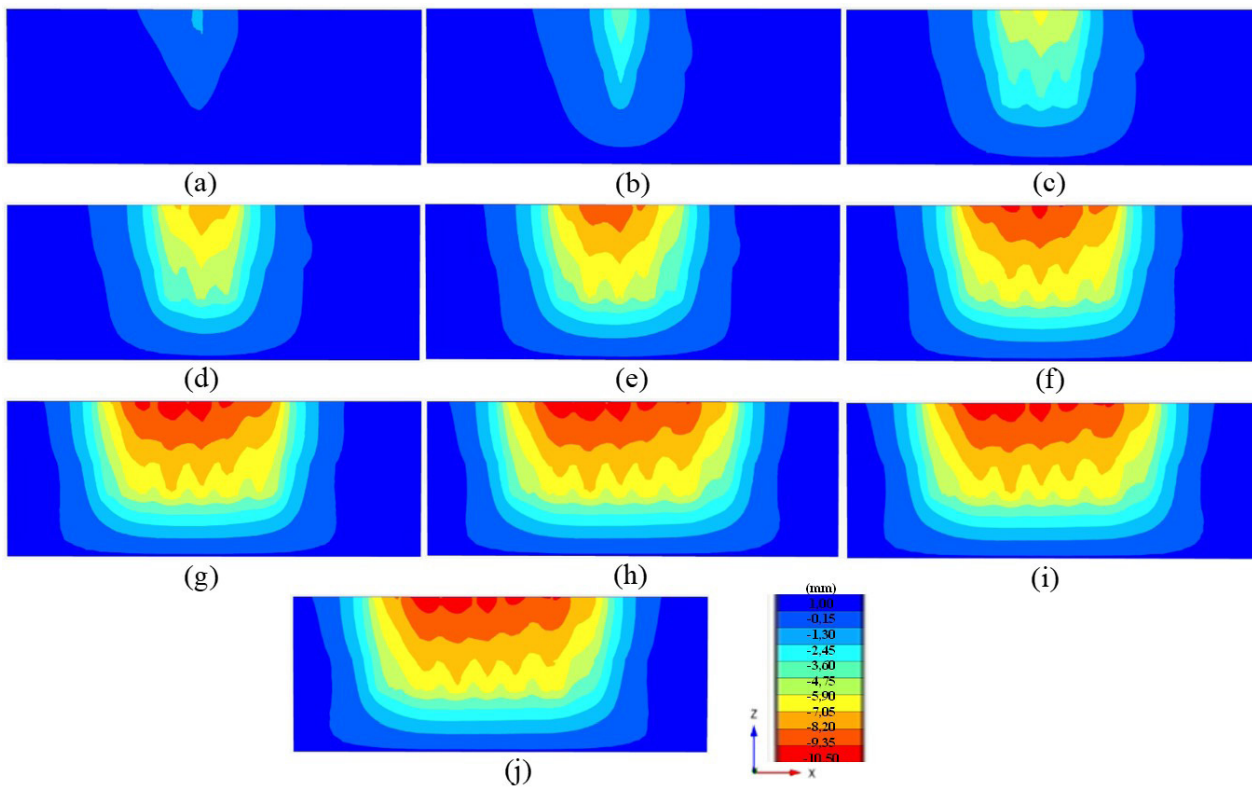


Figure 8. AA cut through the XZ plane showing vertical displacements of the soil in models without soft soil with (a) E129c, (b) B129, and pile groups located at a distance of (c) 2B, (d) 3B, (e) 4B, (f) 5B, (g) 6B, (h) 7B, (i) 8B, and (j) 9B.

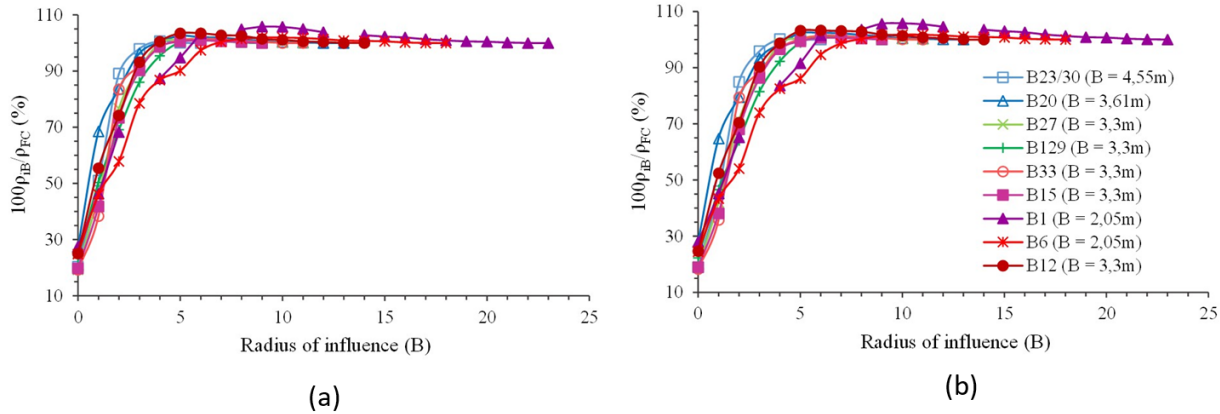


Figure 9. Settlement percentage versus radius of influence curves of models (a) with soft soil layer and (b) without soft soil layer.

which presents the curves of the relationship between the radius of influence (B) and the ratio of the block settlement in the model with a certain radius of influence and the block settlement in the model with the complete foundation, with all the foundation elements (ρ_{IB}/ρ_{OC}). There was no significant effect of the presence of soft soil layers in the analysis of the group effect between pile groups.

Several authors analyze the necessary spacing to eliminate the group effect between piles. Pressley & Poulos (1986) point out that for a group of piles loaded vertically, the spacing of 8 times the diameter (D) of the pile results in a failure mechanism characteristic of a single-pile, that is, without group effect. CGS (1992), in a foundation engineering manual, also analyzes the effect of pile spacing and states that, generally, group interaction doesn't need to be considered when pile spacing is greater than $8D$. Khari et al. (2013) observed that, for a ratio of S/D greater than 6, the interaction between piles and the group effects are eliminated, considering groups of laterally loaded piles installed in sand. Patrocínio (2018) observed that piles work separately in a group with a ratio S/D equal to 5. Souri et al. (2020) observed, for piles installed in clay soil, that the group effect on lateral load capacity could be neglected for spacings greater than $5D$. However, none of these studies analyze the group effect between pile groups.

However, it is noticed that the radius of influence of the group effect between pile groups is of the same order as the radius of influence observed for the group effect between piles of the same pile group. Therefore, it is understood that it is possible to compare the group effect between pile groups to the group effect between piles of the same block. It is understood, therefore, that the pile group behave similarly to the isolated piles, influencing the sided-placed pile groups by overlapping the tension bulbs, causing an increase in the settlement of the adjacent blocks.

It should be noted that the settlement observed in each block in the model simulating the complete foundation was up

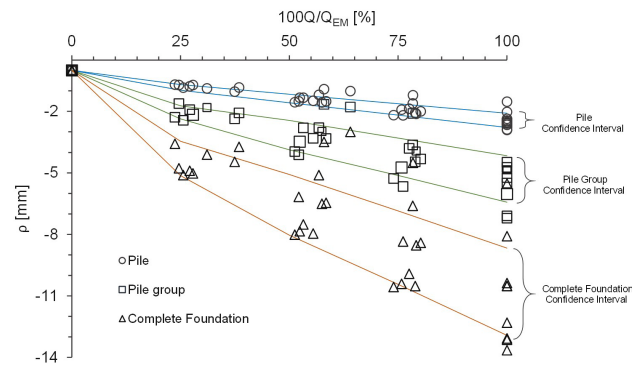


Figure 10. Load-settlement curves of isolated piles, isolated pile groups and the complete foundation.

to approximately 5 times greater than the settlement obtained in the models with isolated piles and up to approximately 3 times greater than the settlement obtained in the models with isolated piles.

The group factor (G), according to the equation presented by Almeida et al. (2019) and Santos et al. (2019), defined by the relationship between the settlement of the group of piles and the settlement of the isolated pile, was up to approximately 3. That is, the effect of overlapping the stress bulbs of neighboring piles generated a settlement up to approximately 3 times greater in the pile groups compared to the settlement of isolated piles, showing the influence of the group effect on the settlements.

Figure 10 shows the relationship between settlement (ρ) and the percentage ratio between the load in a given construction phase (Q) and the estimated load at the end of monitoring (Q_{EM}) obtained in numerical models with isolated piles, isolated blocks and with the complete foundation. The intervals, with 95% confidence, of the load-settlement curves refer to the values obtained in 9 blocks of the models, namely: 3 peripheral (B1, B6, B12), 3 intermediate (B15, B33, B129) and 3 central (B20, B23/30, B27).

5. Conclusion

The group effect between piles and pile groups was analyzed in this research from three-dimensional numerical modeling, using software based on the Finite Element Method. It has been shown that the group effect between pile groups is significant on building behavior. It was observed in numerical models that the group effect between pile groups is similar to the group effect between piles of the same group. This, due to the influence on neighboring pile groups, by overlapping the tension bulbs, resulting in an increase in the settlement of adjacent piles and pile groups. However, this proved to be negligible for pile groups located at a distance greater than 5 times the largest block dimension.

The generalized group effect, in the model with the complete foundation, increased the settlement by up to 3 times, in relation to the settlement of the isolated pile group, and up to 5 times, in relation to the settlement of the isolated pile.

The presence of the soft soil layer generated the vertical displacement of a larger volume of soil and caused higher levels of settlement, however, it did not present a significant influence on the group effect between pile groups.

Acknowledgements

This research was funded by CAPES – Coordination for the Improvement of Higher Education Personnel. The authors would like to thank the researchers who provided the data referring to the work analyzed, M.Sc Lucas Waked and Ph.D. Marta Prellwitz and the researchers who collaborated with the development of this research, M.Sc. Géssica Marquezini and M.Sc Nathani Zampirolli.

Declaration of interest

The authors have no conflicts of interest to declare. All co-authors have observed and affirmed the contents of the paper and there is no financial interest to report.

Authors' contributions

Lorena da Silva Leite: conceptualization, data curation, formal analysis, investigation, methodology, validation, visualization, writing – original draft. Paulo César de Almeida Maia: conceptualization, data curation, supervision, validation, writing – review and editing. Aldo Durand Farfán: supervision, validation, writing – review and editing.

Data availability

The datasets generated analyzed in the course of the current study are available from the corresponding author upon request.

List of symbols

c	cohesion value
B	largest dimension of the pile block
D	pile diameter
E	modulus of elasticity
Q	load in a given construction phase
Q_{EM}	load at the end of monitoring
R_{lat}	maximum lateral resistance
R_t	maximum tip resistance
S	center-to-center space between piles
w	permeability value
γ	specific weight
ν	Poisson coefficient
\mathcal{P}	settlement
\mathcal{P}_{tb}	settlement of the block in a numerical model with a certain radius of influence
\mathcal{P}_{FC}	settlement of the block in a numerical model with the complete foundation

References

- ABNT NBR 6122. (2019). *Projeto e execução de fundações*. ABNT - Associação Brasileira de Normas Técnicas, Rio de Janeiro, RJ (in Portuguese).
- Almeida, A.K.L., Oliveira, P.E.S., Gusmão, A.D., & Maia, G.B. (June 4-6, 2019). Análise do efeito de grupo em fundações profundas através do comparativo da prova de carga estática com a medição de recalques de edifícios em Recife/PE e Salvador/BA. In Associação Brasileira de Empresas de Engenharia de Fundações e Geotecnia (Org.), *9º Seminário de Engenharia de Fundações Especiais e Geotecnia/3ª Feira da Indústria de Fundações e Geotecnia* (pp. 1-10). São Paulo, Brazil: ABEF (in Portuguese).
- Bowles, J.E. (1997). *Foundation analysis and design* (5th ed.). The McGraw-Hill Companies.
- Canadian Geotechnical Society – CGS. (1992). *Canadian foundation engineering manual* (3rd ed.). Canadian Geotechnical Society.
- Costa, A.N., Polivanov, H., & Alves, M.G. (2008). Mapeamento geológico-geotécnico preliminar, utilizando geoprocessamento, no município de Campos dos Goytacazes. *Anuário do Instituto de Geociências*, 31(1), 50-64 (in Portuguese).
- Décourt, L. (October 28, 1995). Prediction of load-settlement relationships for foundations on the basis of the SPT-T. In W. Van Impe & M. Madhav (Eds.), *Ciclo de Conferencias Internacionales Leonardo Zeevaert* (pp. 85-104). Mexico City, Mexico: Universidad Nacional Autónoma de México.
- Godoy, N.S. (1972). *Fundações. Notas de aula: curso de graduação*. Escola de Engenharia de São Carlos/ Universidade de São Paulo (in Portuguese).
- Guo, W.D. (2013). *Theory and practice of pile foundations*. CRC Press.

- Guo, W.D., & Randolph, M.F. (1999). An efficient approach for settlement prediction of pile groups. *Geotechnique*, 49(2), 161-179.
- Khari, M., Kassim, K.A., & Adnan, A. (2013). An experimental study on pile spacing effects under lateral loading in sand. *The Scientific World Journal*, 2013, 734292.
- Lazaretti, A.F., Pinho, D., Dantas, M.E., & Pôssa, J.T. (2017). *Carta geomorfológica: município de Campos dos Goytacazes*. CPRM (in Portuguese).
- Leite, L.S. (2021). *Análise numérica tridimensional do efeito de grupo entre estacas e entre blocos em fundação do tipo hélice contínua monitorada em maciço com presença de solo mole* [Master's dissertation]. Universidade Estadual do Norte Fluminense Darcy Ribeiro (in Portuguese).
- Maia, P.C., Waked, L.V., & Prellwitz, M.F. (2019). Estimativa do módulo de elasticidade do concreto de estacas hélice contínua. *Geotecnia*, 147, 27-40 (in Portuguese).
- Marangon, M. (2018). *Geotecnia de fundações*. Departamento de Transporte e Geotecnia/Universidade Federal de Juiz de Fora.
- Ortigão, J.A. (2007). *Introdução à mecânica dos solos dos estados críticos* (3rd ed.). Terratek.
- Patrocínio, G.M. (2018). *Análise paramétrica de grupos de estacas helicoidais à tração* [Undergraduate thesis]. Universidade Federal do Rio Grande do Norte (in Portuguese).
- Poulos, H.G. (2006). Pile group settlement estimation - research to practice. In R.L. Parsons, L. Zhang, W.D. Guo, K.K. Phoon & M. Yang (Eds.), *Foundation analysis and design: innovative methods* (pp.1-22). American Society of Civil Engineers.
- Poulos, H.G., & Davis, E.H. (1980). *Pile foundation analysis and design*. Wiley.
- Poulos, H.G., & Mattes, N.S. (1971). Settlement and load distribution analysis of pile groups. In Institution of Engineers (Org.), *Golden jubilee of the International Society for Soil Mechanics and Foundation Engineering: commemorative volume* (pp. 18-28). Institution of Engineers.
- Poulos, H.G., & Randolph, M.F. (1983). Pile group analysis: a study of two methods. *Journal of Geotechnical Engineering*, 109(3), 355-372.
- Prellwitz, M.F. (2016). *Aplicação de monitoramento de recalque para estimativa de parâmetro de interação solo-estrutura* [Unpublished doctoral thesis]. Universidade Estadual do Norte Fluminense Darcy Ribeiro (in Portuguese).
- Pressley, J.S., & Poulos, H.G. (1986). Finite element analysis of mechanisms of pile group behaviour. *International Journal for Numerical and Analytical Methods in Geomechanics*, 10, 212-221.
- Randolph, M.F. (January 5-10, 1994). Design methods for pile groups and piled rafts. In International Society for Soil Mechanics and Geotechnical Engineering (Org.), *13th International Conference on Soil Mechanics and Foundation Engineering* (pp. 61-82). London, United Kingdom: ISSMGE.
- Randolph, M.F., & Reul, O. (May 23-24, 2019). Practical approaches for design of pile groups and piled rafts. In INCOTEC S.A., Society of Engineers of Bolivia & Bolivian Society of Soil Mechanics and Geotechnical Engineering (Orgs.), *4th Bolivian International Conference on Deep Foundations* (pp. 1-27). Santa Cruz, Bolivia: ISSMGE.
- Randolph, M.F., & Wroth, C.P. (1979). An analysis of the vertical deformation of pile groups. *Geotechnique*, 29(4), 423-439.
- Santos, D.S., Gusmão, A.D., Bezerra, R.S., Burgos, R., Ferreira, S., & Maia, G.B. (June 4-6, 2019). Análise da curva carga-recalque de um edifício residencial em estacas hélice contínua da cidade do Recife. In Associação Brasileira de Empresas de Engenharia de Fundações e Geotecnia (Org.), *9º Seminário de Engenharia de Fundações Especiais e Geotecnia/3ª Feira da Indústria de Fundações e Geotecnia* (pp. 1-9). São Paulo, Brazil: ABEF (in Portuguese).
- Sheil, B., & McCabe, B.A. (June 28-30, 2012). Predictions of friction pile group response using embedded piles in PLAXIS. In Turkish National Committee of Soil Mechanics Geotechnical Engineering & Near East University (Orgs.), *Third International Conference on New Developments in Soil Mechanics and Geotechnical Engineering* (pp. 1-5). Nicosia, North Cyprus: Near East University.
- Souri, A., Abu-Farsakh, M.Y., & Voyiadjis, G.Z. (2020). Evaluating the effect of pile spacing and configuration on the lateral resistance of pile groups. *Marine Georesources and Geotechnology*, 39(2), 150-162.
- Velloso, D. A., & Lopes, F. R. (2010). *Fundações: critérios de projeto, investigação do subsolo, fundações superficiais, fundações profundas*. Oficina de Texto (in Portuguese).
- Waked, L.V. (2017). *Transferência de carga de estacas hélice contínua monitorada em maciço sedimentar durante a construção de um edifício* [Master's dissertation]. Universidade Estadual do Norte Fluminense Darcy Ribeiro (in Portuguese).

Fiber reinforcement effectiveness in two different sand specimens

Murilo Pereira da Silva Conceição¹ , Camilla Maria Torres Pinto¹ ,

Miriam de Fátima Carvalho¹ , Sandro Lemos Machado^{1#} 

Article

Keywords

FRS
Fiber-reinforced soils
Dilatancy
Grain size curve

Abstract

Fiber Reinforced Soils (FRS) are mixtures of discrete fibers with the soil to create a composite with improved mechanical properties compared to unreinforced material that depends on several soil and fiber properties. Therefore, comparative studies are needed to better understand their influence on FRS mechanical response. This paper analyzes the results of a comprehensive triaxial testing program performed on specimens of two different sands at the same relative density focusing on how the grain size distribution affects the composite behavior in terms of shear strength and dilatancy. It is shown that the grain size curve's uniformity coefficient (C_u) is one of the critical variables controlling FRS's dilatancy. Dune sand specimens ($C_u = 1.79$) presented dilatancy even for confining stresses as high as 300 kPa. The shear gains due to reinforcement were controlled by fiber length (L) and percentage (P_f), and size and shape of soil particles. River sand specimens with $L = 51$ mm and 1% fiber addition (dry mass) presented increments of 47.7 kPa in soil cohesion and a 5.2° increase in the soil friction angle compared to unreinforced material.

1. Introduction

The use of fiber Reinforced Soils (FRS) dates from ancient times. Vegetable fibers of jute and bamboo, among other species, were and are still used. However, Vidal (1966) conceived a soil reinforcement method using metallic strips recognized as the debut of the FRS modern use. FRS are mixtures of discrete fibers or strips with the soil to create a composite with improved mechanical properties compared to unreinforced material. The emergence of plastics offered newly manufactured durable fibers and reinforcement geosynthetics, such as geogrids, as an option to substitute metallic strips. FRS use can improve the mechanical behavior of soil in different applications, such as composing landfill cover layers, where their use could prevent superficial cracking due to wetting/drying cycles and differential waste mass settlements, which can lead to greenhouse gases emissions, embankments, earth dams, and other earthworks (Daniel & Benson, 1990; Daniel & Wu, 1993; Broderick & Daniel, 1990; Shackelford, 2014; Damasceno et al., 2019; Zhang et al., 2022).

Fiber length or aspect ratio (the relationship between the fiber length and its diameter/width), stiffness, fiber content, soil friction angle, and the coupled effects that occur in the soil grain/fiber interfaces are among the main parameters affecting the FRS mechanical behavior (Maher & Gray, 1990;

Gao & Zhao, 2013; Michalowski, 2008; Li et al., 2020). Fiber orientation is also a critical factor interfering with the mechanical behavior of fiber-reinforced soils. Wang et al. (2017) present results of several triaxial tests with jute fibers disposed at different orientations. It is shown that vertical fibers had a negligible effect on composite shear strength. Horizontal fibers are most beneficial to the increase of peak deviator stress, with randomly oriented fibers also producing encouraging results. However, the laboratory moist tamping technique has presented a growing interest when using compacted specimens. This technique offers good control of specimen density, prevents fiber segregation, and produces a soil-fiber fabric that resembles that of FRS compacted in the field, although leading to the sub-horizontal orientation of fibers (Diambra et al., 2010).

Besides the early cited characteristics of fibers, some soil properties also play a paramount role in the overall FRS performance. Considering the universe of nonplastic coarse soils, the density index (I_d) is recognized as the main parameter controlling the mechanical behavior of coarse soils. Variations in friction angle between 6-10° are observed when coarse soils pass from a loose to a dense state (Leonards, 1962; Briaud, 2013). Furthermore, the grain size curve (GSC) parameters such as the coefficient of uniformity, typical grain size, and the roughness and shape of grains are also crucial variables that help understand solid/fiber interactions better.

#Corresponding author. E-mail address: smachado@ufba.br

¹Universidade Federal da Bahia, Departamento de Ciência e Tecnologia dos Materiais, Salvador, BA, Brasil.

Submitted on November 27, 2022; Final Acceptance on March 19, 2023; Discussion open until August 31, 2023.

<https://doi.org/10.28927/SR.2023.012422>



This is an Open Access article distributed under the terms of the Creative Commons Attribution License, which permits unrestricted use, distribution, and reproduction in any medium, provided the original work is properly cited.

The benefits associated with fiber reinforcement include but are not restricted to shear strength gains, higher ductility, smaller post-peak strength losses, and minored cracks appearance and propagation (Gray & Ohashi, 1983; Loehr et al., 2005; Choobbasti et al., 2019; Mandolini et al., 2019; Gao et al., 2020). Furthermore, fiber reinforcement is reported to increase the liquefaction and post-liquefaction shear strength of sand (Jain et al., 2023; Rasouli & Fatahi, 2022).

In this paper, compacted specimens from two different sands were submitted to a comprehensive triaxial testing program to evaluate the effects of fiber length, grain size curve parameters, and size, roughness, and shape of solid particles on the reinforcement effectiveness, measured in terms of the observed increments in the shear strength parameters, and FRS dilatancy.

2. Materials and methods

Table 1 summarizes the main characteristics of the employed sand, which were determined following the Brazilian standards ABNT NBR 6458 (ABNT, 2016a), ABNT NBR

7181 (ABNT, 2016b), ABNT NBR 12004 (ABNT, 1990), and ABNT NBR 12051 (ABNT, 1991). d_{xx} is the sieve equivalent diameter for a given percentage of the particles passing. C_c is the GSC curvature coefficient, and e_{max} and e_{min} are the maximum and minimum void ratios, respectively. G_s is the specific gravity of particles and ϕ_{pk} and ϕ_{ls} are the unreinforced soil friction angles for peak and large strain condition, respectively (approximating the friction angle at critical state conditions). As observed, dune sand presents a more uniform grain size curve and smaller particles. Additional details are provided in Conceição (2021) and Pinto (2021).

Figure 1 illustrates the visual aspect of the river and dune solid particles. The larger size and less uniformity of the river sand grains than dune sand are easily noted, besides the subangular aspect of their particles.

FRS specimens used polypropylene fibers with lengths (L) of 12.5 mm, 25 mm, and 51 mm. As common properties, according to the manufacturer Viapol™, fiber diameter of $D = 0.51$ mm, specific gravity of $G_{sf} = 0.91$, fiber stiffness modulus of $E_f = 5.0$ GPa, and tensile strength of 500 MPa are cited. The adopted fiber contents (P_f , dry mass) were 0.5% and 1%. The experimental program considered fibers as part of the solid particles, calculating the composite's G_s value for each P_f . Figure 2 illustrates the visual aspect of the employed fibers. The specimen molding procedure used the moist tamping technique (Diambra et al., 2010).

Figure 3 illustrates the molding preparation steps. A vacuum pump provided an internal air pressure of about -15 kPa to preserve specimen integrity after mold removal. After molding, the specimen underwent vertical upward water flow until the permeability coefficient (k) stabilized. k values served as an indication of the molding process quality since small variations in molding conditions (especially in the void ratio) have a noticeable impact on k .

The experimental program used specimens with the same I_D (60%). Triaxial tests adopted the back pressure technique (Skempton's B parameter, $B > 0.95$) to saturate the specimens, which were then hydrostatically consolidated and

Table 1. Main characteristics of the employed sand.

Parameter	River sand	Dune sand
Particles' shape	Subangular	Rounded
d_{10} (mm)	0.43	0.176
d_{30} (mm)	0.59	0.25
d_{50} (mm)	0.83	0.29
d_{60} (mm)	0.96	0.315
C_u	2.24	1.79
C_c	0.84	1.13
G_s	2.65	2.657
e_{max}	0.79	0.748
e_{min}	0.52	0.523
ϕ_{pk} (°)	36.5	33.6
ϕ_{ls} (°)	32.8	30.5

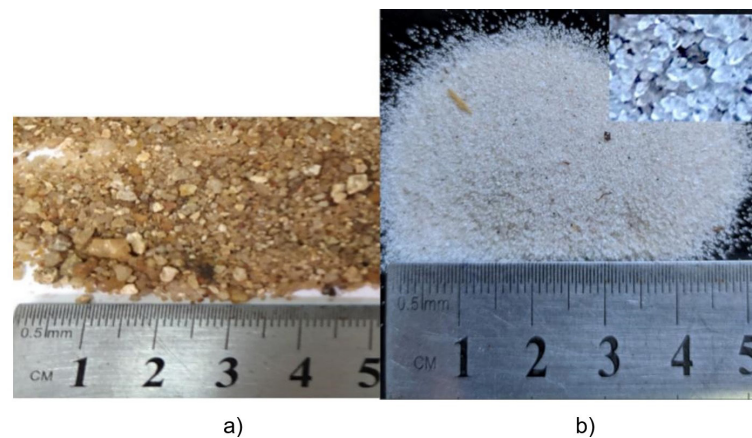


Figure 1. Visual aspect of a) river sand and b) dune sand particles.

sheared under drained conditions (CD tests, Head & Epps, 2014). Tests imposed a displacement rate of 0.67 mm/min, and initial effective confining stresses of 50 kPa, 100 kPa,

200 kPa, and 300 kPa. Axial force, displacement, and volume changes were measured externally to the chamber. All the tests were performed in duplicate. Additional details can be found in Conceição (2021) and Pinto (2021).

3. Results and analysis

Figures 4 and 5 illustrate some triaxial tests results in terms of deviator stress and volumetric strain curves for the performed tests. The presented results refer to tests performed with $P_f = 0.5\%$ and 1% , and confining stresses (σ_c) of 50 and 200 kPa. The results are coherent with many authors who cite the increase in composite cohesion, friction angle, and ductility, as well as the decrease in the after-peak shear strength reduction as fiber reinforcement effects (Ranjan et al., 1994; Diambra et al., 2010; Diambra et al., 2013; Gao & Diambra, 2021; Feuerharmel, 2000; Santiago, 2011; Michalowski & Čermák, 2003; Choobbasti et al., 2019; Li et al., 2020).

The fiber-reinforced sand specimens increased their shear strength with both fiber length and percentage, as reported by many other authors (Choobbasti et al., 2019; Li et al., 2020; Jishnu et al., 2020). Comparing pure soil and reinforced specimens with $P_f = 1\%$ and $L = 51$ mm, the composite shear strengths are approximately double that obtained for pure soil (see Figure 5). The cohesion was the most sensitive shear strength parameter to the fiber reinforcement, reaching values as high as 47.7 kPa for river sand specimens (see Table 2, $P_f = 1\%$ and $L = 51$ mm). For both sand, the fiber length was more effective in reinforcement than the fiber content since samples with $P_f = 0.5\%$ and $L = 25$ mm showed better resistance results than samples with $P_f = 1\%$ and $L = 12.5$ mm (Table 2). The observed behavior is the opposite of that reported by Fang et al. (2020), indicating that fiber-reinforcement effectiveness is dependent not only on P_f and L , but on a combination of fiber and soil characteristics.

Comparing the shear strength results of the two different sand composites, as expected, river sand specimens always presented higher peak and residual shear strength values. This results from its large and subangular particles and the less uniform grain size curve than dune sand.

As expected, specimens dilated more for lower confining stresses. However, dune sand specimens presented a dilation of about 2% even in the tests performed with $\sigma_c = 200$ kPa and higher, contrary to the river sand specimens. Different authors have reported a contradictory influence of fibers on composite dilation (Aguilar, 2015; Diambra et al., 2013; Festugato, 2008; Michalowski & Čermák, 2003; Rasouli & Fatahi, 2022).

Table 2 summarizes the shear strength parameters obtained considering all performed tests. For all the specimens, the failure criterion adopted was the maximum deviator stress. This corresponded to the peak stress in most cases, but in the cases of $P_f = 1\%$ and $L = 51$ mm specimens, the maximum strength occurred at 20% of axial deformation. As observed, the dune sand friction angle varied from 33.6°



Figure 2. Visual aspects of employed reinforcement.



(a)



b)

Figure 3. a) end of the molding process and b) specimen aspect after mold removal (about -15 kPa air pressure applied by vacuum pump).

Fiber reinforcement effectiveness in two different sand specimens

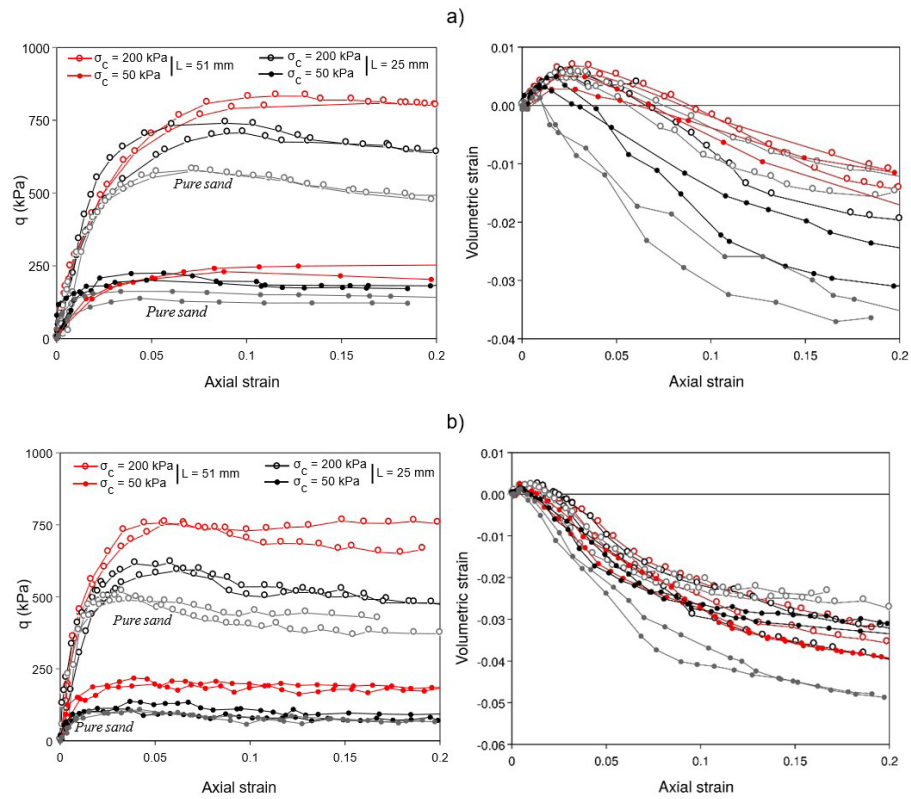


Figure 4. Deviator stress and volumetric strains versus axial strain curves. $P_f = 0.5\%$, $\sigma_c = 50$ kPa and 200 kPa. a) river sand and b) dune sand specimens.

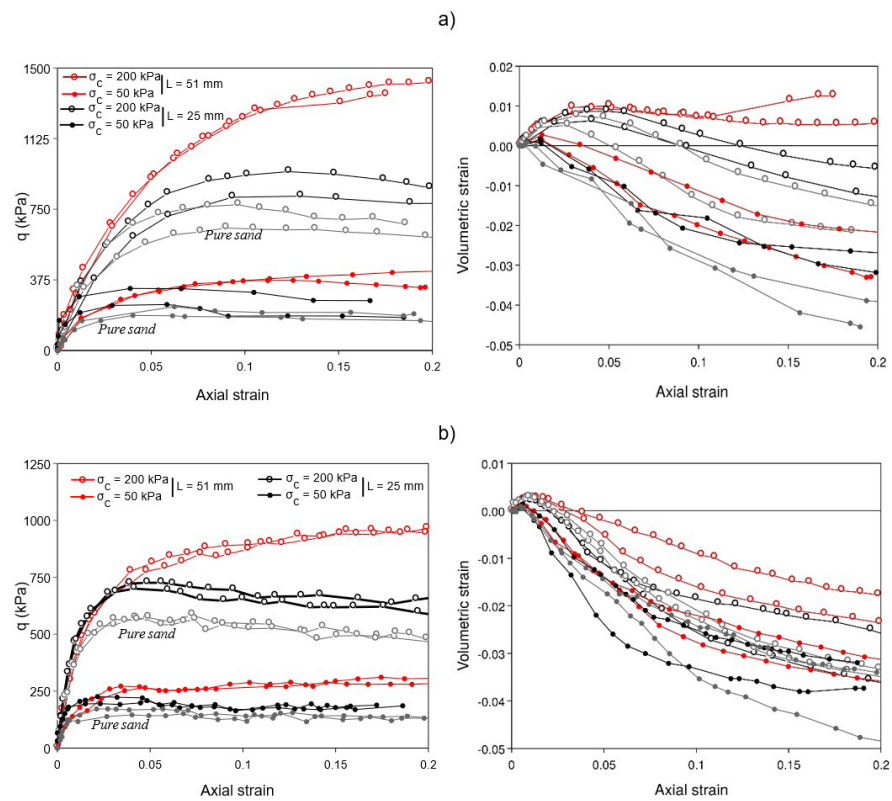
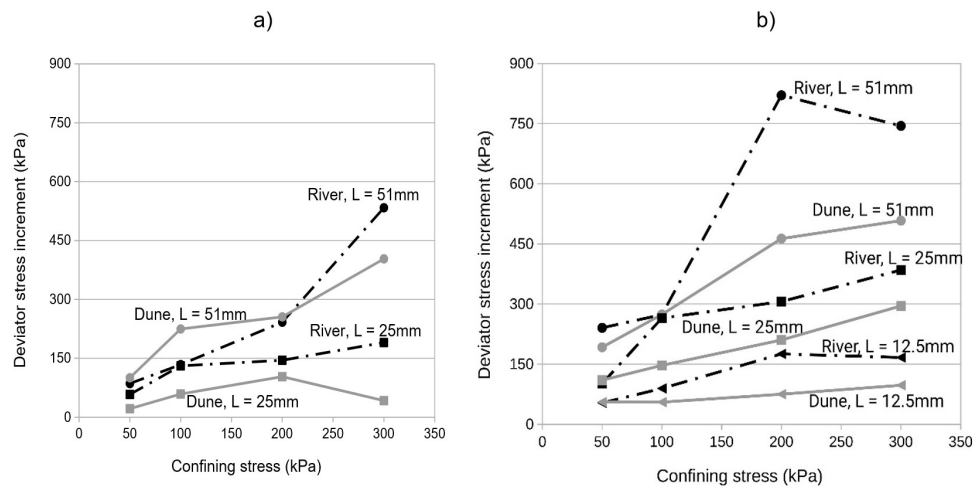


Figure 5. Deviator stress and volumetric strains versus axial strain curves. $P_f = 1\%$, $\sigma_c = 50$ kPa and 200 kPa. a) river sand and b) dune sand specimens.

Table 2. Shear strength parameters for different fiber lengths and contents.

Material	Dune sand				River sand			
	c' (kPa)	ϕ' (°)	R^2 (-)	$\Delta\phi'$ (°)	c' (kPa)	ϕ' (°)	R^2 (-)	$\Delta\phi'$ (°)
Pure sand, $P_f=0$	0	33.6	0.9995	-	0	36.5	0.9998	-
$P_f = 0.5\%$, $L=25$ mm	0	35.8	0.9994	2.2	9.5	39.2	0.9995	2.7
$P_f = 0.5\%$, $L=51$ mm	7.2	40.7	0.9995	7.1	0	43	0.9993	7.4
$P_f = 1\%$, $L=12.5$ mm	2.5	35.8	0.9995	2.2	8.2	39.2	0.9994	2.7
$P_f = 1\%$, $L=25$ mm	8.3	36	0.9995	2.4	19.6	41.7	0.9988	5.2
$P_f = 1\%$, $L=51$ mm	23.9	41.8	0.9987	8.2	47.7	41.7	0.9975	5.2


Figure 6. Fiber reinforcement effectiveness in terms of deviator stress increment. a) $P_f = 0.5\%$ and b) $P_f = 1\%$.

to 41.8° and cohesion changed from 0 to 23.9 kPa from non-reinforced soil to composites with $P_f = 1\%$ and $L = 51$ mm. In contrast, variations from 36.5° to 41.7° and 0 to 47.7 kPa were observed for river sand specimens under the same conditions. Although a slightly smaller variation is kept in the friction angle of the river sand specimens, the cohesion increment was remarkably higher, and the final shear strength values of such composites are very promising.

Figure 6 presents the increments in q_{pk} as a function of P_f and σ_c . As observed, fiber reinforcement was more effective in the case of the river sand specimens. The authors believe the subangular shape and the larger size of the solid particles played an essential role in this case.

Figure 7 illustrates how the fiber length influences the stiffness and compressibility of the tested specimens. As observed (Figure 7a), increasing fiber length becomes samples more ductile in both cases (dune and river sands), and the peak stress occurs for higher axial strains, mainly in the case of fibers with $L = 51$ mm. However, volumetric behavior was much more complex and dependent on the grain size distribution. For lower confining stresses, the fiber tends to increase the soil dilatancy, no matter the soil tested

in this study. For higher values of confining stress, river sand specimens, fibers become more effective in reducing dilatancy. However, this tendency is not observed in the case of the dune sand samples. The rounded shape and the smaller size of the dune specimens reduce the fiber reinforcement action not only in terms of shear strength but also when preventing soil volume increases. It also seems that the grain size curve uniformity prevails over particle size and shape, influencing the soil dilation since different authors (Michalowski & Čermák, 2003 and Ghadr et al., 2022) point to higher dilation in soils with coarser and angular grains.

Figure 8 illustrates how the mean dilatancy ($-\Delta\varepsilon_v/\Delta\varepsilon_a$) before peak stress influences the soil shear strength in terms of the normalized difference between peak (q_{pk}) and large strain (q_{ls}) deviator stress. In this case, N_ϕ is given by Equation 1. As observed, river sand (RS) specimens presented an appreciable amount of tests with negative dilatancy (compression) or dilatancy values inferior to 0.1. This is coherent with the data shown in Figure 7b. Although data scattering, it is clear that dune sand specimens (DS) require higher dilatancy for the same gain in shear strength. However, for dilatancy values higher than 0.1, DS samples are more

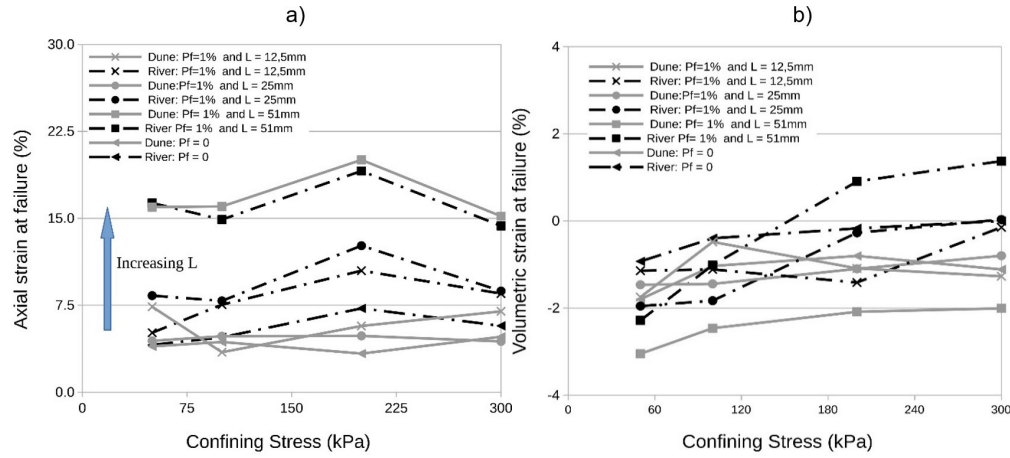


Figure 7. Effect of fiber length on axial and volumetric strains at failure for $P_f = 1\%$ specimens. a) axial strain behavior and b) volumetric strain behavior.

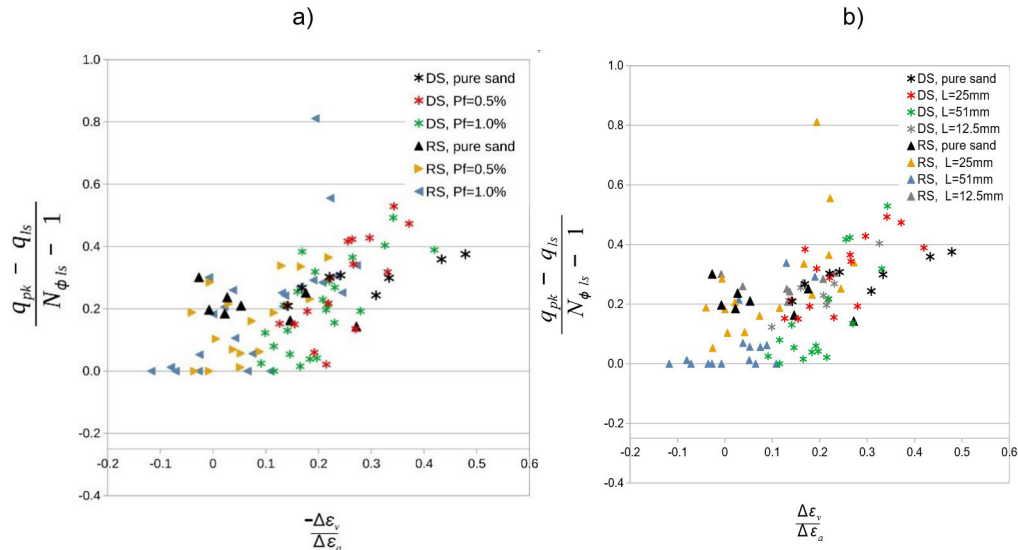


Figure 8. Dilatancy effect in increasing peak stress compared to residual values. a) comparing composites with different fiber percentage and b) comparing composites with fibers of different lengths.

responsive regarding shear strength gains due to dilatancy than RS specimens. In fact, only tests performed with $L = 25\text{mm}$ (see Figure 8b) for RS specimens captured shear strength gains due to dilatancy. Non-reinforced and samples with $L = 12.5\text{mm}$ presented values of normalized deviator stress differences that are less sensitive to dilatancy in both soils. It is impossible to differentiate the behavior obtained for $P_f = 0.5\%$ and 1% (Figure 8a). The more ductile behavior of the reinforced samples with $L = 51\text{mm}$ (Figure 7a) reduced the dilatancy values presented in Figure 8b.

$$N_{\phi} = \tan\left(\frac{90 + \phi_{ls}}{2}\right)^2 \quad (1)$$

4. Conclusions

Although fiber-reinforced soils are an up-and-coming alternative in earthworks, their use requires a deep knowledge of the interactions between the solid particles and the reinforcement elements and how the properties of each phase interfere with the overall composite mechanical performance. This paper used the results of a comprehensive triaxial testing campaign performed in two different sand reinforced with the same type, length, and percentage of fibers. Samples differed mainly in grain shape and grain size curve characteristics, and tests employed composites with the same relative density. As expected, river sand specimens formed by subangular particles with less uniform grain size curves

than dune sand presented higher peak and residual shear strength values. Furthermore, more effective reinforcement effects were also observed for river sand specimens under the same testing conditions. Concerning the stiffness and volumetric behavior, fiber addition increased ductility in composites of both sand, which passed to present peak strength for higher axial values. At least for river sand specimens, composites tended to reduce dilation as the reinforcement increased. For dune sand specimens, this effect was much less noticeable. Composite dilatancy was much less pronounced in river dune specimens, mainly for higher P_f values. Dune sand specimens required higher dilatancy values for the same shear strength increments than river sand composites. However, dilatancy was more effective in increasing DS shear strength for dilatancy values higher than 0.1.

Acknowledgements

The authors would like to thank CAPES and FAPESB for supporting the research development and Viapol for supplying the polymeric fibers used in the tests.

Declaration of interest

The authors have no conflicts of interest to declare. All co-authors have observed and affirmed the contents of the paper and there is no financial interest to report.

Authors' contributions

Murilo Pereira da Silva Conceição: conceptualization, methodology, data curation, visualization. Camilla Maria Torres Pinto: conceptualization, methodology, data curation, visualization. Miriam de Fátima Carvalho: conceptualization, methodology, writing – review & editing. Sandro Lemos Machado: conceptualization, methodology, writing – original draft.

Data availability

The datasets generated analyzed in the course of the current study are available from the corresponding author upon request.

List of symbols

d_{xx}	Sieve's equivalent diameter for xx% of the particles passing
e_f	Void ratio at the end of the tests
e_{max}	maximum void ratio
e_{min}	Minimum void ratio
k	Permeability coefficient
q_{pk}	Deviator stress at peak stress
q_{ls}	Deviator stress at large strains (residual strength)

B	Skempton's B parameter
C_c	Curvature coefficient
C_u	Uniformity coefficient
D	Fibers' diameter
DS	Dune sand
E_f	Fiber stiffness modulus
FRS	Fiber-reinforced soil
G_s	Particles' specific gravity
GSC	Grain size curve
G_{sf}	Fiber's particles specific gravity
I_D	Density index
L	Lengths of the fibers
N_ϕ	Shear strength parameter
P_f	Fiber content (dry mass)
RS	River sand
ϵ_{af}	Axial strain at the end of the tests
ϵ_{vf}	Volumetric strains at the end of the tests
σ_c	Confining stress
ϕ_{ls}	Composite friction angle for large strain conditions
ϕ_{peak}	Composite friction angle for peak stress

References

- ABNT NBR 12004. (1990). *Soil - Determination of the maximum index void ratio of cohesionless soils*. ABNT – Associação Brasileira de Normas Técnicas, Rio de Janeiro, RJ (in Portuguese).
- ABNT NBR 12051. (1991). *Soil - Determination of minimum index void ratio of cohesionless soils - Method of test*. ABNT – Associação Brasileira de Normas Técnicas, Rio de Janeiro, RJ (in Portuguese).
- ABNT NBR 6458. (2016a). *Gravel grains retained on the 4,8 mm mesh sieve - Determination of the bulk specific gravity, of the apparent specific gravity and of water absorption*. ABNT – Associação Brasileira de Normas Técnicas, Rio de Janeiro, RJ (in Portuguese).
- ABNT NBR 7181. (2016b). *Solo: Análise Granulométrica*. ABNT – Associação Brasileira de Normas Técnicas, Rio de Janeiro, RJ (in Portuguese).
- Aguilar, J.R.T. (2015). *Analysis of mechanical behavior of a sandy soil reinforced with coir fibers* [Master's dissertation, Pontifical Catholic University of Rio de Janeiro]. Pontifical Catholic University of Rio de Janeiro's repository (in Portuguese). <https://doi.org/10.17711/PUCRio.acad.25737>.
- Briaud, J.L. (2013). *Geotechnical engineering: unsaturated and saturated soils*. Wiley.
- Broderick, G.P., & Daniel, D.E. (1990). Stabilizing compacted clay against chemical attack. *Journal of Geotechnical Engineering*, 116(10), 1549-1567. [http://dx.doi.org/10.1061/\(ASCE\)0733-9410\(1990\)116:10\(1549\)](http://dx.doi.org/10.1061/(ASCE)0733-9410(1990)116:10(1549)).
- Choobbasti, A.J., Kutanaei, S.S., & Ghadakpour, M. (2019). Shear behavior of fiber-reinforced sand composite. *Arabian Journal of Geosciences*, 12, 1-6. <http://dx.doi.org/10.1007/s12517-019-4326-z>.

- Conceição, M.P.S. (2021). *Análise do comportamento tensão-deformação de um solo reforçado com fibra* [Master's dissertation]. Federal University of Bahia (in Portuguese).
- Damasceno, L.A.G., Carvalho, M.F., & Machado, S.L. (2019). Methane fugitive emissions through the cover system of a MSW landfill cell. *Journal of Environmental Engineering and Science*, 14(3), 1-11. <http://dx.doi.org/10.1680/jenes.19.00005>.
- Daniel, D.E., & Benson, C.H. (1990). Water content-density criteria for compacted soil liners. *Journal of Geotechnical Engineering*, 116(12), 1811-1830. [http://dx.doi.org/10.1061/\(ASCE\)0733-9410\(1990\)116:12\(1811\)](http://dx.doi.org/10.1061/(ASCE)0733-9410(1990)116:12(1811)).
- Daniel, D.E., & Wu, Y.K. (1993). Compacted clay liners and covers for arid sites. *Journal of Geotechnical Engineering*, 119(2), 223-237. [http://dx.doi.org/10.1061/\(ASCE\)0733-9410\(1993\)119:2\(223\)](http://dx.doi.org/10.1061/(ASCE)0733-9410(1993)119:2(223)).
- Diambra, A., Ibraim, E., Russell, A.R., & Wood, D.M. (2013). Fibre reinforced sands: from experiments to modelling and beyond. *International Journal for Numerical and Analytical Methods in Geomechanics*, 37(15), 2427-2455. <http://dx.doi.org/10.1002/nag.2142>.
- Diambra, A., Ibraim, E., Wood, D.M., & Russell, A.R. (2010). Fibre reinforced sands: experiments and modelling. *Geotextiles and Geomembranes*, 28(3), 238-250. <http://dx.doi.org/10.1016/j.geotexmem.2009.09.010>.
- Fang, X., Yang, Y., Chen, Z., Liu, H., Xiao, Y., & Shen, C. (2020). Influence of fiber content and length on engineering properties of MICP-treated coral sand. *Geomicrobiology Journal*, 37(6), 582-594. <http://dx.doi.org/10.1080/01490451.2020.1743392>.
- Festugato, L. (2008). *Análise do comportamento mecânico de um solo micro - reforçado com fibras de distintos índices de aspecto* [Master's dissertation, Federal University of Rio Grande do Sul]. Federal University of Rio Grande do Sul's repository (in Portuguese). Retrieved in November 27, 2022, from <http://hdl.handle.net/10183/14740>.
- Feuerharmel, M.R. (2000). *Behaviour of soils reinforced with polypropylene fibres* [Master's dissertation, Federal University of Rio Grande do Sul]. Federal University of Rio Grande do Sul's repository (in Portuguese). Retrieved in November 27, 2022, from <http://hdl.handle.net/10183/2804>.
- Gao, Z., & Diambra, A. (2021). A multiaxial constitutive model for fibre-reinforced sand. *Géotechnique*, 71(6), 548-560.
- Gao, Z., & Zhao, J. (2013). Evaluation on failure of fiber-reinforced sand. *Journal of Geotechnical and Geoenvironmental Engineering*, 139(1), 95-106. [http://dx.doi.org/10.1061/\(ASCE\)GT.1943-5606.0000737](http://dx.doi.org/10.1061/(ASCE)GT.1943-5606.0000737).
- Gao, Z., Lu, D., & Huang, M. (2020). Effective skeleton stress and void ratio for constitutive modeling of fiber-reinforced sand. *Acta Geotechnica*, 15, 2797-2811. <http://dx.doi.org/10.1007/s11440-020-00986-w>.
- Ghadr, S., Chen, C., Liu, C., & Hung, C. (2022). Mechanical behavior of sands reinforced with shredded face masks. *Bulletin of Engineering Geology and the Environment*, 81, 1-21. <http://dx.doi.org/10.1007/s10064-022-02810-z>.
- Gray, D.H., & Ohashi, H. (1983). Mechanics of fiber reinforcement in sand. *Journal of Geotechnical Engineering*, 109(3), 335-353. [http://dx.doi.org/10.1061/\(ASCE\)0733-9410\(1983\)109:3\(335\)](http://dx.doi.org/10.1061/(ASCE)0733-9410(1983)109:3(335)).
- Head, K.H., & Epps, R.J. (2014). *Manual of soil laboratory testing: effective stress tests* (Vol. III). Whittles Publishing.
- Jain, A., Mittal, S., & Shukla, S.K. (2023). Use of polyethylene terephthalate fibres for mitigating the liquefaction-induced failures. *Geotextiles and Geomembranes*, 51(1), 245-258. <http://dx.doi.org/10.1016/j.geotexmem.2022.11.002>.
- Jishnu, V.P., Sankar, N., & Chandrakaran, S. (2020). Strength behaviour of cohesionless soil reinforced with coconut leaf let as a natural material. *Materials Today: Proceedings*, 31, S340-S347. <http://dx.doi.org/10.1016/j.matpr.2020.04.637>.
- Leonards, G.A. (1962). *Foundation engineering*. McGraw Hill.
- Li, L., Zang, T., Xiao, H., Feng, W., & Liu, Y. (2020). Experimental study of polypropylene fibre-reinforced clay soil mixed with municipal solid waste incineration bottom ash. *European Journal of Environmental and Civil Engineering*. In press. <http://dx.doi.org/10.1080/19648189.2020.1795726>.
- Loehr, J.E., Romero, R.J., & Ang, E.C. (2005). Development of a strain-based model to predict strength of geosynthetic fiber-reinforced soil. In *Proceedings of Geo-Frontiers Congress: Geosynthetics Research and Development in Progress* (pp. 1-7). Austin: ASCE. [http://dx.doi.org/10.1061/40782\(161\)20](http://dx.doi.org/10.1061/40782(161)20).
- Maher, M.H., & Gray, D.H. (1990). Static response of sands reinforced with randomly distributed fibers. *Journal of Geotechnical Engineering*, 16(11), 1661-1677. [http://dx.doi.org/10.1061/\(ASCE\)0733-9410\(1990\)116:11\(1661\)](http://dx.doi.org/10.1061/(ASCE)0733-9410(1990)116:11(1661)).
- Mandolini, A., Diambra, A., & Ibraim, E. (2019). Strength anisotropy of fibre-reinforced sands under multiaxial loading. *Geotechnique*, 69(3), 203-216. <http://dx.doi.org/10.1680/jgeot.17.P.102>.
- Michalowski, R.L. (2008). Limit analysis with anisotropic fibre-reinforced soil. *Geotechnique*, 58(6), 489-501. <http://dx.doi.org/10.1680/geot.2007.00055>.
- Michalowski, R.L., & Čermák, J. (2003). Triaxial compression of sand reinforced with fibers. *Journal of Geotechnical and Geoenvironmental Engineering*, 129(2), 125-136. [http://dx.doi.org/10.1061/\(ASCE\)1090-0241\(2003\)129:2\(125\)](http://dx.doi.org/10.1061/(ASCE)1090-0241(2003)129:2(125)).
- Pinto, C.M.T. (2021). *Estudo do comportamento mecânico de uma areia aluvionar reforçada com fibras* [Master's dissertation]. Federal University of Bahia (in Portuguese).
- Ranjan, G., Vasan, R.M., & Charan, H.D. (1994). Behaviour of plastic-fibre-reinforced sand. *Geotextiles and Geomembranes*, 13(8), 555-565. [http://dx.doi.org/10.1016/0266-1144\(94\)90019-1](http://dx.doi.org/10.1016/0266-1144(94)90019-1).
- Rasouli, H., & Fatahi, B. (2022). Liquefaction and post-liquefaction resistance of sand reinforced with recycled

- geofibre. *Geotextiles and Geomembranes*, 50(1), 69-81. <http://dx.doi.org/10.1016/j.geotextmem.2021.09.002>.
- Santiago, G.A. (2011). *Estudo do comportamento mecânico de compósitos solo-fibras vegetais impermeabilizadas com solução de poliestireno expandido (EPS) e cimento asfáltico de petróleo (CAP)* [Doctoral thesis, Federal University of Ouro Preto]. Federal University of Ouro Preto's repository (in Portuguese). Retrieved in November 27, 2022, from <http://www.repositorio.ufop.br/jspui/handle/123456789/3601>.
- Shackelford, C.D. (2014). The ISSMGE kerry rowe lecture: the role of diffusion in environmental geotechnics. *Canadian Geotechnical Journal*, 51(11), 1219-1242. <http://dx.doi.org/10.1139/cgj-2013-0277>.
- Vidal, H. (1966). La terre Armée. *Annales de l'Institut Technique de Batiment et de Travaux Publics*, 58(259-260), 1-59. (in French)
- Wang, Y, Guo, P., Ren, W. Yuan, B., Yuan, H., Zhao, Y., Shan, S., & Cao, P. (2017). Laboratory investigation on strength characteristics of expansive soil treated with jute fiber reinforcement. *International Journal of Geomechanics*, 17(11), 04017101. [https://doi.org/10.1061/\(ASCE\)GM.1943-5622.0000998](https://doi.org/10.1061/(ASCE)GM.1943-5622.0000998).
- Zhang, J.Q., Wang, X., Yin, Z.Y., & Yang, N. (2022). Static and dynamic behaviors of granular soil reinforced by disposable face-mask chips. *Journal of Cleaner Production*, 331, 129838. <http://dx.doi.org/10.1016/j.jclepro.2021.129838>.

Influence of coconut fiber on the microstructural, mechanical and hydraulic behavior of unsaturated compacted soil

Fernanda Santos Gomes¹ , Mariana Ferreira Benessiuti Motta^{1#} ,

George de Paula Bernardes¹ , Paulo Valladares Soares¹ 

Article

Keywords

Coconut fiber
Unsaturated soil
Compacted soil
Mercury intrusion porosimetry
Soil water retention curve
Tensile strength

Abstract

This study aimed to evaluate the influence of the addition of coconut (coir) fibers on the microstructural, hydraulic and mechanical behavior of an unsaturated compacted soil. Specimens were molded and compacted, forming composites with 0%, 0.1%, 0.5% and 1% fiber in relation to their dry mass. The characterization of pores from the soil and fiber soil mixtures was performed by the Mercury Intrusion Porosimetry tests. Suction values were obtained through the filter paper method and soil water retention curves were adjusted with the Durner model due to the bimodal behavior. Tensile strength values were obtained from the indirect tensile strength test (Brazilian tensile test) for specimens with different suction values. It was found that the increase in fiber content in the material lead to a non-linear increase in macropores, which affected both the hydraulic and mechanical behavior of the soil. Furthermore, the shape of the soil water retention curve was preserved, but there were changes in the values of first and second air entry and residual suction. The tensile strength was negatively influenced, reaching a reduction of about 30% in the situation with higher fiber content. However, for higher levels, the behavior of the soil changed from brittle to ductile, increasing the supported deformations.

1. Introduction

During the development of engineering projects, a typical situation is to come across soils that, in the zone of interest, do not have adequate behavior. The most traditional way to solve this problem is to reallocate the soil, removing what is considered inadequate and replacing it with one with better properties, brought from elsewhere. This procedure, however, can lead to a substantial additional cost.

To ensure that the soil has ideal conditions and guarantees its proper performance, another frequently used solution is to implement procedures for improvements or stabilization by modifying its mechanical properties using chemical substances and/or physical mechanisms.

The addition of fibers to the soil is a type of stabilization approach. Studies such as that by Toledo Filho et al. (1999) demonstrates that fibers can change the mechanical behavior of the compound material, increasing its tensile strength and altering its permeability and ductility.

Savastano Júnior & Pimentel (2000) identified higher energy absorption by the fiber-reinforced soil, which remained with its pieces banded together even after rupture, and Motta (2018) studied the shear strength of soil reinforced with natural fibers, including coconut fiber (coir fiber). This author verified gains in tension after the peak of resistance,

indicating that the material tolerated greater deformations. Cabala (2007) obtained similar results. Consoli et al. (2005) reported a constant increase in strength with increasing axial deformation, characterizing an elastoplastic stiffening behavior.

When comparing natural and synthetic fibers, it is acknowledged that the first option is less environmentally harmful, since its origin is not linked to the use of non-renewable resources. However, the behavior of natural fibers in fiber-reinforced soil is influenced not only by physical-mechanical properties but also by biochemical properties (Gowthaman et al., 2018). Among these natural fibers, coconut fibers are an example of natural waste that have several promising applications but are usually disposed of in landfills.

Brazil's coconut production is close to 1.6 billion units per year (Brainer, 2021). Each one of them generates about one kilogram of natural waste, taking 10 to 15 years to biodegrade and also contributing to the further proliferation of tropical diseases. In areas that grow coconut trees, most of which are coastal, this type of byproduct alone can account for almost 70% of all solid waste deposited in landfills.

Due to its wide availability, coconut fiber has been studied as an element to constitute composite materials. According to Gowthaman et al. (2018), limited researchers have focused on the application of coir fibers in the field

[#]Corresponding author. E-mail address: mariana.motta@unesp.br

¹Universidade Estadual Paulista "Júlio de Mesquita Filho", Faculdade de Engenharia, Guaratinguetá, SP, Brasil.

Submitted on December 3, 2022; Final Acceptance on April 1, 2023; Discussion open until August 31, 2023.

<https://doi.org/10.28927/SR.2023.013322>



This is an Open Access article distributed under the terms of the Creative Commons Attribution License, which permits unrestricted use, distribution, and reproduction in any medium, provided the original work is properly cited.

of Geotechnical Engineering because this material, when exposed to a chemical environment, undergoes significant strength reduction. Lekha et al. (2015) and Yadav & Tiwari (2016) reported that the behavior of reinforced soil depends not only on the optimum quantity of coconut fiber but also on the quality of treated coconut fiber.

Anggraini (2016) and Gowthaman et al. (2018) presented a review on the use of natural fibers, including coconut fibers, where most of the reported studies is related to coir fiber with another additive in the fiber-reinforced soil system. By adding a mixture of these fibers with cement to soil, Raj et al. (2017) achieved improvements in the residual strength of the compound. Danso & Manu (2020) remarked that soil-cement mortar stabilized with lime and coconut fibers have better resistance against water absorption and good resistance against erosion. In addition, Oliveira Junior et al. (2018) and Gusmão & Jucá (2021) also perceived enhancement of shear strength in the new material.

Since Brazil is a tropical country, the occurrence of unsaturated residual soils is usual, and its properties are more complex than those specified in classic Soil Mechanics.

According to Fredlund & Rahardjo (1993), unsaturated soil consists of four phases: solid, composed of soil grains; liquid, formed by water and possible mineral salts dissolved in it; gaseous, composed of air; and the air-water interface, also called the contractile membrane.

In unsaturated soils, the difference between the pressure exerted by air and that exerted by water on the contractile membrane corresponds to the matric suction (Fredlund & Rahardjo, 1993). Lu & Likos (2004) defined that suction consists of quantifying the thermodynamic potential of water in the soil pores in relation to the free water potential.

Oliveira (2004) mentions that with the decrease in water content and consequent increase in matric suction, the soil's strength increases. This happens because seasonality causes variations of soil moisture, thus interfering with suction (Fredlund & Rahardjo, 1993) and superficial tension.

Unfortunately, usually, the variation of suction is not considered in geotechnical engineering projects, which tend to focus only on the past situation of the soil (Carvalho & Gitirana Junior, 2021). That practice can lead to incorrect decisions regarding resistance parameters. Fredlund (2021) asserts that considering in-situ suctions as temporary is a misconception that should be disregarded.

Considering the aforementioned circumstances and combining the necessity to make use of more sustainable resources and the pertinence of understanding the behavior

of unsaturated soils, this study seeks to test the feasibility of incorporating coconut fibers in artificial slopes. For this purpose, the analysis was made based on the evaluation of the effect of additions of different amounts of fiber on the microstructural, hydraulic and mechanical behavior of an unsaturated compacted soil. The assessment was made based on the results of mercury porosimetry tests, soil water retention curves and tensile strength curves (Brazilian tensile tests).

2. Materials and methods

2.1 Materials

The soil used in the tests is characterized by a silty texture and high plasticity, as observed in Table 1.

Fiber produced by a company of gardening artifacts was employed. Performing the cut in a standardized manner and separating the fiber wefts would lead to an unapproachable procedure in means of reproducibility in actual field applications. Thus, it was opted to use fiber cuts with undefined sizes and only restraint that the fragments were smaller than the diameter of the specimen (50 mm). According to Anggraini (2016) the effective length ranged is about 10-50 mm.

The method proposed by Maher & Gray (1990), which reports that random insertion of the fibers does not create specific planes of weakness, was applied in this study.

The evaluated fiber additions were: 0%: corresponds to the soil in its natural composition (without fibers); 0.1% in relation to the dry mass of the soil: amount chosen in order to verify whether a small addition of fiber would already have an effect on soil properties; 1%: the literature (Festugato, 2008; Sachetti, 2012; Anggraini, 2016) indicates that values above this lead to mechanical limitations related to the homogenization with soil and water, which can interfere with the results of the experiments; 0.5%: intermediate value between the lowest and highest contents.

2.2 Preparation of the fiber soil mixture and molding of the specimens

The soil, acquired in the form of deformed samples, was crumbled and air-dried. The fiber was manually untangled, weighed, cut and hand mixed with the soil. There was an adversity in obtaining a homogeneous mixture: the fiber tended to form agglomerations that had to be undone by untangling the threads (except the 0.1% mixture).

Table 1. Physical characterization results and average index properties.

Gravel (%)	Sand (%)	Silt (%)	Clay (%)	LL (%)	PL (%)	PI (%)	USCS	Gs
2.1	40.7	44.8	12.4	58	45	12	MH	2.74

Number of replicates: 3.

Legend: see List of Symbols.

The air-dried soil was passed through sieve number 4 and mixed with distilled water to the target moisture content. The soil was then sealed in bags and stored for at least 1 day to allow moisture equalization. The samples were compacted with the maximum specific dry mass for the Standard Proctor effort of 14.4 kN/m³, corresponding to an optimum water content of 16%.

For molding the specimens, cylindrical PVC ring-shaped molds with 20 mm of height and 50 mm of diameter were used. The fiber soil system was compressed into three layers using a plain compaction apparatus that applied pressure simulating trampling over the entire cross-sectional area of the specimen. In order to evaluate the effect of fiber insertion on the microstructural, hydraulic and mechanical characteristics of the fiber soil composites, the fibers were inserted into the soil after moisture equalization and mixed manually before compaction. It is noteworthy that the fibers replaced part of the dry soil mass, maintaining the same compaction parameters, in terms of specific dry mass and gravimetric water content.

For each fiber addition analyzed (0%; 0.1%; 0.5% and 1%), at least 10 samples were molded with the mentioned characteristics, with a variation of 14.4 ± 0.3 kN/m³ for the specific dry mass and $16 \pm 0.9\%$ for the gravimetric water content.

The hydraulic and mechanical behaviors were evaluated using the soil water retention curve and the tensile strength variation curve as a function of matric suction. For this purpose, the specimens were subjected to a drying path, in which they underwent a capillary saturation process for 3 days and then placed to air dry so that each sample reached a certain water content value (between 2% and 34%).

2.3 Mercury porosimetry test

The characterization of pores from the soil and fiber soil mixtures was performed by Mercury Intrusion Porosimetry (MIP) tests. This technique allows discerning the different pore diameters and their distribution in the analyzed material. For this purpose, the Poresizer 9320 equipment from Micromeritics Instrument Corporation was used, capable of inspecting pores up to 6×10^{-6} mm in diameter at an applied pressure of 212 MPa.

According to Romero & Simms (2008), in the MIP technique an absolute pressure P is applied to a non-wetting liquid (mercury) in order to enter the empty pores. Assuming the pores in soil to be cylindrical, the relationship between the intrusion pressure P and the pore radius r is $P = -2 \gamma \cos \Theta / r$, where γ is the mercury surface tension (0.480 N/m at 20 °C) and Θ is the contact angle (140°) (Wang et al., 2020).

To carry through this experiment, as shown in Figure 1, a specimen from each mixture investigated was selected. They were cut to ensure the size specifications to fit the equipment – approximately 16 mm in diameter and 25 mm in height. For each pressure application stage, the volume of mercury injected into the pores of the sample was determined.

As porosimetry is based on capillarity laws that govern the intrusion of a fluid, it is possible to correlate the MIP results with the soil water retention curve (SWRC) results (Décourt et al., 2022). The phenomenon of water desorption that occurs in the drying SWRC curve can be associated with the expulsion of air from the pores by mercury injection. In this context, the results obtained by MIP tests were compared to the SWRC tests, for the soil and the fiber soil samples (Aung et al., 2001; Sun & Cui, 2020; Décourt et al., 2022).



Figure 1. MIP tests samples. (a) 0% fiber; (b) 0,1% fiber; (c) 0,5% fiber; (d) 1% fiber.

2.4 Soil water retention curve

Following the specifications from ASTM (2017), a Whatman™ 42 filter paper was put in direct contact with the analyzed soils both at the top and bottom of the specimens, which were then wrapped and placed inside a thermal box. They were then kept in this arrangement for at least 7 days in order to allow enough time to transfer moisture from the fiber soil to the filter paper.

After this period, the moisture content of the filter paper was determined (Marinho & Oliveira, 2006). Each paper disc was individually inserted into a weighing scale (Sartorius Analytical Balance BL 210 S, with the readability of 0.0001g and weighing capacity of 210g), and its mass variation was registered for predetermined times (10; 20; 30; 40; 50; 60; 90 and 120 s). With these values, the mass at time zero for both wet and dry conditions was estimated through exponential correlation.

As the studied soil presents a bimodal behavior (referring to the entrance of air in the macro and micropores), the obtained curves were adjusted by the method of Durner (1994), as shown in Equation 1, based on the simple model of van Genuchten (1980). The necessary coefficients for the application of the model were obtained using the SWRC Fit software and the values of the first and second air entry and the first and second residual suction were obtained through graphs.

$$S_e = \sum_i^k w_i \left[\frac{1}{1 + (\alpha_i h)^{n_i}} \right]^{m_i} \quad (1)$$

Where k is the number of subsystems, w_i are weighting factors with $0 < w_i < 1$ and $\sum w_i = 1$, h is the pressure head and α_p , m_p , n_i are water retention parameters.

2.5 Indirect tensile strength test – Brazilian tensile test

After determining the soil suction by the filter paper method, all samples underwent the splitting tensile strength test, standardized by ASTM (2016). To the accomplishment of this analysis, a load at a speed of $0.9 \text{ mm} \cdot \text{min}^{-1}$ was applied. For the samples without fiber and with the lowest addition (0.1%), the test was completed when the load ring indicated a constant or maximum reached value, which was monitored alongside the tracking of the tensile crack. In samples with higher fiber content (0.5% and 1%), the cracks were not as noticeable and the values in the load ring did not stabilize. Thus, an interval of 11 minutes from the start of loading was set as a stopping criterion to end the experiment.

The application of a compressive load on the specimen generates a state of tensile stress, to which the strength value can be provided by applying Equation 2, proposed by Krishnayya & Einsenstein (1974).

$$\sigma_t = \frac{2 \times P}{\pi \times d \times h_s} \quad (2)$$

Where P is the maximum vertical load applied in the test; d is the diameter of the sample and h_s is its height.

3. Analysis and results

3.1 Microstructural behavior of the fiber soil mixture

Figure 2 displays the results obtained from the MIP tests. It can be observed that the microstructural behavior, in general, was consistent for all the evaluated samples. The achieved curves show a bimodal behavior of the materials, both in the natural and reinforced soil samples, with groups of micro and macropores.

Based on BS ISO (2009) and what was assumed by Décourt et al. (2022), the micropores are related to the clay fraction ($\varphi < 0.2 \mu\text{m}$), mesopores to the silt fraction ($0.2 < \varphi < 6 \mu\text{m}$) and macropores to the sand fraction ($\varphi > 6 \mu\text{m}$). Accordingly, when quantifying the curve obtained from each sample, it can be observed in all cases that the highest percentage of pores is located in the micropore zone, followed by the macropore zone.

Regarding the addition of fibers, there is an increase in macropores and a consequent decrease in micropores as the fiber content increases. This development is not presented linearly, as it can be observed that the biggest behavior change occurred in the samples with 0.1% and 0.5% of fiber. Table 2 shows the values for each case studied.

Also, based on the results presented in Table 2, it is possible to compare the total porosity of the samples measured by the MIP tests with the average porosity determined by the physical properties of the soil. It can be inferred that the increase in soil macro and mesoporosity increases the porosity obtained by the mercury intrusion porosimetry tests, which improves the befitting with the average physical porosity index of the samples (47.1%). For samples with 1% fiber, the difference between the mentioned data is 6%. This fact, also observed in Romero et al. (1999) and Décourt et al. (2022), may be associated with isolated and/or occluded micropores, which are not filled with mercury during the test.

3.2 Hydraulic behavior of the fiber soil system

The retention curves for the natural and fiber soils (Figure 3) depict a bimodal behavior which, as already demonstrated by Figure 2, relates to the air entry into both the macro and micropores of the soil.

Although the curves correspond to samples compacted with the same average of dry specific mass and gravimetric water content, they differ from each other, among other aspects, in the shape conceived by the fitting method.

Table 2. Micro, meso, macro and total porosity indexes from MIP tests.

Samples	Micro pores (%)	Meso pores (%)	Macro pores (%)	MIP
	$\phi < 0.2\text{mm}$	$0.2\text{mm} < \phi < 6\text{mm}$	$\Phi > 6\text{mm}$	Porosity (%)
0%	62.2	3.5	34.4	38.0
0.1%	63.9	3.6	32.4	37.9
0.5%	57.0	3.7	39.3	39.5
1%	56.3	4.1	39.6	41.1

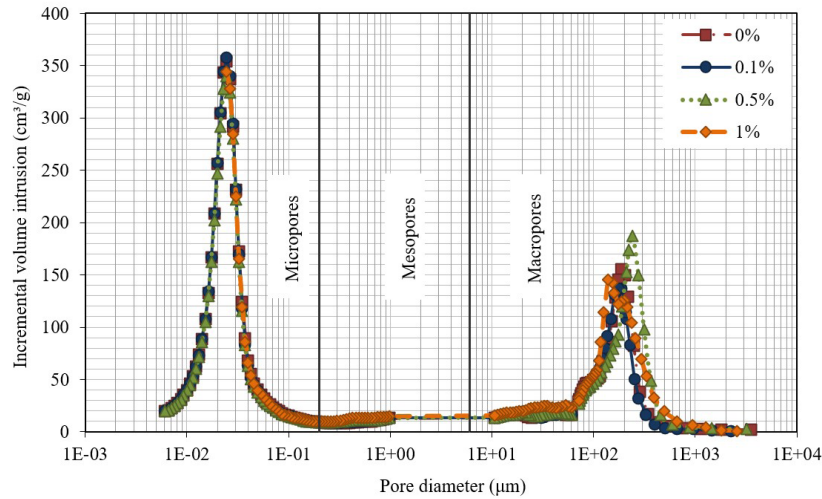


Figure 2. Porosimetry tests results for all samples tested.

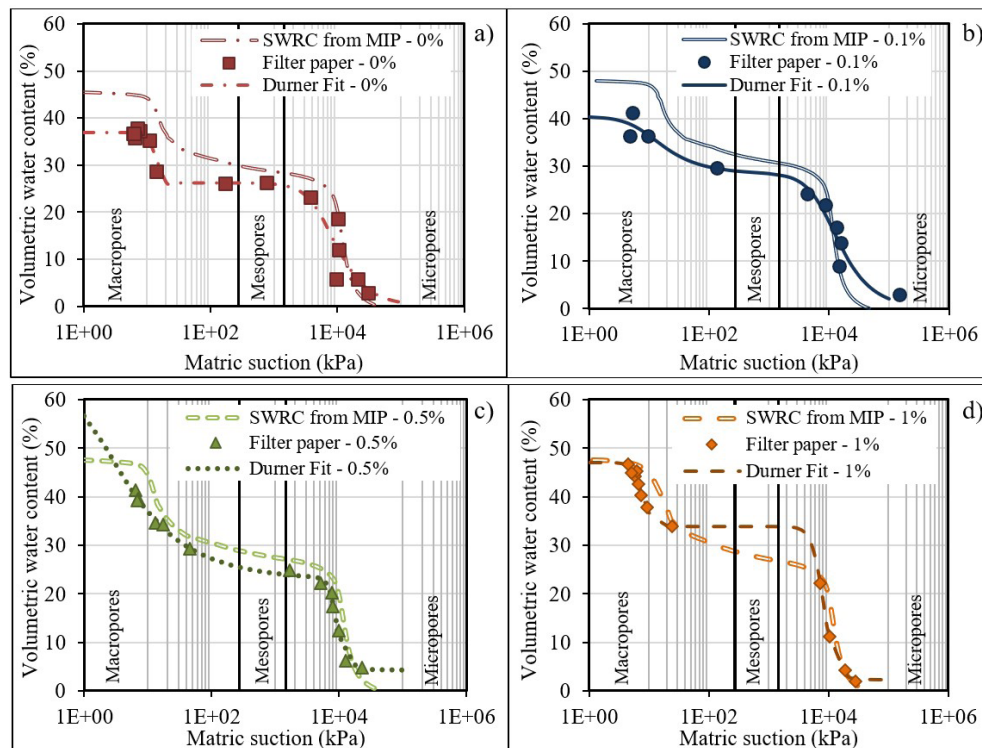


Figure 3. Soil water retention curves and correlation between the filter paper method and MIP tests. (a) Soil without the addition of fiber; (b) Fiber soil with 0.1% fiber; (c) Fiber soil with 0.5% fiber; (d) Fiber soil with 1% fiber.

Compared to the soil in its natural conditions, the level of the saturated zone decreased in the three analyzed fiber soils, thus demanding less energy to drain water from the macropores and conceding the entrance of air. In Figure 3c, the level of the saturated zone is reduced, making it difficult to detect the first air entry. This may have occurred due to curve fitting, as there are not enough data for low suction values with 0.5% fiber addition.

There was also variation in the value of the second air entry amidst the analyzed soils. For the natural soil, the value was 2900 kPa, while in soils with 0.1%, 0.5% and 1% fiber additions, second air entry of 4000 kPa, 6700 kPa and 5900 kPa were determined, respectively. This result implies that the addition of coconut fiber postpones the moment when the air starts to fill the micropores of the soil.

The difference between the curves can also be observed in the residual zone, which was shifted to the right side, suggesting that the stage in which desaturation occurs was more expressive in fiber-reinforced soils.

Furthermore, Figure 3 shows, for all types of samples analyzed, the correlation between the data obtained from the filter paper tests and the retention curve derived from the MIP tests. It can be observed, in general, that the filter paper data were better fitted on the desaturation zone, after the second air entry. This deviation at the beginning of the curve

was also encountered by several other authors (Aung et al., 2001; Mendes & Marinho, 2020; Décourt et al., 2022), but no widely accepted explanation justifies this difference.

Nevertheless, it is worth noting that, for systems with 0.5% and 1% fiber additions (Figure 3c and Figure 3d), a better fit between the two methodologies is established, covering the entire range from macro to micropores. This condition may be related to the further infiltration of pores during mercury injection.

3.3 Mechanical behavior of the fiber soil system

From the suction values obtained with the filter paper test and with the data from the tensile strength test, the curves in Figure 4 were plotted. In all four situations, the soil presented a tensile strength curve with a similar format to that obtained by Benessiuti et al. (2010) for this same soil. As observed, the strength value increases slowly in the first section, which corresponds to the lowest suction values, and is proceeded by considerable gains until reaching a peak, from which the tensile strength begins to decrease.

Motta et al. (2015) found similar results for an undisturbed young residual micaceous soil from Rio de Janeiro, Brazil. The reason for the observed behavior is probably related to the formation of micro-cracks and the breakdown of the

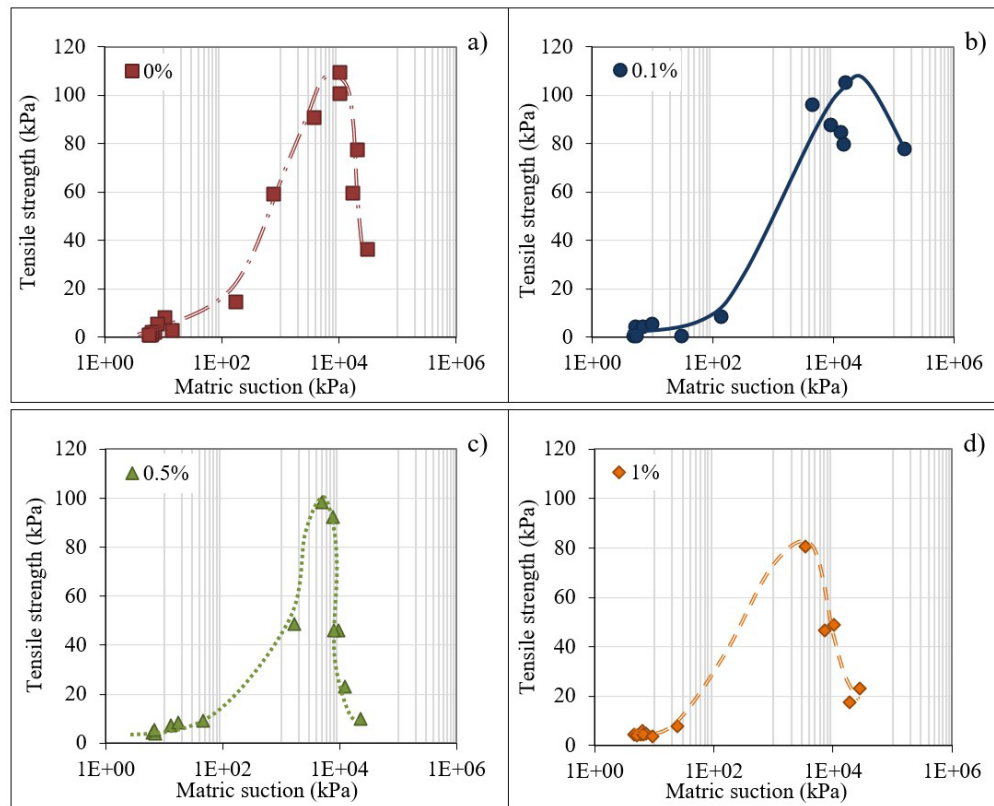


Figure 4. Tensile strength *versus* matric suction curves. (a) Soil without the addition of fiber; (b) Fiber soil with 0.1% fiber; (c) Fiber soil with 0.5% fiber; (d) Fiber soil with 1% fiber.

meniscus for higher suctions that act decreasing the tensile strength.

Bulolo et al. (2021) found two types of behavior for compacted samples of two residual soils from Singapore. For all the sample sets, drying of the soil specimens from the wet of optimum to the dry of optimum showed an increase in tensile strength. These values increase up to a certain limit and then generally become constant despite further drying. However, some data show a slight drop in tensile strength at extremely low water contents. The authors mentioned that after the air entry value (AEV), the water phase becomes increasingly discontinuous in the soil and the contribution of suction to the tensile strength becomes increasingly minimal.

Figures 5a and 5b exemplify the ruptured surfaces seen in fiber soils with lower fiber content. In some samples of the fiber soil systems with higher fiber content, it was possible to delineate the crack, as illustrated in Figure 5b, but not in the majority. Most of the specimens showed a large deformation, making it difficult to identify the failure.

This change in soil behavior from brittle to ductile is in agreement with the results obtained by Cabala (2007), who found that the elastic modulus of a soil-cement reinforced with coconut fiber varied inversely proportional to the amount of fiber content. Specifically, the bigger the fiber amount, the lower the rigidity of the material, which leads to an improvement in its ability to withstand deformations.

Although the visual identification of rupture was inadequate in these cases, the stopping criteria (calculated based on the speed and load applied by the equipment) is within that described in the literature for situations of large deformations, which guarantees that the sample actually failure and that its strength value was obtained correctly.

It is also worth noting that this occurrence did not interfere with acquiring the strength peaks, since this fact is associated with samples with lower suction values. The samples

that showed the highest values of tensile strength presented a clear rupture surface, characterized by a brittle failure. Thus, it was possible to observe a change in the behavior of the fiber soil system as a function of matric suction.

When quantitatively evaluating the graphs, it is evidenced that: for the natural soil, the strength peak was 109 kPa, corresponding to the suction value of 10645 kPa; for the fiber soil with 0.1% fiber, the strength peak was 105 kPa for a suction of 16066 kPa; for the 0.5% fiber soil, the strength peak reached a value of 98 kPa for a suction of 5064 kPa; and for the fiber soil with 1% fiber, the strength peak was 80 kPa for a suction of 3469 kPa. Comparing the fiber soil with the soil without reinforcement, it was deduced that the fiber addition of 0.1% changed less significantly the behavior of the material, being characterized by a decrease in strength of approximately 4%. On the other hand, in the materials with 0.5% and 1% of fiber addition, the tensile strength decreased by approximately 10% and 26%, respectively. Furthermore, a decrease in suction values associated with strength peak values can be observed in the specimens with higher percentages of fiber.

In the literature, studies that evaluated the addition of coconut fiber as soil reinforcement address its effect on other types of strength without associating them with suction, hence it was not possible to effectively compare the results obtained. Cabala (2007) revealed that the flexural strength of the reinforced specimens was lower than that of the natural soil, maybe due to the lack of adhesion between the two phases present in the composite material.

Based on studies regarding natural fibers (Angraini, 2016; Gowthaman et al., 2018), an improvement in the tensile strength of the analyzed material was expected. Nevertheless, it was noted that, for the evaluated components, the addition of fibers equal to or less than 0.1% of the dry mass did not lead to enhancement of the soil behavior regarding its ability to

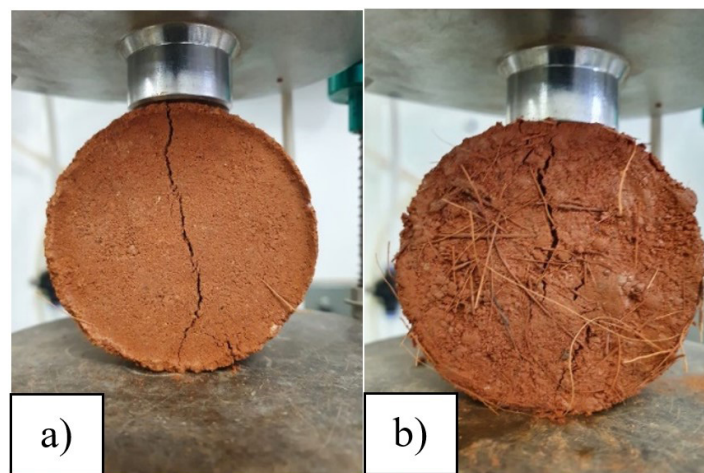


Figure 5. Rupture surfaces in samples subjected to the splitting tensile strength test. (a) Fiber soil with 0.1% fiber; (b) Fiber soil with 0.5% fiber.

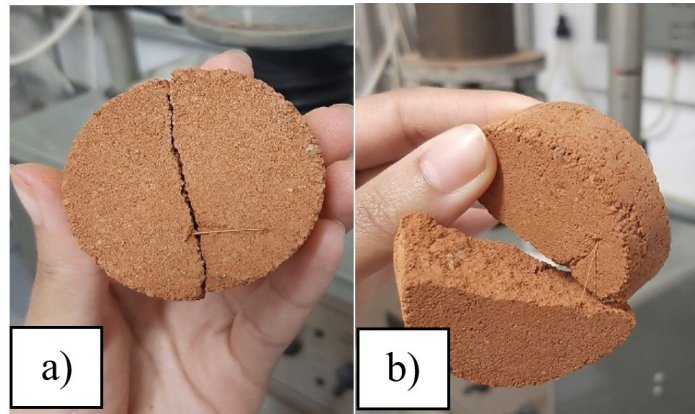


Figure 6. Rupture surfaces in the samples submitted to the diametral compression test. (a) Fiber crossing the rupture surface of the sample; (b) Fiber anchoring effect, keeping the two pieces of the ruptured sample together.

resist tensile stress. This divergence in results can be explained by the particularities of the materials, which differ in each study, and by the decisions made during the preparation and execution of the tests. The lack of standardization of fiber length and diameter and the specimen's structure could have been a source of interference. Moreover, it is worth mentioning that most of the studies is related to fiber-reinforced soil with another additive. This third element could be responsible for the benefits of coir fibers in geotechnical applications.

In the case of fiber soil with a fiber addition of 1%, the main issue may have been the difficulty in homogenizing the material. As the fibers tended to cluster, it is a possibility that the samples had part of their volume filled only by fiber instead of soil.

Although the addition of coconut fibers did not result in an improvement in tensile strength, not preventing the soil from breaking, it was observed that, once broken, the fibers helped to keep the pieces together, working akin a sort of stapler (Figure 6).

3.4 Correlation between the microstructural, hydraulic and mechanical behaviors

By comparing microstructural and hydraulic behavior, from MIP tests and filter paper method (Figure 2 and Figure 3), for all cases concerning natural soil and fiber soil mixtures, two predominant groups of pores could be identified, located in the zone of macro and micropores, where the highest percentage of pores have diameters smaller than $0.2\mu\text{m}$, related to the second air entry value zone. The increase in fiber content from 0.1% to 0.5% caused a greater increase in the soil macroporosity, a greater decrease in the soil microporosity and, consequently, a greater increase in the air entry value. From 0.5% to 1% fiber, the observed variations were smaller in terms of microstructural and hydraulic behaviors.

When comparing the retention curve acquired from the MIP tests with the results from the filter paper tests, better fits

were observed in samples with higher fiber content, which consequently have a higher percentage of macropores. This fact implies that samples with porosity values estimated by MIP tests closer in comparison with the average physical porosity index comprise the best data concurrence.

By correlating the SWRC – obtained by the filter paper test – and the tensile strength graph (Figure 3 and Figure 4), it can be perceived, for the same amount of fiber, that for low suction values, the strength increases at a slow pace. From the first air entry, the property increases significantly until it reaches its peak and then decreases again. In all four analyzed cases, the point of maximum tensile strength is found near the second air entry.

For the natural soil and the fiber soil with 0.1% fiber, the peak is located practically in the center of the second desaturation segment, halfway to the residual phase; for the fiber soil with 0.5% and 1%, it is located just before the second air entry value.

According to Villar et al. (2007), this demeanor of tensile strength decrease after the second air entry is influenced due to the condition of continuous air in the sample. Benessiuti et al. (2010), Motta et al. (2015) and Bulolo et al. (2021) obtained similar results.

The addition of fibers equal to or less than 0.1% did not have a significant effect on tensile strength, decreasing it by 4%. However, the addition of a higher fiber amount (1%) reduced the strength by about 30%. It is assumed that the optimal point of material addition has been exceeded.

4. Conclusions and recommendations

The purpose of this study was to evaluate how the addition of coconut fibers would interfere on the microstructural, mechanical and hydraulic behavior of an unsaturated compacted soil, in order to test the feasibility of incorporating coconut fibers in artificial slopes.

The increase in fiber content in the material lead to a non-linear increase in macropores and a non-linear decrease in micropores, which affected both the hydraulic and mechanical behavior of the soil.

Regarding the hydraulic behavior, it was demonstrated that for all materials tested, the addition of fibers interfered with the SWRC format, modifying the values of the first and second air entry and residual suction. Such changes did not display a linear conduct with the increase in fiber content.

Regarding the mechanical behavior, it can be verified that the change in soil structure affected its tensile strength, where the addition of fibers decreased the tensile strength peak values. Despite the decrease in tensile strength, the samples with the highest fiber content evidently withstood greater deformations than the natural soil, implying that it had its rupture behavior transitioned from brittle to ductile, as expected. In this sense, the fibers operated similarly to vegetation roots on slopes, helping to avoid sudden ruptures that could result in greater damage.

Future research is necessary to understand the behavior of the fiber soil system including: a study of different types of homogenizations of the fiber soil system; analysis of the dimensions, size, diameter and orientation of the fiber; analysis of the effect of time and exposure to climatic conditions on the fibers.

Declaration of interest

The authors have no conflicts of interest to declare. All co-authors have observed and affirmed the contents of the paper and there is no financial interest to report.

Authors' contributions

Fernanda Santos Gomes: conceptualization, data curation, visualization, writing – original draft. Mariana Ferreira Benessiuti Motta: conceptualization, data curation, methodology, supervision, validation, writing – original draft. George de Paula Bernardes: conceptualization, formal analysis, methodology, supervision, validation, writing – review & editing. Paulo Valladares Soares: validation, writing – review & editing.

Data availability

The datasets generated analyzed in the course of the current study are available from the corresponding author upon request.

List of symbols

d	Sample diameter
h	Pressure head
h_s	Sample height

k	Number of subsystems
m	Water retention parameter
n	Water retention parameter
w	Weighting factors
G_s	Specific gravity of grains
LL	Liquidity limit
MIP	Mercury intrusion porosimetry
P	Maximum vertical load applied
PI	Plasticity index
PL	Plasticity limit
PVC	Polyvinyl chloride
S_e	Effective saturation
$SWRC$	Soil water retention curve
$USCS$	Unified soil classification system
α	Water retention parameter
σ_t	Tensile strength

References

- Anggraini, V. (2016). Potential of coir fibres as soil reinforcement. *Pertanika Journal of Scholarly Research Reviews*, 2(1), 95-106.
- Aung, K.K., Rahardjo, H., Leong, E.C., & Toll, D.G. (2001). Relationship between porosimetry measurement and soil-water characteristic curve for an unsaturated residual soil. *Geotechnical and Geological Engineering*, 19(3-4), 401-416. <http://dx.doi.org/10.1023/A:1013125600962>.
- ASTM D3967-08. (2016). *Standard test method for splitting tensile strength of intact rock core specimens*. ASTM International, West Conshohocken, PA.
- ASTM D5298. (2017). *Standard test method for measurement of soil potential (suction) using Filter Paper*. ASTM International, West Conshohocken, PA.
- Benessiuti, M.F., Bernardes, G.P., & Camarinha, P.I.M. (2010). Influência da sucção matricial na resistência à tração de solos residuais de gnaiss compactados. In *Anais do XV Congresso Brasileiro de Mecânica dos Solos e Engenharia Geotécnica*, Gramado.
- Brainer, M.S.C.P. (2021). *Coco: produção e mercado* (Caderno Setorial ETENE, No. 206). Fortaleza: Banco do Nordeste.
- BS ISO 11277. (2009). Soil quality – Determination of particle size distribution in mineral soil material – Method by sieving and sedimentation. International Organization for Standardization, Geneva.
- Bulolo, S., Leong, E.C., & Kizza, R. (2021). Tensile strength of unsaturated coarse and fine-grained soils. *Bulletin of Engineering Geology and the Environment*, 80(3), 2727-2750. <http://dx.doi.org/10.1007/s10064-020-02073-6>.
- Cabala, G.V.E. (2007). *Estudo do comportamento mecânico de estruturas de solo-cimento reforçado com fibras de coco e hastes de bambu* [Master's dissertation, Federal University of Rio Grande do Norte]. Federal University of Rio Grande do Norte's repository (in Portuguese). Retrieved in December 3, 2022, from <https://repositorio.ufrn.br/handle/123456789/18332>

- Carvalho, J.C., & Gitirana Junior, G.F.N. (2021). Unsaturated soils in the context of tropical soils. *Soils and Rocks*, 44(3), 1-25. <http://dx.doi.org/10.28927/SR.2021.068121>.
- Consoli, N.C., Casagrande, M.D.T., & Coop, M.R. (2005). Behavior of a fiber-reinforced sand under large strains. In *16th International Conference on Soil Mechanics and Geotechnical Engineering*, Osaka, Japan.
- Danso, H., & Manu, D. (2020). Influence of coconut fibres and lime on the properties of soil-cement mortar. *Case Studies in Construction Materials*, 12, e00316. <http://dx.doi.org/10.1016/j.cscm.2019.e00316>.
- Décourt, R.T., De Campos, T.M.P., & Antunes, F.S. (2022). Interrelationship among weathering degree, pore distribution and water retention in an unsaturated gneissic residual soil. *Engineering Geology*, 299, 106570. <http://dx.doi.org/10.1016/j.enggeo.2022.106570>.
- Durner, W. (1994). Hydraulic conductivity estimation for soil with heterogeneous pore structure. *Water Resources Research*, 30(2), 211-223. <http://dx.doi.org/10.1029/93WR02676>.
- Festugato, L. (2008). *Análise do comportamento mecânico de um solo micro-reforçado com fibras de distintos índices aspecto* [Master's dissertation, Federal University of Rio Grande do Sul]. Federal University of Rio Grande do Sul's repository (in Portuguese). Retrieved in December 3, 2022, from <http://hdl.handle.net/10183/14740>
- Fredlund, D.G., & Rahardjo, H. (1993). *Soil mechanics for unsaturated soils*. New York: John Wiley & Sons.
- Fredlund, D.G. (2021). Myths and misconceptions related to unsaturated soil mechanics. *Soils and Rocks*, 44(3), 1-19. <http://dx.doi.org/10.28927/SR.2021.062521>.
- Gowthaman, S., Nakashima, K., & Kawasaki, S. (2018). A state-of-the-art review on soil reinforcement technology using natural plant fiber materials: past findings, present trends and future directions. *Materials*, 11(4), 553. <http://dx.doi.org/10.3390/ma11040553>.
- Gusmão, L.R.C., & Jucá, J.F.T. (2021). Influence of green's coconut fibers in the unsaturated behavior of compacted clayey soil. *MATEC Web of Conferences*, 337, 01017.
- Krishnayya, A.V.G., & Einsenstein, Z. (1974). Brazilian tensile test for soils. *Canadian Geotechnical Journal*, 11(4), 632-642. <http://dx.doi.org/10.1139/t74-064>.
- Lekha, B.M., Goutham, S., & Shankar, A.U.R. (2015). Evaluation of lateritic soil stabilized with Arecanut coir for low volume pavements. *Transportation Geotechnics*, 2, 20-29. <http://dx.doi.org/10.1016/j.trgeo.2014.09.001>.
- Lu, N., & Likos, W.J. (2004). *Unsaturated soil mechanics*. Hoboken: John Wiley & Sons.
- Maher, M., & Gray, D. (1990). Static response of sands reinforced with randomly distributed fibers. *Journal of Geotechnical Engineering*, 116(11), 1661-1677. [http://dx.doi.org/10.1061/\(ASCE\)0733-9410\(1990\)116:11\(1661\)](http://dx.doi.org/10.1061/(ASCE)0733-9410(1990)116:11(1661)).
- Marinho, F.A.M., & Oliveira, O.M. (2006). The filter paper method revisited. *Geotechnical Testing Journal*, 29(3), 250-258. <http://dx.doi.org/10.1520/GTJ14125>.
- Mendes, R.M., & Marinho, F.A.M. (2020). Soil Water Retention Curves for residual soils using traditional methods and MIP. *Geotechnical and Geological Engineering*, 38(5), 5167-5177. <http://dx.doi.org/10.1007/s10706-020-01354-x>.
- Motta, M.F.B., Campos, T.M.P., Bernardes, G.P., Viana da Fonseca, A. (2015). Shear modulus G_0 and its correlations with matric suction, unconfined compression strength and tensile strength of an unsaturated residual soil. In D. Manzanal & A.O. Sfriso (Eds.), *Fundamentals to applications in geotechnics* (pp. 2142-2149). Amsterdam: IOS Press.
- Motta, T.G. (2018). *Estudo do comportamento mecânico de solos reforçados com fibras naturais* [Bachelor dissertation, University of Brasília]. University of Brasília's repository (in Portuguese). Retrieved in December 3, 2013, from https://bdm.unb.br/bitstream/10483/21453/1/2018_ThalesGorettoMotta_tcc.pdf
- Oliveira, O.M. (2004). *Study on the shear strength of a compacted residual soil unsaturated* [Doctoral thesis, University of São Paulo]. University of São Paulo's repository (in Portuguese). Retrieved in December 3, 2013, from <https://www.teses.usp.br/teses/disponiveis/3/3145/tde-08032005-160218/pt-br.php>
- Oliveira Junior, A.I., Jucá, J.F.T., & Ferreira, J.A. (2018). Análise da resistência ao cisalhamento de misturas de solo argiloso com resíduos fibrosos da casca do coco (*Coco nucíferas*). In *Anais do XIX Congresso Brasileiro de Mecânica dos Solos e Engenharia Geotécnica*, Porto.
- Raj, S., Mohammad, S., Das, R., & Saha, S. (2017). Coconut fiber-reinforced cement-stabilized rammed earth blocks. *World Journal of Engineering*, 14(3), 208-216. <http://dx.doi.org/10.1108/WJE-10-2016-0101>.
- Romero, E., & Simms, P.H. (2008). Microstructure investigation in unsaturated soils: a review with special attention to contribution of mercury intrusion porosimetry and environmental scanning electron microscopy. *Geotechnical and Geological Engineering*, 26(6), 705-727. <http://dx.doi.org/10.1007/s10706-008-9204-5>.
- Romero, E., Gens, A., & Lloret, A. (1999). Water permeability, water retention and microstructure of unsaturated compacted Boom clay. *Engineering Geology*, 54(1-2), 117-127. [http://dx.doi.org/10.1016/S0013-7952\(99\)00067-8](http://dx.doi.org/10.1016/S0013-7952(99)00067-8).
- Sachetti, D.A. (2012). *Solo reforçado com cal e fibras de polipropileno: comportamento quando submetido à compressão triaxial* [Bachelor dissertation, Federal University of Rio Grande do Sul]. University of Rio Grande do Sul's repository (in Portuguese). Retrieved in December 3, 2013, from <https://www.lume.ufrgs.br/handle/10183/79748>
- Savastano Júnior, H., & Pimentel, L. (2000). Suitability of vegetable fiber residues as construction material. *Revista Brasileira de Engenharia Agrícola e Ambiental*, 4(1), 103-110. <http://dx.doi.org/10.1590/S1415-43662000000100019>.
- Sun, W.J., & Cui, Y.J. (2020). Determining the soil-water retention curve using mercury intrusion porosimetry test in consideration of soil volume change. *Journal of Rock*

- Mechanics and Geotechnical Engineering*, 12(5), 1070-1079. <http://dx.doi.org/10.1016/j.jrmge.2019.12.022>.
- Toledo Filho, R.D., Joseph, K., Ghavami, K., & Englang, G.L. (1999). The use of sisal fibre as reinforcement in cement based composites. *Revista Brasileira de Engenharia Agrícola e Ambiental*, 3(2), 245-256. <http://dx.doi.org/10.1590/1807-1929/agriambi.v3n2p245-256>.
- van Genuchten, M.Th. (1980). A closed-form equation for predicting the hydraulic conductivity of unsaturated soils. *Soil Science Society of America Journal*, 44(5), 892-898. <http://dx.doi.org/10.2136/sssaj1980.03615995004400050002x>.
- Villar, L.F.S., De Campos, T.M.P., & Zornberg, J.G. (2007). Relationship between tensile strength as obtained by the Brazilian test, soil suction, and index properties. In *Proceedings of the 6th Brazilian Symposium on Unsaturated Soils* (Vol. 1, pp. 421-432), Salvador, BA.
- Wang, J., Wang, Q., Kong, Y., Han, Y., & Cheng, S. (2020). Analysis of the pore structure characteristics of freeze-thawed saline soil with different salinities based on mercury intrusion porosimetry. *Environmental Earth Sciences*, 79(161), 161. <http://dx.doi.org/10.1007/s12665-020-08903-w>.
- Yadav, J.S., & Tiwari, S.K. (2016). Behaviour of cement stabilized treated coir fibre-reinforced clay-pond ash mixtures. *Journal of Building Engineering*, 8, 131-140. <http://dx.doi.org/10.1016/j.jobe.2016.10.006>.

Mechanical and numerical behavior of water jet-driven under-reamed concrete piles

Cesar Alberto Ruver^{1#} , Giovanni Jordi Bruschi¹ 

Article

Keywords

Under-reamed pile behavior
Finite element method (FEM)
Laboratory pile tests
Mini-cone tests
Numerical modelling
Water jet pile driving

Abstract

Water jet-driving technique has been shown as a viable practice for driving prefabricated piles in resistant soil layers. However, this technique is also associated with the reduction of load capacity of piles. Along these lines, the use of reams in prefabricated concrete piles improves their mechanical performance. The main objective of this research was to study the efficiency of reams on water jet-driven concrete piles; to this extent, pile loading tests and mini-cone tests were carried out before and after the driving of the piles. In addition, numerical modelling with the finite element method (*FEM*) was applied to study the stress-strain behavior. By means of the numerical modelling, it was possible to identify the stress and strain distribution at the tip, shaft, and reams of the piles; this allowed the understanding of the contribution of these elements in the total load capacity. Results have shown that the reams directly contribute for load capacity, with increases up to 40% when compared to conventional piles. Laboratory tests and numerical modeling proved to be fundamental tools to understand the mechanisms behind the contribution of reams to the load capacity of piles.

1. Introduction

Free fall hammers are traditionally utilized for the driving of prefabricated piles; international and national standards can be found with recommendations regarding the minimum weights of these hammers. The Brazilian standard for foundations (NBR 6122 - ABNT, 2019) indicates that for precast piles, hammers with a minimum weight of 40 kN should be utilized for workloads between 0.7 to 1.3 MN, in addition to a minimum weight of 75% of the pile weight. The aforementioned standard also refers to the maximum limits of compressive and tensile strength of the driving systems, considering the strength of the applied concrete. Sean Yoon (2014), recommends a minimum hammer weight of 12.5 kN, which should also be higher than a fourth of the pile weight. Wardani et al. (2020) state that, the hammer weight should be 50% of the pile weight plus a value of 6 kN. In this sense, if the hammer weight is not enough to surpass the strength of the soil, the specified foundation depth may not be reached or even structural damage to the piles may be evidenced. For such cases, the water jet-driving technique is recommended.

Although the water jet-driving technique is a consolidated practice in foundation engineering, several studies indicate that

this driving method may compromise the strength of the soil, reducing its load capacity (Tsinker, 1988; Gunaratne et al., 1999; Mezzomo, 2009; Ruver et al., 2014; Passini, 2015; Moriyasu et al., 2016a, b). Mezzomo (2009) and Passini (2015) observed that, regardless the initial compaction degree (medium or dense) of the soil, the application of the water jet for pile driving results in a soil with a final loose state. Ruver et al. (2014), verified a load capacity loss between 53% and 90% in reduced models of concrete piles driven in fine sand, compared to the same models driven by percussion; authors also indicated that, higher flow rates also resulted in higher reductions in load capacity. Passini (2015) stated that the construction/operation procedures and the initial soil condition are factors that control the final load capacity of piles. Ruver & Jong (2019) verified that the initial compactness of the soil influences the load capacity of water jet-driven piles; nevertheless, the final soil state around the pile was the same for all cases.

Several authors have studied the effects of enlarged sections (i.e., reams) on the load capacity of piles, varying the number, position and shape (Mohan et al., 1969; Yabuuchi & Hirayama, 1993; Lee, 2007; Hirai et al., 2008; Honda et al., 2011; Choi et al., 2013; Qian et al., 2013; Christopher & Gopinath, 2016; George & Hari, 2015; Shetty et al., 2015;

[#]Corresponding author. E-mail address: cesar@ufrgs.br

¹Universidade Federal do Rio Grande do Sul, Programa de Pós-Graduação em Engenharia Civil, Porto Alegre, RS, Brasil.

Submitted on December 2, 2022; Final Acceptance on April 1, 2023; Discussion open until August 31, 2023.

<https://doi.org/10.28927/SR.2023.012822>



This is an Open Access article distributed under the terms of the Creative Commons Attribution License, which permits unrestricted use, distribution, and reproduction in any medium, provided the original work is properly cited.

Zarrabi & Esmali, 2016; Moayedi & Mosallanezhad, 2017; Vali et al., 2017; Zhang et al., 2018; Majumder & Chakraborty, 2022; Ziyara & Albusoda, 2022). In general, the insertion of reams improved the load capacity of the piles. Ruver (2013) evaluated the efficiency of a model of precast concrete pile with three reams driven by water jet, which presented more than twice the load capacity compared to the same pile without reams.

In order to better understand the bearing mechanism and contribution of the reams to the final load capacity of piles, several authors have been performing numerical modelling (Lee, 2007; Honda et al., 2011; George & Hari, 2015; Harris & Madabhushi, 2015; Moayedi & Mosallanezhad, 2017; Vali et al., 2017; Jong, 2019; Ruver & Jong, 2019; Ruver et al., 2019; Majumder & Chakraborty, 2022; Ziyara & Albusoda, 2022). In this context, the works of Jong (2019) and Ruver et al. (2019) demonstrated that, for short piles, two reams are sufficient, one placed at the toe and the other positioned in the intermediate portion of the shaft with a distance of three times the ream width, regardless of the ream thickness.

In this sense, the objective of this research was to evaluate the influence of reams on the bearing capacity of prefabricated concrete piles. To this extent, pile loading tests in reduced-scale were conducted; in such tests, optimized dimensions were utilized: (a) width/diameter of the reams were twice the width/diameter of the pile shaft; and (b) spacing between three width/diameter of the reams, plus two other configurations with a ream, at the toe or intermediate position of the shaft. FEM numerical modeling was applied to obtain the stress-strain behavior of the tests and determine the plastification strain zones of the soil, in addition to the normal stresses under the reams and shear stresses of the lateral faces of the piles. Penetrometric were carried out with a mechanical mini cone before and after driving the piles with a water jet to confirm the effect of strength loss in the area affected by the water jet.

2. Pile loading test (scaled-down)

The scale-down pile loading tests were conducted on precast square section piles with reduced dimensions, 0.50 m long and 0.05 cm on the shaft side, corresponding to 1:4 scale of a true size pile (0.20 m × 0.20 m cross-section). Four types of piles were studied (Figure 1): (a) without reams; (b) one ream at the toe (*T*); (c) one ream at the toe and one intermediate ream (*TI*); (d) one intermediate ream (*I*). The *TI* pile (a ream at the toe and another above the middle) is the model that presents the optimized geometry; it possesses a spacing of 0.30 m between the reams (3 times the ream width), as indicated by Qian et al. (2013), George & Hari (2015), Shetty et al. (2015), Jong (2019), and Ruver et al. (2019).

The tests were carried out in a stainless-steel tank of 0.7 m in diameter and 0.7 m in height. The tank was filled with a fine sand, from Osório town, south coast of Brazil,

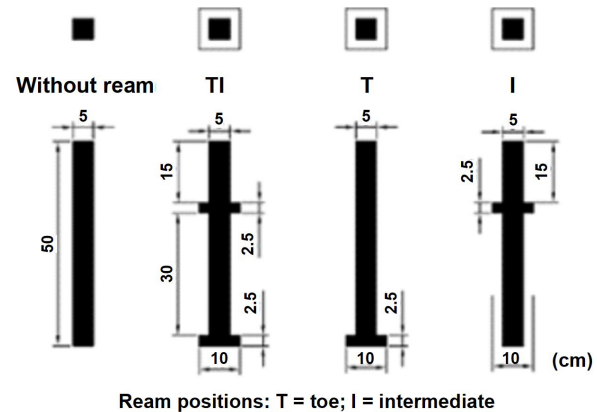


Figure 1. Tested piles models.

($\rho_s = 2.65 \text{ g/cm}^3$, $e_{min} = 0.6$ and $e_{max} = 0.9$). The sand was compacted in 10 cm layers with a manual wood socket, in the wet state (moisture content of 20%), and at a dry unit weight (ρ_d) of 1.559 g/cm^3 (equivalent to a compaction degree of 66.67%). After compacting the sand at the predetermined moisture content, the piles were inserted. First, two tests were carried out with piles without reams, one driven by percussion and the other by pressing, which served as reference for the loading capacity. The other piles were water jet-driven with a flow rate of $2.5 \text{ m}^3/\text{h}$ and jet speed of 5.89 m/s . After the end of the driving procedure, the excess water was drained.

Before and after driving the piles, a mechanical mini-cone was inserted in the compacted soil. The mini-cone had a diameter of 7.9 mm with an inclination of 60° . The mini-cone was inserted at a constant speed of 3.5 mm/s . The driving strength was measured externally at the top of the rod, using a load cell with a capacity of 1 kN; considering that the reading of the applied load is external, it corresponds to the tip strength plus the skin friction of the soil. Before the driving of the piles, the mini-cone penetration was carried out in the center of the tank to evaluate the homogeneity of the compacted soil layers. After pile driving, the mini-cone penetration was performed by water jet within the fluidized zone to identify and quantify the loss of soil strength.

The pile loading tests were conducted after pile driving and mini-cone penetration. The applied load was measured with a 20 kN (2,000 kgf) load cell. Displacements were measured using two 50 mm transducers, installed in opposite positions. For the load application, a 50 kN (5,000 kgf) hydraulic jack was used. The tests followed the procedures indicated by ASTM D 1143M (ASTM, 2020), in which the test is conducted with incremental load with each increment being 5% of the probable failure load, and maintained for 4 to 15 minutes each.

3. Numerical modelling

The Finite Element Method (FEM) with a 3D model was utilized for the numerical modelling. Piles and tank

dimensions are the same presented on section 2. For the fluidized zone, a prismatic zone surrounding the pile was considered with a width equal to twice the largest width of the piles, as indicated by Passini (2015). As for the boundary conditions, displacements in all three dimensions were prevented in the bottom ($\Delta x = \Delta y = \Delta z = 0$); while on the sides, only vertical displacements were allowed, preventing horizontal displacement ($\Delta x = \Delta y = 0$ and $\Delta z = \text{free}$), and the surface (top of the tank) was free.

Considering that the structural behavior was not the focus of this research, a linear-elastic constitutive model was attributed to the piles; with the elastic parameters estimated in accordance with the applied mortar. As for the soil, an elastic perfectly-plastic model was utilized, applying the Mohr-Coulomb failure criterion. The strength parameters for the soil were obtained in the work of Corte et al. (2017). A summary of the utilized parameters can be seen in Table 1.

The numerical modeling was divided into two steps: (a) application of the geostatic conditions; and (b) loading of the piles (total vertical displacement of 50 mm, applied in 50 increments). The displacement was applied at the top central node (master point), with the entire upper face linked to this node (slave surface), so that each applied displacement results in a reaction load at the same node. Steps of 1 second were adopted for the load application time, considering that the analysis was conducted as a drained condition. In the contact interfaces, two configurations were used: (a) rigid connection type (tie) (compacted and fluidized sand); and (b) friction interaction type (with roughness of 0.3) (penalty) and adherence (hard contact). The discretization of the mesh was

made by rectangular elements of the structured type, with the central elements with 25 mm spacing between nodes. For the edge nodes, a spacing of 50 mm was adopted. As it is a three-dimensional modeling, elements composed of 8 nodes were used with reduced integration and processing time control. The average time for each modeling was 3 hours. Figure 2 shows the mesh discretization.

4. Results and discussion

Figure 3 presents the results of load versus settlement obtained in the numerical modeling, in comparison with the results of the laboratory tests carried out with the reduced models. Figure 4 shows a compilation of the results from numerical modeling. Up to a certain load, the numerical models converge with the results of the laboratory tests, at least up to settlements of of 7.5 mm failure criterion of ASTM D1143 (ASTM, 2020). For large loads (and settlements), some of the tested piles presented issues during testing (e.g., cracking of the reams); this behavior was not represented in the numerical modelling, considering that an elastic model was applied to the piles. Nonetheless, the behavior of the piles was fully represented up to the maximum levels of strain of ASTM D1143 (ASTM, 2020). Compared to the percussion-driven pile, the water jet-driven pile without reams presented a lower load capacity. On the other hand, the addition of reams recovered the lost bearing capacity and, in some cases, even increased it depending on the position and quantity of the reams (Figure 4).

Table 1. Numerical modelling parameters.

Material	ρ_{subm} (g/cm ³)	E (MPa)	ν	ϕ' (°)	ψ (°)	c' (kPa)
Pile		20,000.0	0.2	-	-	-
Compacted soil	0.85	3.0	0.3	28	7.5	~2
Fluidized soil		1.8	0.3	20	0	~2

Legend: see List of Symbols.

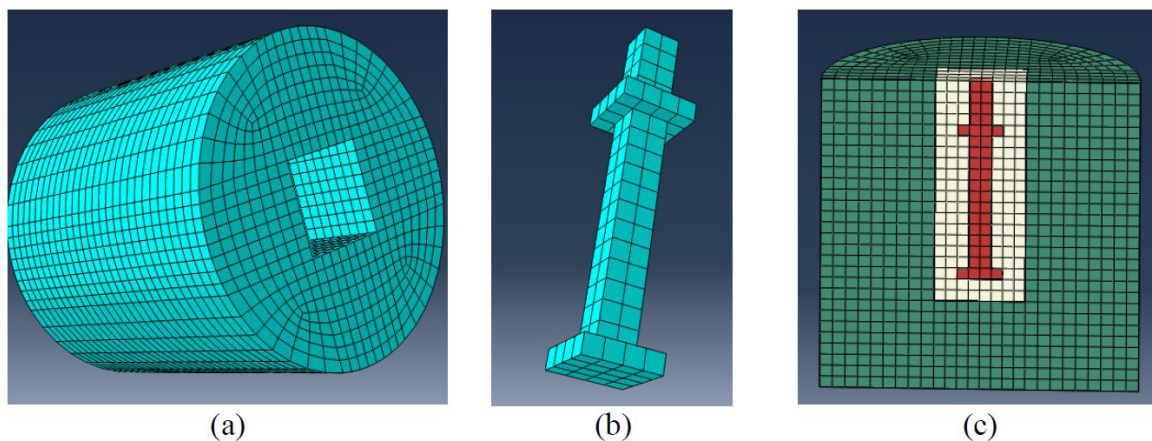


Figure 2. Mesh discretization: (a) compacted soil; (b) pile; (c) 3D model.

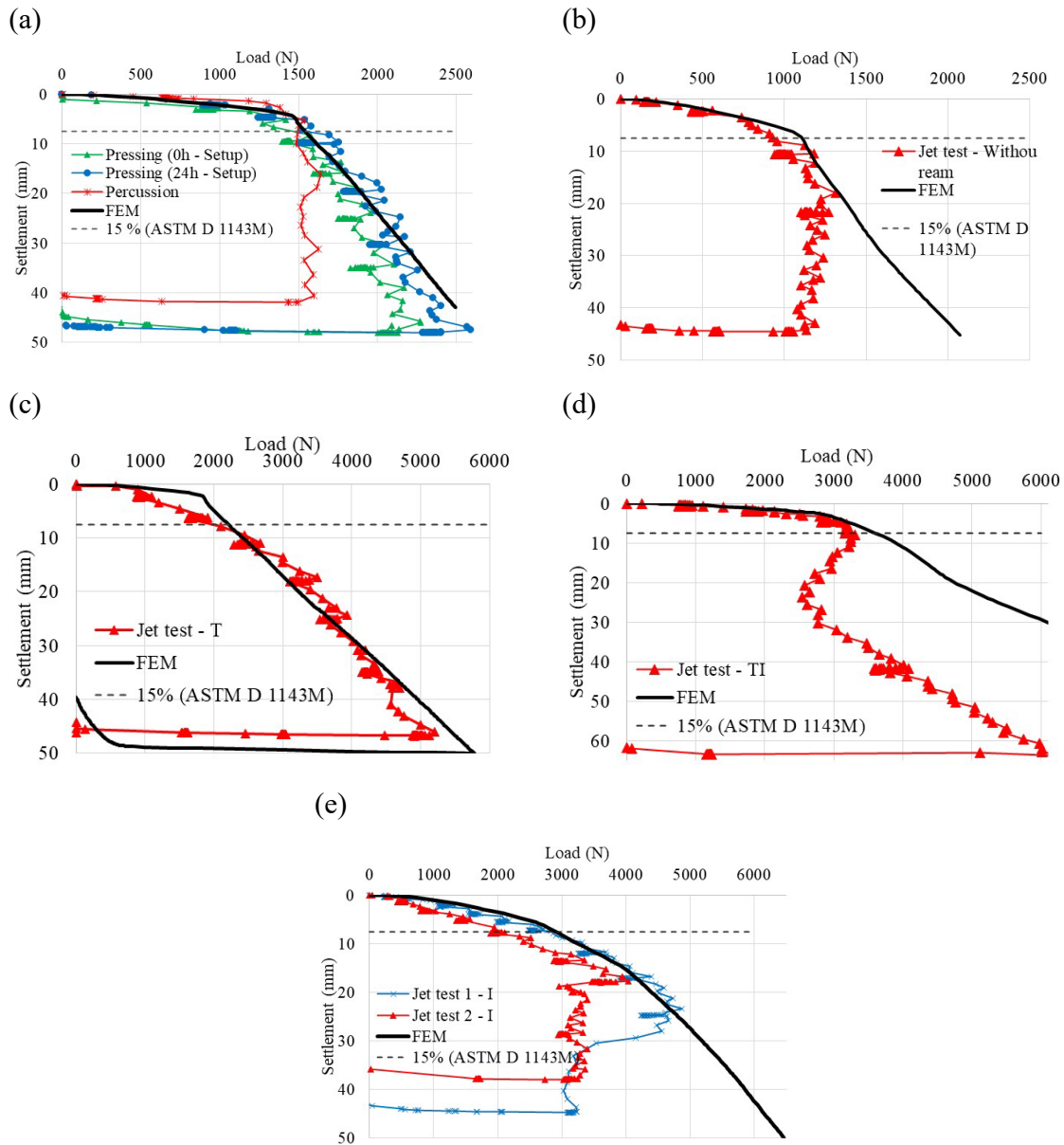


Figure 3. Comparison between laboratory and numerical results: (a) percussion drive – no ream; (b) water jet driven – no ream; (c) *T*; (d) *TI*; (e) *I*.

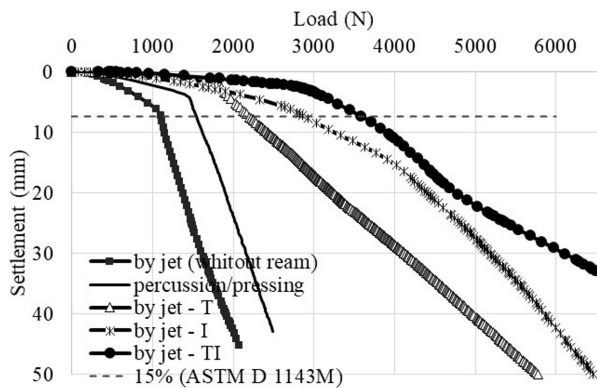


Figure 4. Numerical modeling for all tests.

The pile with two reams (*TI*) presented a better mechanical performance than both one-ream piles [i.e. toe (*T*) and intermediate (*I*)]. When comparing the one-ream piles, *T* piles resulted in a higher load capacity for small displacements, while *I* piles for great displacements. The same behavior was evidenced in the laboratory tests. The aforementioned behavior has also been attested by several studies (e.g., George & Hari (2015), Christopher & Gopinath (2016), Zarrabi & Esmali (2016)), in which two-reams piles result in a better mechanical performance when compared to one-ream ones.

Figure 5 shows the mini-cone results, before and after the driving of the piles. An increasing strength of linear

tendency was evidenced, indicating the homogeneity of the tested soil regarding its dry unit weight and compaction conditions. Also, it was possible to observe the deleterious effect of the water jet; represented by the reduction in strength of the mini-cone after the driving of the piles. Such an effect was more prominent in intermediate ream (*I*) piles, with strength losses up to 66%. The *I* piles presented the most execution/driving difficulties, considering that the water jet was concentrated at the tip and, consequently, was more concentrated near the shaft; thus, for the insertion of the widened portion, the fluidized region was narrower, causing more disturbance on the surroundings. The two-reams pile (*TI*) presented the lowest strength loss (50%); despite

demanding a higher execution period, the disturbed region was wider, facilitating the introduction of the first (toe) and second (intermediate) reams, allowing better confinement of the soil between the reams. As for the *T* pile, the driving process was similar to the *TI* pile; however, as the disturbed region was larger due to the ream, less confinement was evidenced on the soil close to the shaft.

Figure 6 presents the plastic strain results for settlements of 7.5 mm. For the *T* pile (Figure 6a), the plastic strain is concentrated along the lateral of the ream, with a larger strain area below the ream and smaller above it; also, a stress bulb was formed within the non-fluidized zone, while the other strains were concentrated within the fluidized zone. For large strains (settlements of 50 mm), the same behavior was evidenced, with the plastification zone advancing in the surroundings of the ream. As for the *I* pile (Figure 6b), plastic strains were verified along the ream and the tip for small settlements (7.5 mm), also presenting a larger strain area below the ream and smaller above it; for large settlements (50 mm) the same behavior was maintained, with plastic strains along the entire shaft advancing to the surface. Finally, for the *TI* pile (Figure 6c), the formation of a plastic zone within the fluidized zone was evidenced, covering the upper part of the intermediate ream, advancing vertically on the reams reaching the lower base from the ream of the base,

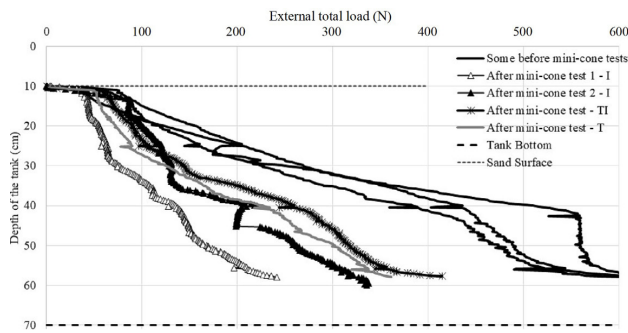


Figure 5. Mini-cone results.

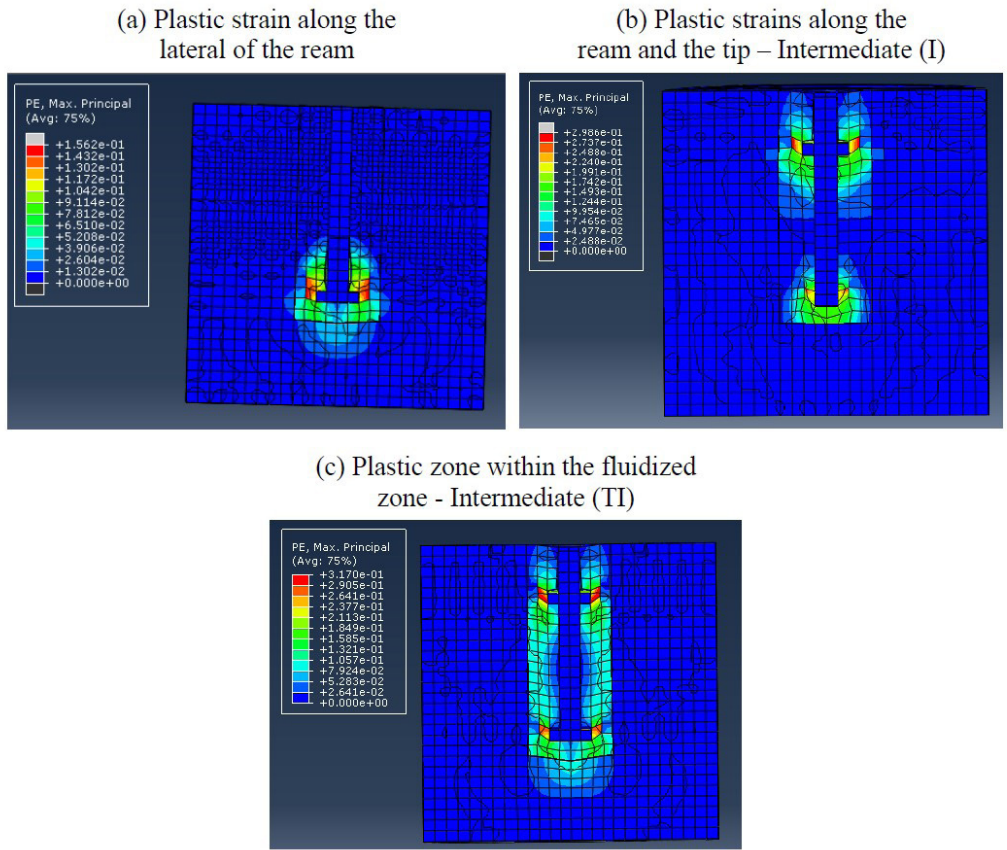


Figure 6. Plastic strains for settlements of 7.5 mm for the (a) *T* pile, (b) *I* pile, and (c) *TI* pile.

with no plastic strain on the soil between the reams. Also, for the pile with two reams (Figure 6c), there was the formation of a plastification zone reaching all the fluidized sand and the base bulb considerably invaded the non-fluidized sand.

Through numerical modeling it was possible to quantify the contribution of each of the components to the final load capacity. For uniform piles (continuous shaft), the load capacity is composed of lateral friction and tip strength. For reamed piles, the reams also contribute for strength generation, which in turn results in compressive loads on the soil. Figure 7a shows the distribution of compressive stresses under the reams and Figure 7b shows the distribution of lateral friction along the shaft and reams. Table 2 presents a compilation of the distribution of each of the portion of the total load capacity for a settlement of 7.5 mm.

Piles driven by conventional techniques presented a total load capacity of 1,576 N, while the one driven by water-jet presented a total load capacity of 1,127 N, which corresponds to a reduction of 28.5%. All three piles presented the same load contribution referring to tip and lateral friction (Figure 7b), with most of the load capacity being associated with tip contribution (>95%).

The toe ream pile (T), driven by water-jet, presented a total load capacity of 2,206 N; 40% higher than the percussion-driven pile and 96% higher than the water-driven pile with no ream (J). For the T pile, the tip strength corresponds to most of the load capacity contribution (>99.7%); this behavior is associated with the ream presence, preventing the confinement of the soil along the shaft and, consequently, the mobilization of lateral friction, as can be seen in Figure 7b.

For the intermediate ream pile (I), the total load capacity was 2,862 N; 82% higher than the conventional piles (P/P). The intermediate ream was shown to be more efficient than the toe ream. In terms of ream contribution, 57.3% of the load capacity was attributed to the ream while 42.6% to the tip strength. The remaining load capacity was attributed to the shaft, being considered insignificant. Friction was only mobilized along the lateral faces of the ream (Figure 7b). For one ream piles (T or I), the tip strength is similar to water jet driven piles with no ream (J), indicating that the load capacity increase (57.3%) is related to the reams presence.

The two reams pile (TI) presented a total load capacity of 3,590 N; corresponding to more than 125% comparing to the reference pile (J/J) and more than triple the total

load capacity of the water jet driven piles with no ream (J). Both reams presented similar contributions: 21.2% for the intermediate ream and 25.6% for the base ream. Together, the reams correspond to almost half of the mobilized load capacity. Analyzing Figure 7b, it is verified that the TI pile presents the highest lateral friction, which in turn reflects the highest value of total friction among the other piles.

The strength reduction of the soil (due to the fluidization process) was similar in all tests (Figure 5), while the increase in bearing capacity was attributed to the reams. The presence of one ream promoted a considerable increase in the bearing

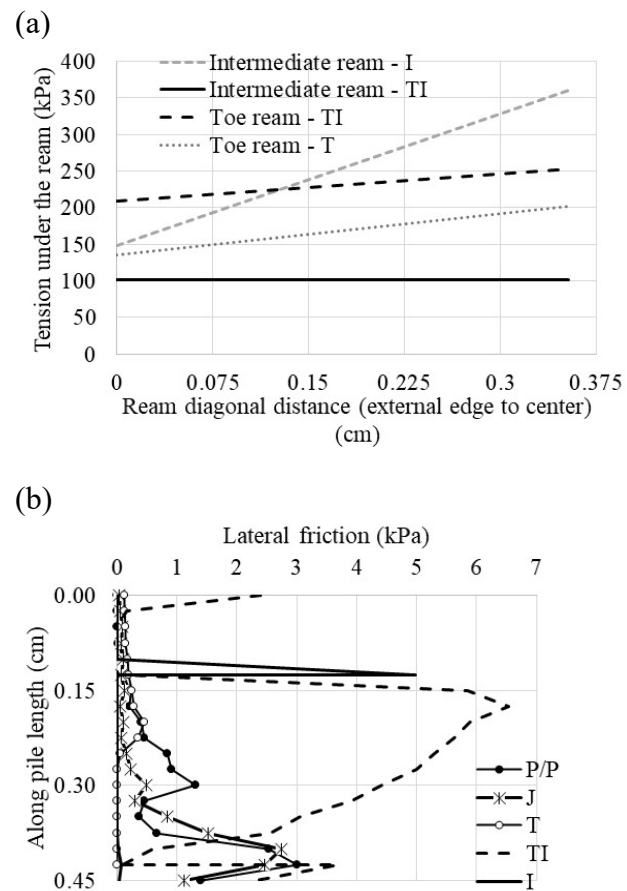


Figure 7. Stress distribution of (a) compression under of the ream, (b) shear (lateral friction) along the shaft and side of the reams for a 7.5 mm settlement.

Table 2. Load contribution of the elements for a settlement level of 7.5 mm.

Pile type	P/P		J		T		I		TI	
	N	%	N	%	N	%	N	%	N	%
Load at 7.5 mm										
Toe	1,514	96.1	1,077	95.6	936	42.4	1,220	42.6	1,720	47.9
Toe ream	-	-	-	-	1,265	57.3	-	-	920	25.6
Intermediate ream	-	-	-	-	-	-	1,641	57.3	760	21.2
Lateral friction	62	3.9	50	4.4	5	0.2	1	0.03	190	5.3
Total	1,576		1,127		2,206		2,862		3,590	

Legend: see List of Symbols.

capacity (96% to 218%), which in turn could be enhanced with the adequate positioning of this structural element. Although presenting a lower initial stiffness (Figure 4), the ream on the intermediate position resulted in a better mechanical performance when compared to the toe ream; with this behavior being attributed to the higher combined strength mobilization of the tip and the ream. For one-ream piles, current studies diverge on the best positioning of the ream, stating that different conditions (e.g., soil type, pile material, and ream shape) directly influence this behavior. Christopher & Gopinath (2016) state that, for metallic piles in sandy soil, toe reams result in the best mechanical behavior, in addition, regarding the ream positioning, the furthest from the tip, the lowest the bearing capacity of the pile. Ziyara & Albusoda (2022) studied piles driven in fine-grained soil, concluding that toe reams also result in the highest bearing capacity for saturated conditions; however, for unsaturated conditions, the best mechanical behavior is evidenced when the ream is more distant from the toe.

For piles with more than one ream, different studies have shown that the higher the number of reams, the higher the bearing capacity (considering a minimum distance so the reams can mobilize strength individually). For short piles, such as the case of this study, the bearing capacity was enhanced with two reams spaced three times the width of each ream. With that in mind, several studies also corroborate that the spacing of the reams is the most important factor for strength mobilization, alongside with ream number (Qian et al., 2013; George & Hari, 2015; Shetty et al., 2015; Moayedi & Mosallanezhad, 2017; Jong, 2019; Ruver et al., 2019).

5. Conclusions

The present research evaluated the influence of reams on the bearing capacity of prefabricated piles, both experimentally and numerically. Based on the findings of this research, the following conclusions can be disclosed:

- The utilization of prefabricated piles with enlarged sections – reams, not only recovers the load capacity lost by the deleterious effect of the water jet but also results in a load capacity superior to a pile of uniform section driven by percussion.
- Carrying out pile loading tests with reduced models in the laboratory, combined with the use of the mini-cone test before and after driving the piles, was essential to understand the bearing mechanism of the reams and the loose of load capacity effect by water-jet;
- The adopted numerical modeling proved to be efficient, as it was able to reproduce the stress-strain behavior of the load tests with the reduced models up to the failure criterion indicated by ASTM (2020);
- Through the numerical modeling it was possible to obtain the plastic deformation diagrams of the soil and the normal and shear stresses that act along all the faces of the piles. These elements were of fundamental importance, as they allowed understanding

the bearing mechanism of the reams, as well as the estimation of the load contribution of each element in the total load capacity of the piles.

Declaration of interest

The authors have no conflicts of interest to declare. All co-authors have observed and affirmed the contents of the paper and there is no financial interest to report.

Authors' contributions

Cesar Alberto Ruver: Conceptualization, Methodology, Data curation, Visualization, Writing, Editing – original draft. Giovanni Jordi Bruschi: data analyzing, writing, reviewing, editing.

Data availability

The datasets generated analyzed in the course of the current study are available from the corresponding author upon request.

List of symbols

c'	effective cohesive intercept
e_{max}	maximum void ratio
e_{min}	minimum void ratio
E	elasticity modulus
I	intermediate ream position
J	jet water driven of pile without under ream
P/P	percussion and pressing driven
T	toe ream position
TI	toe and toe reams positions
ϕ'	effective friction angle
ν	<i>Poisson</i> coefficient
ρ_d	specific mass of dry soil
ρ_s	specific mass of solids
ρ_{subm}	specific mass of submerged soil
Ψ	dilatancy

References

- ABNT NBR 6122. (2019). *Design and construction of foundations*. ABNT - Associação Brasileira de Normas Técnicas, Rio de Janeiro, RJ (in Portuguese).
- ASTM D1143. (2020). *Standard test methods for deep foundation elements under static axial compressive load*. ASTM International, West Conshohocken, PA. https://doi.org/10.1520/D1143_D1143M-20.
- Choi, Y., Kim, D., Kim, S., Nam, M.S., & Kim, T. (2013). Implementation of noise-free and vibration-free PHC screw piles on the basis of full-scale tests. *Journal of Construction Engineering and Management*, 139(8),

- 960-967. [http://dx.doi.org/10.1061/\(ASCE\)CO.1943-7862.0000667](http://dx.doi.org/10.1061/(ASCE)CO.1943-7862.0000667).
- Christopher, T., & Gopinath, B. (2016). Parametric study of under-reamed piles in sand. *International Journal of Engineering Research & Technology (Ahmedabad)*, 5(7), 577-581. <http://dx.doi.org/10.17577/IJERTV5IS070450>.
- Corte, M.B., Festugato, L., & Consoli, N.C. (2017). Development of a cyclic simple shear apparatus. *Soils and Rocks*, 40(3), 279-289. <http://dx.doi.org/10.28927/SR.403279>.
- George, B.E., & Hari, G. (2015). Numerical investigation of under reamed pile. In *6th International Geotechnical Symposium*, Chennai, India. Retrieved in December 2, 2022, from https://igschennai.in/IGC2016_IIT_Madras/igc2016proceedings/papers/THEME2/IGC_2016_paper_487.pdf
- Gunaratne, M., Hameed, R.A., Kuo, C., Reddy, D.V., & Patchu, S. (1999). *Investigation of the effects of pile jetting and preforming* (Technical Report N. 772). Florida Department of Transportation.
- Harris, D. E., Madabhushi, G. S. P. (2015). Uplift capacity of an under-reamed pile foundation. *Proceedings of the Institution of Civil Engineers - Geotechnical Engineering*, 168(6), 526-538. <https://doi.org/10.1680/jgeen.14.00154>.
- Hirai, Y., Wakai, S., & Aoki, M. (2008). Development of multi-belled cast-in-place concrete pile construction method. *Journal of Technology and Design*, 14(28), 433-438. <http://dx.doi.org/10.3130/aijt.14.433>.
- Honda, T., Hirai, Y., & Sato, E. (2011). Uplift capacity on belled and multi-belled piles in dense sand. *Soil and Foundation*, 51(3), 483-496. <http://dx.doi.org/10.3208/sandf.51.483>.
- Jong, G.V.D. (2019). *Modelagem numérica do comportamento de estacas nervuradas cravadas por jato de água* [Undergraduate thesis, Federal University of Rio Grande do Sul]. Federal University of Rio Grande do Sul's repository (in Portuguese). Retrieved in December 2, 2022, from <http://hdl.handle.net/10183/200223>.
- Lee, C.Y. (2007). Settlement and load distribution analysis of underreamed piles. *Journal of Engineering and Applied Sciences (Asian Research Publishing Network)*, 2(4), 36-40.
- Majumder, M., & Chakraborty, D. (2022). Bearing capacity of under-reamed piles in clay using lower bound finite element limit analysis. *International Journal of Geotechnical Engineering*, 16(9), 1104-1115. <http://dx.doi.org/10.1080/19386362.2022.2044102>.
- Mezzomo, S.M. (2009). *Study of the fluidisation mechanism in sandy soils using water jets* [Master's dissertation, Federal University of Rio Grande do Sul]. Federal University of Rio Grande do Sul's repository (in Portuguese). Retrieved in December 2, 2022, from <http://hdl.handle.net/10183/23970>.
- Moayed, H., & Mosallanezhad, M. (2017). Uplift resistance of belled and multi-belled piles in loose sand. *Measurement*, 190, 346-353. <http://dx.doi.org/10.1016/j.measurement.2017.06.001>.
- Mohan, D., Murthy, V.N.S., & Jain, G.S. (1969). Design and construction of multi-underreamed piles. In *7th International Conference of Soil Mechanics and Foundation Engineering* (Vol. 2, pp. 183-186). Mexico: Sociedad Mexicana de Mecanica.
- Moriyasu, S., Ishihama, Y., Takeno, T., Taenaka, S., Kubota, K., Tanaka, R., Nishiumi, K., & Harata, N. (2016a). Development of new-type steel-pile method for port facilities. In *Nippon Steel & Sumitomo Metal Technical Report* (pp. 50-56). Tokyo: Nippon Steel.
- Moriyasu, S., Morikawa, Y., Yamashita, H., & Taenaka, S. (2016b). Evaluation of the vertical bearing capacity of steel pipe piles driven by the vibratory hammer Method with water and cement milk jetting. In *15th Asian Regional Conference on Soil Mechanics and Geotechnical Engineering* (pp. 1291-1295). Tokyo: Japanese Geotechnical Society Special Publication. <https://doi.org/10.3208/jgssp.JPN-126>.
- Passini, L.B. (2015). *Installation and axial load capacity of fluidized model piles in sandy soils* [Master's dissertation, Federal University of Rio Grande do Sul]. Federal University of Rio Grande do Sul's repository (in Portuguese). Retrieved in December 2, 2022, from <http://hdl.handle.net/10183/131011>.
- Qian, Y., Xu, G., Wang, R. (2013). Experimental research on failure behavior of soil around pile under compression. *Indonesian Journal of Electrical Engineering and Computer Science*, 11(4), 2013-2017. <http://dx.doi.org/10.11591/telkomnika.v11i4.2377>.
- Ruver, C.A. (2013). *Estudo do comportamento de estacas pré-fabricadas cravadas por jato de água (research report)*. Rio Grande: FURG. (in Portuguese).
- Ruver, C.A., & Jong, G.V.D. (2019). Estacas nervuradas cravadas por jato de água: análise paramétrica da influência da compactação. In *X Seminário de Engenharia Geotécnica do Rio Grande do Sul* (pp. 1-9). São Paulo: ABMS. (in Portuguese).
- Ruver, C.A., Ferronato, B., Dalla Vecchia, D., Spaniol, E.M.R., Silva, G.G., & Palomino, J.M.V. (2014). Comparação entre cravação por percussão e jato de água. In *XVII Congresso Brasileiro de Mecânica dos Solos e Engenharia Geotécnica* (pp. 1-10). São Paulo: ABMS. (in Portuguese)
- Ruver, C.A., Jong, G.V.D., & Peres, M.S. (2019). Modelagem numérica do comportamento de estacas nervuradas cravadas por jato de água. In *XII Simpósio de Práticas de Engenharia Geotécnica da Região Sul* (pp. 1-10). Joinville: UFSC (in Portuguese).
- Sean Yoon, P.E. (2014). *Pile driving best practice* (TxDOT Bridge Presentations Webinar). Texas Department of Transportation.
- Shetty, P., Naveen, B.S., & Naveen, K.B.S. (2015). Analytical study on geometrical features of under-reamed pile by

- Anslys. *International Journal of Modern Chemistry and Applied Science*, 2(3), 174-180.
- Tsinker, G. (1988). Pile jetting. *Journal of Geotechnical Engineering*, 114(3), 326-334.
- Vali, R., Khotbehsara, E.M., Saberian, M., Li, J., Mehrinejad, M., & Jahandari, S. (2017). A three-dimensional numerical comparison of bearing capacity and settlement of tapered and under-reamed piles. *International Journal of Geotechnical Engineering*, 13(3), 236-248. <http://dx.doi.org/10.1080/19386362.2017.1336586>.
- Wardani, M.K., Aulady, M.F.N., Frido, W., & Handri, S. (2020). Determining the weight of the hammer based on expert experience for estimating load-carrying capacity. *IOP Conference Series. Materials Science and Engineering*, 1010, 012041. Retrieved in December 2, 2022, from <https://iopscience.iop.org/article/10.1088/1757-899X/1010/1/012041/pdf>
- Yabuuchi, S., & Hirayama, H. (1993). Bearing mechanisms of nodal piles in sand. In W.F. Van Impe & P.O. Van Impe (Eds.), *Deep foundations on bored and auger piles* (pp. 333-336). Balkema.
- Zarrabi, M., & Esmali, A. (2016). Behavior of piles under different installation effects by physical modeling. *International Journal of Geomechanics*, 16(5), 04016014. [http://dx.doi.org/10.1061/\(ASCE\)GM.1943-5622.0000643](http://dx.doi.org/10.1061/(ASCE)GM.1943-5622.0000643).
- Zhang, L., Chen, Q., Gao, G., Ninbalkar, S., & Chiaro, G. (2018). A new failure load criterion for large-Diameter under-reamed piles: practical perspective. *International Journal of Geosynthetics and Ground Engineering*, 4(3), 1-9. <http://dx.doi.org/10.1007%2Fs40891-017-0120-8>
- Ziyara, H.M., & Albusoda, B.S. (2022). Experimental and numerical study of the bulb's location effect on the behavior of under-reamed pile in expansive soil. *Journal of the Mechanical Behavior of Materials*, 31(1), 90-97. <http://dx.doi.org/10.1515/jmbm-2022-0010>.

Semi-empirical method for the bearing capacity of continuous flight auger piles based on installation energy

Carlos Medeiros Silva^{1#} , José Camapum de Carvalho² 

Article

Keywords

Continuous Flight Auger (CFA)
Energy
Load capacity
SCCAP methodology

Abstract

The prediction of load capacity and the control of the execution of the Continuous Flight Auger (CFA) piles are often exercised with components of empiricism and intuition. This fact is often added to the uncertainties arising from the formation of the soils and the limitations of preliminary studies that support the project design. In this context, aiming to aid the executive control of CFA, a semi-empirical method is proposed based on the soil type, geometric dimensions of the piles, and the installation energy obtained during the pile excavation. The method makes it possible to determine the CFA pile load capacity during the execution process of each pile of piling. As a consequence of the proposed method, the settlement of each pile can be controlled through the quantification of the energy required or the work carried out to excavate each pile through a specific software installed in the machinery monitoring system that increases the safety and reliability of the piling.

1. Introduction

Safety and reliability in foundation engineering should be the subject of attention because only the current practice of using the safety coefficient does not guarantee the proper assessment of the risks associated with the design and execution of the project. The major source of variability in foundation engineering is the geological-geotechnical formation, affecting the performance of the soil-foundation system that is strongly influenced by stratigraphic variability along the profile and the soil as a whole. Other factors such as climate and geomorphology can also assume great relevance and their dynamics must be observed in each case.

Pile driving seeks to ensure that the design assumptions, in terms of load capacity and deformability, are met during execution. The aim is then to define in the design and execution, among the various possibilities, a resistant surface for the pile foundation's settlement levels that meets the technical, economic, and legal requirements.

In this context, Silva (2011) presented the SCCAP methodology for the control and standardization of excavated piles, specifically of the CFA type, which is based on the interpretation of the energy required or the work performed during the excavation of a pile. The methodology was developed from the understanding of the drilling rig force system and the application of the universal principle of energy conservation, which when applied to the process of excavating a pile, allows for the quantification of the energy required or needed to excavate a pile.

The theoretical basis of the methodology was presented in detail by Silva (2011) and according to the author, it can be extended to any type of excavated or displacement pile as well as to other rotary excavations, as long as it is possible to identify the force system to quantify the energy that is demanded in the process.

But even though the execution of a CFA pile involves advanced technology and controls during execution, the pile settlement quota is almost always defined by empirical and practical criteria with no theoretical or scientific basis, making the process lacking in proven effective methods and methodologies.

2. Energy at the basis of pile foundations

Fundamentally, the performance of a foundation depends on the process adopted during its execution and on the geological-geotechnical characteristics of the soil. Therefore, determining the load-bearing capacity of a foundation, a practical problem present in the daily life of geotechnical engineering, becomes a problem of difficult solution, especially in places with great geotechnical variability, because generally there are insufficient field investigations and little accuracy.

The geotechnical engineer has in most of the projects only deterministic, empirical, and semi-empirical methodologies or limited theoretical methods. Consequently, the geotechnical engineer will never obtain or be certain of the exact value,

[#]Corresponding author. E-mail address: carlos@embre.com.br

¹Embre, Brasília, DF, Brasil.

²Universidade de Brasília, Brasília, DF, Brasil.

Submitted on November 28, 2022; Final Acceptance on March 14, 2023; Discussion open until August 31, 2023.

<https://doi.org/10.28927/SR.2023.012522>



This is an Open Access article distributed under the terms of the Creative Commons Attribution License, which permits unrestricted use, distribution, and reproduction in any medium, provided the original work is properly cited.

obtaining only the order of magnitude of the bearing capacity and deformability.

In driven piles, the uniformity of the pile foundations is accomplished using energy control, in this case, represented by the set and rebound, and are indispensable in the reliability of this type of pile cap. It enables, from dynamic and static formulations, the comparison of results obtained in the field with those of the project and the results of load tests, if any.

Generally, in some CFA foundation designs, the pile settlement is conditioned to a minimum depth and the attainment of a certain value of torque or oil pressure at the end section of the pile. But the torque obtained during the monitoring of the execution of the flight auger pile is thrust-dependent, consequently, the criterion may be satisfied before the design load capacity is reached.

It is worth remembering that the magnitude of the torque is conditioned to the angular velocity and the feedrate imposed on the helix. For example, a force or torque of small magnitude, applied to the helix during a long time interval, can generate the same displacement (final elevation of the pile) caused by a force or torque of high magnitude applied in a short time interval as described by the impulse-momentum theorem (Silva, 2011).

However, in this case, the sum of the helicoid rotations and, consequently, the path of the force applied to the helicoid will be greater for the force of lesser magnitude, compensating for the existing differences between the forces, which perform equivalent work at the end of the excavation. As an example, a machine of greater power generates a torque of great magnitude and performs the work required to excavate a pile in less time, when compared to a machine of less power that will need more time to excavate this same pile, a fact demonstrated by Silva (2011).

To replace the maximum torque criterion, Silva (2011) presented and validated the SCCAP Methodology, Silva & Camapum de Carvalho (2010). This methodology is based on the thesis that the control of mechanized excavations, of CFA piles, through the determination of the energy required in the execution of the drilling, constitutes an element of technological control capable of offering greater safety and less risk to the works that use it. The SCCAP was based on the law of conservation of energy, one of the fundamentals of classical physics, and quantifies the energy required or the work done to excavate each pile of the foundation.

From this quantification Silva (2011) developed routines and proposed statistical criteria for the acceptance of the piles, based on the statistical characteristics of the population or on an energy sample taken from the pile itself and incorporated the routines to the software for monitoring the execution of CFA piles. Silva (2011) presented the methodological framework that supports the thesis that the control of the excavated piles, in particular the CFA piles, through the determination of the energy demanded during the pile excavation, constitutes an element of technological control capable of offering greater safety and less risk to the works that use them.

2.1 Energy and pile foundation control

An important concept that is directly related to energy is the work done, a scalar quantity and therefore without associated direction. The universality of the concept of energy makes it possible, for example, to understand how the mechanical energy produced by a motor is transformed into kinetic energy and in turn dissipated by work, in the case of a pile, by friction (heat), so that even with these energy transformations, the total energy is a constant.

Physically, work describes what is accomplished by the action of a force, being defined by Young & Freedman (2008), as the product of displacement by the force parallel to the displacement. If a body, moving from the initial pile elevation (c_i) to the final one (c_f) along any trajectory (x), is under the action of a variable force (F), work (W) can be defined in Equation 1.

$$W = \lim_{\Delta x_i \rightarrow 0} \sum_i^n F_i \cdot \Delta x_i = \int_{c_i}^{c_f} F \cdot dx \quad (1)$$

Another form of energy associated with an object is potential energy, which depends on the position and configuration of the system. For example, to lift the auger of a continuous propeller machine, work must be done and, consequently, energy will be consumed to move it from one point to another (Young & Freedman, 2008).

If energy is conserved, how is this energy stored? We can say that this energy is accumulated in terms of gravitational potential energy, which depends only on the position of the object relative to the Earth's center and its mass. Therefore, the work done by the gravitational force (w) when a mass (m) changes its elevation (y) relative to the Earth's surface is given by Equation 2.

$$W = F \Delta y = mg (y_1 - y_2) \quad (2)$$

where "g" is the gravity acceleration.

Another important principle is Hamilton's, which starts from the concept of conservative energy, in which energy cannot be created or destroyed, only transformed. In the case of structural system dynamics, the concept can be summarized by Equation 3, according to Clough & Penzien (1975):

$$\int_{t_1}^{t_2} \delta(T - V) dt + \int_{t_1}^{t_2} \delta(W_{nc}) dt = 0 \quad (3)$$

where T is the total kinetic energy; V is the potential energy, including the strain energy and the potential energy of any external conservatively acting forces; W_{nc} is the work done by the nonconservative forces acting on the system, including damping, friction, and external forces.

This principle in variational form, applied to a system in equilibrium, states that the variation occurring within the system, of kinetic and potential energy, added to the variation in work done by nonconservative forces acting during any time interval ($t_2 - t_1$) is equal to zero.

Therefore, it is evident that Hamilton's principle can be applied to the case of loading of any system, in static or dynamic equilibrium, and particularly to the pile-soil system. One should also remember the first law of thermodynamics: in any transformation of energy, its absolute value is conserved. That is, energy cannot be created or destroyed, only transformed, a principle applied by Aoki et al. (2007) to calculate the work, energy, and efficiency of the dynamic SPT test.

Foundation engineering is based on field tests, which are energy measurements, a fact studied by Odebrecht et al. (2007), who realized the need to standardize the measurement of the number of blows of the SPT test in terms of energy. They suggested a new approach and an analytical solution to calculate the delivered energy and the efficiency of the system. Schnaid et al. (2009) warn that interpretations of dynamic penetration testing (SPT) results are traditionally interpreted based on empirical correlations, and this is a frequent criticism of these tests.

Thus, they proposed an interpretation method based on the system energy measurement, because, from this value, one can calculate the dynamic force that represents the soil reaction to the sampler penetration, enabling the interpretation of soil properties such as the angle of internal friction and undrained shear strength.

Knowing this force, Lobo et al. (2009) presented a new method for predicting pile load capacity developed based on the interpretation of SPT test results. Unlike other methodologies established in the engineering practice, of essentially empirical nature, the new approach was based on concepts of dynamics and makes use of the principles of energy conservation involved in the driving of the SPT sampler. The energy absorbed by the soil was calculated from the number of blows N_{SPT} (or directly from the corresponding measure of penetration of the sampler) and analytically converted into a dynamic reaction force to penetration.

This force allowed determining the unit resistances mobilized in the SPT sampler and estimating the unit resistances mobilized in the pile. According to the authors, the methodology is simple and presents advantages over empirical methods, because the use of different equipment and procedures, resulting from local factors and the degree of regional technological development, do not interfere with the method if the efficiency of each SPT system is properly gauged, since the energy transmitted by the hammer-rod-sampler system is a function of the soil type. Therefore, the method captures the influence of the soil in predicting the pile load capacity.

In practice, the geotechnical engineer defines the test campaign, and consequently the soil-bearing capacity, essentially based on his experience and knowledge of the region, leaving the control and reliability that should be associated with the project in second place.

It is observed that only piling made of precast piles and Frank types are, for the most part, controlled through energy measurement, through elastic rebound, final set, and dynamic or static load tests.

Tsuha & Aoki (2010), through the results of physical modeling tests in a centrifuge, verified a theoretical relationship between installation torque during driving and the tensile load capacity of flight auger-driven piles in sandy soils, indicating that there is a relationship between the accumulated torque, the energy required to excavate a CFA pile and its load capacity. However, it is warned that torque, being dependent on thrust, can only be adopted as a control measure if angular and drilling speeds are controlled during excavation.

3. Energy required to excavate a pile

van Impe (1998) proposed Equation 4 to calculate the energy required to excavate a pile per unit volume.

$$E_s = \frac{N_d \cdot v_i + n_i \cdot M_i}{\Omega \cdot v_i} \quad (4)$$

where: E_s = installation energy per unit volume [J/m^3]; N_d = vertical thrust force [N]; v_i = auger vertical velocity [m/s]; n_i = angular velocity [Hz]; M_i = applied torque [N.m]; Ω = area of the plane projection of the auger [m^2].

Therefore, the total energy (E_{sT}), Equation 5, necessary to execute a pile with radius (r), excavated in a certain amount of helicoid rotations (θ) in any time (t), must be multiplied by the volume of the pile ($\Omega \cdot L$), as shown.

$$E_s \cdot (\Omega \cdot L) = \left(\frac{N_d \cdot v_i + n_i \cdot M_i}{\Omega \cdot v_i} \right) \cdot (\Omega \cdot L)$$

$$E_{sT} = N_d \cdot L + \frac{2 \cdot \pi \cdot \theta \cdot (F_T \cdot r) \cdot L}{\left(\frac{L}{t} \right)}$$

$$E_{sT} = N_d \cdot L + F_T \cdot 2 \cdot \pi \cdot r \cdot \theta \quad (5)$$

According to Silva (2011), the total work done by external forces, Figure 1, is the sum of the work done by the tangent force to the helicoid, plus the work done by the gravitational force and the work done by the downward force that is equal to the mechanical energy applied to the helicoid. Therefore, the work is a scalar quantity represented and defined by Equation 6. Knowing that the vertical thrust force (N_d) is the sum of the weight force ($m_{hc} \cdot g$) of the system with the downward force applied to the helicoid (F_d), it can be verified that Equation 5, proposed by van Impe (1998) is an approximation of Equation 6, proposed by Silva & Camapum de Carvalho (2010) that is presented in integral form and without approximations:

$$W_R = \int_0^{z_b} m_{hc} \cdot g \cdot dz + \int_0^{z_b} F_d \cdot dz + \int_0^{m2\pi} F_i \cdot r \cdot d\theta \quad (6)$$

where, WR = work done or energy required to excavate a pile [J]; F_i = force applied to the helicoid [N]; m_{hc} = mass of the excavation system [kg]; r = radius of the auger pile [m];

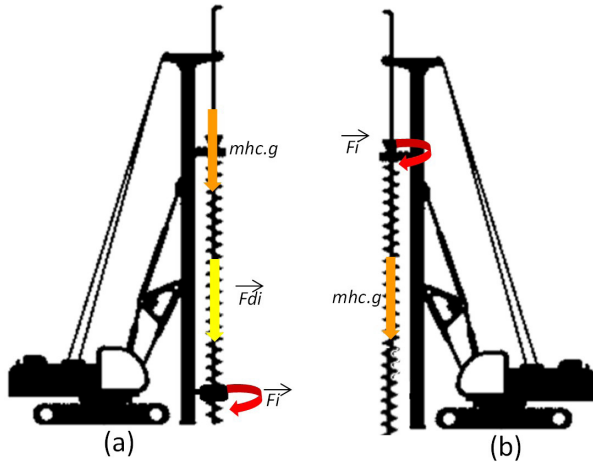


Figure 1. Drilling system and forces, (a) CFA bottom drive and (b) CFA system (Silva, 2011).

g = acceleration of gravity [m/s^2]; z_b = length of the pile [m]; F_{di} = downward force applied to the helicoid [N]; m = number of turns of the helicoid during excavation.

The proposed formulation, Equation 6, can be implemented in any monitoring system. For example, they can and were implemented in the monitoring system that is used by most of the continuous propeller auger-type machines existing in Brazil. The system described by Silva (2011), basically consists of a computer and sensors, whose data acquisition, treatment, and control of the execution are performed in specific software.

An analytical model to estimate the load capacity of a CFA pile as a function of the torque applied by the machinery was proposed by Hortegal & Cavalcante (2016). The model can be easily rewritten as a function of force or energy, since the lever arm and the force-displacement are known and monitored, consequently proving, once again, that the load capacity is also a function of the energy required in the executive process.

The proposed model considers that the installation energy of the CFA pile is defined by the sum of the penetration energy and the energy lost by the system. It is assumed that the installation energy is a function of the drilling torque and the downward force. On the other hand, the downward force is associated with the installation of the CFA and involves the rotation of the auger within the soil. Based on these hypotheses, a model was proposed and solved to find an analytical solution to evaluate the load capacity of the CFA piles, C , per meter, as a function of the execution torque, Equation 7.

$$C(T) = \frac{6\delta(2\pi T + F_{di}p) \left[r^2 + \sum_{i=1}^n (R_i^2 - r^2) \right]}{3\delta^2 \left[r^2 + \sum_{i=1}^n (R_i^2 - r^2) \right] + 8\pi\alpha \left[3r^3\lambda + \sum_{i=1}^n (R_i^3 - r^3)t_i \right]} \quad (7)$$

where, d = pile deflection at ultimate load capacity [m]; T = execution torque [$\text{kN} \cdot \text{m}$]; F_{di} = downward force, or pull down force [kN]; p = blade pitch [mm/rev]; r = radius of the propeller auger [m]; t_i = thickness of the propeller [m]; n = total number of propellers; R_i = helicoid radius, approximately equal to the radius of the EHC [m]; l = effective length of the tube penetrating the soil, approximately equal to the length of the EHC [m]; a = constant of proportionality between the torque due to shear along the tube and the penetration stress [dimensionless].

Thus, the admissible load, C_{adm} [kN], of the CFA piles, per meter, is presented in Equation 8:

$$C_{adm} = \frac{C(T)}{FS} \quad (8)$$

4. Semi-empirical method based on pile installation energy

Given the proof that the bearing capacity of the pile is related to the installation energy of the pile, Silva (2011), 12 load tests were analyzed in order to balance, propose and validate the semi-empirical method presented.

The piles tested were installed in the Federal District soil, whose geomorphological context was described by Cardoso (2002), who disserted on the genetic, geological, and mineralogical aspects of the region. The soil of the region is predominantly composed of a porous clay that is collapsible on its surface, but due to excavations imposed by the existence of at least two subsoils in the studied works and the presence of water table, the piles, in their majority, were deployed in less weathered soils with low collapse potential, transition soils and saprolitic soils texturally characterized as clays and silts.

In summary, the studied piles were installed in horizon classified as silt, the soil found until approximately 10.0 m depth in the analyzed areas is the collapsible porous clay of the Federal District, as a result of the weathering associated with the leaching process and laterization and, from this point on, there is the transition soil, layer generally not very thick, followed by the saprolitic soil, a layer that ends in the saprolite. Mineralogically, the soil profile is generally rich in kaolinite and iron and aluminum oxyhydroxides in the deeply weathered mantle and progresses to 2:1 clay minerals as they lose in weathering until they reach the primary minerals in the rocks.

Quartz, being a mineral that is difficult to weather, is generally found throughout the profile, and according to the hypothesis presented by Senaha (2019) it can also be neoformed. Texturally, the composition of these soils is linked to the source rock, for example, in slates it consists of silts and clays. These materials generally exhibit increasing compactness to the parent rock.

To evaluate the ultimate load, it was adopted the criteria proposed by Vesic (1977), which is defined as the load corresponding to a deformation of 10% of the pile diameter, deformation that was defined as conventional rupture by

Décourt (2008). The load versus settlement curves that did not reach conventional failure were extrapolated by van der Veen (1953), the methodology showed adequate load prediction when tested on the curves obtained in the load tests that reached conventional failure.

In the studied works, the pile settlement depths were controlled by the SCCAP methodology, through the control of the installation energy, described in Silva (2011). Consequently, in each work, soil type, and for each type of pile there was a minimum depth and reference energy that should be reached, similar to what happens during the control of driven piles that are also controlled by energy, represented by the rebound and the set.

It is noteworthy that, in dozens of works, controlled by the SCCAP methodology, it was observed that there was a pattern, in terms of installation energy, for a given load,

soil type and pile type, suggesting that the pile load capacity was directly related to the installation energy required during execution. It was also observed that the installation energy for a given diameter and pile load capacity fluctuated within a narrow range in terms of energy and that its variation was directly related to soil type and soil condition and pile depth.

Table 1 presents the geometric characteristics of the 12 tested piles that were used to validate the proposed formulation by means of load tests. Also presented are the results in terms of ultimate load, the energies required during installation, and the soil type defined in the SPT borings. All the piles studied were executed with machinery and tools manufactured by CZM Equipment (bottom drive CFA) whose characteristics are described by Silva (2011).

Figure 2 shows the variability in terms of load vs displacement behavior of the tested piles. Probably, three

Table 1. Characteristics of the tested piles, installation energy and soil type.

Analyse cases (pile load test)	D [m]	L [m]	Q_c [kN]	E_i [MJ]	Soil type
E184	0,6	20.0	1900	42	silt
E202	0,6	12.0	1673	25	silt
E206	0,6	12.0	1897	31	silt
E277	0,6	20.0	1900	45	silt
E1	0,6	13.0	1900	31	silt
E2	0,6	12.0	1899	30	silt
E3	0,6	12.0	1900	30	silt
E4	0,6	13.0	1900	32	silt
APB-31	0,5	14.0	1819	32	clay
BPA-23	0,6	14.0	1833	35	clay
BPC-24	0,6	14.0	1839	40	clay
CPD-36	0,6	14.0	1698	27	clay

Where, D is the diameter; L is the length; Q_c is the conventional failure load; E_i is the installation energy.

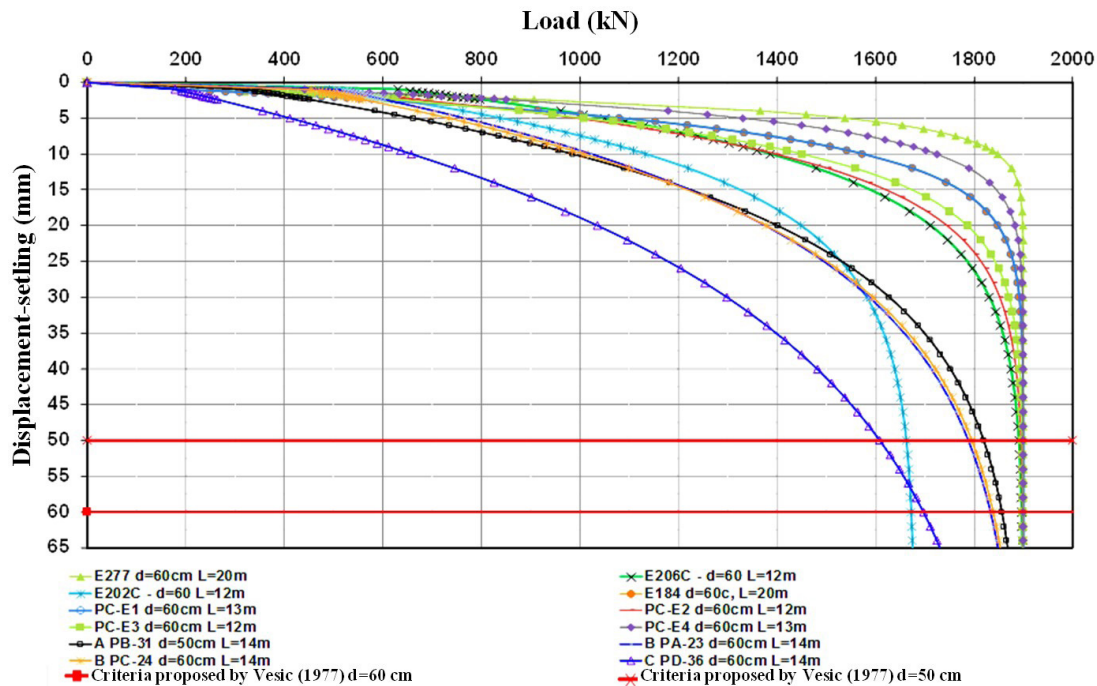


Figure 2. Load vs displacement (settling).

factors impacted the performance of the piles, in terms of load capacity and deformability, and were determinants for the dispersion of the results, they are: soil type; settlement elevation of the pile, longer the length of the pile the more material will be transported to the surface and more energy will be required; and the load capacity at the tip of the pile which is influenced by its state of cleanliness. Silva (2011) instrumented the tip of 11 CFA piles and concluded that the tip's cleanliness condition is determinant in the performance of the tip and consequently of the pile itself, in terms of load capacity and deformability. Other factors such as pile location, soil morphology, and moisture along the soil profile, when not saturated, can also impact the results.

The proposed method has as dependent variables the diameter, depth, and soil type, variables studied by Silva (2011), who observed that the magnitude of the measured energy is dependent on the type and strength of the soil, the efficiency of the machinery, the depth of pile excavated, the geometry of the drilling tools and the procedures adopted during excavation.

Also warned that the behavior of the CFA piles, in terms of load capacity and deformability, depends not only on the installation process but also on the procedures adopted during concreting, particularly the injection pressure used during concreting, especially when it takes place in the deeply weathered and collapsible mantle.

Added to this intricate matrix is another variable difficult to solve, the system of nonconservative forces involved in the process of excavation, destructuring, and soil transport during the execution of a propeller auger-type pile. The system is complex and difficult to solve, as it consumes and dissipates energy, for example, among other factors: - in the friction and adhesion between the helicoid and the soil; - in the friction and residual adhesion between the pile shaft and the helicoid/soil assembly.

However, the universal law of conservation of thermodynamic energy, synthesized in Hamilton's principle, allowed us to conclude that the energy or work done to excavate a pile is the sum of the work done by the system of external forces applied to the helicoid, Figure 1. This fact simplifies the resolution of the problem and was synthesized in Equation 6. Silva (2011) reminds us that in a set (machine and operator), the energy demanded or the work done during the excavation of the piles of a pile foundation presents acceptable variability, because the drill rig, the tool (helicoid) and the process adopted in the operation of the machinery during excavation and concreting tend to be repetitive and systematized, with hits and errors incorporated into the process, consequently the installation energy can be controlled and measured.

Equation 9 was proposed based on the results presented in Table 1 and in Figures 2 and 3, being valid for diameters greater or equal to 40 cm. For diameters smaller than 40 cm it was observed, in most cases, that the energy required was greater than that predicted by the proposed method. Probably

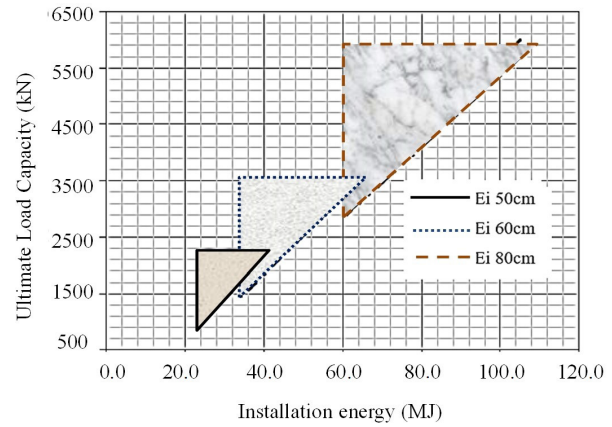


Figure 3. Ultimate Load Capacity versus Installation Energy - Silt.

due to the ratio between the diameter of the concrete injection tube, between 150 mm and 180 mm, and the diameter of the pile, transforming the process of pile excavation into a hybrid process of excavation and soil displacement, a process of semi-displacement, which demands more energy.

The system of non-conservative forces involved in the process of excavating these piles, including soil compaction between the helicoids, soil transport to the surface, and even the compressive stresses of the excavated soil against the pile shaft, a process of semi-displacement, must be better studied and understood.

In any case that applies the proposed formulations, Equations 9, 10, and 11, the ultimate load capacity and the allowable must be predicted by the designer through empirical, semi-empirical or theoretical methods that are usually adopted in the practice of foundation engineering. From this prediction, the geometric characteristics of the pile and the geotechnical characteristics of the soil, the installation energy is estimated, which will serve as a reference for the control of pile driving during execution. Therefore, based on the observation of the behavior of energy-controlled piles in the Federal District, on the load tests performed in these works, on the geometric characteristics of the piles and soil geotechnical characteristics, the formulations for estimating the installation energy, Equations 10 and 11, are proposed.

$$E_i = \left[\left(\frac{C_{ult}}{70} \right) + D^2 \cdot L \right] \cdot \alpha \cdot \beta \quad (9)$$

$$C_{ult} = \left[\left(\frac{E_i}{\alpha \cdot \beta} \right) - D^2 \cdot L \right] \cdot 70 \quad (10)$$

$$C_{adm} = \frac{C_{ult}}{2} \quad (11)$$

where, E_i =installation energy [MJ]; C_{ult} = ultimate pile load capacity [kN]; C_{adm} = allowable load capacity [kN]; D =pile diameter [m]; L =pile length [m]; α =set factor for soil; β =set factor for machinery and its tools.

For the soils of the region and the machines studied, it is proposed: $\alpha=1,00$ (silt and sand) and $\alpha=1,20$ (clays); $\beta=1.00$ (CZM, bottom drive CFA).

In Figure 3, the proposed formulation was used to determine regions where the pairs of ultimate load capacity versus installation energy are expected to be possible for piles of 50, 60 and 80 cm. For example, for the 60 cm piles it was considered the ultimate load ranging from 1500 to 3600 kN and lengths ranging between 10.0 and 30.0 m, similarly, it was determined the region for the 50 and 80 cm piles. It can be observed that all pairs of ultimate load capacity versus installation energy presented in Table 1 are within the regions delimited in Figure 3. It should be noted that for each case, there is only one possibility for the abscissa and ordinate, ultimate load versus installation energy.

5. Applicability of the semi-empirical method

The performance of a foundation depends, fundamentally, on the process adopted during its execution and on the geological-geotechnical characteristics of the soil. Therefore, determining the bearing capacity of a pile is a difficult problem to solve, especially in places with great geotechnical variability, because generally there are insufficient and inaccurate field investigations.

To this is added the difficulty, almost always of cultural order, in performing previous tests to verify performance, such as load tests in the design phase and drilling after the completion of embankments and/or excavations. Their realization in the execution phase only serves to adjust the part not executed and to subsidize eventual reinforcements in those already executed.

Consequently, the geotechnical engineer has, in most works, only empirical and semi-empirical deterministic methodologies or limited theoretical methods. But he should at least be aware of these restrictions, knowing that he will never obtain or be certain of the exact value, obtaining only

the order of magnitude of the load capacity and deformability, Silva (2011).

One of these uncertainties, which was observed by Aoki & Cintra (1996) during the execution of pile foundations, is the existence of a resistant surface where the pile foundations are placed, a surface that should geotechnically and structurally meet the ultimate limit states and states of utilization. However, the location of the resistant surface depends on the geological-geotechnical formation of the soil, the driving or excavation process and the level of application of the foundation element, being difficult to determine during the execution of a pile foundation, particularly the excavated ones, because there are no control tools available, such as the control of the set or elastic rebound present in precast piles.

In the traditional executive method, the depth of excavation is previously fixed by the designer and is generally not changed during execution. However, in a profile with folded structural geology, such practice can lead to errors, especially when the unsampled soil, soil between boreholes, is in the depression zone of the fold (synclinal), leading to low resistances up to the settlement quota foreseen in the project. When the bend is reversed (anticlinal), many times the drill does not reach the desired depth, causing doubts about the pile's bearing capacity to persist. The proposed method, which adds to the SCCAP Methodology (Silva, 2011), will help the execution, because, in addition to the settlement level, predicted by empirical, semi-empirical, and theoretical methodologies, it will be possible to control each pile during execution, by means of the installation energy.

Consequently, it is verified if the pile meets the design assumption in terms of load capacity. The proposed formulation can be easily implemented in the monitoring system of the CFA piles employing specific software and will help the designer and the executioner in the decision-making process and, as a consequence, will increase the reliability of the piling. Figure 4 shows a resistant surface for a set of 40 and 50 cm piles after standardization presented by Silva (2011). It can be

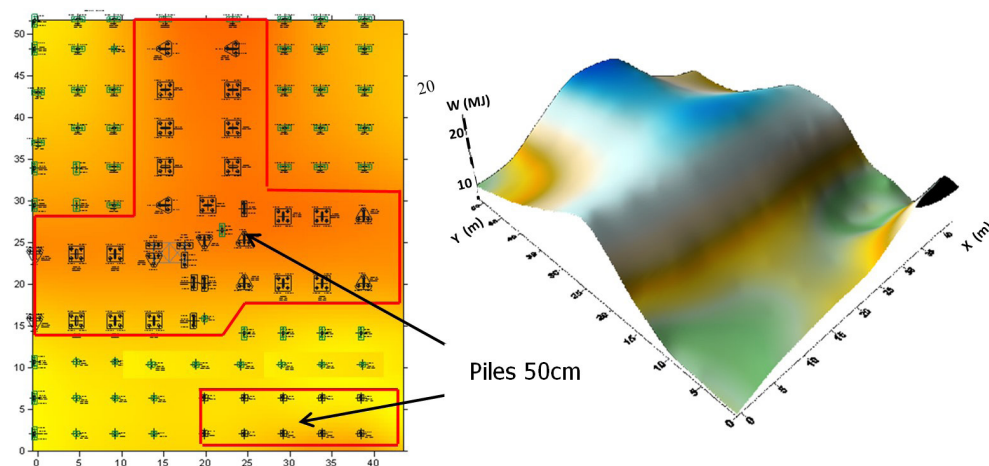


Figure 4. Energy resistant surface - piles 40 cm and 50 cm (Silva, 2011).

seen in this figure that the methodology uniformed the piling in terms of energy, clearly identifying through the energy level the regions where 50 cm piles and 40 cm piles predominate.

6. Conclusions

The proposed method has proven to be accurate and of great importance in the piles in the Federal District and Goiás that were controlled with the technique. The method conferred quality, reliability, and safety to these pile foundations. It ensured that the design precepts in terms of load capacity and deformability were met by reducing variability in terms of installation energy and performance. It is observed that the method provides an additional criterion to determine the pile settlement level, a complementary and corrective drilling stop criterion, contributing to the reduction of variability in pile load capacity and failure probability.

Undoubtedly, the method brings greater safety to foundation works without eliminating the valuable professional performance of the engineer, remembering that knowledge undergoes transformations and additions over time. The experience, although valuable, is only sporadically repeated in the geotechnical area, because the situations, the soils, the rocks, the stratigraphies, the drainage conditions, the equilibrium humidity, the water table when present, the hydrogeological flows, among others, present often spatial, temporal, and relative alterations to the execution of the pile. Particularities such as these, if on one hand highlight the relevance of the proposed technique, on the other, it shows the need for the engineer to be constantly observing, reflecting, and taking complementary decisions. Although apparently, the executed foundation is close to the reality of the work, there are temporal factors to be considered that can generate differences from the real situation. For simplicity, the soil shear strength equation can be considered, which is a function of cohesion, friction angle, and normal stress to the shear plane. Considering the more complex context, it would have to be considered, in this case, soils not saturated with matrix suction. Added to this is the fact that these are foundations concreted in situ, consequently one would have to consider the osmotic suction that will pass in the surroundings of the foundation due to alterations over time, something still little studied and generally not considered. But staying in the simplest situation, that of the shear strength of the saturated soil, the horizontal stresses that directly affect the lateral friction and the load capacity of a pile will change over time with the stiffening of the surrounding foundations that alter the propagation stresses and generate, for example, differences in the load capacity of the piles that make up a raft (Collantes, 2017). Influences like this, which are at the same time temporal and spatial, must be considered not only in the evaluation of the execution energy of the foundation but also in the results of tests such as the SPT and CPT and the load tests.

Regarding the execution of the pile, its load capacity, and the energy demanded and controlled during the execution,

which is directly linked to its geometry and type of soil, other factors can interfere with the load capacity, among them, the process of execution and the concreting pressure. Concreting pressure may have some practical implications, for example, in non-saturated collapsible soils, it will induce an increase in the diameter of the pile and the collapse generated in the surrounding soil matrix may or may not be beneficial, depending on the constitution and composition of the soil. and how the chemistry derived from the concrete will act on this soil, stabilizing or destabilizing it as exemplified by Camapum de Carvalho & Gitirana Junior (2021).

Therefore, concluding these final considerations, the proposed methodology is undoubtedly of great value, but it does not put aside the importance of the engineer's performance, his sense of observation, and his capacity for reflection.

Declaration of interest

The authors have no conflicts of interest to declare. All co-authors have observed and affirmed the contents of the paper and there is no financial interest to report.

Authors' contributions

Carlos Medeiros Silva: conceptualization, methodology, validation, writing – original draft. José Camapum de Carvalho: data analysis, supervision, validation, writing – review & editing.

Data availability

The datasets generated analyzed in the course of the current study are available from the corresponding author upon request.

List of symbols

a	Constant of proportionality between the torque due to shear along the tube and the penetration stress [dimensionless]
d	Pile deflection at ultimate load capacity [m]
g	Gravity acceleration
l	Effective length of the tube penetrating the soil, approximately equal to the length of the EHC [m]
m	Number of turns of the helicoid during excavation
m_{hc}	Mass of the excavation system [kg]
n	Total number of propellers
n_i	Angular velocity [Hz]
p	Blade pitch [mm/rev]
r	Radius of the auger pile [m]
t_i	Thickness of the propeller [m]
v_i	Auger vertical velocity [m/s]
z_b	Length of the pile [m]
C_{adm}	Admissible load

C_{ult}	Ultimate pile load capacity [kN]
D	Pile diameter [m]
E_i	Installation energy [MJ]
E_s	Installation energy per unit volume [J/m ³]
F_S	Safety factor
L	Pile length [m]
F	Force
F_i	Force applied to the helicoid [N]
Fd_i	Downward force applied to the helicoid [N]
M_i	Applied torque [N.m]
N_d	Vertical thrust force [N]
R_i	Helicoid radius, approximately equal to the radius of the EHC [m]
T	Total kinetic energy
T	Execution torque [kN. m]
V	Potential energy
W	Work
W_{nc}	Work done by the nonconservative forces acting on the system
WR	Work done or energy required to excavate a pile [J]
α	Set factor for soil
β	Set factor for machinery and its tools
Ω	Area of the plane projection of the auger [m ²]

References

- Aoki, N., Esquivel, E.R., Neves, L.F.S., & Cintra, J.C.A. (2007). The impact efficiency obtained from static load test performed on the SPT sampler. *Soil and Foundation*, 47(6), 1045-1052. <http://dx.doi.org/10.3208/sandf.47.1045>.
- Aoki, N., & Cintra, J.C.A. (1996). Influência da variabilidade do maciço de solos no comprimento de estacas. In *Anais do III Seminário de Engenharia de Fundações Especiais e Geotecnia* (pp. 173-184), São Paulo (in Portuguese).
- Camapum de Carvalho, J., & Gitirana Junior, G.P.N. (2021). Unsaturated soils in the context of tropical soils. *Soils and Rocks*, 44(3), 1-25. <http://dx.doi.org/10.28927/SR.2021.068121>.
- Cardoso, F.B.F. (2002). *Propriedades e comportamento mecânico de solos do planalto central brasileiro* [Doctoral thesis]. University of Brasilia (in Portuguese). Retrieved in November 28, 2022, from <https://repositorio.unb.br/handle/10482/31224>
- Clough, R.W., & Penzien, J.P. (1975). *Dynamics of structures* (5th ed.). New York: McGraw-Hill.
- Collantes, C.A.P. (2017). *Avaliação da influência da posição da estaca integrando um radier estaqueado em sua capacidade de carga lateral* [Master's dissertation]. Programa de Pós-graduação em Geotecnia, Universidade de Brasília. Retrieved in November 28, 2022, from <https://repositorio.unb.br/handle/10482/765>
- Décourt, L. (2008). Provas de carga em estacas podem dizer muito mais do que têm dito. In *Anais do 6º Seminário de Engenharia de Fundações Especiais e Geotecnia - SEFE* (pp. 221-245). São Paulo: ABMS (in Portuguese).
- Hortegal, M.V., & Cavalcante, A.L.B. (2016). Controle fuzzy no desempenho de estacas hélice contínuas. In *Anais do XVIII Congresso Brasileiro de Mecânica dos Solos e Engenharia Geotécnica*, Belo Horizonte, Brazil (in Portuguese). Retrieved in November 28, 2022, from <https://repositorio.unb.br/handle/10482/22636>
- Lobo, B.O., Schnaid, F., Odebrecht, E., & Rocha, M.M. (2009). Previsão de capacidade de carga de estacas através de conceitos de transferência de energia no SPT. *GEOTECNIA Revista Luso Brasileira de Geotecnia*, 115(115), 5-20. http://dx.doi.org/10.14195/2184-8394_115_1.
- Senaha, S.C.F. (2019). *A quartzização em perfis de intemperismo tropical* [Master's dissertation]. University of Brasília (in Portuguese). Retrieved in November 28, 2022, from <https://repositorio.unb.br/handle/10482/37641>
- Schnaid, F., Odebrecht, E., Lobo, B.O., & Rocha, M.M. (2009). Discussion of SPT Hammer Energy Ratio versus Drop Height by T. Leslie Youd, Hannah W. Bartholomew, and Jamison H. Steidl. *Journal of Geotechnical and Geoenvironmental Engineering*, 135(11), 1777-1778. [http://dx.doi.org/10.1061/\(ASCE\)GT.1943-5606.0000202](http://dx.doi.org/10.1061/(ASCE)GT.1943-5606.0000202).
- Silva, C.M., & Camapum de Carvalho, J. (2010). Monitoramento e controle de qualidade dos estaqueamentos tipo hélice contínua durante a execução da obra. In *XV Congresso Brasileiro de Mecânica dos Solos e Engenharia Geotécnica* (pp. 1-12). Gramado: ABMS.
- Silva, C.M. (2011). *Energia e confiabilidade aplicadas aos estaqueamentos tipo hélice contínua* [Doctoral thesis]. Universidade de Brasília (in Portuguese). Retrieved in November 28, 2022, from <https://repositorio.unb.br/handle/10482/10456>
- Tsuha, C.H.C., & Aoki, N. (2010). Relationship between installation torque and uplift capacity of deep helical piles in sand. *Canadian Geotechnical Journal*, 47(6), 635-647. <http://dx.doi.org/10.1139/T09-128>.
- Odebrecht, E., Schnaid, F., Rocha, M.M., & Bernardes, G.P. (2007). Discussion of energy efficiency for standard penetration tests. *Journal of Geotechnical and Geoenvironmental Engineering*, 133, 486-490. [http://dx.doi.org/10.1061/\(ASCE\)1090-0241\(2007\)133:4\(488\)](http://dx.doi.org/10.1061/(ASCE)1090-0241(2007)133:4(488)).
- Young, H.D., & Freedman, R.A. (2008). *Sears and Zemansky's university physics* (12th ed., 1598 p.). Hoboken: Pearson Education.
- van der Veen, C. (1953). The Bearing capacity of a pile. In *3rd International Conference on Soil Mechanics and Foundation Engineering* (pp. 84-90), Zurich.
- van Impe, W.F. (1998). Considerations on the auger pile design. In *1st International Geotechnical Seminar on Deep Foundations on Bored and Auger Piles* (pp. 193-218), Ghent.
- Vesic, A.S. (1977). *Design of pile foundations* (Synthesis of Highway Practice, No. 42, 68 p.). Washington: National Cooperative Highway Research Program, Transportation Research Board, National Research Council, National Academy of Sciences.

Geotechnical behavior of gravity dams built on sedimentary rocks: pore pressures and deformations analysis of Dona Francisca HPP foundation

Verlei Oliveira dos Santos^{1#} , Luiz Antônio Bressani² ,
Camila de Souza Dahm Smirdele³ 

Article

Keywords

Behavior of concrete gravity dam
Sedimentary rocks foundation
Pore pressure and deformation analysis
Dona Francisca HPP case study

Abstract

In Brazil, some dams have been built on sedimentary rock masses, which usually present greater deformability and permeability in comparison to metamorphic or igneous rock masses. This article describes a case study whose goal is to present and analyze the main data related to the monitoring of foundation behavior of the Dona Francisca dam, whose foundation is essentially constituted by sedimentary rocks. Dona Francisca gravity dam is a hydroelectric power plant (HPP) and was built in 2000, on the Jacuí River, in the central region of the Rio Grande do Sul State, Brazil. The analysis of the foundation behavior was done in terms of pore pressures and deformations recorded during seventeen years of dam operation. The geological and geotechnical conditions of the foundation are related to the Formação Caturrita rocks, made up mainly of sandstones and intercalated levels of siltstone and argillite. In the first five years of operation there was an intense stabilization process of the foundation rocky mass. After this period, it was verified the occurrence of stabilization at a lower rate. The deformation of the Dona Francisca HPP foundation is higher when compared with other larger dams, such as the Itaipu HPP dam. It was carried out an analysis of the 18 vibrating wire piezometers data, allowing a global assessment about the uplift water pressures behavior. Most piezometers indicated a reduction in the pore pressure values over time with a current trend of stabilization, and readings below the control values recommended in design.

1. Introduction

Kanji et al. (2020) drew attention to the investigations on soft rocks are important mainly due to the fact that in designing important workings involving soft rocks, their properties are difficult to establish and most of the times their parameters are adopted on the conservative side, against the economy of the project. The definition of soft rocks has been largely discussed in the literature (Terzaghi & Peck, 1967; Rocha, 1975; Dobreiner, 1984; Johnston, 1993; Gonzales de Vallejo et al., 2002; Kanji, 2014). The lower limit of uniaxial compressive strength for soft or very soft rocks has been advocated by several authors as 2 MPa and the upper, around 20 MPa.

In Brazil, some dams have been built on sedimentary rock masses, which usually present greater permeability and deformability in comparison to metamorphic and igneous rocks – other examples of materials that also constitute the

foundation of many dams around the world. Foundations formed by soft rocks – such as sedimentary masses – can even be suitable for gravity dam's construction because a dam failure is the product of more factors than just the foundation geology type. Although, in such cases, a large deformation of the foundation can take place during the dam construction and its operation period.

It is essential to evaluate the dam massif safety and its foundation through the prediction of pore pressures and deformations levels during the design stage. In addition, it is also necessary to investigate the dam massif performance during its construction and operation period, to verify the safety at field and confirm that the assumptions adopted in the design stage were appropriate. The investigation process related to dam performance is commonly done through the auscultation by in situ hydro-geotechnical instrumentation, which includes the measurement of pore pressures, flows, deformations, and displacements.

[#]Corresponding author. E-mail address: verleioliveira@gmail.com

¹Universidade de Brasília, Brasília, DF, Brasil.

²Universidade Federal do Rio Grande do Sul, Porto Alegre, RS, Brasil.

³Companhia Estadual de Energia Elétrica do Rio Grande do Sul, Departamento de Geração e Transmissão, Porto Alegre, RS, Brasil.

Submitted on December 3, 2022; Final Acceptance on April 1, 2023; Discussion open until August 31, 2023.

<https://doi.org/10.28927/SR.2023.013622>



This is an Open Access article distributed under the terms of the Creative Commons Attribution License, which permits unrestricted use, distribution, and reproduction in any medium, provided the original work is properly cited.

The comparison with the performance of other similar dams is important for safety analysis based on dam's behavior experience. But in the case of dams built on sedimentary rocks, only a few instrumentation data from other structures can be found in the literature to help professionals involved in dam monitoring. Within this context, this paper describes a case study whose goal is to present and analyze the main data related to the monitoring of foundation behavior of the Dona Francisca hydroelectric power plant (HPP) gravity dam, whose foundation is essentially constituted by sedimentary rocks. The foundation behavior analysis was done in terms of pore pressures and deformations recorded during seventeen years of dam operation by vibrating wire piezometers and multiple rod extensometers, respectively.

The rock formation at the Dona Francisca dam site is very stratified and made up mainly of sandstones, with also intercalated levels of siltstone and argillite. Due to the concern about the behavior of this type of foundation in relation to the stability of the structures, the Dona Francisca HPP was contemplated with a broad instrumentation plan, composed mainly of direct pendulums, multiple rod extensometers, triorthogonal joint meters, foundation piezometers, v-notch weirs, vibrating wire piezometers and thermometers. In this paper, only the vibrating wire piezometers and multiple rod extensometers data were analyzed because they are instruments that allow directly monitoring the dam foundation behavior over time.

2. Dona Francisca dam

The Dona Francisca dam was built at the end of 2000, on the Jacuí River, in the central region of the Rio Grande do Sul State, Southern Brazil. Its structure is constituted by rolled compacted concrete (*RCC*) and has approximately 63 meters of maximum height and 660 meters in length. The Dona Francisca dam (Figure 1) is part of the Jacuí power generation system and has an installed capacity of 125 Megawatts from two Francis turbines. The construction

was started in August/1998 and the reservoir was filled in November/2000, when in one week it reached a quota of 94.50 m, corresponding to the crest of spillway.

2.1 Geology and geomechanical parameters of the foundation

The geological and geotechnical conditions of the dam foundation in the spillway region of the Dona Francisca HPP are associated to the rocks from Formação Caturrita, belonging to the Rosário do Sul Group, of the Paraná Basin. However, the dam abutments are in contact with basaltic rocks so that the power station building, and water intake blocks are set on these rocks. In terms of geological-geotechnical conditions, two of the initial concerns during the design phase were the geomechanical parameters of the Formação Caturrita rocks and the contact regions between these and the basaltic massifs.

Antunes Sobrinho et al. (1999) describes the dam foundation material as predominantly composed of fine-grained to medium-sized arkose sandstones, reddish to grayish color, massive or cross-stratified, found at varying degrees of lithification due to variations in nature and in the amount of the cementitious material. Interspersed to the sandstones there are also sub-horizontal layers of siltstones, argillite and resistant and persistent intraformational breccia / conglomerates, with thicknesses ranging from centimeters to meters and lateral extension of meters to tens of meters. In some locals, siltstones and weathered argillites were sampled showing characteristics of soils at different levels, ranging from millimeters to tens of centimeters – generally from 1 to 20 cm.

The foundations near the dam base in the riverbed region are composed by sandstones of the Formação Caturrita with degrees of coherence A-I and A-III. As an example, the Figure 2 shows the geological section of block B21 located in the spillway region with a stratified profile in this location. There were found sandstones with unconfined compressive strength (*UCS*) greater than 10 MPa for A-I condition and

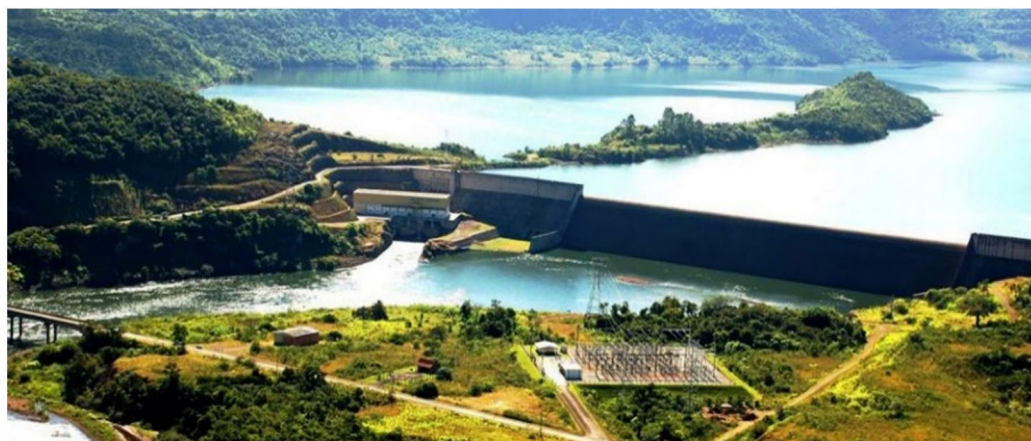


Figure 1. Panoramic view of the Dona Francisca dam.

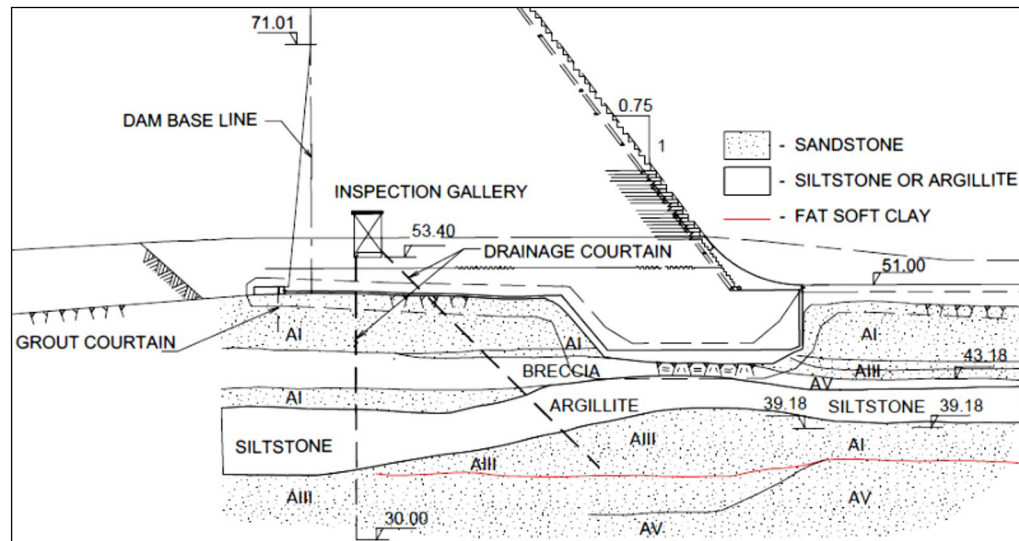


Figure 2. Geological section of block B21 foundation in the spillway region.

Table 1. Results of the uniaxial compression tests carried out on siltstone and argillite samples (adapted from Antunes Sobrinho et al., 1999).

Type of Rock	Sample number	Specific weight (g / cm ³)	UCS (MPa)	Modulus (MPa)		
				Secant	Tangent	
Siltstone	5	2.233	9.1	707.0	941.0	
	6	2.324	5.4	984.0	1200.0	
	7	2.312	7.2	733.0	991.0	
	11	2.372	9.5	937.0	990.0	
	12	2.386	7.1	1157.0	902.0	
	Mean		2.325	7.7	903.6	1004.8
Argillite	8	2.361	4.0	620.0	770.0	
	14	2.364	8.3	994.0	750.0	
	9	2.155	4.6	725.0	766.0	
	10	2.270	3.8	390.0	344.0	
	Mean		2.288	5.2	682.2	657.5

varying from 2 to 10 MPa in A-III condition. Laboratory tests indicated that the siltstone UCS ranged from 7 to 20 MPa and from 4 to 8 MPa for the argillite.

According to Pastore et al. (2005), the adoption of an RCC dam implies in rigorous foundation requirements. The authors also mention a particularly critical situation in the sliding stability verification and in the dam profile definition. It all depended on the determination of the behavior of the foundation rocky package and its geomechanical characteristics – mainly involving the layers of siltstone and argillite.

The Table 1 presents the results of the uniaxial unconfined compression tests carried out on siltstone and argillite samples during the design phase in 1998.

The graphs in Figure 3 show the strength envelopes, indicating the values of cohesion (c) and friction angle (φ) for these materials.

From the results presented in Table 1 and in the graphs of strength envelopes in Figure 3, it is observed a large variation in geomechanical parameters of these rocks. After several studies and tests carried out on the materials which compose

the Dona Francisca dam foundation, the designers in charge had the task of defining the geomechanical parameters to use in stability calculations. This task was not easy for the design team because the foundation is composed by stratified sedimentary rocks and little was known about other dams built in these conditions. Thus, conservative criteria were adopted to define the geomechanical parameters during the stability analysis carried out by the engineers and consultants. The Dona Francisca HPP had a careful design of hydrogeotechnical instrumentation also due to the concern with the behavior of this type of foundation in terms of dam's massif stability.

2.2 Instrumentation “key sections”

The instrumentation of the Dona Francisca dam's massif is composed by direct pendulums, multiple rod extensometers, triorthogonal joint meters, foundation piezometers (standpipe and vibrating wire piezometers), v-notch weirs and thermometers. In terms of deformation monitoring – in addition to the triorthogonal joint meters

installed along the dam – “key sections” were defined at blocks IW (intake works region), B17, B21, B25 and B28 for direct pendulums or extensometers installation. These blocks were chosen strategically according to location or because they had the highest heights. In blocks B17 and B21, direct pendulums were installed to monitor crest displacements. In blocks IW, B25 (in the spillway) and B28 (in the left abutment) multiple rod extensometers (*MRE*) rosettes were installed. In blocks IW, B06, B17, B21, B25, B28 and B30 vibrating wire piezometers (*VWP*) were installed to monitor the foundation pore pressures.

From the peculiar geological and geotechnical conditions already reported, this paper aims to describe the behavior of the Dona Francisca HPP dam foundation throughout time from the records of pore pressures and deformations, obtained from instruments installed at the abutments and the spillway. The Figure 4 presents a general arrangement of the

dam concrete blocks divided into blocks with an average length of 20.0 m and indicating the “key sections” location where the *MRE* were installed.

The Figure 5 shows the rosettes of extensometers set on the blocks IW and B25 of the Dona Francisca dam. The block B28 (left abutment) has the multiple rod extensometers arranged similarly to those in block B25. It is also observed in the region of intake works one extensometer (*MRE*-IW-04) that monitors foundation deformation right below of two penstocks.

The Figure 6 indicates the “key sections” location where the vibrating wire piezometers were installed.

The Figure 7 shows, as an example, the relative positions of the vibrating wire piezometers installed in block B30. One of the *VWP* is willing upstream at the dam base and two are willing downstream – one at the dam base and the other at the foundation rock mass. Others blocks section has the *VWP* arranged similarly to those in block B30.

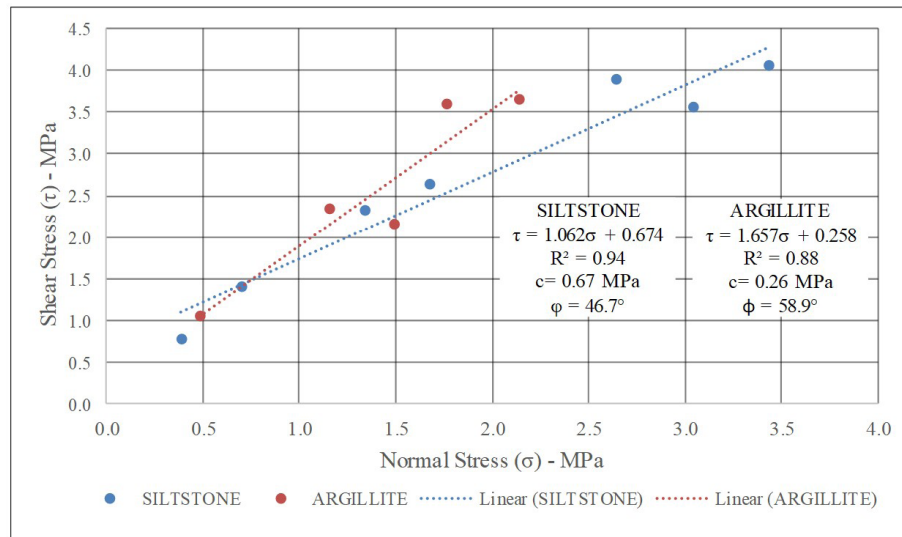


Figure 3. Resistance envelopes line of siltstone and argillite (adapted from Antunes Sobrinho et al., 1999).

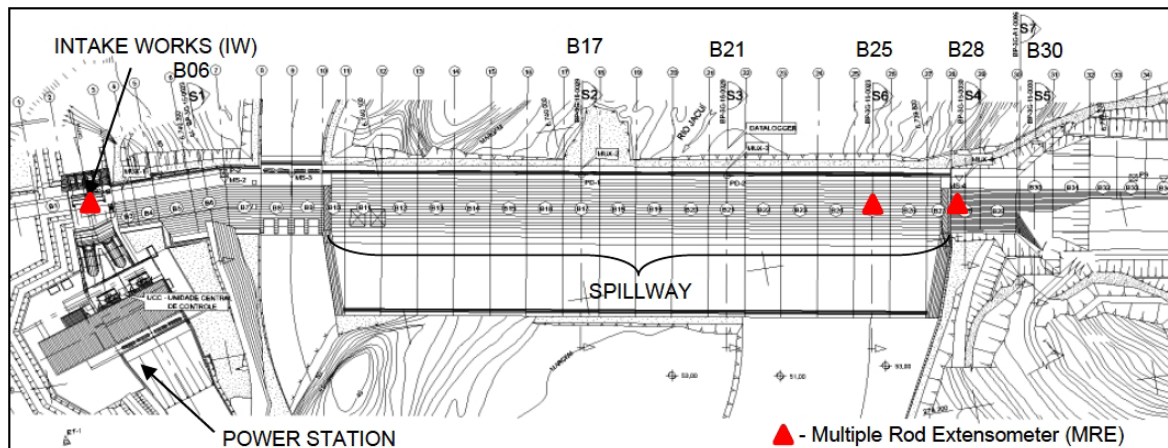


Figure 4. General arrangement of concrete blocks of the Dona Francisca HPP and MRE location.

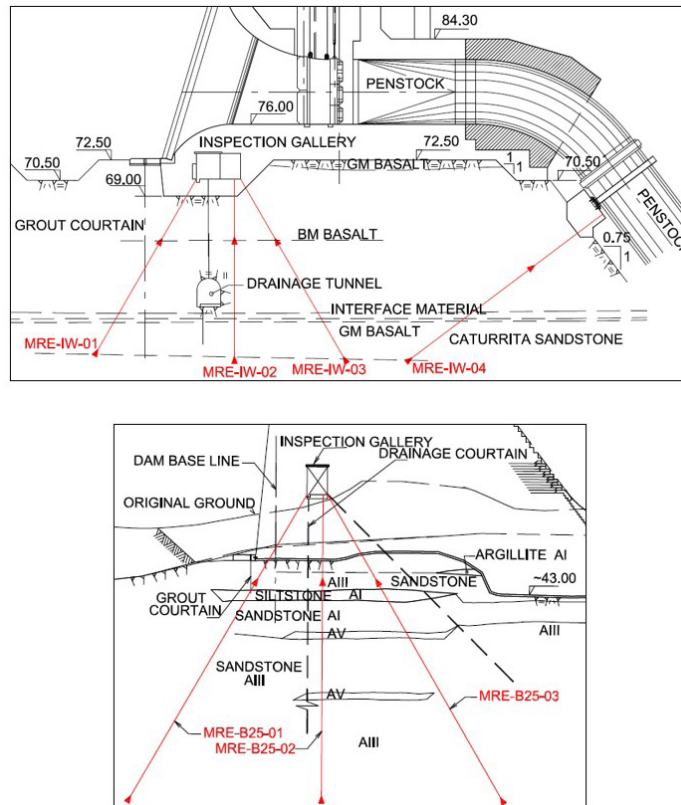


Figure 5. Multiple rod extensometers placed in the IW and B25 blocks.

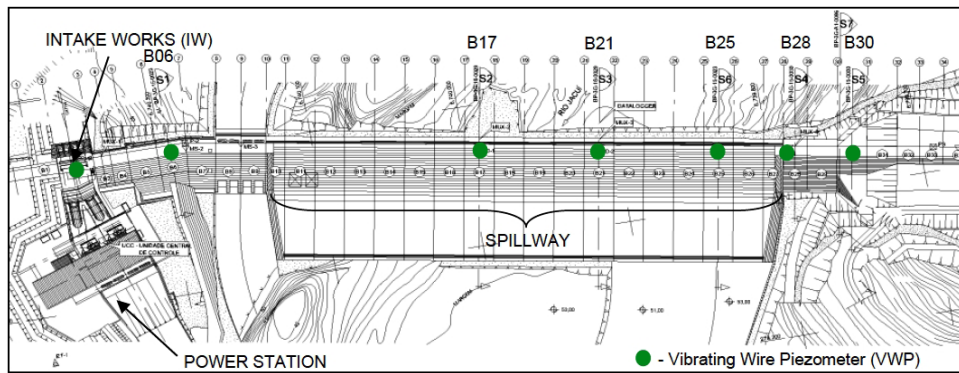


Figure 6. Key sections of Dona Francisca dam location where the VWP were installed.

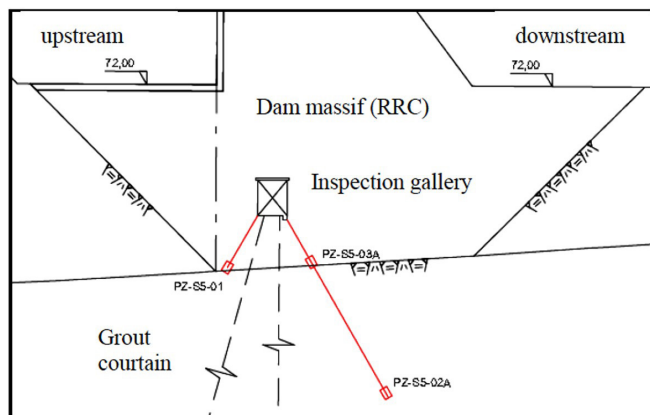


Figure 7. Vibrating wire piezometer's arrangement in block section B30.

3. Pore pressures analysis of Dona Francisca dam foundation

Data from the 18 vibrating wire piezometers (*VWP*) will be analyzed in this article. In the right abutment region, there are 2 *VWP* in the intake works section and 2 *VWP* in the S1 section, related to B06 block. In the spillway region there are 3 *VWP* in the S2 section, related to B17 block; 3 *VWP* in the S3 section, in B21 block; and 3 *VWP* in the S6 section; in B25 block. On the left abutment, there are 2 *VWP* in the S4 section, related to B28 block, and 3 *VWP* in the S5 section of B30 block.

The analysis in terms of hydraulic pressures in the foundation and at the base of the dam due to uplift water pressure (*U*) is carried out by converting the piezometric quota (*PQ*) into their corresponding loads, through the difference between PE and the installation quota (*IQ*) of each piezometer (Equation 1). The unit of measurement obtained for *U* is given in meters of water column (m H₂O).

$$U = PQ - IQ \tag{1}$$

Table 2 presents a comparison between the observed uplift pressures in each of the piezometers (*PZ*) and their design predicted values. The *PZ* highlighted in bold in the “piezometer code/block” column (second column) corresponds to the instruments installed at the dam base, facing downstream. The *PZ* highlighted in italics correspond to the instruments installed at the dam base, facing upstream. The other piezometers are located inside the rock mass.

According to design forecasts, the uplift pressures at the dam base facing downstream should be lower than

the values recorded inside the foundation mass. About the uplift pressures at the dam base recorder by *VWP* facing upstream, they were estimated during design period disregarding the possible influence of the injection curtains in the overall reduction of uplift water pressures. In this way, their values are higher than the uplift water pressures recorded by downstream *VWP*. This may also justify the control parameters and pore pressure limits being high in relation to what has been observed in these 17 years of monitoring.

However, the influence of injection curtains in reducing uplift water pressures is still a controversial topic. It is known that they are essential to reduce seepage through the foundation and, consequently, can increase the effectiveness of drains – especially in a very permeable rock mass – since otherwise the drains could be overloaded with excessive flows. On the other hand, Costa (2012) comments that in areas of low permeability of a dam foundation, injections do not have any “positive effect”, regardless of the purpose for which they were programmed. Injections should reduce percolation in very permeable areas, but only drainage will relieve uplift water pressure. Therefore, the best solution tends to be the simultaneous use of these two systems – injection curtains and drains.

The graphs in Figure 8 and Figure 9 show the variation in uplift water pressures over the 17 years of monitoring the *VWP* in the inspection gallery region and in the stilling basin, respectively.

From the graph in Figure 8, it is highlighted that the highest pressures currently tend to be registered in *VWP*

Table 2. Hydrostatic uplift pressures comparison (design *versus* observed loads).

Dam region	Piezometer code / block	U (m H ₂ O)		Umax: greatest record (mH ₂ O)	Current trend of U (mH ₂ O)
		Control	Limit		
IW/RA	PZ-TA-01 (downstream)	1.43	11.43	1.13	0.63 to 0.93
	PZ-TA-02 (downstream)	0.60	0.60	0.80	-0.40 to 0.70
RA	PZ-S1-01 (downstream) / B06	19.49	32.39	6.69	3.29 to 4.09
	PZ-S1-02 (downstream) / B06	11.71	23.91	4.61	0.81 to 1.81
Spillway	PZ-S2-01 (downstream) / B17	21.50	23.50	4.20	1.60 to 2.10
	PE-S2-01 (stilling basin) / B17	-	-	8.95	1.45 to 2.45
	PE-S2-02 (stilling basin) / B17	-	-	12.85	2.25 to 3.75
	PZ-S3-01 (downstream) / B21	16.50	17.50	3.40	2.80 to 3.10
	PZ-S3-02 (downstream) / B21	9.04	9.98	3.84	3.34 to 3.54
	PE-S3-01 (stilling basin) / B21	-	-	9.60	2.00 to 4.00
	<i>PZ-S6-01 (upstream) / B25</i>	24.21	28.21	11.61	6.61 to 7.61
	PZ-S6-02 (downstream) / B25	11.80	12.50	4.30	3.80 to 4.20
	PZ-S6-03 (downstream) / B25	8.64	9.64	4.14	3.54 to 3.94
	LA	PZ-S4-01 (downstream) / B28	23.64	37.04	7.54
PZ-S4-02 (downstream) / B28		11.31	23.61	4.71	3.11 to 4.11
<i>PZ-S5-01 (upstream) / B30</i>		31.60	38.80	8.70	5.90 to 6.30
PZ-S5-02 (downstream) / B30		15.61	28.21	1.41	0.51 to 0.91
PZ-S5-03 (downstream) / B30		2.5	16.1	9.90	9.10 to 9.40

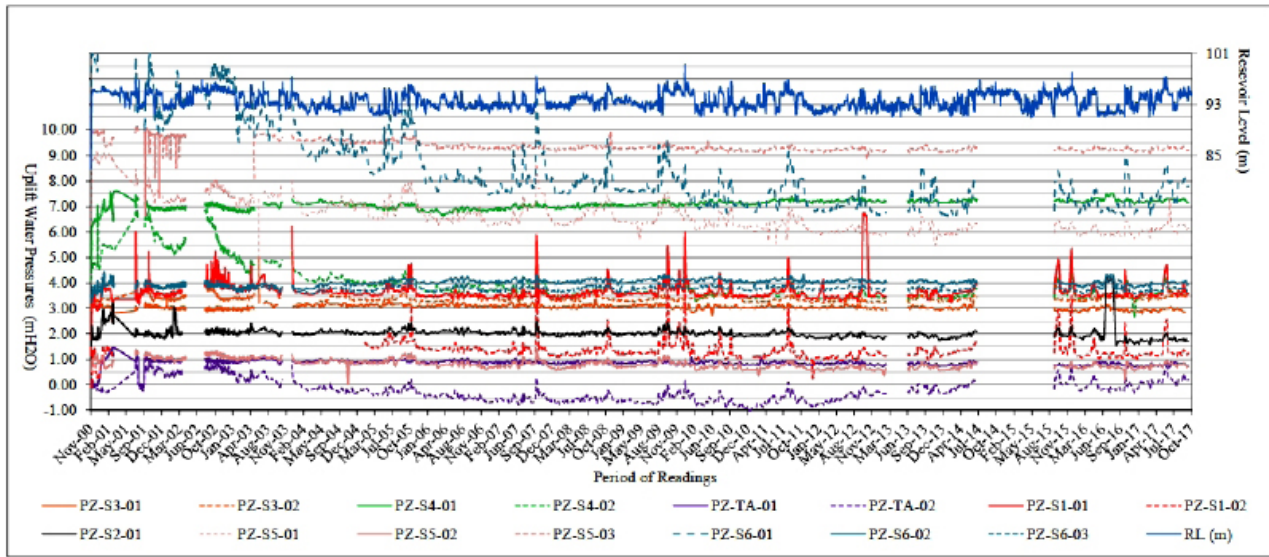


Figure 8. Variation of uplift pressures in the inspection gallery *VWP*.

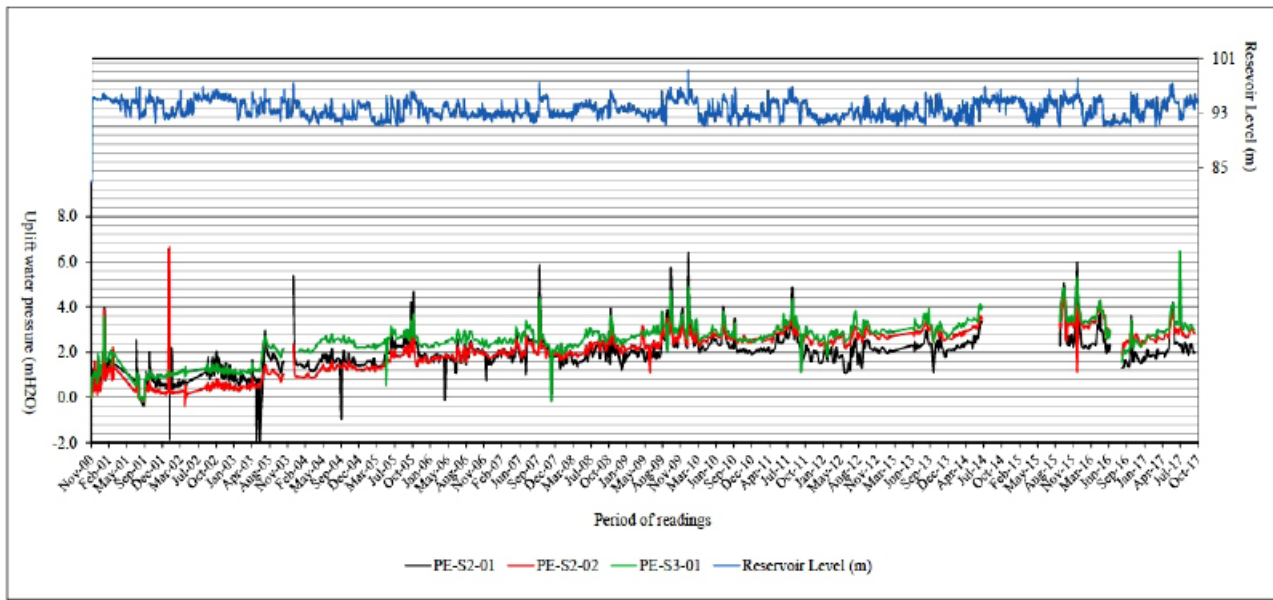


Figure 9. Variation of uplift pressures in the stilling basin *VWP*.

PZ-S5-03 and PZ-S6-03, both facing upstream, and it is also observed that under normal operating conditions there is an uplift pressures oscillation trend as a reservoir level upstream (RL) function. The uplift pressures observed in the stilling basin piezometers (Figure 9) present the same order of magnitude and increased until mid-2009. From then on, their records stabilized between 1.5 and 3.0 m H₂O.

It is interesting to observe how quickly the system responds. In July 2016, during a maintenance procedure to carry out an inspection of the stilling basin, the pumping system of well N. 02 – located on the spillway – was shut down for a few days. The flows that discharged in well N.02 were

diverted to well N. 01. As a result, there was an increase in the water level inside well No. 2 and the uplift pressures in this region increased immediately after the pumps were turned off. On this occasion, several piezometers reached their historic maximums.

The uplift pressures verified in the right abutment region (*RA*) from the records at the dam base (contact of the *RCC* with the basaltic or sandstone rock) are in the same instrumented section lower than the uplift pressures inside the rock mass underlying the dam base.

The uplift pressures in the *RA* piezometers tend to be lower than those of the control or slightly higher (~ 0.10 m.c.a.), as

in the PZ-TA-02 case. Its lower record of the current reading trend is a slightly negative uplift pressure (- 0.40 m.c.a.), which reveals that the region is well drained – close to the drainage tunnel. In general, the conditions referring to the piezometry data in this region can be considered normal.

In the region of the stilling basin, the PE-S2-01, PE-S2-02 and PE-S3-01 *VWP* present uplift pressures in the same order of magnitude. Considering the trend of stability of these *VWP* readings, it is possible to infer that the uplift pressure conditions in the stilling basin region were always within the expected behavior, except when the well drainage pump No. 2 was turned off. Unfortunately, the control or limits values for these *VWP* were not estimated in design phase so that some comparison could be made with the database.

The uplift pressures observed in the spillway region tend to be lower than the control values. The pore pressures at the downstream dam base – indicated by PZ-S3-02 and PZ-S6-03 *VWP* – are of the same order of magnitude and appear to be stabilized. In section S3, the uplift pressure at the dam base is slightly higher than that recorded inside the foundation mass by PZ-S3-01 *VWP*.

In section S6, the uplift pressure at the downstream dam base (PZ-S6-03) is of the same order of magnitude as that observed in PZ-S6-02 instrument, which is installed inside the sandstone mass. Since the uplift pressure at the upstream dam base – indicated by PZ-S6-01 – is approximately twice the one observed at the downstream dam base by PZ-S6-03, it is possible to infer that the drains in this region are reducing the pressures by about 50%. It should be noted that the injection curtain was not considered in the design phase when estimating the control and limit piezometric quotas and, given the possibility of its influence, it is justified that the control and limit parameters are relatively high. In general, the conditions from the piezometry in this region can be considered normal.

4. Deformation analysis of Dona Francisca dam foundation

The data of foundation deformation of a concrete dam consists in one of the most important information in the monitoring of the behavior of these structures, throughout the time. These deformations result from the loads imposed by the construction of dam's massif, reservoir filling and variations in reservoir level during operational period. The measured settlements in the construction period and in the first years of operation of the dam allow a first assessment of the real deformability of the foundation, through comparison with design estimates.

Extensometers are the most indicated instruments for direct monitoring of deformation that occur between the anchor points and the head of the rods of these instruments installed in the foundation. Typically, they are installed from the inside of drainage gallery, close to the base of the dam.

In the case of Dona Francisca dam, the settlements during constructive period were not measured. However, after this stage, multiple rod extensometers (*MREs*) were installed in key sections of blocks IW, B25 and B28, allowing the monitoring of deformations due to the filling of the reservoir and during operational phases.

The settlement, resulting deformation and horizontal translation at the base of a concrete dam can be estimated from the installation of a rosette of extensometers in a given block. The rosette is a set of three *RMEs* installed from the inspection gallery, in which the vertical is at the center and the other two are inclined approximately 30 ° in relation to the vertical. The *MREs* installed were made of fiberglass rods and mounted on site. Each rod was inserted into a rotary drilling hole, fixed at its lower end through a grout-injected section, and the upper end was placed in an easily accessible location – in the region of the inspection gallery. A polyethylene tube protects each rod by avoiding contact with the grouting. The standard diameter of the rods is 8.0 mm and each *MRE* has two rods: a short rod (*SR*) with a length of 7.0 to 10.0 m and a long rod (*LR*) with a length of 30.0 to 40.0 m. The function of the *SR* is monitoring the deformation of the rocky massif right below the base of the dam.

The Figure 10 present the evolution of deformations recorded by the long rods of the *MREs* installed in B25 and B28 blocks, and the Figure 11 present the evolution of deformations recorded by the long rods of the *MREs* installed in *IW* block – during about 17 years of monitoring. The negative values of deformations correspond to distension of the rods as a consequence of stresses relieving in the rocky massif at foundation. The positive values of deformations are related to compression of the rods, as consequence of the compression in the rocky massif at foundation. Some gaps observed in deformation records occurred due to technical problems with the *MREs* reading equipment, making it impossible to monitor during this associate period.

Due to the horizontal loading, resulting from elevation of the reservoir level, it is expected that stress relief will occur and hence uplift/elevation of the rocky massif at the upstream dam base, in addition to the increase of stresses and settlements at the downstream dam base. This can be verified from the correlation shown in the Figure 10 and Figure 11, linking deformations and the oscillation of the reservoir level all over time. It is observed that the *MREs* placed at upstream zone of the dam are more sensitive to the *RL* oscillation.

Through the analysis of deformation data of the foundation, acquired from the extensometers positioned in the *IW* block and shown in the graphs of Figure 11, it is possible to verify that the magnitudes of the records are lower to those found in the blocks of the spillway region (B25) and left abutment (B28). The reason for this behavior is that the foundation at the *IW* block region is composed of basaltic rocks which present lower deformability in comparison to the sedimentary rocks which are predominant in other

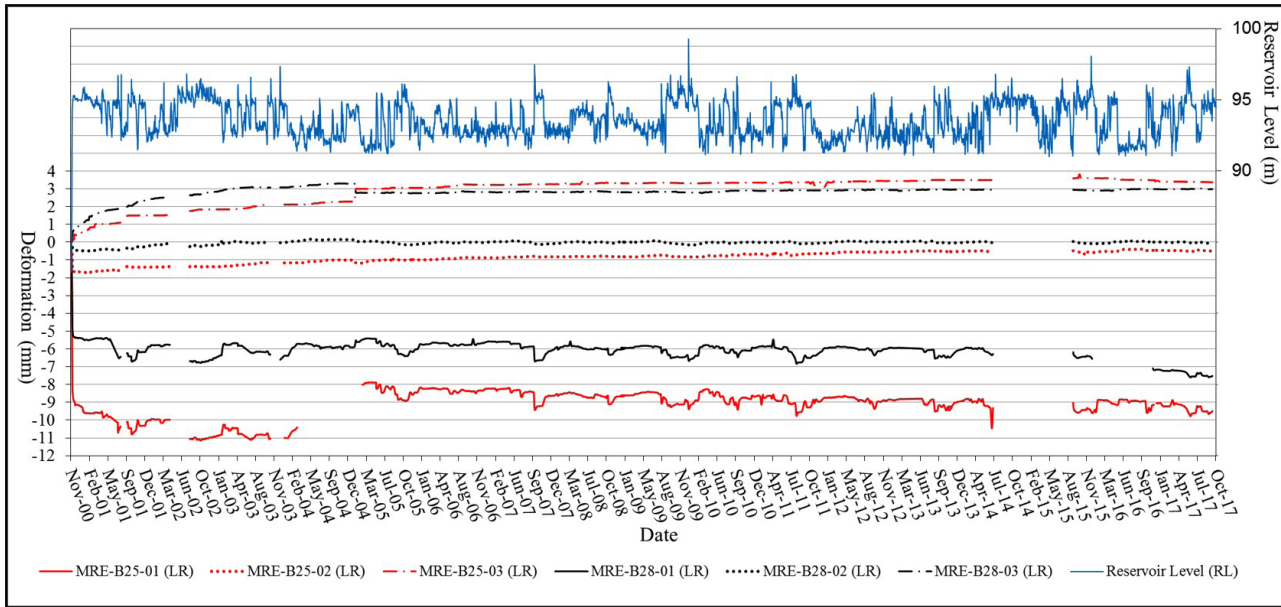


Figure 10. Total deformation recorded from the *MREs* long rods placed in the B25 and B28 blocks.

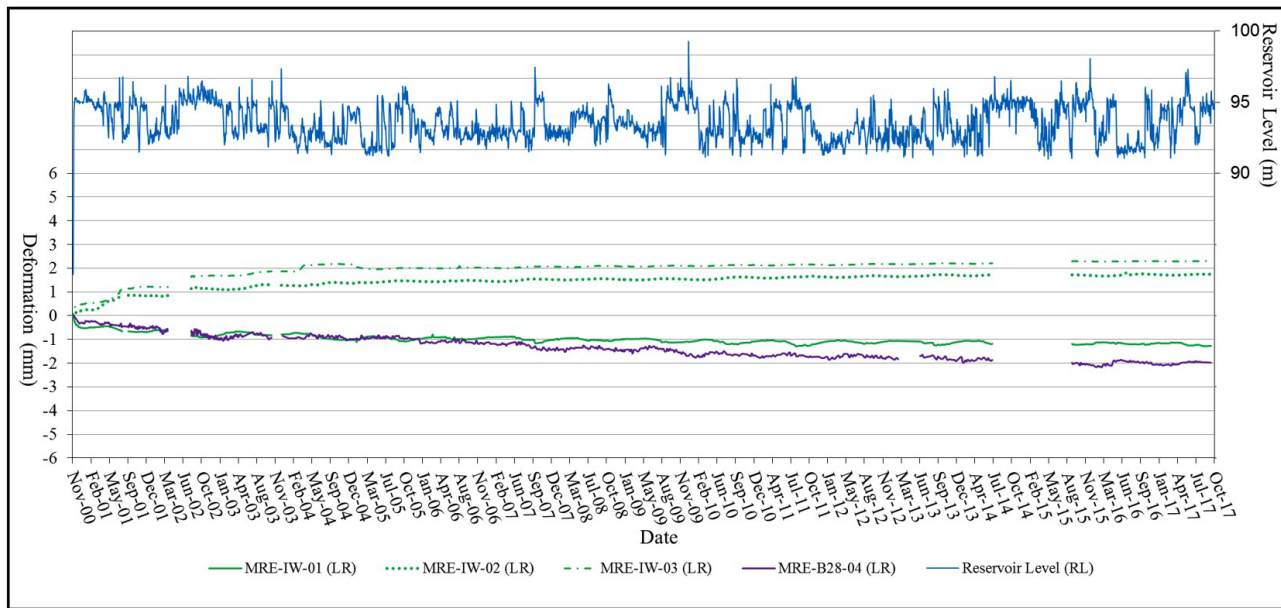


Figure 11. Total deformation recorded from the *MREs* long rods placed in the IW block.

regions of the dam. In general, the deformation data of the Dona Francisca dam foundation are consistent in terms of expected behavior.

The upstream directed extensometers (*MREs*-01) have always been stretched. The extensometers installed vertically (*MREs*-02) tended to indicate either small compression, or distension. The *MREs* at downstream (*MREs*-03) have always been stretched. However, it should be noticed that the theoretical design predictions for the

extensometer readings indicated distension values even for the instruments placed at downstream sections of the dam, highlighting the difficulty of predicting the behavior for this specific type of foundation. In terms of magnitude of deformations, most of the design estimates were lower than the actual structure behavior.

The Table 3 presents a summary of the elastic (δ_e) and total (δ_t) deformations observed in the *MREs* installed in the Dona Francisca HPP dam. The data refer to the initial period

Table 3. Summary of the elastic (δe), slow (δs) and total (δt) deformations recorded from the MREs.

MRE / LR – Long Rod / SR – Short Rod		Δe (two weeks)		$\delta t = \delta s + \delta e$				
				5 years (Jan - 2005)		17 years (Out - 2017)		
		δe^* (mm)	$\delta e/\delta t17$ (%)	$\delta t5^*$ (mm)	$\delta t5/\delta t17$ (%)	Rate of δs - 2000 to 2005 (mm/year)	$\delta t17^*$ (mm)	Rate of δs - 2005 to 2017 (mm/year)
MRE-IW-01	LR	-0.28	22	-1.03	81	-0.150	-1.27	-0.020
	SR	-0.28	70	-0.25	62	0.006	-0.40	-0.013
MRE-IW-02	LR	0.18	10	1.36	78	0.236	1.75	0.033
	SR	0.14	25	0.58	105	0.088	0.55	-0.002
MRE-IW-03	LR	0.37	16	2.16	94	0.358	2.30	0.012
	SR	0.24	27	0.84	93	0.120	0.90	0.005
MRE-IW-04	LR	-0.27	14	-0.99	50	-0.144	-1.98	-0.083
	SR	-0.36	26	-0.94	69	-0.116	-1.37	-0.036
MRE-B25-01	LR	-8.86	93	-8.00	84	0.172	-9.50	-0.125
	SR	-4.84	46	-9.27	89	-0.886	-10.41	-0.095
MRE-B25-02	LR	-1.65	337	-1.17	239	0.096	-0.49	0.057
	SR	-0.71	473	-0.32	213	0.078	-0.15	0.014
MRE-B25-03	LR	0.15	4	3.00	89	0.570	3.37	0.031
	SR	0.85	23	3.00	82	0.430	3.67	0.056
MRE-B28-01	LR	-5.30	70	-5.91	79	-0.122	-7.52	-0.134
	SR	-1.36	52	-2.04	79	-0.136	-2.59	-0.046
MRE-B28-02	LR	-0.40	667	0.14	-	0.108	-0.06	-0.017
	SR	-0.29	45	-0.43	66	-0.028	-0.65	-0.018
MRE-B28-03	LR	0.65	22	3.30	110	0.530	2.99	-0.026
	SR	0.12	27	0.52	118	0.080	0.44	-0.007

* Compression (+) or distension (-).

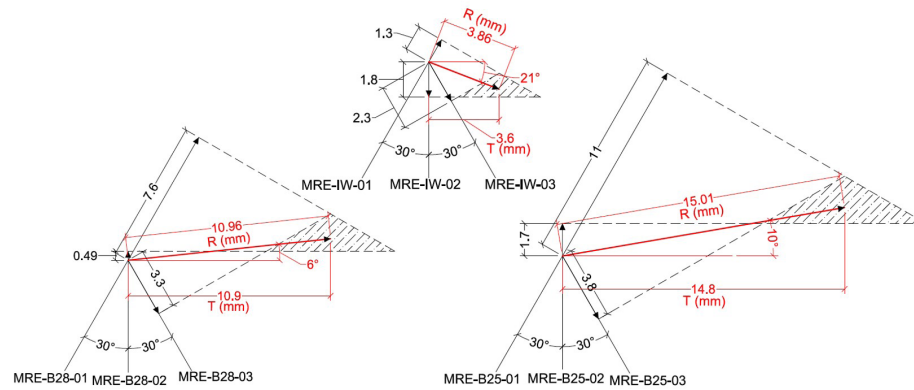


Figure 12. Resulting maximum deformation (R) and horizontal displacement (T) in the dam base.

and after 5 and 17 years of operation. The percentages – in relation to the total period of 17 years of monitoring – of δe and δt after 5 years of operation are presented. In addition, the rate in which the slow deformations (δs) occurred in the first 5 years and past 12 years are showed below.

Analyzing the previous graphs from Figure 10 and Figure 11 and the data presented in Table 3, it is observed that the process of settlement of the rocky massif was more intense in the first 5 years of dam operation. From that period on, although the deformations continued to occur, mainly in the deeper layers of the foundation, it was observed that it took place in a lower rate. At the end of 17 years of

monitoring, it is possible to notice the tendency of a final stage of stabilization of the rocky massif. The experience reported by some authors – mainly regarding dams on basaltic massifs – shows that these long-term or slow deformations can occur in periods superior to 20 years after reservoir filling – such as the cases of Itaipu and São Simão – Brazilian dams presented in Silveira (2003).

The Figure 12 presents the vector calculations of the resulting maximum deformation (R) and horizontal displacement (T) of the Dona Francisca HPP dam base, from the maximum deformations recorded by the MREs rosettes installed in blocks IW, B28 and B25.

According to Silveira (2003), since the lower anchoring points of the extensometers are in an absolute reference, calculating a composition of the distension or compression recorded by the three *MREs* (long rods) results in a triangle and not a point. For the calculation of the resulting deformation, this same author recommends the determination of the geometric center of a triangle formed by the intersection of the three bisectors of the projected vectors. From the vector calculations presented, it is possible to estimate that the resultant deformations (*R*) and the horizontal displacement (*T*) at the dam base in the spillway region were of the order of 10.0 to 15.0 mm – higher than that one verified for the intake works region, whose value was approximately 4.0 mm.

5. Conclusions

Argillites, siltites and sandstones are sedimentary rocks that are commonly referred to as soft rocks because of their low resistance. According to Kanji (2014), these rocks are a critical material since they present a series of problems. They have a behavior intermediate between soil and hard rock and often, they cannot be tested neither in soil mechanics laboratories due to its high resistance, nor in rock mechanics laboratories as they are too soft to be trimmed and tested. Because of soft rocks' complexity in structure, material property, and geological environment, knowledge and understanding about soft rocks is a challenge in geotechnical engineering, mainly in the case of dams built on these massifs.

The comparison with the performance of other similar dams is important for safety analysis based on dam's behavior experience. But in the case of dams built on sedimentary rocks, only a few instrumentation data from other structures can be found in the literature to help professionals involved in dam monitoring. Within this context, this paper brings a case study about the geotechnical behavior of Dona Francisca gravity dam that was built on sedimentary rocks.

The deformability of rocky masses – related to a certain loading – is influenced by four factors: mineralogical composition, alteration degree, discontinuity plans and the relationship between the direction of the load applied and the discontinuity direction. These influences could be verified from the deformations observed in the foundation of Dona Francisca dam, since they presented a higher magnitude than most of the records of other Brazilian dams, reported in Silveira (2003).

This fact is mainly related to the foundation characteristics of Dona Francisca dam that usually present larger deformability than, for example, the basaltic masses on which several dams were built in Brazil. Therefore, the construction of dams in such foundation conditions requires special attention from the design stage, especially through the implementation of a good instrumentation plan, allowing the monitoring of structure behavior in a continuous way and evaluating its safety.

The deformation data recorded from the extensometers are consistent and enable the describing of foundation

behavior of Dona Francisca HPP dam. The influence of time factor can be observed on the deformations of the rock mass when permanent loading due to self-weight of the dam and hydraulic loadings are associated. The rock layer near the dam base and monitored by the short rods of the extensometers was practically stabilized after the first 5 years of operation. The deeper layers of foundation, monitored by long rods, tended to be in a final stage of stabilization, indicating a normal situation – although a small rate of deformation (0.025 mm/year) can be observed.

The uplift pressures at the base and foundation of the Dona Francisca HPP dam tended to decrease and / or stabilize over time. In this way – except for specific situations that presented some unexpected situation – the scenario obtained in terms of structure safety from the piezometric analysis can be considered normal.

Finally, it is worth emphasizing the importance of carrying out the dam's hydrogeotechnical instrumentation analysis together with the observations obtained from the visual inspections, which are also relevant to guarantee adequate control and comprehensive monitoring of the concrete dam behavior.

Acknowledgements

The authors acknowledge the Postgraduate Program in Civil Engineering / Federal University of Rio Grande do Sul (PPGEC/UFRGS) and the Electric Power State Company of Rio Grande do Sul – Generation and Transmission (CEEE-GT) for their partnership and the technical support given to this research, also the Coordination for the Improvement of Higher Education (CAPES) and the National Council for Scientific and Technological Development (CNPq) for the financial support provided to the first author during this study.

Declaration of interest

The authors have no conflicts of interest to declare.

Authors' contributions

Verlei Oliveira dos Santos: Conceptualization, Data curation, Investigation, Formal analysis, Methodology, Validation, Writing – original draft. Luiz Antonio Bressani: Conceptualization, Methodology, Supervision, Project administration, Validation, Visualization, Writing – review & editing. Camila de Souza Dahm Smirdele: Project administration, Data curation, Resources, Supervision, Visualization.

Data availability

Data generated and analyzed in the course of the current study are not publicly available because they are owned by

CEEE-GT. However, a complete or limited dataset can be made available upon reasonable request.

List of symbols

c	cohesion
<i>HPP</i>	Hydroelectric power plant
<i>IQ</i>	Installation quota
<i>IW</i>	Intake works
<i>LR</i>	Long rods
MRE	Multiple rod extensometers
<i>PQ</i>	Piezometric quota
<i>PZ</i>	Piezometer
<i>R</i>	Resulting maximum deformation
<i>RA</i>	Right abutment region
<i>RCC</i>	Rolled compacted concrete
<i>RL</i>	Reservoir level upstream
<i>T</i>	Horizontal displacement
<i>U</i>	Uplift water pressure
<i>UCS</i>	Unconfined compressive strength
<i>VWP</i>	Vibrating wire piezometer
δe	Elastic deformation
δs	Slow deformation
δt	Total deformation
σ	Normal stress
τ	Shear stress
φ	Friction angle

References

- Antunes Sobrinho, J., Albertoni, C.A., Tajima, R., & Moraes, R.B. (1999). Investigaç o dos materiais de funda o da UHE Dona Francisca. In *Proceedings of the XXIII Semin rio Nacional de Grandes Barragens* (Vol. 1, pp. 229-236). Belo Horizonte/Brazil. Rio de Janeiro: CBDB. (in Portuguese).
- Costa, W.D. (2012). *Geologia de barragens* (1. ed.). Oficina de Textos. (in Portuguese).
- Dobereiner, L. (1984). *Engineering geology of weak sandstones* [Doctoral thesis]. University of London.
- Gonzales de Vallejo, L.I., Ferrer, M., Ortu o, L., & Oteo, C. (2002). *Ingenieria Geologica*. Pearson Education. (in Spanish).
- Johnston, I.W. (1993). Soft rock engineering. In J.A. Judson, E.T. Brown, C. Fairhurst & E. Hoek (Eds.), *Comprehensive rock engineering: principles, practice & projects* (Vol. 1, pp. 367-393). Pergamon Press.
- Kanji, M.A. (2014). Critical issues in soft rocks. *Journal of Rock Mechanics and Geotechnical Engineering*, 6, 186-195.
- Kanji, M.A., He, M., & Sousa, L.R. (2020). *Soft rock mechanics and engineering*. Springer.
- Pastore, E.L., Cruz, P.T., & Freitas Junior, M.S. (2005). Funda es de barragens e estruturas em arenito: natureza dos maci os e controle de fluxo e eros es. In *Proceedings of the XXX Semin rio Nacional de Grandes Barragens*, Foz do Igua u/Brazil. Rio de Janeiro: CBDB. (in Portuguese).
- Rocha, M. (1975). Some problems related to the rock mechanics of low strength natural materials. In *Proceedings of the 5th Pan-American conference on soil mechanics and foundation engineering* (pp 489-514), Buenos Aires. Geotecnia. (in Portuguese).
- Silveira, J.F.A. (2003). *Instrumenta o e comportamento de funda es de barragens de concreto*. Oficina de Textos (in Portuguese).
- Terzaghi, K., & Peck, R. (1967). *Soil mechanics in engineering practice*. Wiley.

TECHNICAL NOTE

Soils and Rocks
v. 46, n. 2

Predicting driving transferred energy without needing the hammer efficiency: three case studies

André Querelli^{1#} , Tiago de Jesus Souza^{1,2} 

Technical Note

Keywords

Piled Foundation
Efficiency
Steel pile
Dynamic load test
Effective transferred energy

Abstract

This study presents case studies on the implementation of an innovative method of calculating effective driving energy with no need to account for hammer efficiency. The approach is based on measurements of set and elastic rebound, as well as a site-specific parameter (λ) calibration. The study applied this method to steel piles located in the cities of Santos (SP), Itaguaí (RJ), and Óbidos (PA), with the latter site being built in the Amazon region, near the Amazon River. Following coefficient calibration, the effective driving energy estimation technique exhibited a strong correlation with realistic and accurate energies directly obtained from dynamic loading tests. The method provides a highly accurate means of calculating effectively transferred energy to piles due to hammer blows, without relying on knowledge of the driving system performance. In that way, it can be applied to all the piles at the site (100% of them), including those that are not tested. This optimized and agile approach represents a significant breakthrough in foundation engineering and an enhance of pile foundation quality control.

1. Introduction

In Brazil, as many other countries worldwide, deep foundation control is often carried out using the “dynamic formulae” method. In the mid-20th century, Engineering News-Record documented over 450 dynamic formulae, according to Smith (1960). Over time, hundreds of equations have been developed, with one important distinction being that earlier versions did not account for energy losses due to the hammer stroke. The publication of the well-known Hiley formula (Hiley, 1925) increased the consideration of energy losses in dynamic equations.

Efficiency and effective energy of the blow are important factors in improving dynamic equations and ensuring successful pile driving quality control. As such, it is an important area of research for the advancement of pile driving.

This paper will assess the applicability of the “Querelli’s energy method”. Querelli (2019) method was developed using a large number of load tests and has been shown to be effective in determining the effective driving energy. One of the benefits of this method is that it eliminates the need for hammer efficiency or instrumentation during the hammer blow. This study evaluates the applicability of the method to reproduce the driving energy in three cases (Itaguaí, Santos, and Óbidos) involving steel-driven piles, using only the measures of pile set and elastic rebound in a rational way.

2. The importance of the energy effectively transferred to the pile

Equations known as dynamic formulae are widely used in the design and quality control of driven foundations to estimate the soil resistance mobilized in response to an impact to a driven pile. Theoretical support for these formulae comes from the concepts of energy conservation, Newtonian shocks, or the elasticity of Hooke’s law. Typically, the resistance is estimated using either the set (s), the elastic rebound (K), or both measures.

According to Querelli (2019), there are three primary components of the driving event: the energy (and its losses), the displacement (elastic or permanent), and the mobilized resistance (as a response to the stroke). These components are all correlated in one way or another. The effective energy is one of the base components of the tripod; however, this energy was not always correctly considered for resistance calculation.

One of the earliest formulations is from the first part of the nineteenth century, created by engineer Johann Eytelwein in 1820. Chellis (1961) also noted that this equation is comparable to (or equivalent to) the well-known “Dutch formula”. According to Chellis, this equation implicitly assumes a driving system efficiency of 100% (i.e., without losses), and the energy delivered to the pile is regarded as the gravitational potential energy of the blow ($W \cdot h$), as shown in Equation 1:

[#]Corresponding author. E-mail address: andre.querelli@solotechnique.com.br

¹Solotechnique Consultoria e Engenharia Geotécnica, Jundiaí, SP, Brasil.

²Instituto Tecnológico de Aeronáutica, São José dos Campos, SP, Brasil.

Submitted on January 3, 2023; Final Acceptance on April 4, 2023; Discussion open until August 31, 2023.

<https://doi.org/10.28927/SR.2023.000223>



This is an Open Access article distributed under the terms of the Creative Commons Attribution License, which permits unrestricted use, distribution, and reproduction in any medium, provided the original work is properly cited.

$$R = \frac{W \cdot h}{s \cdot \left(1 + \frac{W_p}{W}\right)} \quad (1)$$

where R is static resistance of the pile-ground assembly, W is the hammer weight, h is the hammer fall height, s is the set (permanent pile displacement), and W_p is the pile weight.

Two other well-known equations from the 19th century that use the same method to calculate the nominal energy applied are the Engineering News Records equation and Sanders' Formula (Chellis, 1961). Equation 2 was created in 1851 by Major Sanders and compares the nominal energy of the stroke to the work of the ground (product of resistance and permanent displacement). The Engineering News Records formula uses a similar strategy but adds the constant C to account for a part related to the elastic displacement of the pile (Equation 3).

$$R = (W \cdot h) / s \quad (2)$$

$$R = (W \cdot h) / (s + C) \quad (3)$$

Equations 1, 2, and 3, which were published in the 19th century, did not take energy losses into account. However, most of the dynamic formulae stated in later technological contexts started to consider such losses during the 20th century, particularly after the release of the well-known Hiley formula (Hiley, 1925), which is shown in Equation 4.

$$R = \frac{e \cdot W \cdot h}{s + \frac{C}{2}} \cdot \frac{W + \mu^2 \cdot W_p}{W + W_p} \quad (4)$$

where e is the impact efficiency and μ is the coefficient of restitution after the blow.

Equation 5 shows the "energy approach equation" (Paikowsky & Chernauskas, 1992), which also uses effective energy by adding a blow efficiency factor (η). This is another significant formula that was more recently published in the literature.

$$R = K_{sp} \frac{\eta \cdot W \cdot h}{s + (D - s) / 2} \quad (5)$$

where K_{sp} is the total strength reduction coefficient due to dynamic effects.

The main causes of this loss (or dissipation) of energy were listed by Chellis (1961) as follows: effects of winching and hammer-guide-tower friction (in the case of free fall), internal friction of the hammer with the confining case (for hydraulic hammers), energy dissipated in the generation of heat, sound, lateral movements of the pile, eccentric blows, elastic compression of the stump-cap.

The energy delivered to the pile during impact can no longer be considered nominal (weight vs height), as strength estimates must be based on a more realistic measure of energy

effectively transferred to the pile during the blow. Consequently, the inclusion of energy losses associated with the driving mechanism in equations improves their reliability significantly.

Thilakasiri et al. (2003) investigated the reliability of different formulae and found that the Janbu, Danish, and Hiley equations provided more dependable estimates than the Engineering News Formula. Similarly, Danziger & Ferreira (2000) reported high reliability in the Danish formula estimates made by Sorensen & Hansen (1957) for steel piles.

A study published by Tavenas & Audy (1972) clearly demonstrates how earlier formulae failed to accurately consider energy, resulting in strength estimates with errors on the order of more than 70%. The authors evaluated 478 pile driving records in non-cohesive soil and conducted 45 static load tests, concluding that any pile driving formula using the usual energy estimate will also be erroneous.

It is evident that the proper estimation of this quantity is crucial for accurately estimating the resistance of soil-pile systems. The issue of effectively transferred energy during impact represents a paradigm shift in the field of "dynamic formulae". In this regard, the practical methodology developed and published by Querelli (2019) has made a significant contribution to measuring effective energy.

3. Querelli's energy method

Using just the conventional measures of set and elastic rebound, Querelli (2019) proposed a way to estimate the effective (transferred) energy delivered to the pile due to the blow. Unlike usual, the suggested technique does not require instrumenting the pile at the moment of the stroke neither earlier evaluation of the drive system's effectiveness.

The author defined two starting points for the theoretical deduction:

- the idealized resistance vs pile displacement curve following the application of the blow; and
- Hooke's law, as expressed by the Chellis' (1961) formula.

This leads to the application of two simplifying assumptions: the first is that the set is so little compared to the elastic rebound that it can be disregarded ($s = 0$), and the second is that the soil *quake* exhibits a proportionality connection with the elastic rebound (K), *i.e.*, $C3$ is not constant.

Thus, Querelli created the fundamental equation of the method, which determines the maximum displacement of the pile after the blow (D) (Equation 6). In this equation, the key calibration factor is the λ coefficient. The method deduction was first presented in Querelli (2019), in Portuguese, and later in Querelli & Massad (2019b), in English.

$$D = \lambda \cdot \sqrt{\frac{\eta \cdot W \cdot h \cdot L}{E \cdot A}} \quad (6)$$

When the terms are rearranged to isolate the aimed parameter (effective energy; $E_{ef} = \eta \cdot W \cdot h$), the Equation 7 is achieved as:

$$E_{ef} = \frac{1}{\lambda^2} \cdot \frac{D^2 \cdot E \cdot A}{L} \quad (7)$$

An important finding regarding the coefficient λ emerged from the author’s in-depth analysis of the equation and application method: previous calibrations of λ should always be carried out, as the most suitable value for λ differs from site to site (Querelli, 2019). This formed the basis for the five-step process for applying the methodology.

- (a) Choose a sample of piles for testing in the Dynamic Loading Test;
- (b) Perform dynamic tests on the piles with increasing energy, simultaneously measuring set and elastic rebound for each blow;
- (c) With these two measurements, the geometry (area and length), and the elastic modulus (E) of the pile material, plot the graph of D vs $\sqrt{\left[\frac{E_{ef} \cdot L}{E \cdot A} \right]}$ for each of the monitored blows;
- (d) A line of best fit passing through the origin [0,0] is plotted for the points. The slope of this line (angular coefficient) represents the parameter λ , calibrated for the specific project;
- (e) This (calibrated) λ coefficient, along with the set and elastic rebound measures of blows in unmonitored piles, should be applied to Equation 7 to estimate the effectively transferred energy in each impact of the driving hammer.

This study refers to the approach as “Querelli’s energy method” because Querelli (2019) is the original developer

of it. The first study assessed fifteen cases in Brazil that used either concrete or steel piles, and the results showed that the λ values ranged from 1.22 to 1.71 for concrete piles and 1.13 to 1.35 for steel piles. To document these findings, Querelli & Massad (2019b) also republished (in English) twelve of these fifteen datasets.

Later, Querelli & Massad (2019a) also presented three new sites in the state of Rio de Janeiro on concrete piles. Their methodology was efficient, obtaining λ values equal to 1.22, 1.28 and 1.39, respectively. There is also a previous case study by Querelli & Massad (2017) in which no mention is made of the referred methodology or even the λ coefficient. However, it is possible to infer, from the presented database, λ values of 1.28 and 1.29 for two neighboring construction sites located in the city of Duque de Caxias (RJ). Souza (2022) also presented two sites verifying the Querelli’s method.

4. Case studies

4.1 Geological-geotechnical characterization

The piles are from three independent building sites in the cities of Santos (SP), Itaguaí (RJ) and Óbidos (PA). The location is presented in Figure 1, being important to point that all projects are in Brazil.

The subsoil characteristics of the fields are similar, consisting of coastal formations typical of lowland areas in Santos and Itaguaí or near-river geological formations in Óbidos, which is near the Amazon River. Predominantly,

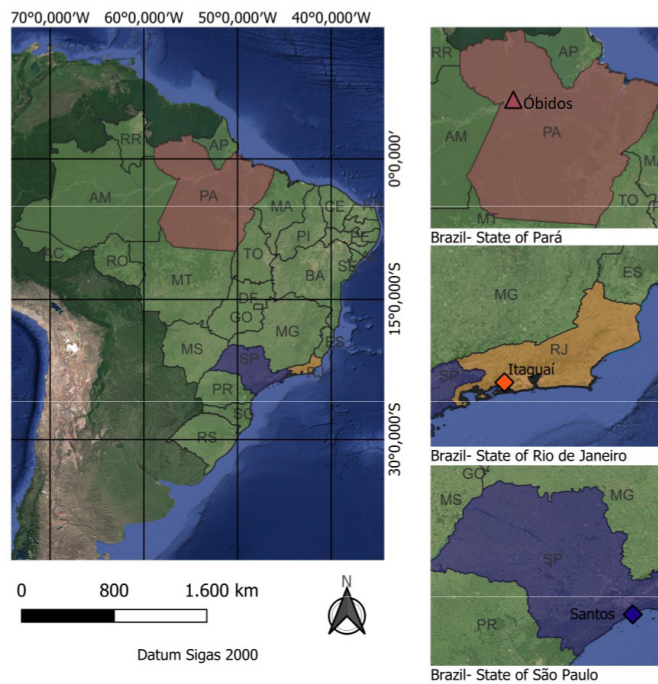


Figure 1. Study area.

the soil is sedimentary, with a layer of compacted backfill followed by very soft dark grey and black organic clay, a layer of medium-sized layers of compacted sand or hard sandy clay with sediments, another layer of soft clay, and finally a layer of very compact residual soil. The water level was found to be quite close to the surface at all sites, and the thicknesses of each layer are summarized in Table 1.

Several authors have researched and distributed information on the unique characteristics of the sediments that make up the soils in lowland and river near areas in the technical literature. Examples of authors that made significant contributions to the study and characterization of soils in the Baixada Santista are Suguio & Martin (1994), who combined the findings of several earlier studies on this topic.

4.2 On-site testing

The dynamic loading tests were conducted using the modality of increasing energy, with a total of 27 piles tested in Santos, 10 in Itaguaí, and 64 in Óbidos. In total, 223 records (blows) were obtained from the dynamic tests. The hammer used in Santos was an 83 kN free-fall type, while in Itaguaí it was a 70 kN hydraulic hammer and in Óbidos a 24 kN free-fall hammer.

The tested piles were steel profiles, including HP 310×110, HP 310×125, and W 360×122, as well as 406 mm-diameter

tubed steel piles (9.5 mm thick) cross-sections. Table 2 presents a summary of all tested and evaluated piles.

The analysis methodology adopted the application script presented previously. For each pile, the individual information of each blow applied was used to plot points on graphs of D vs $\sqrt{\left[\frac{E_{ef} L}{E A} \right]}$.

Subsequently, the best linear regression (with the highest R^2 value) was plotted through the origin point [0,0]. The angular coefficient of the obtained straight line was then calculated and it is numerically equivalent to the average λ coefficient for each pile.

5. Results and analysis

Figures 2 to 4 show the results in the form of graphs and regressions, with a focus on the λ coefficient, which is the angular coefficient of the linear regression equations.

The site-specific findings are summarized in Table 3, highlighting the importance of the ratio $1/\lambda^2$ as the angular coefficient in Equation 7 for accurately estimating the energy effectively transmitted to the piles.

The λ coefficient obtained was equal to 1.01, 1.17 and 1.11 in Santos, Itaguaí and Óbidos, respectively. The low coefficients of variation observed ranging 7.4% to 13.4%, in association with the high coefficients of determination (R^2)

Table 1. Thickness of the subsoil layers at each evaluated site.

Layer	N_{SPT} (range) average	Soil layer thickness (m)		
		CASE 1: Santos (SP)	CASE 2: Itaguaí (RJ)	CASE 3: Óbidos (PA)
Compacted embankment	7-14	2.5-4.5	2-3.5	-
Very soft clay (organic)	0-1	16-20.5	12-14	9-16
Sand / Sandy Clay	12-20	9-12	4-7	-
Soft Clay	1-4	6-10	3-4.5	4-7
Compact to very compact sand (residual)	19-40	15-18.5	9-13	8-13

Table 2. Summary of data.

Case/ Municipality	Number of tested piles	Number of records of the dynamic test	Pile length range (m)	Tested Section
Case 1 - Santos (SP)	27	126	47.4 to 59.5	126 W360×122
Case 2 - Itaguaí (RJ)	10	33	36.0 to 39.5	8 HP310×110 and 25 HP310×125
Case 3 - Óbidos (PA)	64	64	20.0 to 30.0	6 TUBE 406 mm diam., 9.5 mm thick

Table 3. Summary of results.

Case	Location	λ (average)	Standard deviation	Coefficient of variation (%)	R^2	$1/\lambda^2$ (average)
Case 1	Santos (SP)	1.01	0.075	7.4	0.95	0.98
Case 2	Itaguaí (RJ)	1.17	0.115	9.8	0.86	0.73
Case 3	Óbidos (PA)	1.11	0.149	13.4	0.99	0.81

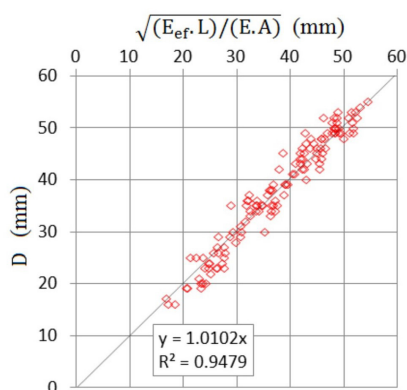


Figure 2. Case 1: Santos (SP).

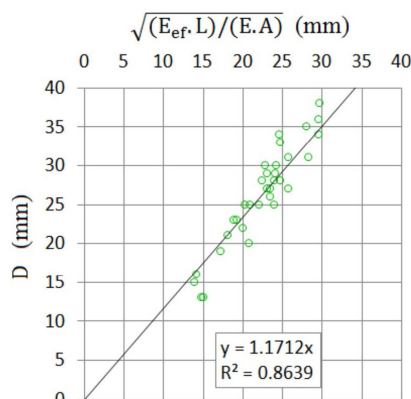


Figure 3. Case 2: Itaguaí (RJ).

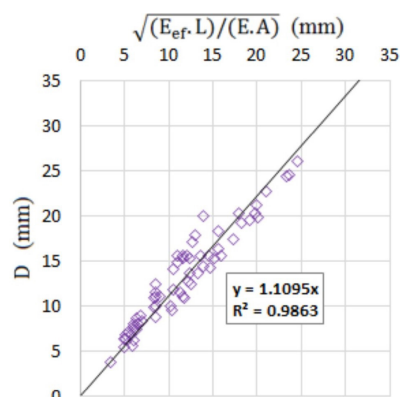


Figure 4. Case 3: Óbidos (PR).

of the calibrations, demonstrate the degree of effectiveness of the average adjustment of the method.

6. Conclusion

The results confirm the effectiveness of Querelli's method as it was possible to obtain average λ values

with high determination coefficients (R^2 equal to 0.95, 0.86, and 0.99) and low coefficient of variation of λ ($< 13.5\%$).

The average λ for the Santos site (1.01) is even lower than the lowest value found by Querelli (2019) and Querelli & Massad (2019b) for steel piles (1.17).

The average value of 0.98 obtained for the ratio $1/\lambda^2$ in Case 1 (Santos) is almost 35% higher than that obtained for Case 2 (Itaguaí), which is equal to 0.73. The Óbidos site falls in the mid-range of the others. This reinforces Querelli's (2019) finding that the method should be applied through previous calibrations ("site-to-site") of the λ ratio through dynamic tests to contemplate local particularities, making its use more effective. It is a "site-specific" parameter.

The article contributes to the validation of the method proposed by Querelli (2019), which is a paradigm shift in foundation engineering because it allows for the estimation of the effective energy of pile driving without requiring the efficiency of the hammer or instantaneous instrumentation (at the moment of the blow).

Declaration of interest

We authors have no conflicts of interest to disclose.

Authors' contributions

André Querelli: conceptualization, methodology, data curation, formal analysis, writing – original draft. Tiago de Jesus Souza: data curation, validation, writing – reviewing and editing.

Data availability

The data that support the findings of this study are available from the corresponding author upon reasonable request.

List of symbols

e	Impact efficiency
h	Hammer fall height
s	set; permanent pile displacement
A	Cross-section area
C	Elastic deformation coefficient. Equal to 2.54 cm for free fall hammers and 0.254 cm for steam hammers
$C3$	Soil Quake; elasticity of soil below pile toe
D	Maximum displacement of the pile after the blow (set + elastic rebound)
E	Pile material's Young Modulus
E_{ef}	Energy effectively transferred to the pile (equal to $\eta \cdot W \cdot h$)
K_{sp}	Total strength reduction coefficient due to dynamic effects
K	Pile's elastic rebound

L	Pile length
N_{SPT}	Number of blows in the SPT test for penetration of the last 30cm of the standard sampler in the soil
R	Static resistance of the pile-ground assembly
W	Hammer weight
W_p	Pile weight
μ	coefficient of restitution after the blow
η	Efficiency of the driving system
λ	Lambda; coefficient of the energy estimation method

References

- Chellis, R.D. (1961). *Pile foundations*. McGraw-Hill.
- Danziger, B.R., & Ferreira, J.S. (2000). Backanalysis of steel pile driving for quality assurance. In *6th International Conference on the Application of the Stress-Wave Theory to Piles* (pp. 657–663). São Paulo: Balkema.
- Hiley, A. (1925). A rational pile-driving formula and its application in piling practice explained. *Engineering (London)*, 119, 657-721.
- Paikowsky, S.G., & Chernauskas, L.R. (1992). Energy approach for capacity evaluation of driven piles. In *4th International Conference on the Application of Stress-Wave Theory to Piles* (pp. 21-24). Rotterdam: CRC Press.
- Querelli, A. (2019). *Dynamic monitoring in pile driving: applicability of the Energy Approach equation and compression stresses estimation* [Master's dissertation, University of São Paulo]. University of São Paulo's repository (in Portuguese). <https://doi.org/10.11606/D.3.2019.tde-27082019-133407>.
- Querelli, A., & Massad, F. (2017). Simplified Hiley's formula calibration for precast concrete piles in Duque de Caxias. In *International Conference on Advances in Structural and Geotechnical Engineering – ICASGE'17* (pp. 1–15). Hurghada: Egyptian Geotechnical Society.
- Querelli, A., & Massad, F. (2019a). Proposição de um método alternativo para estimativa da energia efetiva na cravação de estacas. In *9º Seminário de Engenharia de Fundações Especiais e Geotecnia* (pp. 1-9). São Paulo: ABMS/ABEF. (in Portuguese).
- Querelli, A., & Massad, F. (2019b). An alternative method to estimate the effective energy during pile driving based on set and elastic rebound records. *Soils & Rocks*, 42(2), 179-189. <http://dx.doi.org/10.28927/SR.422179>.
- Smith, E.A.L. (1960). Pile-driving analysis by the wave equation. *Journal of the Engineering Mechanics Division*, 86(4), 35-61. <http://dx.doi.org/10.1061/JSFEAQ.0000281>.
- Sorensen, T., & Hansen, B. (1957). Pile driving formulae - an investigation based on dimensional considerations and a statistical analysis. In *4th International Conference Soil Mechanics and Foundation Engineering* (pp. 161-65). London: Butterworths.
- Souza, T.J. (2022). Aplicação do método de Querelli (2019) para previsão da energia efetiva de cravação sem a necessidade da eficiência do martelo. In *XX Congresso Brasileiro de Mecânica dos Solos e Engenharia Geotécnica* (pp. 2488-2495). São Paulo: ABMS. (in Portuguese). <https://doi.org/10.4322/cobramseg.2022.0313>.
- Suguo, K., & Martin, L. (1994). Geologia do quaternário. In F.F. Falconi & Negro Junior, A. (eds.), *Solos do litoral de São Paulo* (pp. 69-97). ABMS-NRSP. (in Portuguese).
- Tavenas, F., & Audy, R. (1972). Limitations of the driving formulas for predicting the bearing capacities of piles in sand. *Canadian Geotechnical Journal*, 9(1), 47-62. <http://dx.doi.org/10.1139/t72-004>.
- Thilakasiri, H.S., Abeyasinghe, R.K., & Tennekoon, B.L. (2003). *A study of ultimate carrying capacity estimation of driven piles using pile driving equations and the wave equation method*. Annual Transactions of the Institution of Engineers Sri Lanka.

CASE STUDY

Soils and Rocks
v. 46, n. 2

Shear strength of municipal solid waste rejected from material recovery facilities in the city of São Paulo, Brazil

Mariana Barbosa Juarez^{1#} , Giulliana Mondelli¹ , Heraldo Luiz Giacheti¹ 

Case Study

Keywords

Municipal solid waste
Sorting
Shredding
Compaction
Friction angle
Cohesion

Abstract

The mechanical behavior of municipal solid waste (MSW) is a critical issue in environmental geotechnics, given the pollution and public health risks associated with slope failures. In Brazil, waste composition is expected to change due to the hierarchy of sustainable practices established by the National Solid Waste Policy, which aims to improve the recovery of organic and recyclable materials. Not much progress has been made since the implementation of this law; thus, its effects on the design and operation of landfills are not fully clear. This study presents and discusses compaction and shear strength parameters of dry MSW after mechanical sorting of medium and large recyclable items and shredding. The maximum dry unit weight for the standard Proctor compaction test ranged from 6.6 to 10.0 kN/m³ and the optimum moisture content ranged from 20% to 42%. Stress-displacement curves of direct shear tests showed strain hardening and shear strength parameters of Mohr-Coulomb envelopes were displacement-dependent. The friction angle ranged from 3.2° to 42.9° and the cohesion intercept ranged from 1.3 to 31.3 kPa, at a displacement of 9 mm (15% of the specimen length). These results are in line with the literature, since a high content of waste materials that proved to affect geotechnical properties, such as plastic, paper, cardboard, textile, and glass, remained after pre-treatment.

1. Introduction

Due to the increasing generation of municipal solid waste (MSW) worldwide and the impact of improper disposal sites on the environment and public health, the circular economy model has gained attention (Kaza et al., 2018). The National Solid Waste Policy was implemented in Brazil by Federal Law No. 12,305/2010, providing for the following targets: non-generation reduction, reuse, recycling, treatment, and environmentally adequate final disposal (Brasil, 2010). Despite its introduction over the past decade, the transition from a conventional waste management system to an integrated system has been slow, unevenly taking place across the country. Waste materials are usually source-separated into dry (recyclable and non-recyclable) and wet (organic) streams in cities with a selective collection program (Lima et al., 2018). Less than 3% of dry materials are estimated to be recycled, and an even lower percentage of organic waste is treated (Brasil, 2022).

Many authors have assessed the environmental, economic, and social effects of different reverse logistics scenarios, including material recovery facilities (MRFs), waste pickers cooperatives, mechanical-biological treatment (MBT), and thermal treatment of MSW (Leme et al., 2014; Maier & Oliveira, 2014; Ferri et al., 2015; Lima et al., 2018;

Fuss et al., 2020; Rodrigues & Mondelli, 2022). However, information is missing on how the hierarchy of the law can affect the design and operation of landfills (van Elk & Boscov, 2016). With treatment alternatives becoming available, typical values of properties and parameters essential to landfill engineering may evolve due to changes in the waste stream (Kavazanjian, 2006).

Previous studies showed that the stress-strain response of waste is controlled by friction forces between granular particles and tensile forces of fibrous components, which is similar to results found for reinforced soils (Machado & Karimpour-Fard, 2011; Marçal et al., 2020). Only friction forces act at low strains (concave downward curve), according to Kölsch (1995). When tensile forces are mobilized, the overall shear strength gradually exceeds frictional strength (concave upward curve), reaching a peak and decreasing when fibers tear and slip out at high strains (concave downward curve). The model suggests that tensile strength increases with normal stress since fiber anchoring improves. The failure envelope is therefore bilinear. The author classified particles smaller than 8 mm as grains (three sides short) and larger than 8 mm as fibers (one side long, two sides short), foils (two sides long, one side short), and boxes (three sides long). Large-scale direct shear tests performed by Bray et al. (2009) and Zekkos et al. (2010) showed that the shear strength of MSW

[#]Corresponding author. E-mail address: mariana.juarez@unesp.br

¹Universidade Estadual Paulista "Júlio de Mesquita Filho", Departamento de Engenharia Civil e Ambiental, Bauru, SP, Brasil.

Submitted on December 2, 2022; Final Acceptance on April 1, 2023; Discussion open until August 31, 2023.

<https://doi.org/10.28927/SR.2023.013022>



This is an Open Access article distributed under the terms of the Creative Commons Attribution License, which permits unrestricted use, distribution, and reproduction in any medium, provided the original work is properly cited.

is highly anisotropic. Fibers were classified as particles larger than 20 mm, mostly made of soft plastic, paper, wood, and gravel. When fibers were parallel to the horizontal shear plane, the stress-displacement curve was concave downwards until reaching the maximum displacement of the testing device. Fiber orientation angles other than 0° provided concave upward stress-displacement curves and higher shear stress values. These studies also highlighted the influence of unit weight (γ) and displacement rate.

The average composition of MSW in Brazil is 45.3% food, garden, and wood waste, 16.8% plastic, 10.4% paper and cardboard, 5.6% textile, leather, and rubber, 2.7% glass, 2.3% metal, 1.4% multilayered packaging, and 15.5% sanitary, contaminated recyclable, unidentified, and incorrectly sorted waste (ABRELPE, 2020). Maximizing the recovery of recyclable and organic materials may result in changes in shear strength, compressibility, and permeability compared with the currently considered parameters. Direct shear and triaxial tests on fresh and aged MSW samples from many locations showed a strain-hardening behavior attributed to the reinforcing effect of plastic, textile, and other fibrous components (Vilar & Carvalho, 2004; Martins, 2006; Cardim, 2008; Karimpour-Fard et al., 2011; Abreu, 2015; Araújo Neto et al., 2021). High organic matter contents and biodegradation, which affects the extent of settlements, physical properties, and pore pressures, were related to variations in the long-term mechanical response of Brazilian landfills (Melo et al., 2016; Abreu & Vilar, 2017; Jucá et al., 2021).

These findings suggest that data from laboratory testing, field measurements, and back analyses performed to date may not be suitable for future landfills. This study aims to present and discuss compaction and shear strength parameters of MSW rejected from MRFs in the city of São Paulo, where some progress has been made in waste management. The presented results contribute to the database on MSW in Brazil and provide mechanical properties required for the analysis of slope stability of landfills in order to ensure safety and prevent pollution and health risks. Pre-treated dry waste can be used for other geotechnical purposes, such as backfill and embankment construction, if geoenvironmental parameters are suitable.

2. Materials and methods

2.1 MSW samples

In São Paulo, the most populated city in Brazil, with over 12 million inhabitants (IBGE, 2022), waste management services are provided by Ecurbis Ambiental, which is in charge of the southeastern region (989.86 km²), and Logística Ambiental de São Paulo (LOGA), in charge of the northwestern region (535.56 km²). In total, 14 sampling campaigns were conducted in material recovery facilities managed by Ecurbis (MRF-Ecurbis) and Loga (MRF-Loga) from May 2017 to

May 2018. According to the local authority, MRFs received part of the 91 thousand tons of dry waste from the selective collection performed door-to-door and in pick-up points during the sampling period (SPREGULA, 2022). Materials were sorted by size, mass, and shape, using rotating sieves and ballistic separators. Metals were detected using magnetic and inductive sensors and plastic, paper, and cardboard were detected using air blowers (2D items) and optical sensors (3D items). Recyclable items separated at every step were manually analyzed before shipment for commercialization (Correa et al., 2022).

MSW samples were collected from input and rejected streams of both MRFs. The material was shredded in a knife mill with a final sieve of 6 mm and stored at 4°C after gravimetric and particle size distribution analyses to enable the subsequent laboratory testing program. Mondelli et al. (2022) discussed in detail the geoenvironmental characterization of all samples. In this study, geotechnical characterization tests were performed only for MSW from the rejected stream. On average, its composition included 7.0% paper, 6.8% cardboard, 0.6% non-ferrous metal, 0.3% ferrous metal, 1.6% Tetra Pak packaging, 15.8% glass, 23.3% plastic, 3.5% textile, 0.8% rubber, 1.2% wood, 1.6% styrofoam, 1.6% electronic waste, 35.6% rejects (e.g., food, garden waste, used napkins, and used diapers), and 0.3% hazardous waste. Table 1 shows the composition of each campaign.

2.2 Compaction tests

Standard Proctor compaction tests were performed on MSW samples collected during campaigns 1 and 6 at each MRF. The material was placed in three layers into a 1,000-cm³ mold. Each layer was compacted with 26 blows using a 2.5-kg hammer falling from a height of 30.5 cm (energy = 583 kJ/m³), according to ABNT (2016). After determining the total weight of mold plus waste, duplicate samples were dried at 65°C for 24 hours. The standard temperature of 100°C was not used to avoid mass loss. This procedure was repeated five times to obtain the correlation between dry unit weight (γ_d) and moisture content (w).

2.3 Direct shear tests

Direct shear tests were performed on MSW samples collected during campaigns 2, 3, 4, 5, and 7 at each MRF. The material was placed in the Proctor mold in a single layer compacted with 26 blows and then transferred to the 60 mm square shear box. Compaction was not conducted in the shear box due to the circular shape of the hammer, preventing it from reaching the corners. Figure 1 describes the steps.

The normal stress range was chosen based on the age of samples at the time of the testing program (2-3 years) and compaction parameters from standard Proctor tests. Feng et al. (2017) collected 0.3-, 2-, and 4-year-old samples from the Laogang landfill, in China, at depths of 4, 11, and

Table 1. Composition of MSW rejected from MRFs in the city of São Paulo (Mondelli et al., 2022).

Material (%)	Campaigns at MRF-Ecourbis							Campaigns at MRF-Loga						
	1	2	3	4	5	6	7	1	2	3	4	5	6	7
Paper	9.9	0.0	1.6	2.4	5.4	0.0	2.6	10.2	11.7	24.7	12.9	3.1	9.8	3.1
Cardboard	7.1	0.0	0.0	2.5	2.6	0.2	0.3	1.4	1.5	45.5	17.1	9.4	0.0	7.4
Non-ferrous metal	0.2	0.0	0.0	0.0	1.8	0.0	0.2	0.5	4.4	0.0	0.0	0.0	0.8	0.0
Ferrous metal	0.8	1.1	0.1	0.3	0.0	0.0	0.0	0.6	0.8	0.0	0.0	0.0	0.0	0.0
Tetra Pak	2.1	5.5	0.7	1.5	1.8	3.4	0.9	0.0	1.9	0.0	0.0	2.6	1.6	0.0
Glass	45.4	22.1	19.6	12.8	23.6	11.7	24.7	26.6	2.9	10.9	9.9	3.7	5.0	2.8
1-PET	3.2	2.3	4.3	5.5	2.8	2.8	4.7	6.6	15.6	0.3	3.0	1.7	0.7	1.7
2-HDPE	1.6	0.4	0.0	2.3	0.1	0.7	0.4	20.5	4.5	0.1	0.3	4.0	0.0	1.2
3-PVC	0.0	0.0	0.2	0.0	0.0	0.2	0.0	0.0	0.0	0.0	0.0	0.0	0.0	0.0
4-LDPE	0.5	1.3	2.6	3.6	1.8	0.7	2.4	0.7	1.7	4.5	1.0	3.4	1.3	2.1
5-PP	0.9	1.0	0.9	1.0	1.0	1.2	0.3	11.0	12.6	0.7	0.3	2.6	0.8	1.2
6-PS	0.0	0.9	0.4	0.1	0.0	0.0	0.0	1.0	1.4	0.4	0.2	0.7	0.5	0.6
7-Others	8.5	5.0	0.2	0.3	1.1	0.2	0.1	2.7	9.4	0.9	0.8	1.1	0.1	0.0
Non-identified plastic	0.0	7.5	13.7	20.1	6.9	6.3	9.7	0.8	1.6	4.5	16.3	10.9	14.2	23.3
Textile	2.1	8.4	0.2	1.2	0.1	0.0	2.5	1.3	0.0	0.5	5.2	6.6	13.6	7.1
Leather	0.0	0.0	0.0	0.0	0.0	0.0	0.0	0.0	0.0	0.0	0.0	0.0	0.0	0.0
Rubber	0.0	0.0	0.0	2.4	0.0	0.0	0.0	2.8	5.8	0.0	0.2	0.0	0.0	0.2
Wood	0.8	0.0	2.9	0.3	6.1	0.0	0.0	0.4	6.3	0.0	0.0	0.0	0.0	0.0
Styrofoam	0.5	2.8	1.7	1.2	1.6	0.4	0.5	1.3	1.5	2.3	1.0	6.3	0.5	1.4
Electronic	0.1	0.6	3.0	8.0	0.0	4.0	0.8	0.9	1.3	0.0	0.0	0.9	0.0	2.8
Rejects	14.1	41.1	47.7	34.2	43.0	67.5	49.7	9.8	15.2	4.7	31.9	42.9	51.2	45.3
Hazardous	2.2	0.0	0.1	0.2	0.0	0.5	0.0	1.1	0.0	0.0	0.0	0.0	0.0	0.0

16 m, respectively. Specimens in this study were consolidated and sheared at 50, 100, and 150 kPa to simulate depths of 10 to 15 m, considering a range from 5 to 10 kN/m³ for γ_d . The displacement rate should be estimated as the ratio between the relative lateral displacement and the total time estimated for failure, according to ASTM (2011). However, no failures occurred up to the maximum displacement of the device (about 11 to 12 mm) during previous tests on the material. The rate of 0.3 mm/min was adopted, in line with other studies with shredded MSW (Bareither et al., 2012; Zhao et al., 2014).

3. Results and discussion

3.1 Compaction tests

Figure 2 shows compaction curves. The maximum dry unit weight ($\gamma_{d,max}$) was 9.5 and 10.0 kN/m³ and the optimum moisture content (w_{opt}) was 20% and 21% for MSW samples collected during campaigns 1 and 6 at MRF-Ecourbis, respectively. Moreover, $\gamma_{d,max}$ ranged from 6.6 to 8.1 kN/m³ and w_{opt} ranged from 30% to 42% for samples collected during campaigns 1 and 6 at MRF-Loga, respectively. These parameters were similar to other studies in Brazil (Calle, 2007; Araújo Neto et al., 2021). From the fourth to the fifth compaction test on the sample collected during campaign 1 of MRF-Loga, there was a slight decrease in the dry unit weight. But, in general, γ_d remained almost constant with w increasing above 30%. This possibly occurred

due to the difficulty in compacting on the wet side of w_{opt} since the material may not densify when it is close to full saturation. Similar behavior was observed in compaction curves of MSW presented by Gabr & Valero (1995) and Reddy et al. (2009).

Pulat & Yukselen-Aksoy (2013) showed that $\gamma_{d,max}$ decreases and w_{opt} increases as the paper, cardboard, plastic, or organic content increase in synthetic waste samples tested in the modified Proctor test. These effects may explain the findings of this study. Considering both campaigns 1, the lowest $\gamma_{d,max}$ and the highest w_{opt} of the sample from MRF-Loga can be associated with increased plastic content compared with MRF-Ecourbis (43.2% against 14.7%). In the case of both campaigns 6, the lowest $\gamma_{d,max}$ and highest w_{opt} of the sample from MRF-Loga can be associated with increased paper and plastic content compared with MRF-Ecourbis (9.8% against 0% and 17.6% against 12.2%, respectively).

3.2 Direct shear tests

Figures 3 and 4 show the results of duplicate direct shear tests (1 and 2) on MSW samples collected during campaigns 2, 3, 4 5, and 7 at MRF-Ecourbis and MRF-Loga, respectively. The primary consolidation of all specimens was completed in a few minutes, as they were shredded and compacted. Most stress-displacement curves have a continuous concave-downward shape. Two hypotheses were suggested for strain hardening regardless of specimen composition and applied normal stress, based on the findings of other studies with direct shear tests:

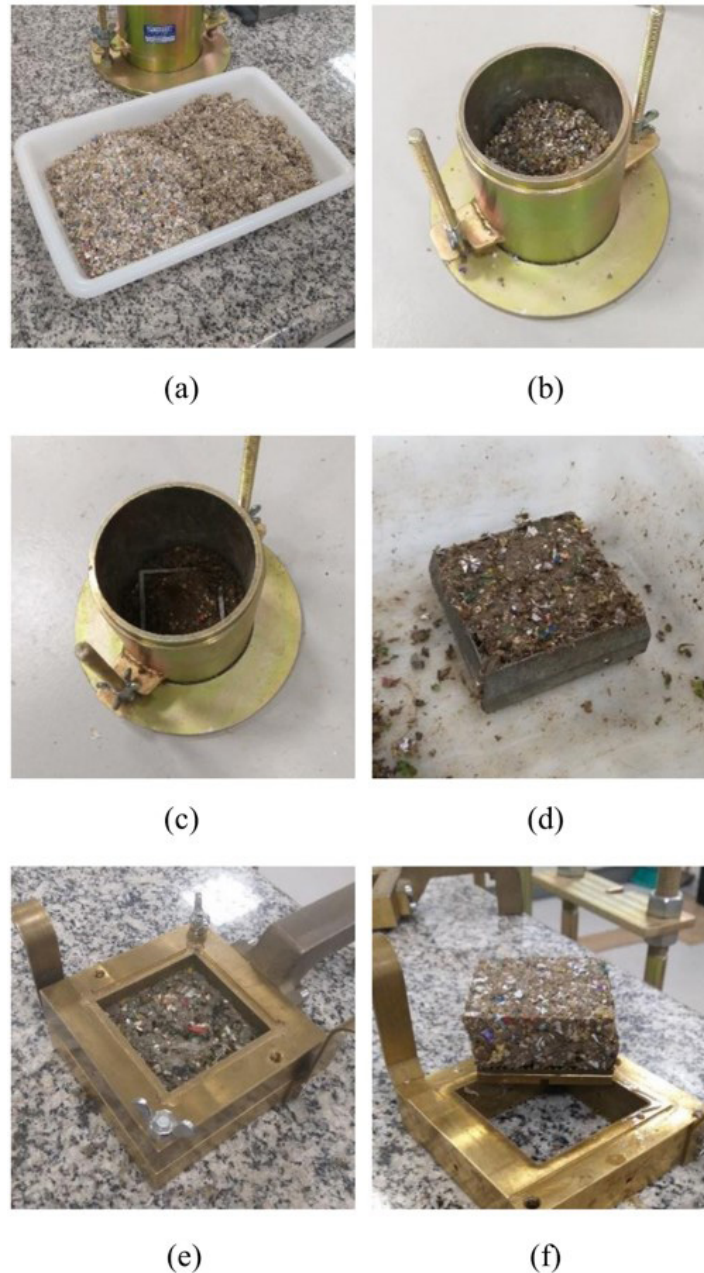


Figure 1. Direct shear test: (a) MSW sample, (b) placement into the mold, (c) single-layer compaction, (d) specimen preparation, (e) transfer to the shear box, and (f) specimen after shearing.

- (1) Frictional strength controlled shear strength because soft plastic, paper, textile, wood, and other fibrous particles were shredded into sizes too small to produce a reinforcing effect, but the displacement range was insufficient to fully mobilize it.
- (2) Fibers generated tensile forces that contributed to the overall response, regardless of their particle size, but to a minor extent because they were nearly parallel to the shear plane after compaction (Zekkos et al., 2010).

Displacements of 5% to 20% of the specimen length are commonly adopted to obtain shear strength envelopes in the absence of failure or peak strength (Abreu, 2015), as observed in this study. The chosen displacements were 3, 6, and 9 mm or 5%, 10%, and 15% of the specimen length, respectively. A displacement of 12 mm was not included because it was not reached in some tests. Figures 3 and 4 show Mohr-Coulomb envelopes at the third displacement level. No significant discontinuities were found; thus, the linear

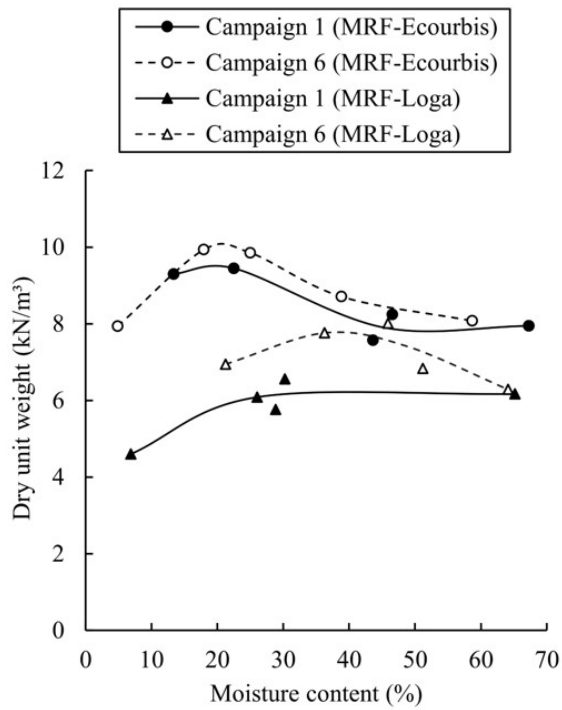


Figure 2. Standard Proctor compaction curves of MSW rejected from MRFs in the city of São Paulo.

failure criterion was reasonably adequate to describe the relationship between shear and normal stresses ($R^2 \geq 0.7331$). Both the friction angle (ϕ) and cohesion intercept (c) were displacement-dependent (Tables 2 and 3).

3.3 Data analyses

Table 4 presents the conditions and results of many direct shear tests on MSW performed in Brazil. Different displacement failure criteria were adopted, but this table includes only shear strength parameters at a displacement of 10% of the specimen length to enable comparison. Figure 5 shows that most ϕ and c values are in line with the literature, except for the sample collected during campaign 3 at MRF-Loga, for which ϕ was lower than 8° . The composition of this sample includes 70% paper and cardboard, and the corresponding specimens were prepared at moisture contents above 130%. Previous studies reported the ϕ of 33° for shredded paper (Gabr et al., 2007). Thus, excess pore pressures may have caused low friction angles. Although the initial plan was to compact specimens at moisture contents close to the optimum values, transferring them to the shear box was feasible after adding water.

A considerable variation in the cohesion intercept was observed, even between duplicates (e.g., c increased from

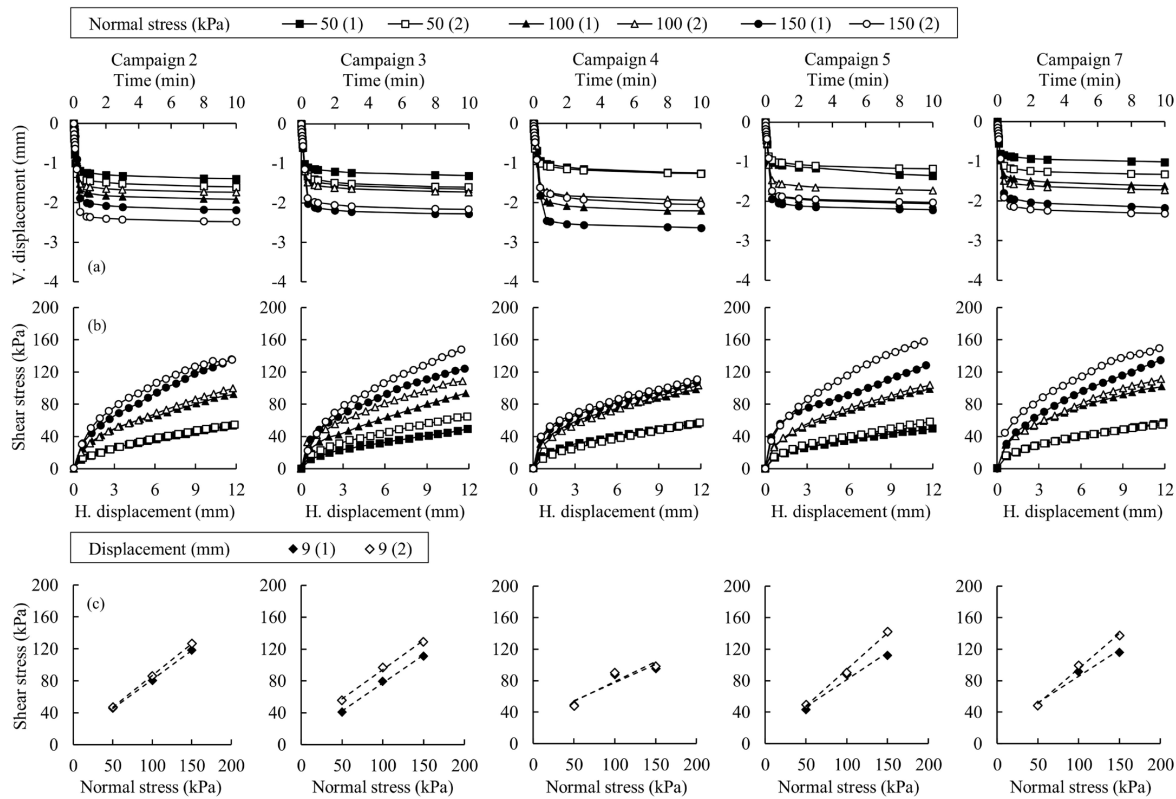


Figure 3. Duplicate direct shear tests performed on MSW rejected from MRF-Ecourbis: (a) consolidation curves, (b) stress-displacement curves, and (c) Mohr-Coulomb envelopes.

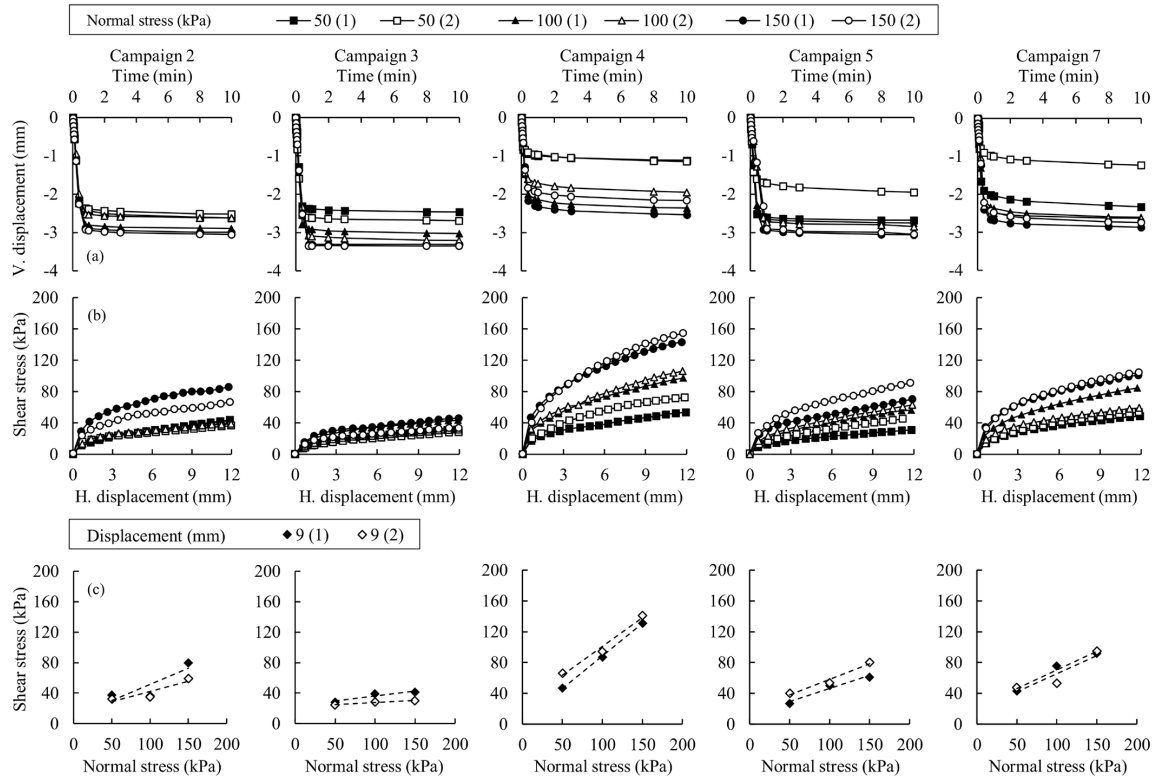


Figure 4. Duplicate direct shear tests performed on MSW rejected from MRF-Loga: (a) consolidation curves, (b) stress-displacement curves, and (c) Mohr-Coulomb envelopes.

Table 2. Shear strength parameters of MSW rejected from MRF-Ecourbis.

Displacement (mm)	Test	Campaign 2		Campaign 3		Campaign 4		Campaign 5		Campaign 7	
		ϕ (°)	c (kPa)								
3 (5%)	1	21.5	7.5	24.0	1.0	19.4	16.7	25.9	3.3	20.3	13.7
6 (10%)	1	29.6	8.3	30.6	3.4	22.4	24.6	29.1	10.7	28.8	16.0
9 (15%)	1	36.1	8.7	35.1	7.1	24.8	31.3	34.6	12.2	34.0	18.2
3 (5%)	2	27.2	0.0	24.1	12.1	23.5	6.0	28.9	1.7	29.2	1.5
6 (10%)	2	34.2	2.4	31.8	15.1	25.8	17.0	37.8	0.0	36.1	5.3
9 (15%)	2	38.5	7.0	36.3	20.7	26.7	28.4	42.9	1.3	41.8	6.0

Table 3. Shear strength parameters of MSW rejected from MRF-Loga.

Displacement (mm)	Test	Campaign 2		Campaign 3		Campaign 4		Campaign 5		Campaign 7	
		ϕ (°)	c (kPa)								
3 (5%)	1	18.4	1.0	7.5	12.0	29.0	2.0	13.5	5.9	19.5	11.5
6 (10%)	1	21.9	3.9	6.8	19.3	36.5	0.6	15.6	10.5	23.2	17.8
9 (15%)	1	23.0	8.9	7.4	23.1	40.2	3.9	18.8	12.3	25.8	21.9
3 (5%)	2	10.1	12.0	3.7	12.8	24.4	16.2	16.5	7.3	18.9	9.3
6 (10%)	2	13.8	12.1	3.4	17.7	31.3	22.8	19.9	12.3	22.3	15.3
9 (15%)	2	15.0	15.2	3.2	22.0	36.8	26.1	22.0	17.7	25.2	18.4

Table 4. Summary of direct shear tests on MSW performed in Brazil.

Author (year)	Description	Max. particle size (mm)	Initial conditions		Displacement (mm) ^a	ϕ (°)	c (kPa)
			γ (kN/m ³)	w (%)			
Lamare Neto (2004)	MBT waste	19.0	8.3	-	-	42.6 ^c	6.0 ^c
	MBT waste	9.5	7.3	-	-	37.2 ^c	11.0 ^c
Martins (2006)	Fresh waste	-	10.0	69	70 (10%)	14.6	21.2
	Fresh waste	-	8.0	68	70 (10%)	16.8	13.5
	MBT waste	-	8.0	56	70 (10%)	10.5	37.1
Calle (2007)	MBT waste	9.5	9.0	-	≈6 (10%) ^b	37.0	34.0
	MBT waste	9.5	6.7	-	≈6 (10%) ^b	34.0	28.0
	MBT waste	2.0	6.7	-	≈6 (10%) ^b	34.0	20.0
	MBT waste	9.5	7.0	-	≈6 (10%) ^b	32.0	50.0
	MBT waste	9.5	5.2	-	≈6 (10%) ^b	34.0	18.0
Cardim (2008)	Fresh waste	-	6.0	301	100 (10%)	33.2	0.3
	Fresh waste	-	6.0	278	100 (10%)	33.8	0.0
	Fresh waste	-	6.0	274	100 (10%)	28.1	3.1
Abreu (2015)	Landfilled waste	85.0	8.7	42	50 (10%)	18.0	9.8
	Landfilled waste	85.0	10.3	44	50 (10%)	23.0	2.9
	Landfilled waste	85.0	14.3	51	50 (10%)	22.0	3.0
	Landfilled waste	85.0	15.1	51	50 (10%)	23.0	1.9
	Landfilled waste	85.0	9.3	43	50 (10%)	26.0	0.0
	Landfilled waste	85.0	9.1	44	50 (10%)	23.0	2.6
Araújo Neto et al. (2021)	Landfilled waste	30.0	5.7	28	-	16.0 ^d	17.0 ^d
This study	MRF waste	6.0	13.5	63	6 (10%)	29.6	8.3
	MRF waste	6.0	13.4	68	6 (10%)	34.2	2.4
	MRF waste	6.0	13.7	40	6 (10%)	30.6	3.4
	MRF waste	6.0	13.8	44	6 (10%)	31.8	15.1
	MRF waste	6.0	13.7	53	6 (10%)	22.4	24.6
	MRF waste	6.0	14.1	51	6 (10%)	25.8	17.0
	MRF waste	6.0	15.2	49	6 (10%)	29.1	10.7
	MRF waste	6.0	14.8	53	6 (10%)	37.8	0.0
	MRF waste	6.0	13.9	41	6 (10%)	28.8	16.0
	MRF waste	6.0	13.1	41	6 (10%)	36.1	5.3
	MRF waste	6.0	8.7	92	6 (10%)	21.9	3.9
	MRF waste	6.0	7.7	82	6 (10%)	13.8	12.1
	MRF waste	6.0	9.5	148	6 (10%)	6.8	19.3
	MRF waste	6.0	8.6	139	6 (10%)	3.4	17.7
	MRF waste	6.0	12.6	45	6 (10%)	36.5	0.6
	MRF waste	6.0	13.1	49	6 (10%)	31.3	22.8
	MRF waste	6.0	10.8	107	6 (10%)	15.6	10.5
	MRF waste	6.0	10.7	103	6 (10%)	19.9	12.3
	MRF waste	6.0	11.1	104	6 (10%)	23.2	17.8
	MRF waste	6.0	11.7	109	6 (10%)	22.3	15.3

Legend: MBT = Mechanical-biological treatment; MRF = Material recovery facility. ^aPercentage of the specimen length in parentheses. ^bDisplacement in mm estimated based on the specimen height of 41.6 mm and strain of 14%. ^cParameter determined at a normalized displacement of 10%, which correlation with displacement in mm was not reported. ^dParameter determined at a strain of 10%, which correlation with displacement in mm was not reported.

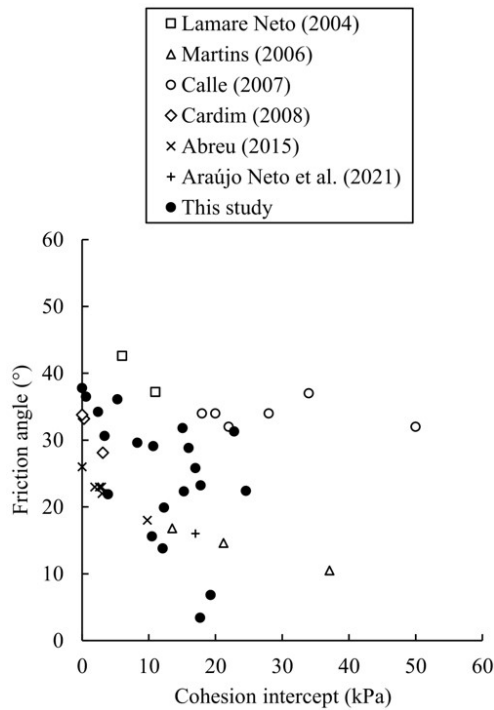


Figure 5. Shear strength parameters of direct shear tests on MSW performed in Brazil.

0.6 kPa in the first test to 22.8 kPa in the second test on the MSW sample collected during campaign 4 at MRF-Loga). Some authors show the influence of soft plastic and fiber content on c values (Calle, 2007; Borgatto et al., 2014; Abreu & Vilar, 2017). The wide range was probably due to differences in the internal arrangement of particles and specimen composition from test to test.

4. Conclusion

Pre-treated dry MSW samples from MRFs in the city of São Paulo were tested for compaction and shear strength. Standard Proctor compaction and direct shear tests showed responses similar to previous studies conducted in Brazil. Despite source separation and mechanical sorting, high content of recyclable materials was observed in the rejected stream, highlighting some challenges of implementing the National Solid Waste Policy, such as the contamination with food waste, the lack of plastic identification codes on packaging, and inefficiencies of current reverse logistics systems.

The maximum dry unit weight ranged from 6.6 to 10.0 kN/m³ and the optimum moisture content from 20% to 42%, depending on the composition of the sample. Shear stress increased up to the maximum displacement in the direct shear test, but its values seemed to be affected by the unit weight and moisture content. The friction angle and cohesion intercept at displacements of 5%, 10%, and 15% of the specimen length varied widely, similar to the

literature. Further studies are required to better understand the mechanisms behind the shear strength of shredded MSW, using higher normal stress and displacement levels and a rigorous control of specimen preparation.

In any case, removing biodegradable materials (food and garden waste) and shredding MSW may be advantageous for the monitoring of physical and mechanical properties in landfills. Pre-treatment can help minimize the temporal variation of particle size distribution and the extent of settlements, providing a more homogeneous porous medium. Therefore, permeability, moisture content, unit weight, and shear strength tend to change less over time. However, the spatial variation of geotechnical parameters within the waste mass is expected to be lower if the waste composition is less heterogeneous. This is challenging not only due to the aforementioned factors, but also due to alterations in consumption patterns and the development of new materials that are not recyclable until feasible solutions become available.

Acknowledgements

The authors acknowledge the financial support (Grant No. 23006.000123/2018-23) and infrastructure (Laboratory of Geotechnics) provided by the Federal University of ABC (UFABC) during this research.

Declaration of interest

The authors have no conflicts of interest to declare. All co-authors have observed and affirmed the contents of the paper and there is no financial interest to report.

Authors' contributions

Mariana Barbosa Juarez: conceptualization, data curation, methodology, analysis, writing – original draft. Giulliana Mondelli: conceptualization, methodology, supervision, writing – review & editing. Heraldo Luiz Giacheti: discussion, writing – review & editing.

Data availability

All data produced or examined in the course of the current study are included in this article.

List of symbols

c	Cohesion intercept
w	Moisture content
w_{opt}	Optimum moisture content
HDPE	High-density polyethylene
LDPE	Low-density polyethylene
Others	Mixed plastic with or without other material
MSW	Municipal solid waste

PET	Polyethylene terephthalate
PP	Polypropylene
PS	Polystyrene
PVC	Polyvinyl chloride
γ_d	Dry unit weight
$\gamma_{d,max}$	Maximum dry unit weight
ϕ	Friction angle

References

- ABNT NBR 7182. (2016). *Soil - compaction test*. ABNT - Associação Brasileira de Normas Técnicas, Rio de Janeiro, RJ (in Portuguese).
- ABRELPE. (2020). *Panorama de Resíduos Sólidos no Brasil 2020*. ABRELPE - Associação Brasileira de Empresas de Limpeza Pública e Resíduos Especiais (in Portuguese). Retrieved in November 2, 2022, from <https://abrelpe.org.br/panorama/>
- Abreu, A.E.S. (2015). *Geophysical investigation and shear strength of municipal solid wastes with different landfilling ages* [Doctoral thesis, University of São Paulo]. University of São Paulo's repository (in Portuguese). <http://dx.doi.org/10.11606/T.18.2015.tde-03082015-115017>
- Abreu, A.E.S., & Vilar, O.M. (2017). Influence of composition and degradation on the shear strength of municipal solid waste. *Waste Management*, 68, 263-274. <http://dx.doi.org/10.1016/j.wasman.2017.05.038>.
- Araújo Neto, C.L., Gurjão, R.Í.L., Farias, A.P., Melo, M.C., & Monteiro, V.E.D. (2021). Physical, chemical, and mechanical properties of landfilled waste from Campina Grande, Brazil. *Environmental Science and Pollution Research International*, 28(47), 66819-66829. <http://dx.doi.org/10.1007/s11356-021-15230-5>.
- ASTM D3080/D3080M. (2011). *Standard test method for direct shear test of soils under consolidated drained conditions*. ASTM International, West Conshohocken, PA.
- Bareither, C.A., Benson, C.H., & Edil, T.B. (2012). Effects of waste composition and decomposition on the shear strength of municipal solid waste. *Journal of Geotechnical and Geoenvironmental Engineering*, 138(10), 1161-1174. [http://dx.doi.org/10.1061/\(ASCE\)GT.1943-5606.0000702](http://dx.doi.org/10.1061/(ASCE)GT.1943-5606.0000702).
- Borgatto, A.V.A., Mahler, C.F., Münnich, K., & Webler, A.D. (2014). Influence of the fibre component of soft plastic on shear strength parameters of pre-treated municipal solid waste. *Soils and Rocks*, 37(2), 151-157. <http://dx.doi.org/10.28927/SR.372151>.
- Bray, J.D., Zekkos, D., Kavazanjian Junior, E., Athanasopoulos, G.A., & Riemer, M.F. (2009). Shear strength of municipal solid waste. *Journal of Geotechnical and Geoenvironmental Engineering*, 135(6), 709-722. [http://dx.doi.org/10.1061/\(ASCE\)GT.1943-5606.0000063](http://dx.doi.org/10.1061/(ASCE)GT.1943-5606.0000063).
- Brasil. (August 3, 2010). Federal Law No. 12,305/2010. National Solid Waste Policy. *Diário Oficial [da] República Federativa do Brasil*. (April 14, 2022). Decree No. 11.043/2022. National Solid Waste Plan. *Diário Oficial [da] República Federativa do Brasil*.
- Calle, J.A.C. (2007). *Geomechanical behavior of urban solid waste* [Doctoral thesis, Federal University of Rio de Janeiro]. Federal University of Rio de Janeiro's repository (in Portuguese). Retrieved in November 2, 2022, from http://objdig.ufrj.br/60/teses/coppe_d/JoseAntonioCancinoCalle.pdf
- Cardim, R.D. (2008). *Estudo da resistência de resíduos sólidos urbanos por meio de ensaios de cisalhamento direto de grandes dimensões* [Master's dissertation, University of Brasília]. University of Brasília's repository (in Portuguese). Retrieved in November 2, 2022, from <https://repositorio.unb.br/handle/10482/3290>
- Correa, C.A., de Oliveira, M.A., Jacinto, C., & Mondelli, G. (2022). Challenges to reducing post-consumer plastic rejects from the MSW selective collection at two MRFs in São Paulo City, Brazil. *Journal of Material Cycles and Waste Management*, 24(3), 1140-1155. <http://dx.doi.org/10.1007/s10163-022-01387-9>.
- Feng, S.J., Gao, K.W., Chen, Y.X., Li, Y., Zhang, L.M., & Chen, H.X. (2017). Geotechnical properties of municipal solid waste at Laogang Landfill, China. *Waste Management*, 63, 354-365. <http://dx.doi.org/10.1016/j.wasman.2016.09.016>.
- Ferri, G.L., Chaves, G.D.L.D., & Ribeiro, G.M. (2015). Reverse logistics network for municipal solid waste management: the inclusion of waste pickers as a Brazilian legal requirement. *Waste Management*, 40, 173-191. <http://dx.doi.org/10.1016/j.wasman.2015.02.036>.
- Fuss, M., Vergara-Araya, M., Barros, R.T., & Pogonietz, W.R. (2020). Implementing mechanical biological treatment in an emerging waste management system predominated by waste pickers: a Brazilian case study. *Resources, Conservation and Recycling*, 162, 105031. <http://dx.doi.org/10.1016/j.resconrec.2020.105031>.
- Gabr, M.A., Hossain, M.S., & Barlaz, M.A. (2007). Shear strength parameters of municipal solid waste with leachate recirculation. *Journal of Geotechnical and Geoenvironmental Engineering*, 133(4), 478-484. [http://dx.doi.org/10.1061/\(ASCE\)1090-0241\(2007\)133:4\(478\)](http://dx.doi.org/10.1061/(ASCE)1090-0241(2007)133:4(478)).
- Gabr, M.A., & Valero, S.N. (1995). Geotechnical properties of municipal solid waste. *Geotechnical Testing Journal*, 18(2), 241-251. <http://dx.doi.org/10.1520/GTJ10324J>.
- IBGE. (2022). *São Paulo*. IBGE – Instituto Brasileiro de Geografia e Estatística (in Portuguese). Retrieved in November 2, 2022, from <https://www.ibge.gov.br/cidades-e-estados/sp/sao-paulo.html>
- Jucá, J.F.T., Norberto, A.D.S., Santos Júnior, J.I.D., & Marinho, F.A. (2021). Brasília municipal solid waste landfill: a case study on flow and slope stability. *Soils and Rocks*, 44(3), 1-13. <http://dx.doi.org/10.28927/SR.2021.067321>.
- Karimpour-Fard, M., Machado, S.L., Shariatmadari, N., & Noorzad, A. (2011). A laboratory study on the

- MSW mechanical behavior in triaxial apparatus. *Waste Management*, 31(8), 1807-1819. <http://dx.doi.org/10.1016/j.wasman.2011.03.011>.
- Kavazanjian, E. (2006). Waste mechanics: recent findings and unanswered questions. In L.R. Hoyos & L.N. Reddi (Eds.), *Advances in unsaturated soil, seepage, and environmental geotechnics* (pp. 34-54). Reston: ASCE. [http://dx.doi.org/10.1061/40860\(192\)2](http://dx.doi.org/10.1061/40860(192)2).
- Kaza, S., Yao, L., Bhada-Tata, P., & Van Woerden, F. (2018). *What a waste 2.0: a global snapshot of solid waste management to 2050*. Washington: World Bank Publications.
- Kölsch, F. (1995). Material values for some mechanical properties of domestic waste. In *Proceedings of the 5th International Landfill Symposium* (Vol. 2, pp. 711-729), Cagliari, Italy: CISA.
- Lamare Neto, A. (2004). *Shearing resistance of urban solid waste and granular materials with fibers* [Doctoral thesis, Federal University of Rio de Janeiro]. Federal University of Rio de Janeiro's repository (in Portuguese). Retrieved in November 2, 2022, from <http://objdig.ufrj.br/60/teses/642969.pdf>
- Leme, M.M.V., Rocha, M.H., Lora, E.E.S., Venturini, O.J., Lopes, B.M., & Ferreira, C.H. (2014). Techno-economic analysis and environmental impact assessment of energy recovery from Municipal Solid Waste (MSW) in Brazil. *Resources, Conservation and Recycling*, 87, 8-20. <http://dx.doi.org/10.1016/j.resconrec.2014.03.003>.
- Lima, P.D.M., Colvero, D.A., Gomes, A.P., Wenzel, H., Schalch, V., & Cimpan, C. (2018). Environmental assessment of existing and alternative options for management of municipal solid waste in Brazil. *Waste Management (New York, N.Y.)*, 78, 857-870. <http://dx.doi.org/10.1016/j.wasman.2018.07.007>.
- Machado, S.L., & Karimpour-Fard, M. (2011). A study on the effects of MSW fiber content and solid particles compressibility on its shear strength using a triaxial apparatus. *Soils and Rocks*, 34(2), 115-127. <http://dx.doi.org/10.28927/SR.342115>.
- Maier, S., & Oliveira, L.B. (2014). Economic feasibility of energy recovery from solid waste in the light of Brazil's waste policy: the case of Rio de Janeiro. *Renewable & Sustainable Energy Reviews*, 35, 484-498. <http://dx.doi.org/10.1016/j.rser.2014.04.025>.
- Marçal, R., Lodi, P.L., Correia, N.S., Giacheti, H.L., Rodrigues, R.A., & McCartney, J.S. (2020). Reinforcing effect of polypropylene waste strips on compacted lateritic soils. *Sustainability (Basel)*, 12(22), 9572. <http://dx.doi.org/10.3390/su12229572>.
- Martins, H.L. (2006). *Avaliação da resistência de resíduos sólidos urbanos por meio de ensaios de cisalhamento direto em equipamento de grandes dimensões* [Master's dissertation, Federal University of Minas Gerais]. Federal University of Minas Gerais's repository (in Portuguese). Retrieved in December 2, 2022, from <http://hdl.handle.net/1843/FRPC-6ZJ2D>
- Melo, M.C., Farias, R.M.S., Caribé, R.M., Sousa, R.B.A., & Monteiro, V.E.D. (2016). A case of study about the influence of organic matter in municipal solid waste settlement. *Soils and Rocks*, 39(2), 139-148. <http://dx.doi.org/10.28927/SR.392139>.
- Mondelli, G., Juarez, M.B., Jacinto, C., Oliveira, M.A., Coelho, L.H.G., Biancardi, C.B., & Castro Faria, J.L. (2022). Geo-environmental and geotechnical characterization of municipal solid waste from the selective collection in São Paulo City, Brazil. *Environmental Science and Pollution Research International*, 29(13), 19898-19912. <http://dx.doi.org/10.1007/s11356-021-18281-w>.
- Pulat, H.F., & Yukselen-Aksoy, Y. (2013). Compaction behavior of synthetic and natural MSW samples in different compositions. *Waste Management & Research*, 31(12), 1255-1261. <http://dx.doi.org/10.1177/0734242X13507967>.
- Reddy, K.R., Gangathulasi, J., Parakalla, N.S., Hettiarachchi, H., Bogner, J.E., & Lagier, T. (2009). Compressibility and shear strength of municipal solid waste under short-term leachate recirculation operations. *Waste Management & Research*, 27(6), 578-587. <http://dx.doi.org/10.1177/0734242X09103825>.
- Rodrigues, E., & Mondelli, G. (2022). Assessment of integrated MSW management using multicriteria analysis in São Paulo City. *International Journal of Environmental Science and Technology*, 19(8), 7981-7992. <http://dx.doi.org/10.1007/s13762-021-03681-9>.
- SPREGULA. (2022). *Resíduos sólidos - quantitativos*. SPREGULA - Agência Reguladora de Serviços Públicos do Município de São Paulo (in Portuguese). Retrieved in November 2, 2022, from <https://www.prefeitura.sp.gov.br/cidade/secretarias/spregula/>
- van Elk, A.G.H.P., & Boscov, M.E.G. (2016). Desafios geotécnicos advindos da Política Nacional de Resíduos Sólidos. In *Anais do 18 Congresso Brasileiro de Mecânica dos Solos e Engenharia Geotécnica*, Belo Horizonte. ABMS (in Portuguese).
- Vilar, O.M., & Carvalho, M.F. (2004). Mechanical properties of municipal solid waste. *Journal of Testing and Evaluation*, 32(6), 438-449. <http://dx.doi.org/10.1520/JTE11945>.
- Zekkos, D., Athanasopoulos, G.A., Bray, J.D., Grizi, A., & Theodoratos, A. (2010). Large-scale direct shear testing of municipal solid waste. *Waste Management*, 30(8-9), 1544-1555. <http://dx.doi.org/10.1016/j.wasman.2010.01.024>.
- Zhao, Y.R., Xie, Q., Wang, G.L., Zhang, Y.J., Zhang, Y.X., & Su, W. (2014). A study of shear strength properties of municipal solid waste in Chongqing landfill, China. *Environmental Science and Pollution Research International*, 21(22), 12605-12615. <http://dx.doi.org/10.1007/s11356-014-3183-2>.

REVIEW ARTICLE

Soils and Rocks
v. 46, n. 2

Use of longitudinal wave in non-destructive methods: approach to foundation and retaining elements

Isabela Grossi da Silva^{1#} , Vítor Pereira Faro¹ 

Review Article

Keywords

Non-destructive tests
Sonic tests
Piles
Nails
Tiebacks

Abstract

Non-destructive tests (*NDT*) are used to verify the length or integrity of elements embedded in soils or rocks. These elements can be piles in foundations or nails and tiebacks in retaining walls. *NDTs* differ by the types of waves, ways to generate and receive the signal and to analyze data. Tests using sonic wave do not require a pre-installed pipe or wire and they are based on acoustic impedance theory. Despite its dissemination on piles, the application in retaining elements is recent and requires more studies to increase knowledge about these methods. This paper aims to present studies of sonic wave methods in foundation and retaining elements, presenting results, similarities, and differences. Studies from different dates are presented with their relevance, considerations for the different types of elements tested, objectives and methodologies used, to evidence the variables involved within this solution. The sonic test in foundation is widespread and has a greater number of studies. Withing this paper, the variables that interfere in the results of these methods were observed: the velocity of propagation of the sonic wave, the soil stiffness, the location of wave generation and reception and the type of hammer used, evidencing the necessity of further studies, especially in retaining elements.

1. Introduction

Buried elements such as piles, nails and tiebacks need special techniques to be inspected, so, a non-destructive or destructive methods are used. Destructive methods, among them the most known is the pullout test, have elevated cost, high execution time and it disables the tested element (Zima & Rucka, 2017). On the other hand, non-destructive methods (*NDT*) have faster execution time, relatively low cost per element, portability of equipment and the possibility to test all elements, since they do not damage the structure (Jayawickrama et al., 2007). Thus, the *NDT* becomes a good alternative to evaluate the integrity of elements embedded in the soil, besides allowing the verification of their lengths when there is no geotechnical project or to verify the execution of the project.

In the bibliography, there are several non-destructive tests, such as Sonic Echo (Cheung, 2003), Impact Echo (Carino, 2001), Impulse Response (Liao et al., 2008), Crosshole Sonic Logging (Jayawickrama et al., 2007), Time Domain Reflectometry (Lee & Arup, 2007), Parallel Seismic (Olson et al., 1998), and others. They are distinguished by the wave used, by its frequency, if it is necessary or not pre-installed elements and how the signals are obtained or interpreted. For example, the Sonic Echo, Impact Echo and Impulse Response methods are sonic methods that have

acoustic impedance as a principle, but they are different by the way the wave is generated or how the data is interpreted. Crosshole Sonic Logging is an ultrasonic test that requires pre-installed tubes. Time Domain Reflectometry uses an electromagnetic wave and a wire that must be inserted during the execution of the element that serves as a reference for this method.

The use of non-destructive techniques is widespread in the context of foundations, with a large amount of works and the most known method is the Pile Integrity Test (*PIT*). On the other hand, in retaining walls, such as soil nail and tieback elements, the application is recent and it is necessary more studies to better understand the peculiarities of these methods.

The sonic methods, such as Sonic Echo (*SE*) and Impulse Response (*IR*), use longitudinal mechanical waves to interpret the results and have the main advantage that they do not need pre-installed tubes or wires to its execution. Thus, elements can be tested even if this was not planned during their execution. These techniques are based on acoustic impedance for the interpretation of results and they have some variables involved.

This article aims to present studies on low strain sonic methods in foundation and retaining elements, presenting a critical analysis of their results, similarities and differences between the method due to the elements tested.

[#]Corresponding author. E-mail address: isa.grossisilva@gmail.com

¹Universidade Federal do Paraná, Programa de Pós-Graduação em Engenharia da Construção Civil, Curitiba, PR, Brasil.

Submitted on December 2, 2022; Final Acceptance on April 3, 2023; Discussion open until August 31, 2023.

<https://doi.org/10.28927/SR.2023.013222>



This is an Open Access article distributed under the terms of the Creative Commons Attribution License, which permits unrestricted use, distribution, and reproduction in any medium, provided the original work is properly cited.

2. Theoretical background

This item presents the topics that explain how it works and which variables are involved in the use of sonic methods, which have the same theory for application in foundations and retaining walls.

2.1 Theory about sonic methods

The sonic methods use the acoustic wave, also known as shock wave or stress wave (Cheung & Lo, 2005) and they are based on acoustic impedance theory and these tests differ from each other in the way they are generated and interpreted. The acoustic wave has a frequency audible by humans, with values between 20 Hz and 20 kHz. Sonic techniques have as their principle the generation, transmission and reception of the acoustic wave in the element, which travels through it without generating reflection until it finds a section of discontinuity or change of physical properties, which causes the wave's reflection (Cheung & Lo, 2005). The equipment for these low strain tests, as they are also known, currently consists of a 1.5 kg hand hammer, a geophone or accelerometer-type signal receiver and a data acquisition device connected to a portable computer (Gong et al., 2006; Ni et al., 2006).

Jayawickrama et al. (2007) argue that the wave propagates in the element until there is a change in impedance, which may present partial or total reflection, and the reflected part is captured by the receiver. Thus, the impedance is generated when there is a change in the physical environment through which the wave travels, this change can be either in the resistance of the material or in the cross section. The impedance depends on the combination of the cross-sectional area, the modulus of elasticity and the density of the material tested (Thilakasiri, 2006), as shown in Equation 1. Where: Z = acoustic impedance ($\text{kg}\cdot\text{m}^2\cdot\text{s}^{-1}$); A = cross-sectional area (m^2); E = Young's modulus of the material (Pa); ρ = specific mass of the material (kg/m^3).

$$Z = A\sqrt{E\cdot\rho} \quad (1)$$

The reflection is captured by the receiver and can be difficult to differentiate the main reflection, referring to the toe element, from the other reflections, caused by variation of the element cross section and by different material existing in the length of the element (Lo et al., 2010).

Some considerations are made in relation to the sign direction of reflection captured by the receiver. According to Thilakasiri (2006) and the Brazilian Association of Non-Destructive Testing and Inspection (ABENDI, 2016) the sign direction of reflection is associated with impedance, which remains the same direction when there is a reduction in impedance and it becomes opposite when there is an increase in this variable. To exemplify, if the reflection from the toe element presents the opposite direction to that of the initial pulse, then it is fixed in a material of higher impedance, that

is, more rigid. Regarding the reflections captured before the toe element, if it has the same direction as the initial pulse, it suggests a decrease in impedance, which may be a reduction in the section or in the stiffness of the material and if there is an increase in the impedance, the direction will be opposite. An example of a result by Sonic Echo method is presented in Figure 1 where a reflectogram is exhibited in time domain.

2.2 Variables involved in sonic method

The variables considered capable of interfering in the sonic tests are presented in more detail in this item, which are: the wave velocity, the ground stiffness, the place of generation and reception of the wave and the tip hammer to create the shock wave.

2.2.1 Acoustic wave velocity

The waves originated in sonic methods are considered low strain and propagate as elastic waves, also called mechanical waves. Mechanical waves need a medium to propagate which happens in a three-dimensional way. The propagation velocity is a characteristic of the medium and it is independent of the wave frequency created, so it is a medium constant.

Finno et al. (1997) presented that, in general, there are three types of waves generated from the stress wave, they are: primary waves (P waves), secondary waves (S waves) and Rayleigh-type surface waves (R waves). However, as in sonic tests the P wave has a higher velocity than the others, it is identified more clearly and is used to determine the length of the elements.

P waves are called primary, compressional or longitudinal and their velocity can be calculated as shown in Equation 2 (Lee, 2017). Where: V_p = primary wave velocity (m/s); E = Young's modulus of the material (Pa); ρ = specific mass of the material (kg/m^3). In this way, a stiffer material

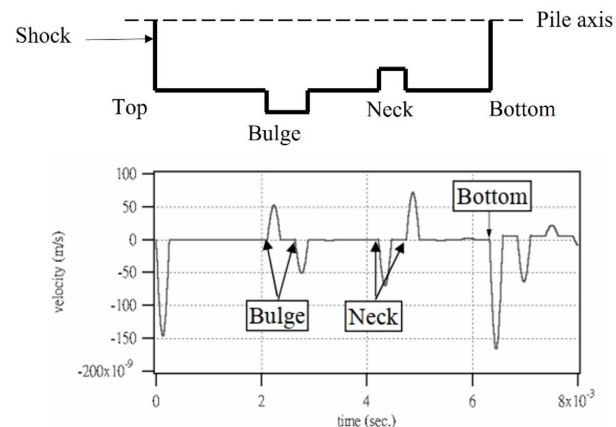


Figure 1. Reflectogram in time domain from SE method [adapted to Lai et al. (2006)].

will have a higher velocity in relation to another with less stiffness, if the same specific mass is maintained.

$$V_p = \sqrt{\frac{E}{\rho}} \quad (2)$$

The *S*-wave, called secondary, shear or transverse, can have its velocity calculated according to Equation 3 (Lee, 2017), where: V_s = secondary wave velocity (m/s); G = material shear modulus (Pa). In this case, the particle moves perpendicularly to the direction of wave propagation. Also, according to Probst (2013), this type of wave propagates only in solid elements, since liquid and gaseous media do not support shear forces.

$$V_s = \sqrt{\frac{G}{\rho}} \quad (3)$$

As known, Young's modulus and shear modulus are related through Poisson's ratio as described in Equation 4. Where: ν = Poisson's ratio. Poisson's ratio can have a value between 0 and 0.5 in the case of an elastic material, but in the case of steel, grout and soil it has a value around 0.2 to 0.3. Thus, following these values, the shear modulus results between 0.42 and 0.38 of the Young's modulus and the shear wave velocity becomes something between 0.65 and 0.62 of the longitudinal.

$$G = \frac{E}{2(1+\nu)} \quad (4)$$

The Rayleigh wave (*R* wave) propagates along the material surface and has a decreased amplitude as it permeates. This wave results from the interference of *P* and *S* type waves, causing vibrations in the opposite direction to the wave propagation. As exposed by Finno et al. (1997), its velocity can be calculated by Equation 5 which correlates it with the velocity of the shear wave, where: V_r = Rayleigh wave velocity. By this equation it is verified that, if the Poisson's ratio is considered variable from 0 to 0.5, the velocity of the Rayleigh wave is 0.862 to 0.955 of the shear wave.

$$V_r = \frac{0.862 + 1.14\nu}{1 + \nu} V_s \quad (5)$$

By the Equations 2-5, it can be concluded that the propagation velocity of the types of waves decreases in the order: $V_p > V_s > V_r$.

When the element length tested is known, it is also possible to calibrate the velocity wave V through Equation 6. Where: L = length of the element and $2L$ refers to the way traveled by the round trip of the wave (m); t = time between generation and receipt of wave reflection (s).

$$V = \frac{2L}{t} \quad (6)$$

When analyzing Equation 6, it is observed that if the velocity varies by 10% from its presumed value, it will reflect in a direct variation of 10% in the length of the element. However, as the length of the buried elements in the soil is, normally, one of the parameters that is wanted through the test, this verification is not always possible to be carried out, making it of greater use in laboratory calibration tests.

The wavefront geometry is another characteristic that can qualify acoustic waves, it can be planar or circular. The planar geometry waves have the wavefront located in a plane that propagates in a space and the circular waves, which occur in 2D elements; or spherical, which occur in 3D elements, propagate symmetrically around a reference point (Azhari, 2010). The wavefront geometry can be impacted by the dimensions of the element in which it propagates and affect the results obtained in the sonic tests.

In sonic tests, the ability to detect defects depends on the wavelength, frequency of the wave and the size of these fails. The wave propagated in the element will reflect upon encountering an anomaly when its wavelength is shorter than the defect (Finno et al., 1997). Finno et al. (1997) expose Equation 7 which correlates the wavelength λ (m) with the frequency f (Hz) and the propagation velocity of the wave V_p (m/s).

$$V_p = f \cdot \lambda \quad (7)$$

The authors showed that in the case of a concrete with a propagation velocity of 4000 m/s and the hammers tip that generate a frequency from 0 to 2000 Hz, then the shortest wavelength is 2 m. Andreucci (2018) emphasizes that it is essential to know the wavelength, as it is directly associated with the size of the defect to be detected. Thus, using low frequencies reduces the sensitivity of the method.

2.2.2 Soil stiffness

Thilakasiri (2006) says that in the graphs of low strain methods it is common to observe positive or negative reflections that are not caused by the impedance change of the pile axis, but rather from the stiffness of the soil layers present along the element. The amplitude of the reflection referring to the analyzed defect is reduced with the increase of the soil stiffness (Huang et al., 2010), in the same way the toe reflection can be difficult to identify due to the high stiffness of the soil. Liao et al. (2008) reiterate that it becomes more uncertain to determine the location of the toe element or the anomaly, the closer is the element stiffness and the ground. It is noted that when the tested element is included in the ground, there is radiation from the waves that are propagated along this element. The main consequence of this effect is an

increase in the damping of the wave, making its reflection more difficult to detect (Ambrosini & Ezeberry, 2005).

Due to the influence of this variable, the operator may misinterpret the result by considering that some reflections are related to the change in impedance caused by the variation of the cross section, when in fact it refers to the change in stiffness of the soil that the element is included in (GDFC, 2000; Thilakasiri, 2006). However, Thilakasiri (2006) observed in his study that the reflections from the variations of the soil layer along the element are characterized by having relatively small magnitude and greater pulse width when compared to the reflections due to axis defects.

2.2.3 Local of impact and receiving signal

Sonic methods may present variations in the location of the accelerometer and the local of generation of the acoustic wave, this characteristic influences the result and it is more deeply studied in piles (Chow et al., 2003; Wang et al., 2014; Zheng et al., 2015), but it also interferes in nails, as reported by Jayawickrama et al. (2007). Studies show that this variable must be considered in the interpretation of the result, because depending on the material present in the local of generation and reception of the wave and the distance between these two points, there may be greater damping of the wave, greater presence of noise in the generated signal and greater difficulty in interpreting the results.

2.2.4 Type of hammer used to generate the wave

Another possible variation is to use different tips in hammers with different materials stiffness for better detection of length or defects in the tested element. Many authors (Finno et al., 1997; Cheung & Lo, 2005; Liao et al., 2008; Rashidyan, 2017) cite that hammers with different tips materials and, consequently, different stiffnesses affect the impact duration that create waves with varied characteristics, modifying the wave frequency and wavelength traveled by the tension wave.

According to Jayawickrama et al. (2007), soft tip hammer generates a low frequency wave despite a longer wavelength, traveling greater distances with less attenuation. However, loss of accuracy occurs for small defects, and it can be used with better results for the element length detection. In opposition to this, the hammer with a stiff tip produces a wave of higher frequency and shorter wavelength, creating a greater dissipation in its trajectory, but it has good results for the identification of small failures. Thus, the use of both types of hammers is ideal for detecting the length of the element, small and large defects at different depths.

Davis (2003) says that tension levels range from 5 MPa for rubber tip hammers up to 50 MPa for aluminum tips. It is important to know the magnitude and duration of the hammer induced pulse. For Ambrosini & Ezeberry (2005) better results are obtained when high energy levels are incorporated in as little time as possible. This characteristic results from stiff tips.

Kirsch & Plaßmann (2002) expose hammers with tips of different materials, producing different forces and contact time. The use of the iron hammer produces greater force intensity and shorter contact time when compared to the rubber hammer. It is observed that the curves presented have the shape of a symmetric Gaussian.

2.2.5 Advantages and limitations

Regarding the *PIT* and Sonic Echo assays, one of the main advantages presented in the bibliography (GDFC, 2000; Cheung, 2003; Ni et al., 2006; Jayawickrama et al., 2007) is related to the test execution speed, being possible to test several elements in just one day, reducing the cost of the test per element. For this reason, this technique has great acceptance in the market. In addition, the authors cite the advantage of no need pre-installed pipes in the tested elements (GDFC, 2000; Lee & Arup, 2007; Ozyildirim & Sharp, 2012) and the ease of application of the method since it is only necessary to have access to the element head to perform the test (GDFC, 2000; Cheung, 2003; Lee & Arup, 2007).

Furthermore, there is a limitation discussed among the authors associated with the maximum length/diameter (L/D) ratio of the element for which there is a wave signal and acceptable results are obtained from the element. This relationship tends to be considered as a general rule for the decision to perform sonic tests on piles and often on nails. Jayawickrama et al. (2007) state that for stiff clays, the average L/D ratio tends to be 30/1 and for soils with low Young's modulus, results up to 50/1 can be obtained in the same way. ABENDI (2016) ensures that the maximum L/D ratio is between 30/1 and 50/1. Huang et al. (2010) consider that the maximum L/D ratio depends on the soil stiffness around the nail and it is between 10/1 and 32/1. The tests carried out by Lee (2017) in their research tested elements with L/D between 10/1 and 70/1 and the author considered the results satisfactory. GDFC (2000) and Likins & Rausche (2000) argue that the 30/1 ratio is commonly cited as limiting, however, the last authors elucidate that with recent electronic techniques, leading to lower noise and therefore this relationship can be higher. Ambrosini & Ezeberry (2005) studied piles with a L/D ratio of 40/1 and concluded that the results were satisfactory. Klingmüller & Kirsch (2004) and Ni et al. (2006) claim that the low strain method has an accuracy of $\pm 5\%$ in determining the length of the tested element and GDFC (2000) comments that the accuracy of the method for defect location is between 5 and 20%.

This method is highly dependent on the professional's experience for the execution and interpretation of the results, as commented by Cheung (2003), Cheung & Lo (2005), Hertlein & Davis (2007) and Rashidyan (2017).

3. Discussion

In this item, studies from different periods are discussed exposing their relevance and conclusions. They were chosen

to present studies and considerations on the different types of elements, such as piles and nails. This research presents varied objectives and methodologies, including laboratory tests, field tests and/or numerical modeling, in order to cover the different variables involved. With this result exhibition it is possible to observe characteristics, differences and similarities of the tests in the different elements.

3.1 Studies on foundation elements

Seitz (1985) says that the low strain method may be limited by the length/diameter ratio and by the wave dissipation caused by soil resistance or concrete damping. The author also reports it is necessary skilled labor to carry out the test and the data interpretation. Low strain tests were carried out on a pile cast in place using vibrating equipment and the wave propagation velocity obtained was between 3900 and 4700 m/s, with an average value of 4000 m/s. For large diameter drilled piles the average velocity was 4230 m/s and 4200 m/s for piles excavated with bentonite mud.

Chow et al. (2003) studied the effect of three-dimensionality in piles, as they observed that although the one-dimensional theory can be and is widely used in these elements for the interpretation of results, in cases where the hammer diameter is too small in relation to the pile diameter, it can result in a misinterpretation of the results. The authors show as an example a hammer with a diameter of 4 to 5 cm and a pile with a diameter of 1.60 m, so the pile would have a diameter between 32 and 40 times greater than that of the hammer. Inadequate interpretation is due to the fact that, when analyzing the problem in 3D, the initial impact response generates an opposite signal peak right after this first peak, this is due to the proximity between the impact site and the receiver. Thus, this reflection can be interpreted as an anomaly near the head of the pile. This error can be avoided by keeping a distance greater than 50% of the pile radius between pulse generation and reception according to the authors.

Chai et al. (2010) modeled a pile in a finite element software to study an optimal position for locating the receiver, in which the generated surface responses have less disturbance caused by the multireflections of the *P*, *S* and *R* waves on the side surface of the pile. The authors state that when the characteristic wavelength is relatively large, that is, the impact contact time is at least four times the pile radius divided by the propagation velocity of the stress wave, the waves that are far from the top of the pile are little affected by the wave's source radius and their behavior is dominated by the longitudinal wave propagation mode, approaching plane waves with little dispersive behavior. Furthermore, it is recommended that the results be analyzed by the one-dimensional wave theory only when the defects are located at a depth greater than twice the diameter of the pile in relation to the element head, when the characteristic wavelength is relatively large and when the receiver is coupled to about 60% of the pile radius in relation to its axis.

Lo et al. (2010) tested bridge foundations with the Sonic Echo method. They found errors of 8.0 to 9.1% in the length of the elements, and they warn that the wave reflection at the toe element is not always easy to identify due to the noises picked up. The authors obtained the velocity of the stress wave in the concrete, considering a specific mass of 2400 kg/m³, can vary from 2000 to 4500 m/s depending on its quality.

Cosic et al. (2014) modeled a 2D and 3D pile with discontinuities and defects simulating a *PIT*-type non-destructive test to examine how the generated reflectogram behaves. For this, first, an integrated pile was modeled as a comparison in relation to the others with defects. The simulated anomalies were piles with defects near the head of the element, impedance reduction along the pile, piles with shorter and longer length than the intact pile and piles with weak reflection at the toe element. It was possible to clearly perceive the difference produced by the different elements in a satisfactory way. The study also created results with the change of the Young's modulus of the soil around or below the pile together with simulations of defects in different locations. It was observed that when the modulus of elasticity of the soil below the pile was too high (10 GPa), the tip reflection was deficient when compared to the other values tested (1 GPa, 500 MPa, 250 MPa, 100 MPa, 50 MPa and 1 MPa). When different Elasticity moduli of the soil around the pile were simulated, it was found that the greater the stiffness of the soil, the lower the tip reflection, and the value of 10 GPa produced great reflection along the entire length of the element and little toe reflection, making it difficult to identify. In addition, different result acquisition sites were tested for the same impact region. These locations varied symmetrically and were simulated in the intact pile and with defects. In the intact pile, the local where the result was obtained did not influence the response and, for piles with defects, the results varied.

Wang et al. (2014) modeled a pile in order to analyze the difference produced in the reflectograms about the initial impulse width, the data acquisition point and the soil Young's modulus were varied. The modeled pile was 16 m long and 1 m in diameter. Pulses with a width of 0.5, 1.0, 1.2, 1.5 and 2.0 ms were also tested, and the pulse that generated the best result, that is, greater tip reflection, was the one with the greatest width (2 ms). In addition, different location distances of the signal receiver were simulated in relation to the center of the pile, as in the center of the element, in $\frac{3}{4}$ of the radius, $\frac{2}{3}$ of the radius and $\frac{1}{2}$ of the radius. Data acquisition points between $\frac{2}{3}$ to $\frac{3}{4}$ of the radius were considered the most suitable for concrete piles, but in reinforced concrete piles, the best distance for data acquisition was $\frac{2}{3}$ of the radius, because if the signal is received close to $\frac{3}{4}$ of the radius the result may have interference from steel vibration.

Wu et al. (2015) tested three types of non-destructive tests on six piles with pre-installed damage and the results for the Sonic Echo test, which is the objective of the present study, are presented below. First, the six piles without the

block above their head were tested. The first pile was designed to be the reference pile, that is, without defect. In this case, it was possible to identify the tip reflection and estimate the length with an error of only 3.33% using the average wave velocity of 3000 m/s. Four piles were simulated with minor defects, in which the tip reflections were identified, resulting in the element length very close to the real one. In the sixth pile, as it contained a more severe defect (rupture in the cross section of 20 mm), it was possible to identify only the location of the defect. The second test methodology was carried out after the execution of the block on the piles and it was concluded that they significantly interfere with the captured signal. The intact pile and the other four with minor defects still had the tip reflection identified, but the error was approximately 15% of the actual length and it was not possible to identify the location of the defects. For the element with the greatest damage, only the reflection of the defect was identified in the same way as in the previous test.

Zheng et al. (2015) analyzed the effects of the low strain test on piles through numerical modeling focusing on the optimal location of the receiver in relation to the pile radius. For this, they tested the distances of 20%, 40%, 60%, 80% and 100% of the pile radius in relation to its axis and concluded that the interferences captured by the receiver are minimal in 60% of the radius and most noticeable near the center and near the edge of the element. Thus, they defined that locating the receiver at a distance of 50 to 70% of the pile radius would produce the least interference in the results.

Jwary (2017) tested different non-destructive methods on wooden piles and the Sonic Echo technique was successful in 94% of the determinations and generated an accuracy of $\pm 15\%$ in the results. The author used four different hammer tips and the velocity found was around 4500 m/s, varying a little more or less depending on the hammer used.

Rashidyan (2017) listed some factors that can influence the Sonic Echo trial, explained the consequences and proposed corrective measures for each of them. Firstly, the impact can be weak or generated incorrectly, resulting in weak longitudinal waves, to avoid this, always hit perpendicularly to the element and with adequate force. The use of incorrect hammers can generate waves that do not reach the toe element due to the high frequency, short wavelength and high attenuation of the same, as occurs with hammers with more rigid points. The use of hammers with a more flexible tip generates waves of low frequency and great length that reach greater depths, but can be confused with reflections from defects in small depths. The author states that the correct choice of the best equipment depends on the judgment and experience of the operator. Soil resistance also influences the results, generating undue reflections that can be confused with a change in the impedance of the pile and attenuating the wave in a way that makes it difficult to interpret the test. Furthermore, the author explains that the wave propagation velocity is one of the test variables and, when erroneously estimated, causes an error in the location of the defect or in

the determination of the length of the element. The author explains that large diameter piles can generate plane waves that propagate longitudinally along the pile axis and one way to avoid them is to make the wavelength greater than the pile diameter, however, if the pile diameter is too large, another non-destructive method is recommended. Another aspect that can hinder the performance of this technique is the existence of defects near the head of the element or the existence of multiple defects in depth. In addition, the author performed numerical modeling in which the presence of the anchor block and its shape, the location of wave generation, the duration and shape of the initial pulse were investigated.

3.2 Studies on retaining elements

Salloum et al. (2003) used the Impulse Response (*IR*) method to estimate the length of nails. They performed experimental tests and numerical analysis. The study showed that the length of steel bars and nails were easily determined with the *IR* technique. It is important to emphasize that the mechanical properties and the condition of the mortar dominated the behavior of these elements. The authors emphasize that knowledge of the longitudinal wave velocity of the mortar was the key parameter to obtain a reasonable estimate of the length of the nail.

Cheung & Lo (2005) studied different non-destructive methods to verify the integrity of nails installed on the ground. The authors mentioned that the propagation velocity wave in the mortar is between 3500 and 4000 m/s. The authors state that no significant interpretation could be performed, as there were considerable difficulties in identifying the wave reflection due to the presence of discontinuity in the mortar, that activities close to the site may have interfered with the results and that it is necessary to have an experienced person to conduct the test and interpret the results.

Gong et al. (2006) carried out a preliminary survey of available non-destructive methods to choose which would be most appropriate for the intended study. In this case, the Sonic Echo and Impulse Response methods stood out. The authors argue that the Impulse Response method is more favorable for the detection of shallow defects. The authors built a soil nail containing 32 nails of different lengths, with pre-established defects, and used mortar and cement grout as a binder to wrap the steel bar. The average wave propagation velocity in the cement grout was around 3900 m/s with a standard deviation of approximately 14 m/s and for the mortar it was 4240 m/s with a standard deviation of 47 m/s. The Sonic Echo method proved to be effective in locating large defects at greater depths and in some cases identified minor fails.

Jayawickrama et al. (2007) studied different locations in nails for the generation and receipt of the acoustic wave, being carried out in the bar and/or in the cement grout. They concluded that the combination with both in the cement grout proved to be more effective to detect defects and their

locations, however it is essential to have good condition of this material in the part close to the head of the nail, which becomes a great limiting factor. In the research carried out by these authors, nails were included in the soil of approximately 1.50 m to 7.60 m. For nails, the conclusions obtained are that with a maximum length of around 4.50 m, there was an approximation of the result between the real and measured lengths. For elements between 6.00 and 7.60 m, the values obtained had a greater distance from the projected ones and, therefore, it is a method that needs further study to prove total efficiency. Furthermore, two speeds were used in the graphs presented, 16000 ft/s (4877 m/s) and 16500 ft/s (5029 m/s), in 75 graphs presented in the study.

Liao et al. (2008) evaluated the Sonic Echo and Impulse Response method in nails exposed to different boundary conditions and the results were showed by graphs in the original paper. The authors calculated the propagation velocity in the steel resulting in 5095 m/s. For the test performed only with the steel bar in the air, the error was considered to be 0% and in the original paper, the graphs presented there is no wave attenuation. Another test was performed with the bar buried in the ground, in this case the error was 3%, but in the original paper it is observed that the curve has great damping due to the wave dissipation in the ground. A third case tested was nails from 1 to 6 m in length molded side by side, in this case it was difficult to identify the reflection corresponding to the toe element. The authors suppose that this difficulty is due to the similar stiffness value of the materials tested, a condition proven by impedance theory. The maximum error in this case was 52%. Two other nails were tested in situ, it was found that the recognition of the toe element was more complicated in this case and the errors were greater than the errors obtained in laboratory tests. For the 1 m bar the error was 7% and for the 4 m bar the error was 5%, which were considered low errors.

Liu et al. (2014) presented considerations about ultrasonic *NDT* in nails, which, despite not being the same technique studied in this work, has similar principles to the Sonic Echo and, therefore, its use was considered relevant. The authors performed laboratory tests and numerical modeling. Different materials with a diameter of 10 mm were simulated to verify their influence on the wave propagation velocity, obtaining a velocity of 4918 m/s for steel and 2294 m/s for mortar. One other simulation refers to steel bars with different diameters as 10 and 60 mm. The velocity varied although only the diameter was changed, this conclusion is not expected for the Sonic Echo. The velocity of the 10 mm diameter steel bar as mentioned was 4918 m/s and for the 60 mm bar 4491 m/s was obtained.

Lee (2017) tested nails fully filled with cement grout of 1, 3, 5 and 7 m in length, being the 7 m element the result of the coupling of a 5 m bar with a of 2 m. The velocity obtained was 3324 m/s and the sign of the reflection at the toe element was the same as the initial pulse due to the presence of material of equal or less rigidity at the bottom

of the clamp. The coupler was identified by the author and the location shows the opposite sign to the impact due to the increase in stiffness and cross-section.

Zima & Rucka (2017) studied the ultrasonic test of guided wave propagation on tie rods. For that, they carried out numerical and experimental tests focusing on the recognition of the energy transferred between the tie rod components. The authors tested and modeled tie rods with different anchored lengths and mortar thickness. They analyzed how the guided waves propagate in the unbonded and bonded length, in the interface between the bar and the part with surrounding mortar, as well as the diffracted waves at the beginning of the element. With this study it was possible to conclude that the presence of the mortar in the anchored part of the tie-rod influenced the wave propagation velocity and the amplitude of the signals. The free and anchored length and the thickness of the mortar were determined based on the wave propagation signals recorded at the free toe element. It was possible to determine the mortar thickness based on the knowledge of the surface wave velocity and the time of flight between the diffracted wave (another ultrasonic technique) and the reflection of the external surface of the mortar.

Yu et al. (2018), first, tested in the laboratory steel bars, steel bars partially filled with cement grout of different lengths, then installed such elements in the soil and, in addition, tested elements already present in the field. Several results are presented in this article, but what stood out is that the velocities found in the nails tested in the laboratory were the same as when the nails were tested after being buried in the ground. The first test carried out used only steel bars with a length of 1, 2, 3, 5 and 7 m, being a single 5 m bar and another consisting of a 2 m bar coupled into another 3 m. The study presents such graphs, in which it is possible to identify the time referring to the toe reflection and to the place of the coupled, in the case of the 2 m bar spliced with the 3 m one. The sign of the impact and the toe element are the same as the bar is in the air and so there is no increase in impedance. However, the sign of the coupler location is opposite to that of the initial pulse, as there is an increase in impedance. In this case, a minimum velocity of 4975 m/s and a maximum of 5195 m/s were obtained. In the case of bars partially filled with cement grout, 3 m nails were tested without the presence of grout in the last 1.5 m and another with 4.85 m with 0.5 m of void in the middle of the element. In this case, more reflections are presented in the graphics, but the authors still identified the defect location and the toe element. The average velocity in the elements was 3489 and 4026 m/s, respectively. In the tests carried out with bars completely fully filled with cement grout and placed on the ground, single bar with 1, 3, 5 and 7 m bars were tested, and a 5 m bar coupled with another 2 m. In the graphs presented, the defect and the toe element were located, but there is great wave damping and the calculated velocities were between 3304 and 3618 m/s. The simulated bars with defects were placed on the ground, and it was possible to locate the anomalies,

in the same way as the toe elements, there was great wave damping and the same velocities described in the case of the nails tested in air. The last test was to test nails in situ already installed on a slope and the minimum velocity was 3181 m/s and the maximum was 3324 m/s. A large amount of noise is observed at the beginning of the graph and it is possible to identify the length of the elements.

Silva et al. (2021) studied a new system to create the acoustic wave using a magnetic field to propel the mechanical wave-generating projectile in the element to be tested. With this, the shock for the generation of the mechanical wave has no operator interference and the wave is always generated with the same intensity and control in the place of generation and signal reception. Furthermore, the results reproducible is guarantee. The authors tested, in the laboratory, the new wave generation device in 1 m long bars, obtaining a velocity of 5172 m/s and an error of 0.74% for results analyzed in the time domain and of -0.19% when analyzed in the frequency domain.

4. Conclusion

Non-destructive methods emerge as an alternative for measuring the length and integrity of elements buried in soil, such as piles, nails and tiebacks. There are several types of these tests in the literature although this work has focused on the low strain tests which is known as Pile Integrity Test in foundation and retaining elements is subdivided into Sonic Echo and Impulse Response. These tests are based on the theory of acoustic impedance and as variables that interfere in the tests as: the propagation velocity of the sonic wave, the stiffness of the soil, the place of generation and reception of the wave and the type of hammer.

With the exposition of studies on sonic tests on foundation and retaining elements, it is observed that the propagation velocity of the sonic wave is a variable of great importance in determining the length and integrity of the objects tested and that it varies with the characteristics of the material and its quality (presence of voids) interferes with its value. Soil stiffness is another variable present, however it affects in a more accentuated way the tests in piles, since the predominantly horizontal stratigraphy of the soil causes greater variation of its stiffness in these vertically buried elements. When the tested element and the ground have similar stiffness, it is difficult to identify the reflections caused by the impedance variation. The wave generation and reception location are more studied in piles due to the greater transversal dimension of these elements, despite interfering in the result of both elements. The type of hammer is a factor that also deserves attention and presents studies in retaining and foundation elements, with the contact time and its material being decisive for the generated wave.

It is evident that the *NDT* can be used in foundation and containment elements and it is important to emphasize that they still need further studies and innovation both for their

execution and for the interpretation of the techniques. After these approach about *NDT* using acoustic wave, the authors observe a variable which could be controlled. Looking for this subject, it has highlighted how about the experience operator can affect the generation of the sonic wave. In this way, the authors suggest studies to control the generation of the acoustic wave like related by Silva et al. (2021). With this conception is possible to control the local and intensity of wave generation, the results reproducibly is guarantee and a variable is deleted in the signal interpretation.

Acknowledgements

This article is invited to be published by COBRAMSEG 2022 conference as it was one of the highlights of the event. The authors are grateful for this invitation.

Declaration of interest

The authors have no conflicts of interest to declare. All co-authors have observed and affirmed the contents of the paper and there is no financial interest to report.

Authors' contributions

Isabela Grossi da Silva: conceptualization, data curation, visualization, writing – original draft. Vítor Pereira Faro: conceptualization, supervision, validation – original draft.

Data availability

No dataset was generated or evaluated in the course of the current study; therefore, data sharing is not applicable.

List of symbols

f	wave frequency
t	time between generation and receipt of wave reflection
A	cross-sectional area
E	Young's modulus or elasticity modulus of soil
G	shear modulus material
L	element length
V_p	primary wave velocity
V_r	Rayleigh wave velocity
V_s	secondary wave velocity
Z	acoustic impedance
IR	impulse response
NDT	non-destructive test
PIT	pile integrity test
SE	sonic echo
ν	Poisson's ratio
ρ	specific mass
λ	wavelength

References

- Ambrosini, D., & Ezeberry, J. (2005). Long piles integrity trough impact echo technique. *Computational Mechanics*, 24, 651-669.
- Andreucci, R. (2018). *Ensaio por ultrassom: aplicação industrial*. ABENDI. In Portuguese.
- Associação Brasileira de Ensaios Não Destrutivos e Inspeção – ABENDI. (2016). *Práticas recomendadas: execução e diagnóstico de ensaio de integridade de estaca com baixa deformação. PRe-001-2016*. ABENDI. In Portuguese.
- Azhari, H. (2010). *Basics of biomedical ultrasound for engineers*. John Wiley & Sons.
- Carino, N.J. (2001) The impact-echo method: an overview. In P.C. Chang (Ed.), *Structures 2001: a structural engineering odyssey* (pp. 1-18). American Society of Civil Engineers.
- Chai, H.-Y., Phoon, K.-K., & Zhang, D.-J. (2010). Effects of the source on wave propagation in pile integrity testing. *Journal of Geotechnical and Geoenvironmental Engineering*, 136(9), 1200-1208.
- Cheung, W.M. (2003). *Non-destructive tests for determining the lengths of installed steel soil nails*. Geotechnical Engineering Office/Civil Engineering Department. Geo Report 133.
- Cheung, W.M., & Lo, D.O.K. (2005). *Interim report on non-destructive tests for checking the integrity of cement grout sleeve of installed soil nails*. Geotechnical Engineering Office/Civil Engineering and Development Department. Geo Report 176.
- Chow, Y.K., Phoon, K.K., Chow, W.F., & Wong, K.Y. (2003). Low strain integrity testing of piles: three-dimensional effects. *Journal of Geotechnical and Geoenvironmental Engineering*, 129(2), 1057-1062.
- Cosic, M., Folic, B., & Folic, R. (2014). Numerical simulation of the pile integrity test on defected piles. *Acta Geotechnica Slovenica*, 11(2), 5-19.
- Davis, A.G. (2003). The nondestructive impulse response test in North America: 1985–2001. *NDT & E International*, 36(4), 185-193.
- Finno, R.J., Gassman, S.L., & Osborn, P.W. (1997). *Non-destructive evaluation of a deep foundation test section at the Northwestern University National Geotechnical Experimentation Site. A report submitted to the Federal Highway Administration*. Northwestern University.
- G-I Deep Foundations Committee – GDFC (2000). Nondestructive evaluation of drilled shafts. *Journal of Geotechnical and Geoenvironmental Engineering*, 126(1), 92-95.
- Gong, J., Jayawickrama, P.W., & Tinkey, Y. (2006). Nondestructive evaluation of installed soil nails. *Transportation Research Record: Journal of the Transportation Research Board*, 1976(1), 104-113. <http://dx.doi.org/10.1177/0361198106197600112>.
- Hertlein, B., & Davis, A. (2007). *Nondestructive testing of deep foundations*. John Wiley & Sons.
- Huang, Y.-H., Ni, S.-H., Lo, K.-F., & Charng, J.-J. (2010). Assessment of identifiable defect size in a drilled shaft using sonic echo method: numerical simulation. *Computers and Geotechnics*, 37(6), 757-768. <http://dx.doi.org/10.1016/j.compgeo.2010.06.002>.
- Jayawickrama, P.W., Tinkey, Y., Gong, J., & Turner, J. (2007). *Non-destructive evaluation of installed soil nails. Report n° FHWA/TX-07-0-4484-1*. Texas Tech University.
- Jwary, A.F. (2017). *Practical considerations in determining timber pile depth using the sonic echo method* [Master's dissertation]. University of New Mexico.
- Kirsch, F., & Plößmann, B. (2002). Dynamic methods in pile testing: developments in measurement and analysis. In M.W. O'Neill & F.C. Townsend (Eds.), *Deep foundations 2002: an international perspective on the theory, design, construction, and performance* (868-882). American Society of Civil Engineers.
- Klingmüller, O., & Kirsch, F. (2004). A quality and safety issue for cast-in-place piles-25 years of experience with low-strain integrity testing in Germany: from scientific peculiarity to day-to-day practice. In J.A. DiMaggio & M.H. Hussein (Eds.), *Current practices and future trends in deep foundations* (pp. 202-221). American Society of Civil Engineers.
- Lai, J.R., Yu, C.P., & Liao, S.T. (2006). Assessment of the integrity of piles by impedance log technique. *Key Engineering Materials*, 321, 340-343.
- Lee, C.F., & Arup, O. (2007). *Review of use of non-destructive testing in quality control in soil nailing works*. Geotechnical Engineering Office/Civil Engineering and Development Department. Geo Report 219.
- Lee, J.-S. (September 17-22, 2017). Geo-characterization using waves - principle to application. In International Society for Soil Mechanics and Geotechnical Engineering (Org.), *19th International Conference on Soil Mechanics and Geotechnical Engineering* (pp. 245-264). London, United Kingdom: ISSMGE.
- Liao, S.-T., Huang, C.-K., & Wang, C.-Y. (2008). Sonic echo and impulse response tests for length evaluation of soil nails in various bonding mediums. *Canadian Geotechnical Journal*, 45(7), 1025-1035.
- Likins, G.E., & Rausche, F. (September 13, 2000). Recent advances and proper use of PDI low strain pile integrity testing. In S. Niyama & J. Beim (Eds.), *Proceedings of the Sixth International Conference on the Application of Stress-Wave Theory to Piles* (pp. 211-218). Rotterdam, Netherlands: Brookfield.
- Liu, J., Zhang, D.-Y., Lin, P., Cai, Z., & Rong, X. (2014). *Ultrasonic non-destructive testing of soil nails*. Ryerson University.
- Lo, K.-F., Ni, S.-H., & Huang, Y.-H. (2010). Non-destructive test for pile beneath bridge in the time, frequency, and time-frequency domains using transiente loading. *Nonlinear Dynamics*, 62(1-2), 349-360.

- Ni, S.-H., Lehmann, L., Charng, J.-J., & Lo, K.-F. (2006). Low-strain integrity testing of drilled piles with high slenderness ratio. *Computers and Geotechnics*, 33(6-7), 283-293.
- Olson, L.D., Jalinoos, F., & Aouad, M.F. (1998). Parallel seismic test method. In L.D. Olson, F. Jalinoos & M.F. Aouad (Eds.), *Determination of unknown subsurface bridge foundations* (pp. 36–38). Federal Highway Administration. Report submitted to NCHRP.
- Ozyildirim, H.C., & Sharp, S.R. (2012). *Preparation and testing of drilled shafts with self-consolidating concrete*. U.S. Department of Transportation/Federal Highway Administration/Virginia Center for Transportation Innovation and Research.
- Probst, G.M. (2013). *Evaluation of the constructive characteristics of electromagnetic acoustic transducers for communication through metallic walls* [Master's dissertation]. Federal University of Santa Catarina. In Portuguese.
- Rashidyan, S. (2017). *Characterization of unknown bridge foundations* [Doctoral thesis]. University of New Mexico.
- Salloum, T., Pernica, G., Glazer, R., & Law, K.T. (2003). Using the impulse response technique to estimate the length of in-situ soil nails. In *56th Canadian Geotechnical Conference*, Winnipeg, Sept. 29-Oct. 1 2003. National Research Council Canada.
- Seitz, J. (May 27-30, 1985). Low strain integrity testing of bored piles. In G. Holm, H. Bredenberg & C.J. Gravare (Eds.), *Application of stress-wave theory on piles: proceedings of the second international conference on the application of stress-wave theory on piles* (pp. 94-102). Stockholm, Sweden: Swedish Pile Commission.
- Silva, I.G., Bonfim, M.J.C., & Faro, V.P. (2021). Electromagnetic launching system as an alternative to non-destructive sonic wave generation for steel bar length determination. *IEEE Latin America Transactions*, 19(2), 306-313.
- Thilakasiri, H. (2006). Interpretation of pile integrity test (PIT) results. *Annual Transactions of IESL*, 78-84.
- Wang, Z., Wu, Y., & Xiao, Z. (2014). Numerical assessment of factors affecting waveform based on low strain testing of piles. *The Open Civil Engineering Journal*, 8, 64-70.
- Wu, S., Lai, J., Yang, B.-H., & Cheng, C.-F. (2015). Integrity testing of model piles with pile cap. *Proceedings of NDT-CE*, 920-927.
- Yu, J.-D., Kim, N.-Y., & Lee, J.-S. (2018). Nondestructive integrity evaluation of soil nails using longitudinal waves. *Journal of Geotechnical and Geoenvironmental Engineering*, 144(11), 04018080.
- Zheng, C., Kouretzis, G.P., Ding, X., Liu, H., & Poulos, H.G. (2015). Threedimensional effects in low-strain integrity testing of piles: analytical solution. *Canadian Geotechnical Journal*, 53(2), 225-235.
- Zima, B., & Rucka, M. (2017). Non-destructive inspection of ground anchors using guided wave propagation. *International Journal of Rock Mechanics and Mining Sciences*, 94, 90-102.

GABIÃO BELGO. UMA ESCOLHA PARA ELEVAR A QUALIDADE DA SUA OBRA.



A linha **Belgo GeoTech** traz ao mercado soluções em aço para aplicações geotécnicas. Entre os nossos produtos, disponibilizamos **gabiões**, **malhas talude**, **fibras de aço Dramix®**, **telas de fortificação**, **cordoalhas** e **barras helicoidais**. Mas também oferecemos suporte técnico qualificado para atender a todas as necessidades do seu projeto. **Aqui se faz geotecnia com a força do aço.**



Saiba mais em: belgogeotech.com.br

BELGO
GeoTech

Belgo Bekaert Arames

ArcelorMittal

BEKAERT
better together

PIONEERING AND INNOVATION

SINCE 1921



 **TEIXEIRA DUARTE**
ENGENHARIA E CONSTRUÇÕES, S.A.

PORT FACILITY CONSTRUCTION
NACALA - MOZAMBIQUE

LICENCE NO. 24 - PUB



Building a better world.
teixiraduarteconstruction.com



Safety is our nature

Líder mundial em pesquisa, desenvolvimento, fabricação e comercialização de soluções em aço de alta resistência contra desastres naturais.

Leading research, development, manufacturing and supplying high tensile steel solutions against natural hazards.



Petrópolis/RJ-Brasil

SEGURANÇA É A NOSSA NATUREZA

Estabilização de taludes |
Slope stabilization

Queda de rochas |
Rockfall

Escorregamento Superficial |
Shallow landslides

Corridas detríticas |
Debris flow

Escavações subterrâneas |
Underground support

Para mais informações, acesse
www.geobruigg.com



The Best Solution!

Tecnilab Portugal, S.A. will provide you with answers to your Geotechnical engineering needs.

Tecnilab Portugal, S.A. is a professional Geotechnical engineering company and has a lot of experience as a professional group that mainly engages in measurement engineering in dam, subway(Metro), harbor, power plant, soft ground and structure construction.

WE ARE THE DISTRIBUTOR OF PORTUGAL OF ACE INSTRUMENT CO., LTD. IN KOREA.

ACE INSTRUMENT CO., LTD. is a company that obtains worldwide reputation for supplying high precision, high reliability products in all Geotechnical instruments, data logger and in-situ test equipments. Independently developed automatic monitoring system can be used anywhere in the world, including buildings, bridges, ground and any constructions.

Data Acquisition System & Web Monitoring Program



Sales company



Tecnilab Portugal, S.A.

A: Rua Gregorio Lopes, Lote 1512B 1449-041 Lisboa Portugal
T: +351 217 220 870 F: +351 217 264 550
www.tecnilab.pt

Manufacturer



ACE INSTRUMENT CO., LTD.

The first value in Geotechnical & Structural Instrumentation
A: 9, Dangjung-ro 27 beon-gil, Gunpo-si, Gyeonggi-do, Korea
T: +82 31 459 8753-7 F: +82 31 459 8758 E: acens@naver.com
www.aceinstrument.com

ENGINEERING AND ENVIRONMENTAL CONSULTANTS



COBA

GEOLOGY AND GEOTECHNICS

Hydrogeology • Engineering Geology • Rock Mechanics • Soil Mechanics • Foundations and Retaining Structures • Underground Works • Embankments and Slope Stability
Environmental Geotechnics • Geotechnical Mapping



- Water Resources Planning and Management
- Hydraulic Undertakings
- Electrical Power Generation and Transmission
- Water Supply Systems and Pluvial and Wastewater Systems
- Agriculture and Rural Development
- Road, Railway and Airway Infrastructures
- Environment
- Geotechnical Structures
- Cartography and Cadastre
- Safety Control and Work Rehabilitation
- Project Management and Construction Supervision



PORTUGAL

CENTER AND SOUTH REGION
Av. 5 de Outubro, 323
1649-011 LISBOA
Tel.: (351) 210125000, (351) 217925000
Fax: (351) 217970348
E-mail: coba@coba.pt
www.coba.pt

Av. Marquês de Tomar, 9, 6.
1050-152 LISBOA
Tel.: (351) 217925000
Fax: (351) 213537492

NORTH REGION

Rua Mouzinho de Albuquerque, 744, 1.
4450-203 MATOSINHOS
Tel.: (351) 229380421
Fax: (351) 229373648
E-mail: engico@engico.pt

ANGOLA

Praceta Farinha Leitão, edifício nº 27, 27-A - 2.º Dto
Bairro do Maculusso, LUANDA
Tel./Fax: (244) 222338 513
Cell: (244) 923317541
E-mail: coba-angola@netcabo.co.ao

MOZAMBIQUE

Pestana Rovuma Hotel. Centro de Escritórios.
Rua da Sé nº114. Piso 3, MAPUTO
Tel./Fax: (258) 21 328 813
Cell: (258) 82 409 9605
E-mail: coba.mz@tdm.co.mz

ALGERIA

09, Rue des Frères Hocine
El Biar - 16606, ARGEL
Tel.: (213) 21 922802
Fax: (213) 21 922802
E-mail: coba.alger@gmail.com

BRAZIL

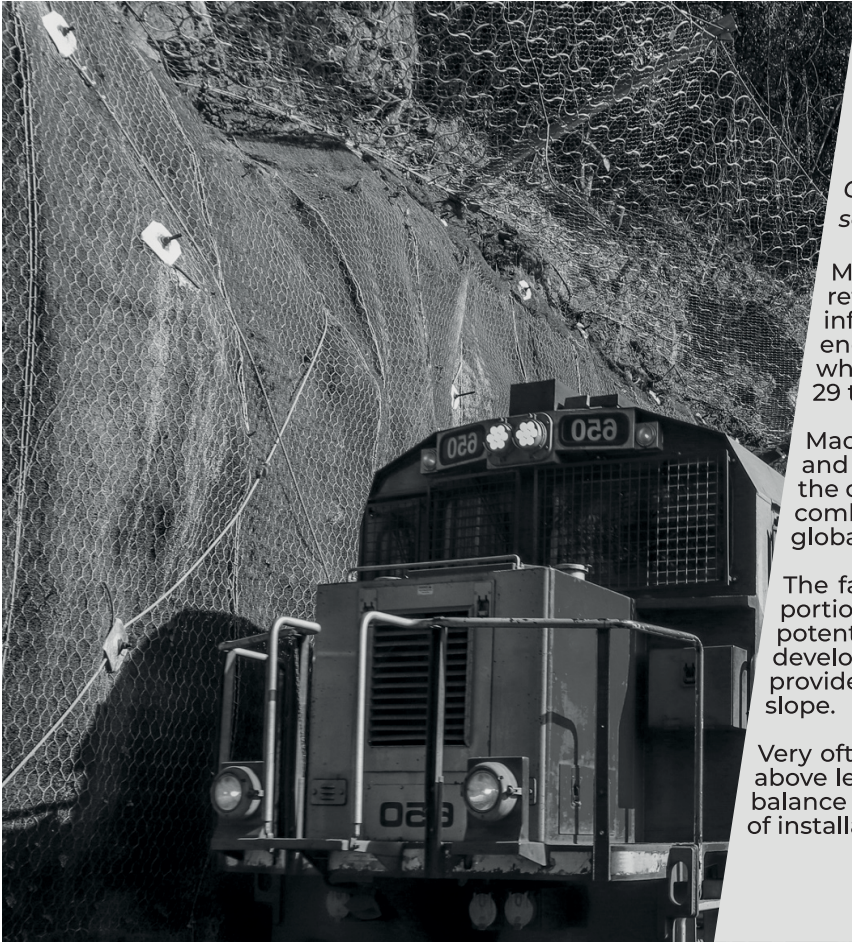
Rio de Janeiro
COBA Ltd. - Rua Bela 1128
São Cristóvão
20930-380 Rio de Janeiro RJ
Tel.: (55 21) 351 50 101
Fax: (55 21) 258 01 026

Fortaleza

Av. Senador Virgílio Távora 1701, Sala 403
Aldeota - Fortaleza CEP 60170 - 251
Tel.: (55 85) 3261 17 38
Fax: (55 85) 3261 50 83
E-mail: coba@esc-te.com.br

UNITED ARAB EMIRATES

Corniche Road - Corniche Tower - 5th Floor - 5B
P. O. Box 38360 ABU DHABI
Tel.: (971) 2 627 0088
Fax: (971) 2 627 0087



Maccaferri Rockfall barrier installed alongside mesh systems

Combining different systems to provide the most effective solution for rock faces and soil slopes.

Maccaferri RB Series of rockfall barriers is specifically designed to retain impacts of falling boulders, protecting people and infrastructure. Maccaferri rockfall barriers are available with energy absorption capacity starting from 35 kJ and up to 9,000 kJ, which is equivalent to the kinetic energy generated by a block of 29 tons falling at 90 km/h.

Maccaferri additionally developed numerous rockfall mitigation and erosion protection system to be implemented directly within the detachment zone. Among those, soil nailing is a technique that combines the use of steel anchors and facing systems to provide global and surficial stability to soil and weathered rocks.

The facing system plays a key role since it restrains the superficial portion of the slope which can mobilise between the anchors, potentially destabilizing the overall slope. Therefore, Maccaferri developed MacMat®, an innovative reinforced 3D geomat that provide surficial stabilization while promoting the revegetation of the slope.

Very often the use of combined solutions such as the two mentioned above leads to the best results. It also provides the most cost-effective balance between technical performance, risk, client value, ease/safety of installation and environmental benefits.



/maccaferri



/maccaferrimatriz



@Maccaferri_BR



/MaccaferriWorld



/maccaferriworld

MACCAFERRI



The Ground is our Challenge

MAIN ACTIVITY AREAS

Consultancy, Supervision and Training

- Earth Retaining Structures
- Special Foundations
- Ground Improvement
- Foundations Strengthening and Underpinning
- Façades Retention
- Tunnels and Underground Structures
- Slope Stability
- Geological and Geotechnical Investigation
- Demolition

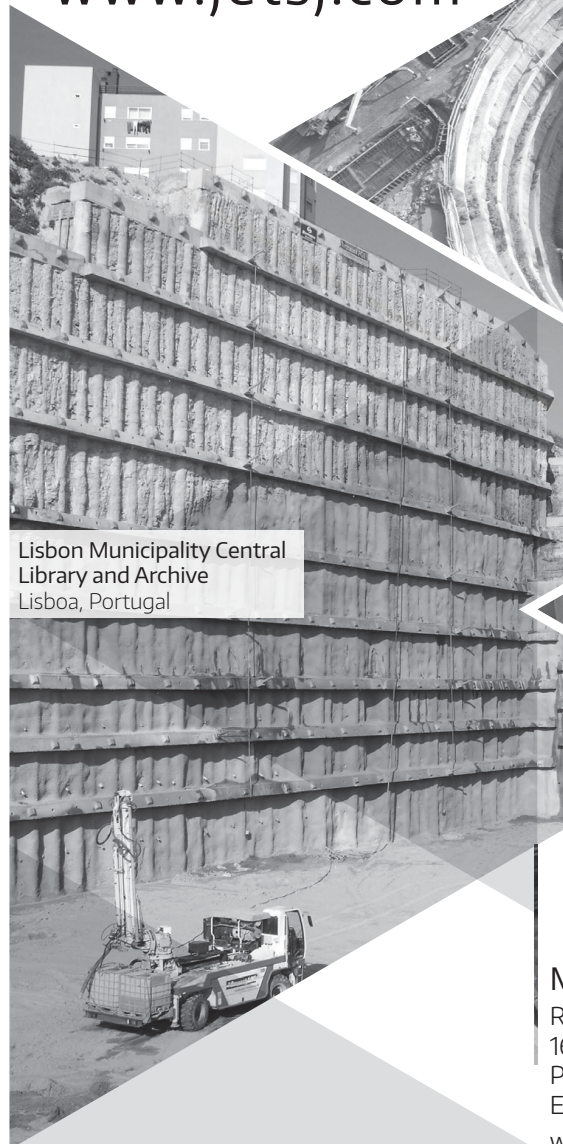
www.jetsj.com



Tool Plazas P2 and P3
Santa Catarina, Brazil



Mining Shaft
Kamsar, Guiné



Lisbon Municipality Central
Library and Archive
Lisboa, Portugal



Solar Santana Building
Lisboa, Portugal

Main Office

Rua Julieta Ferrão, 12 - Office 1501

1600-131 LISBOA, Portugal

Phone.: [+351] 210 505 150 / 51

Email: info@jetsj.com

www.linkedin.com/company/jetsj-geotecnia-lda/



- > **Prospecção Geotécnica**
Site Investigation
- > **Consultoria Geotécnica**
Geotechnical Consultancy
- > **Obras Geotécnicas**
Ground Treatment-Construction Services
- > **Controlo e Observação**
Field Instrumentation Services and Monitoring Services
- > **Laboratório de Mecânica de Solos**
Soil and Rock Mechanics Laboratory

Certificada ISO 9001 por



Geocontrole



Parque Oriente, Bloco 4, EN10
2699-501 Bobadela LRS
Tel. 21 995 80 00
Fax. 21 995 80 01
e.mail: mail@geocontrole.pt
www.geocontrole.pt


Geocontrole
Geotecnia e Estruturas de Fundação SA



TPF - CONSULTORES DE ENGENHARIA E ARQUITETURA, S.A.

BUILDING THE WORLD, BETTER



ENGINEERING AND ARCHITECTURAL CONSULTANCY

- > GEOLOGY, GEOTECHNICS, SUPERVISION OF GEOTECHNICAL WORKS
- > EMBANKMENT DAMS, UNDERGROUND WORKS, RETAINING STRUCTURES
- > SPECIAL FOUNDATIONS, SOIL IMPROVEMENT, GEOMATERIALS

www.tpf.pt



**TRANSFORMATIVE
ENGINEERING,
MANAGEMENT,
AND INNOVATION
DELIVERING RESULTS**



DF+ IS AN INTEGRATED ENGINEERING CONSULTING FIRM WITH OVER 25 YEARS OF EXPERIENCE IN THE SECTORS OF MINING, INFRASTRUCTURE, AGRIBUSINESS, AND INDUSTRIAL.

WE DEVELOP PROJECTS BASED ON CONSOLIDATED TECHNICAL SOLUTIONS THAT ENCOMPASS THE STATE OF THE ART IN DIGITAL ENGINEERING.



AV. BARÃO HOMEM DE MELO, 4554 - 5th floor
ESTORIL, BELO HORIZONTE/MG

+55 31 2519-1001

dfmais.eng.br
comercial@dfmais.eng.br



Guide for Authors

Soils and Rocks is an international scientific journal published by the Brazilian Association for Soil Mechanics and Geotechnical Engineering (ABMS) and by the Portuguese Geotechnical Society (SPG). The aim of the journal is to publish original papers on all branches of Geotechnical Engineering. Each manuscript is subjected to a single-blind peer-review process. The journal's policy of screening for plagiarism includes the use of a plagiarism checker on all submitted manuscripts.

Soils and Rocks embraces the international Open Science program and is striving to meet all the recommendations. However, at this moment, the journal is not yet accepting preprints and open data, and has not adopted open peer reviews.

Soils and Rocks provides a manuscript template available at the journal's website.

1. Category of papers

Submissions are classified into one of the following categories:

Article – an extensive and conclusive dissertation about a geotechnical topic, presenting original findings.

Technical Note – presents a study of smaller scope or results of ongoing studies, comprising partial results and/or particular aspects of the investigation.

Case Study – report innovative ways to solve problems associated with design and construction of geotechnical projects. It also presents studies of the performance of existing structures.

Review Article – a summary of the State-of-the-Art or State-of-the-Practice on a particular subject or issue and represents an overview of recent developments.

Discussion – specific discussions about published papers.

Authors are responsible for selecting the correct category when submitting their manuscript. However, the manuscript category may be altered based on the recommendation of the Editorial Board. Authors are also requested to state the category of paper in their Cover Letter.

When submitting a manuscript for review, the authors should indicate the category of the manuscript, and is also understood that they:

- a) assume full responsibility for the contents and accuracy of the information in the paper;
- b) assure that the paper has not been previously published, and is not being submitted to any other journal for publication.

2. Paper length

Full-length manuscripts (Article, Case Study) should be between 4,000 and 8,000 words. Review articles should have up to 10,000 words. Technical Notes have a word count limit of 3,500 words. Discussions have a word count limit of 1,000 words. These word count limits exclude the title page, notation list (e.g., symbols, abbreviations), captions of tables and figures, acknowledgments and references. Each single column and double column figure or table is considered as equivalent to 150 and 300 words, respectively.

3. Scientific style

The manuscripts should be written in UK or US English, in the third person and all spelling should be checked in accordance with

a major English Dictionary. The manuscript should be able to be readily understood by a Civil Engineer and avoid colloquialisms. Unless essential to the comprehension of the manuscript, direct reference to the names of persons, organizations, products or services is not allowed. Flattery or derogatory remarks about any person or organization should not be included.

The author(s) of Discussion Papers should refer to himself (herself/themselves) as the reader(s) and to the author(s) of the paper as the author(s).

The International System (SI) units must be used. The symbols are recommended to be in accordance with Lexicon in 14 Languages, ISSMFE (2013) and the ISRM List of Symbols. Use italics for single letters that denote mathematical constants, variables, and unknown quantities, either in tables or in the text.

4. Submission requirements and contents

A submission implies that the following conditions are met:

- the authors assume full responsibility for the contents and accuracy of the information presented in the paper;
- the manuscript contents have not been published previously, except as a lecture or academic thesis;
- the manuscript is not under consideration for publication elsewhere;
- the manuscript is approved by all authors;
- the manuscript is approved by the necessary authorities, when applicable, such as ethics committees and institutions that may hold intellectual property on contents presented in the manuscript;
- the authors have obtained authorization from the copyright holder for any reproduced material;
- the authors are aware that the manuscript will be subjected to plagiarism check.

The author(s) must upload two digital files of the manuscript to the Soils and Rocks submission system. The size limit for each submission file is 20 MB. The manuscript should be submitted in docx format (Word 2007 or higher) or doc format (for older Word versions). An additional PDF format file of the manuscript is also required upon submission. Currently, the journal is not accepting manuscripts prepared using LaTeX.

The following documents are required as minimum for submission:

- cover letter;
- manuscript with figures and tables embedded in the text (doc or docx format);

manuscript with figures and tables embedded in the text for revision (PDF format);

- permission for re-use of previously published material when applicable, unless the author/owner has made explicit that the image is freely available.

4.1 Cover letter

The cover letter should include: manuscript title, submission type, authorship information, statement of key findings and work novelty, and related previous publications if applicable.

4.2 Title page

The title page is the first page of the manuscript and must include:

- A concise and informative title of the paper. Avoid abbreviations, acronyms or formulae. Discussion Papers should contain the title of the paper under discussion. Only the first letter of the first word should be capitalized.
- Full name(s) of the author(s). The first name(s) should not be abbreviated. The authors are allowed to abbreviate middle name(s).
- The corresponding author should be identified by a pound sign # beside his/her and in a footnote.
- The affiliation(s) of the author(s), should follow the format: Institution, (Department), City, (State), Country.
- Affiliation address and e-mail must appear below each author's name.
- The 16-digit ORCID of the author(s) – mandatory
- Main text word count (excluding abstract and references) and the number of figures and tables

4.3 Permissions

Figures, tables or text passages previously published elsewhere may be reproduced under permission from the copyright owner(s) for both the print and online format. The authors are required to provide evidence that such permission has been granted at the moment of paper submission.

4.4 Declaration of interest

Authors are required to disclose conflicting interests that could inappropriately bias their work. For that end, a section entitled "Declaration of interest" should be included following any acknowledgments and prior to the "Authors' contributions" section. In case of the absence of conflicting interests, the authors should still include a declaration of interest.

4.5 Authors' contributions

Authors are required to include an author statement outlining their individual contributions to the paper according to the CASRAI CRediT roles (as per <https://casrai.org/credit>). The minimum requirements of contribution to the work for recognition of authorship are: a) Participate actively in the discussion of results; b) Review and approval of the final version of the manuscript. A section entitled "Authors' contributions" should be included after the declaration of interest section, and should be formatted with author's name and CRediT role(s), according to the example:

Samuel Zheng: conceptualization, methodology, validation. **Olivia Prakash:** data curation, writing - original draft preparation. **Fatima Wang:** investigation, validation. **Kwame Bankole:** supervision. **Sun Qi:** writing - reviewing and editing.

Do not include credit items that do not follow the Taxonomy established by CASRAI CRediT roles.

The authors' contributions section should be omitted in manuscripts that have a single author.

5. Plagiarism checking

Submitted papers are expected to contain at least 50 % new content and the remaining 50 % should not be verbatim to previously published work.

All manuscripts are screened for similarities. Currently, the Editorial Board uses the plagiarism checker Plagius (www.plagius.com) to compare submitted papers to already published works. Manuscripts will be rejected if more than 20 % of content matches previously published work, including self-plagiarism. The decision to reject will be under the Editors' discretion if the percentage is between 10 % and 20 %.

IMPORTANT OBSERVATION: Mendeley software plug-in (suggested in this guide) for MS-Word can be used to include the references in the manuscript. This plug-in uses a field code that sometimes includes automatically both title and abstract of the reference. Unfortunately, the similarity software adopted by the Journal (Plagius) recognizes the title and abstract as an actual written text by the field code of the reference and consequently increases considerably the percentage of similarity. Please do make sure to remove the abstract (if existing) inside Mendeley section where the adopted reference is included. This issue has mistakenly caused biased results in the past. The Editorial Board of the journal is now aware of this tendentious feature.

6. Formatting instructions

The text must be presented in a single column, using ISO A4 page size, left, right, top, and bottom margins of 25 mm, Times New Roman 12 font, and line spacing of 1.5. All lines and pages should be numbered.

The text should avoid unnecessary italic and bold words and letters, as well as too many acronyms. Authors should avoid to capitalize words and whenever possible to use tables with distinct font size and style of the regular text.

Figures, tables and equations should be numbered in the sequence that they are mentioned in the text.

Abstract

Please provide an abstract between 150 and 250 words in length. Abbreviations or acronyms should be avoided. The abstract should state briefly the purpose of the work, the main results and major conclusions or key findings.

Keywords

A minimum of three and a maximum of six keywords must be included after the abstract. The keywords must represent the

content of the paper. Keywords offer an opportunity to include synonyms for terms that are frequently referred to in the literature using more than one term. Adequate keywords maximize the visibility of your published paper.

Examples:

Poor keywords – piles; dams; numerical modeling; laboratory testing

Better keywords – friction piles; concrete-faced rockfill dams; material point method; bender element test

List of symbols

A list of symbols and definitions used in the text must be included before the References section. Any mathematical constant, variable or unknown quantity should appear in italics.

6.1 Citations

References to other published sources must be made in the text by the last name(s) of the author(s), followed by the year of publication. Examples:

- Narrative citation: [...] while Silva & Pereira (1987) observed that resistance depended on soil density
- Parenthetical citation: It was observed that resistance depended on soil density (Silva & Pereira, 1987).

In the case of three or more authors, the reduced format must be used, e.g.: Silva et al. (1982) or (Silva et al., 1982). Do not italicize “et al.”

Two or more citations belonging to the same author(s) and published in the same year are to be distinguished with small letters, e.g.: (Silva, 1975a, b, c).

Standards must be cited in the text by the initials of the entity and the year of publication, e.g.: ABNT (1996), ASTM (2003).

6.2 References

A customized style for the Mendeley software is available and may be downloaded from this link.

Full references must be listed alphabetically at the end of the text by the first author’s last name. Several references belonging to the same author must be cited chronologically.

Some formatting examples are presented here:

Journal Article

Bishop, A.W., & Blight, G.E. (1963). Some aspects of effective stress in saturated and partly saturated soils. *Géotechnique*, 13(2), 177-197. <https://doi.org/10.1680/geot.1963.13.3.177>

Castellanza, R., & Nova, R. (2004). Oedometric tests on artificially weathered carbonatic soft rocks. *Journal of Geotechnical and Geoenvironmental Engineering*, 130(7), 728-739. [https://doi.org/10.1061/\(ASCE\)1090-0241\(2004\)130:7\(728\)](https://doi.org/10.1061/(ASCE)1090-0241(2004)130:7(728))

Fletcher, G. (1965). Standard penetration test: its uses and abuses. *Journal of the Soil Mechanics Foundation Division*, 91, 67-75.

Indraratna, B., Kumara, C., Zhu S-P., Sloan, S. (2015). Mathematical modeling and experimental verification of fluid flow through deformable rough rock joints. *International Journal of Geomechanics*, 15(4): 04014065-1-04014065-11. [https://doi.org/10.1061/\(ASCE\)GM.1943-5622.0000413](https://doi.org/10.1061/(ASCE)GM.1943-5622.0000413)

Garnier, J., Gaudin, C., Springman, S.M., Culligan, P.J., Goodings, D., König, D., ... & Thorel, L. (2007). Catalogue of scaling laws and similitude questions in geotechnical centrifuge modelling. *International Journal of Physical Modelling in Geotechnics*, 7(3), 01-23. <https://doi.org/10.1680/ijpmg.2007.070301>

Bicalho, K.V., Gramelich, J.C., & Santos, C.L.C. (2014). Comparação entre os valores de limite de liquidez obtidos pelo método de Casagrande e cone para solos argilosos brasileiros. *Comunicações Geológicas*, 101(3), 1097-1099 (in Portuguese).

Book

Lambe, T.W., & Whitman, R.V. (1979). *Soil Mechanics, SI version*. John Wiley & Sons.

Das, B.M. (2012). *Fundamentos de Engenharia Geotécnica*. Cengage Learning (in Portuguese).

Head, K.H. (2006). *Manual of Soil Laboratory Testing - Volume 1: Soil Classification and Compaction Tests*. Whittles Publishing.

Bhering, S.B., Santos, H.G., Manzatto, C.V., Bognola, I., Fasolo, P.J., Carvalho, A.P., ... & Curcio, G.R. (2007). *Mapa de solos do estado do Paraná*. Embrapa (in Portuguese).

Book Section

Yerro, A., & Rohe, A. (2019). Fundamentals of the Material Point Method. In *The Material Point Method for Geotechnical Engineering* (pp. 23-55). CRC Press. <https://doi.org/10.1201/9780429028090>

Sharma, H.D., Dukes, M.T., & Olsen, D.M. (1990). Field measurements of dynamic moduli and Poisson’s ratios of refuse and underlying soils at a landfill site. In *Geotechnics of Waste Fills - Theory and Practice* (pp. 57-70). ASTM International. <https://doi.org/10.1520/STP1070-EB>

Cavalcante, A.L.B., Borges, L.P.F., & Camapum de Carvalho, J. (2015). Tomografias computadorizadas e análises numéricas aplicadas à caracterização da estrutura porosa de solos não saturados. In *Solos Não Saturados no Contexto Geotécnico* (pp. 531-553). ABMS (in Portuguese).

Proceedings

Jamiolkowski, M.; Ladd, C.C.; Germaine, J.T., & Lancellotta, R. (1985). New developments in field and laboratory testing of soils. *Proc. 11th International Conference on Soil Mechanics and Foundation Engineering*, San Francisco, August 1985. Vol. 1, Balkema, 57-153.

Massey, J.B., Irfan, T.Y. & Cipullo, A. (1989). The characterization of granitic saprolitic soils. *Proc. 12th International Conference on Soil Mechanics and Foundation Engineering*, Rio de Janeiro. Vol. 6, Publications Committee of XII ICSMFE, 533-542.

Indraratna, B., Oliveira D.A.F., & Jayanathan, M. (2008b). Revised shear strength model for infilled rock joints considering overconsolidation effect. *Proc. 1st Southern Hemisphere International Rock Mechanics Symposium*, Perth. ACG, 16-19.

Barreto, T.M., Repsold, L.L., & Casagrande, M.D.T. (2018). Melhoramento de solos arenosos com polímeros. *Proc. 19º Congresso Brasileiro de Mecânica dos Solos e Engenharia Geotécnica*, Salvador. Vol. 2, ABMS, CBMR, ISRM & SPG, 1-11 (in Portuguese).

Thesis

Lee, K.L. (1965). *Triaxial compressive strength of saturated sands under seismic loading conditions* [Unpublished doctoral dissertation]. University of California at Berkeley.

Chow, F.C. (1997). *Investigations into the behaviour of displacement pile for offshore foundations* [Doctoral thesis, Imperial College London]. Imperial College London's repository. <https://spiral.imperial.ac.uk/handle/10044/1/7894>

Araki, M.S. (1997). *Aspectos relativos às propriedades dos solos porosos colapsíveis do Distrito Federal* [Unpublished master's dissertation]. University of Brasília (in Portuguese).

Sotomayor, J.M.G. (2018). *Evaluation of drained and non-drained mechanical behavior of iron and gold mine tailings reinforced with polypropylene fibers* [Doctoral thesis, Pontifical Catholic University of Rio de Janeiro]. Pontifical Catholic University of Rio de Janeiro's repository (in Portuguese). https://doi.org/10.17771/PUCRio.acad.36102*

* official title in English should be used when available in the document.

Report

ASTM D7928-17. (2017). Standard Test Method for Particle-Size Distribution (Gradation) of Fine-Grained Soils Using the Sedimentation (Hydrometer) Analysis. *ASTM International, West Conshohocken, PA*. <https://doi.org/10.1520/D7928-17>

ABNT NBR 10005. (2004). Procedure for obtention leaching extract of solid wastes. *ABNT - Associação Brasileira de Normas Técnicas*, Rio de Janeiro, RJ (in Portuguese).

DNIT. (2010). Pavimentação - Base de solo-cimento - Especificação de serviço DNIT 143. *DNIT -Departamento Nacional de Infraestrutura de Transportes*, Rio de Janeiro, RJ (in Portuguese).

USACE (1970). Engineering and Design: Stability of Earth and Rock-Fill Dams, Engineering Manual 1110-2-1902. Corps of Engineers, Washington, D.C.

Web Page

Soils and Rocks. (2020). *Guide for Authors*. Soils and Rocks. Retrieved in September 16, 2020, from <http://www.soilsandrocks.com/>

6.3 Artworks and illustrations

Each figure should be submitted as a high-resolution image, according to the following mandatory requirements:

- Figures must be created as a TIFF file format using LZW compression with minimum resolution of 500 dpi.
- Size the figures according to their final intended size. Single-column figures should have a width of up to 82 mm. Double-column figures should have a maximum width of 170 mm.
- Use Times New Roman for figure lettering. Use lettering sized 8-10 pt. for the final figure size.
- Lines should have 0.5 pt. minimum width in drawings.
- Titles or captions should not be included inside the figure itself.

Figures must be embedded in the text near the position where they are first cited. Cite figures in the manuscript in consecutive numerical order. Denote figure parts by lowercase letters (a, b, c, etc.). Please include a reference citation at the end of the figure caption for previously published material. Authorization from the copyright holder must be provided upon submission for any reproduced material.

Figure captions must be placed below the figure and start with the term "Figure" followed by the figure number and a period. Example:

Figure 1. Shear strength envelope.

Do not abbreviate "Figure" when making cross-references to figures.

All figures are published in color for the electronic version of the journal; however, the print version uses grayscale. Please format figures so that they are adequate even when printed in grayscale.

Accessibility: Please make sure that all figures have descriptive captions (text-to-speech software or a text-to-Braille hardware could be used by blind users). Prefer using patterns (e.g., different symbols for dispersion plot) rather than (or in addition to) colors for conveying information (then the visual elements can be distinguished by colorblind users). Any figure lettering should have a contrast ratio of at least 4.5:1

Improving the color accessibility for the printed version and for colorblind readers: Authors are encouraged to use color figures because they will be published in their original form in the online version. However, authors must consider the need to make their color figures accessible for reviewers and readers that are colorblind. As a general rule of thumb, authors should avoid using red and green simultaneously. Red should be replaced by magenta, vermillion, or orange. Green should be replaced by an off-green color, such as blue-green. Authors should prioritize the use of black, gray, and varying tones of blue and yellow.

These rules of thumb serve as general orientations, but authors must consider that there are multiple types of color blindness, affecting the perception of different colors. Ideally, authors should make use of the following resources: 1) for more information on how to prepare color figures, visit <https://jfly.uni-koeln.de/>; 2) a freeware software available at <http://www.vischeck.com/> is offered by Vischeck, to show how your figures would be perceived by the colorblind.

6.4 Tables

Tables should be presented as a MS Word table with data inserted consistently in separate cells. Place tables in the text near the position where they are first cited. Tables should be numbered consecutively using Arabic numerals and have a caption consisting of the table number and a brief title. Tables should always be cited in the text. Any previously published material should be identified by giving the original source as a reference at the end of the table caption. Additional comments can be placed as footnotes, indicated by superscript lower-case letters.

When applicable, the units should come right below the corresponding column heading. Horizontal lines should be used at the top and bottom of the table and to separate the headings row. Vertical lines should not be used.

Table captions must be placed above the table and start with the term “Table” followed by the table number and a period. Example:

Table 1. Soil properties.

Do not abbreviate “Table” when making cross-references to tables. Sample:

Table 1. Soil properties

Parameter	Symbol	Value
Specific gravity of the sand particles	G_s	2.64
Maximum dry density (Mg/m ³)	$\rho_{d(max)}$	1.554
Minimum dry density (Mg/m ³)	$\rho_{d(min)}$	1.186
Average grain-size (mm)	d_{50}	0.17
Coefficient of uniformity	C_u	1.97

6.5 Mathematical equations

Equations must be submitted as editable text, created using MathType or the built-in equation editor in MS Word. All variables must be presented in italics.

Equations must appear isolated in a single line of the text. Numbers identifying equations must be flushed with the right margin. International System (SI) units must be used. The definitions of the symbols used in the equations must appear in the List of Symbols.

Do not abbreviate “Equation” when making cross-references to an equation.